Low Field Microwave Absorption Studies on $BiFe_{(1-x)}Mn_{(x)}O_3$ Multiferrioc System

By

Brian Sibanda

Submitted in accordance with the requirements for the degree of

Master of Science

In the subject

Physics

at the

University of South Africa

Supervisor: Prof. V. S. Vallabhapurapu

Decemeber 2021

Declaration

Name : Brian Sibanda

Student number : 61365564

Degree : Master of Science in Physics

Exact wording of the title of the dissertation as appearing on the electronic copy submitted for examination: Low Field Microwave Absorption Studies on $BiFe_{(1-x)}Mn_{(x)}O_3$ Multiferrioc System.

I declare that the above dissertation is my own work and that all the sources that I have used or quoted have been indicated and acknowledged by means of complete references.

I further declare that I submitted the dissertation to originality checking software and that it falls within the accepted requirements for originality.

I further declare that I have not previously submitted this work, or part of it, for examination at Unisa for another qualification or at any other higher education institution.

_bsibanda_____ _____01-October-2021_____

SIGNATURE DATE

Dedication

- I am thankful to Professor V. S. Vallabhapurapu for giving me an exposure to the topic of multiferroic double perovskite $BiFe_{(1-x)}Mn_{(x)}O_3$. It sharpened, deepened and remolded my knowledge base.
- I am also grateful to Dr. T. Mahule for extensive and undivided support and attention during lab experiments.
- Davide Delmonte, Edmondo Gilioli and Andrea Sala for their support during the material synthesis process.
- The UNISA physics department was also supportive during project proposal defense phase and registration periods. I am grateful for their support.
- The encouragement from my family during the sleepless nights of simulations, computations and document compilations cannot be forgotten.
- Glory to The Creator who makes us observe and explain physics hidden in nature.

Publications

1. Brian Sibanda, Tebogo Sfiso Mahule, Davide Delmonte, Andrea Sala, Edmondo Gilioli and V.V. Srinivasu. “First detection of low field microwave absorption in the disordered multiferroic double perovskite $BiFe_{(1-x)}Mn_{(x)}O_3$” *Mater. Res. Express* 8 (2021): 066101

Glossary of Abbreviations and Symbols

ESR	:	Electron Spin Resonance.
DFT	:	Density functional theory.
P_{DM}	:	Polarization due to Dzyloshinskii-Moriya interactions.
DMI	:	Dzyaloshinskii-Moriya interaction.
d_{DM}	:	Dzyloshinskii-Moriya coupling coefficient
J	:	Superexchange magnitude.
U	:	Hubbard parameter.
GGA	:	Generalized Gradient Approximation
$\dot{A}$	:	Amstrong.
EPR	:	Electron Paramagnetic Resonance.
DOS	:	Density of States.
ODOS	:	Orbital density of states.
FC	:	Field cooled.
ZFC	:	Zero field cooled.
BMO	:	$BiMnO_3$.
BFO	:	$BiFeO_3$.
BFMO1	:	$BiFe_{0.5}Mn_{0.5}O_3$.
BFMO2	:	Bi_2FeMnO_6.
NNN	:	next nearest neighbor.
LFMA	:	Low field microwave absorption.
LF	:	Low field.
FE	:	Ferroelectric.
FM	:	Ferromagnetic.

AFM	:	Antiferromagnetic.
XRD	:	X-ray diffraction.
CFO	:	$CrFeO_3$.
Mn	:	Manganese.
Fe	:	Iron.
Bi	:	Bismuth.
Si	:	Silicon.
O	:	Oxygen.
Ag	:	Silver.
Y	:	Yttrium.
Pb	:	Lead.
Pt	:	Platinum.
Ni	:	Nickel.
DC	:	Direct Current.
AC	:	Alternating Current.
C	:	Coulomb.
K	:	Kelvin.
°C	:	Degrees Celsius.
T / T	:	Temperature.
E	:	Electric field strength.
χ'	:	Real magnetic susceptibility.
χ''	:	Imaginary susceptibility.
Hz	:	Hertz.
B	:	Bohr.

G	:	$\times 10^9$
M	:	$\times 10^6$
k	:	$\times 10^3$
μ	:	$\times 10^{-6}$
μ_B	:	Bohr magneton.
μ_s	:	Saturation magnetization.
μ_S	:	Spin magnetic moment.
μ_N	:	Nucleus magnetic moment.
B_{eff}	:	Effective magnetic moment.
M_p	:	Magnetization of paramagnetic material.
N	:	Atoms per given volume of material.
m_e	:	Electron mass.
e	:	Electron charge
h	:	Plank constant.
S	:	Spin angular momentum.
L	:	Orbital angular momentum.
g_L	:	Factor due to orbital angular momentum.
g_S	:	Lãnde factor due to spin angular momentum.
M_s	:	Saturation magnetism.
H_{ac}	:	Alternating magnetizing force.
H_o	:	Applied external magnetizing force.
H_{PP}	:	Line width.
H_1/H_2	:	Peak and minimum intensity signal Gauss or y axis reading.
V_S	:	Sample volume.

RWP	:	weighted-profile R-factor.
T_P	:	Temperature at point P.
Oe	:	Oersted
R_{in} / R_{out}	:	Inward rotation vector / Outward rotation vector.
eV	:	Electron volts.
emu	:	Electromagnetic unit.
c	:	Carrier mobility.
J/m^2	:	Joules per square meter.
IP	:	In phase.
OOP	:	Out of phase.
mol/h	:	Mole per hour.
$\vec{S}_i/\vec{S}_j$	:	Neighboring spin magnetic moments.
e_{ij}	:	Unit vector connecting neighboring spins.
a	:	Spin orbit and spin exchange constant of proportionality.
ξ'	:	First increased order insulating material rigour.
ξ''	:	Second increased order dielectric hardness.
χ_p	:	Dielectric stiffness.
Φ_n	:	Cyclon propagation mode.
Ψ_n	:	Extra-cyclon propagation mode.
X_{SM}	:	Potential barrier in pure semiconductor.
Φ_B	:	Schottky barrier in metal semiconductor junction.
Φ_M	:	Potential barrier in pure metal.
M_0	:	Magnetic moment of unit cell.
M_u	:	Magnetization of unit area.

P_r	:	Remanent polarization.
P_{eq}	:	Resultant polarization.
U_E	:	Electric field energy stored in cavity
U_H	:	Magnetic field energy stored in cavity
×	:	Multiplication sign.
P_l	:	Microwave power to load in square law detector.
P_W	:	Maximum microwave power.
R_0	:	Cavity resistance at resonance.
R_c	:	Cavity resistance off resonance.
R_l	:	Load resistance.
∂	:	Partial derivative.
Δ	:	Change in parameter
$VSWR$	:	Voltage standing wave ratio.
$n_1/\ n_2$	:	Transformer turns.
β	:	Bohr magnetron.
γ	:	Gyromagnetic ratio.
T_1/T_2	:	Transverse and longitudinal spin relaxation times.
E_c	:	Conduction band edge potential.
E_v	:	Valency band edge potential
LGD	:	Landau-Ginzburg-Devonshire
M.O.D.	:	Metal–organic decomposition
MVRH	:	Mott's Variable Range Hopping
XAS	:	X-Ray Absorption Spectroscopy
CW/CCW	:	Clockwise / Counter Clockwise

CSD	:	Chemical Solution Deposition
SCLC	:	Space Charge Limited Conduction
XPS	:	X ray photon spectroscopy
SRO	:	Strontium ruthenate
STO	:	Strontium titanate
EDS	:	Energy Dispersive X–ray spectroscopy
ß	:	Magneto-electric interaction multiplicative factor.
w. r.t.	:	with respect to.
ATC	:	Air Traffic Control

List of figures

List of equations

List of tables

Key Terms

$BiFe_{(1-x)}Mn_{(x)}O_3$; Double Perovskite; Multiferroics; Resonant microwave absorption; Low field microwave absorption; Line width; Electron paramagnetic resonance; magnetic hysteresis; Cryogenic studies; Paramagnetism.

Contents

Chapter 1

1 Multiferroics Fundamentals

1.1 Introduction

Multiferroics are materials are identified by a pair or more ferroic attributes such as ferrotorodial, ferromagnetic and ferroelectricity all existing side by side at the same time. They can be a single phase or multiple phases. In single phase systems a single compound is constructed by the bonding of peculiar atoms, while in multiple phase or composite multiferroics, different compounds are brought to exist together in an attempt to couple the different ferroic properties in the compounds. Influence of these ferroic properties on each other is very limited due to that it results from the different orbital configurations that drive magnetism and electric polarization in the material. For example, ferromagnets are characterized by d orbitals that are not totally filled are electrical transmitters as a result. Under ferroelectric conditions, due to the filled d orbitals they are non-conductive. The contradicting underlying ferroic nature of the two characteristics due to in part filled d orbitals hinders the existence of multiferroic characteristics at natural room temperatures (Hill 2000). Of the predominantly investigated or experimented compounds with multiferrioc nature, Bi based $BiFeO_3$ and $BiMnO_3$, the later has been determined as being ferromagnetic possessing a concentrated magnetic magnetization μ_s of 3.6 $\mu_s/f.u.$ At fairly elevated temperatures of approximately four hundred kelvin, (transition temperature), $BiMnO_3$ loses its ferromagnetic property. The loss in coupling in these single phase compounds gives way to multiphase ferroics. The coexistence of a ferroelectric and magnetic field characteristics within the same material can occur with coupling effects of 2 fields. There then arises a possibility of controlling one of the fields with the other as the two are coupled opening the door of various applications (N. A. Spaldin 2007).

1.2 Types of single phase multiferroic materials

1.2.1 Category one single form multiferroics

In such types of multiferroics, the source of magnetism and ferroelectricity properties are different ions in the compounds. Because of the independence of the origin of these two well-defined characteristics, they are therefore considerably unconstrained by each other. Critical temperatures (curie temperature) of magnetic and ferroelectric transformation is remarkably greater than Neel temperature (Khomskii. 2009.). According to (Golrokh. 2013) these types of multiferroics are characterized with substantial spontaneous polarization magnitudes in the range 10 to 100 $\mu C/cm^2$. This Type 1 multiferroic class is farther divided basing on the origin of their ferroelectric properties.

1.2.1.1 Geometric induced ferroelectricity.

(Aken, Palstra and A. Filippetti 2004) suggests that the partitioning of positive and negative charges in compounds such as (manganese (III) oxide) $EMnO_3$ is realized due to the twisting of the stacked polyhedra MnO_5 structure which then causes the shifting of the Y cations from their normal position.

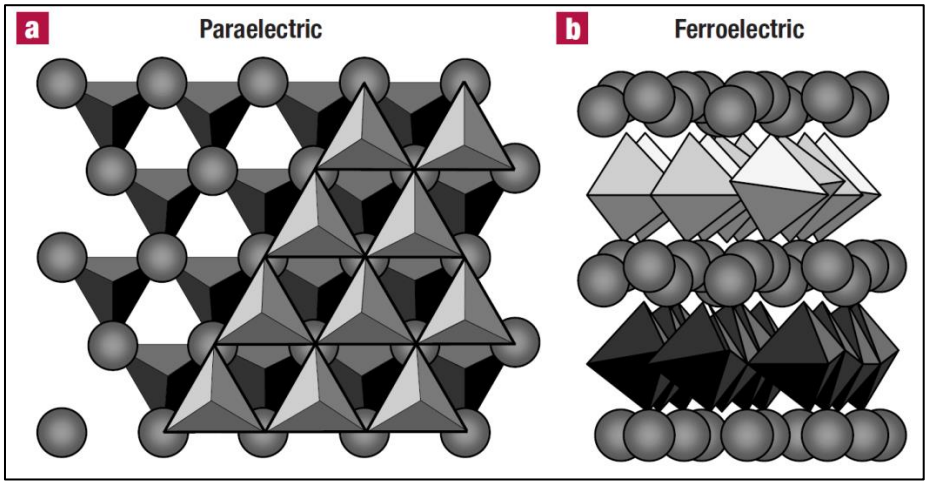

Figure 1: Paraelectric and ferroelectric crystal structure of $EMnO_3$. (a) The MnO_5 structures are assembled perfectly aligned with E cations in between the layers. (b) Twisting of the M pentaoxide causing a shifting of E cations from normal position (Aken, Palstra and A. Filippetti 2004).

Since E^{3+} and Mn^{3+} lack any lone pair of electrons, the realized ferroelectric characteristics arising from spatial arrangement of ions do not originate from lone pair activities. The chemical mechanism which then which then facilitates this process is ligand-field hybridization. The Mn cation at the center of the polyhedra MnO_5 remains unmoved and is the source of magnetism (Khomskii. 2009.).

1.2.1.2 Lone pair driven ferroelectricity

In the compounds $PbVO_3$, bismuth iron (111) oxide and $BiMnO_3$ the elements bismuth and lead both have electrons in the 6^{th} *s* spherical orbital. The electrons in this orbital do not take part in the chemical bonding and are believed to influence the ferroelectric characteristics in these compounds. These lone pair of electrons, feasibly are influenced by an external electric field giving way to positive and negative charges being segregated, which results in a ferroelectric property. The non-bonded pair of electrons in Pb and Bi can be remarkably oriented in a particular direction. This is suggested to be the mechanism by which ferroelectricity is realized in Bi and Pb compounds which are ferroelectric. It is the same mechanism by which double perovskite $PbZr_xTi_{(1-x)}O_3$ (Golrokh. 2013).

1.2.1.3 Charge ordering driven ferroelectricity

When the oxidation states of the transition elements in a particular compound are different, this leads to a ferromagnetic characteristic in the given compound. When the charges are not similarly arrange in space, there will be an electric dipole generated resulting in ferroelectricity.

1.2.2 Category 2 single form multiferroics

These are characterized by a robust relationship linking the ferroelectric and magnetic property in the material. Due to this a variation in one of the properties corresponding affects the magnitude of the other property. That is to say the electric polarization magnitude can be varied

by altering the material's magnetization and vice versa. These can be farther placed into two groups of collinear spin magnetic structures and spiral multiferroics. Spiral magnetic architecture is illustrated in Figure 2.

The spiral multiferoics are then divided into transverse-conical spin ferroelectrics, proper-screw spin multiferroics and perovskite manganites with cycloidal spin orders. When the electron spins on atoms located next to each other are inclined, there will be a disappearance of the symmetry observed in the horizontal mirror plane (Katsura and N. Nagaosa 2005) (I. A. Sergienko 2006) (Mostovoy. 2006). This is diagrammatically illustrated in Figure 2(b). Without practical experimentation, it has been demonstrated computationally that an electric polarization is set up by inclined spins of adjacent atoms which have protruding wave functions. This electric polarization is a result of spin-orbit interaction. Thus, to say that there will be a movement of spin current between the canted sites that have overlapping wave functions.

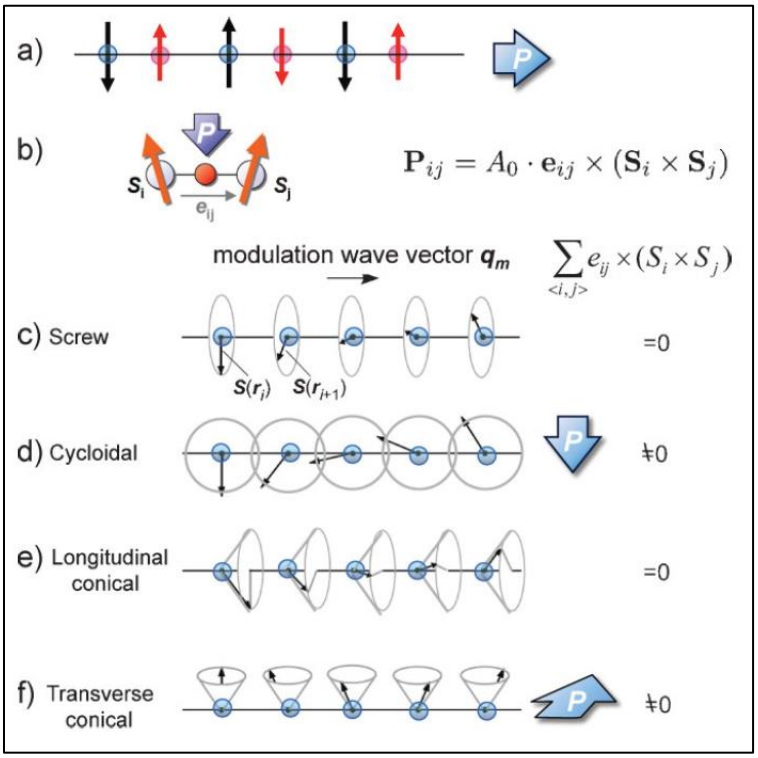

Figure 2: Inversion symmetry destruction in (a) strictly parallel magnetic structure (b) spin canted magnetic structure (c-f) Magnetically generated ferroelectricity in different spiral spin structures (Y. Tokura 2010).

1.3 Single phase simple perovskite multiferroic $BiMnO_3$

1.3.1 Dielectric and vibration characteristics of single phase multiferroic $BiMnO_3$

By means of interferometer Bruker 66 V ratio of the EMR intensity reflected to the quantity of EMR incident on the BMO sample was determined. The detector was a mercury cadmium telluride and for other spectral ranges a Si photodiode was utilized which allowed a detection scope of 2 cm^{-1} in the phonon region. The three axes of unequal lengths of a, b and c of simple perovskite $BiMnO_3$ do not permit the use of polarized radiation to extract data about the sample, therefore unpolarized radiation was employed (Mohamed, et al. 2016). Using steps of ±2 K resolution the sample temperature was kept between 10 and 300 K so as to prevent thermal instability. A datum of a gold mirror which was placed near the perovskite $BiMnO_3$ and parallel aligned using helium–neon gas laser was used. The Kramers-Kronig transformation was used to mathematically break down the complex reflectance spectrum of the $BiMnO_3$ into a refractive index spectra and extinction coefficient spectra (Gruner. 2002). It is from these that the absorption spectrum was computed. Input values were taken from out of the required boundary of 50 ÷ 700 cm^{-1} to 30 to 10000 cm^{-1} so as to improve on the accuracy.

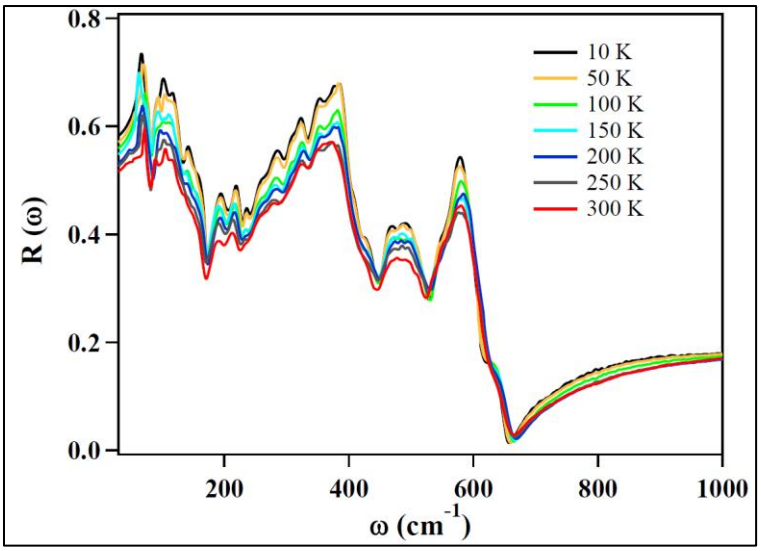

Figure 3: Reflectivity spectra of bulk $BiMnO_3$ within the infrared spectrum (Mohamed, et al. 2016).

The ratio of the light reflected from the $BiMnO_3$ sample in relation to an amount of incident within the infrared spectra is shown in Figure 3. The reflectivity increase to a maximum as the temperature approached 0 K. Between 590 to 690 cm^{-1} reflectivity was observed to be independent of the temperature.

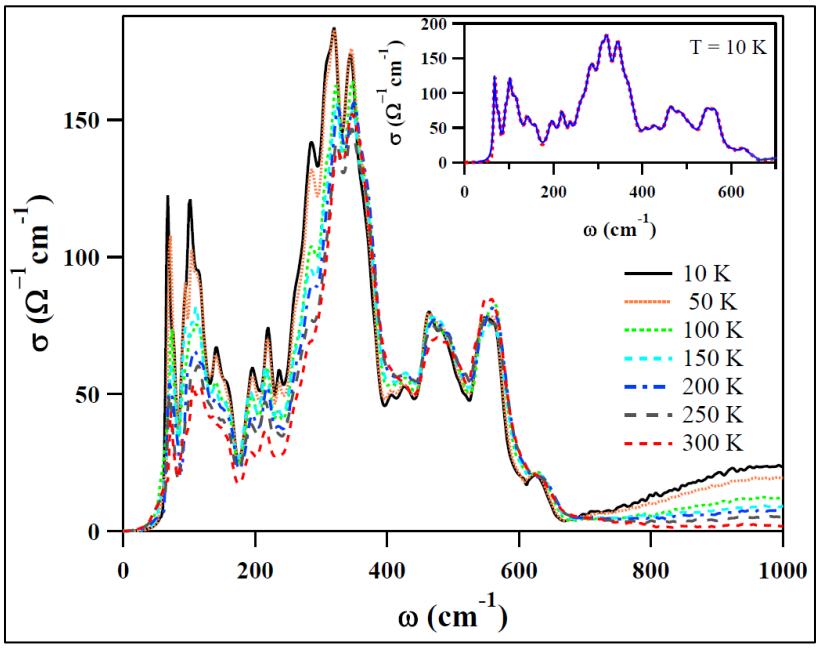

Figure 4: Optical conductivity of multiferroic simple perovskite $BiMnO_3$ in the infrared zone the with an insert of optical conductivity at 10 K (Mohamed, et al. 2016).

In Figure 4 optical conductivity computed by Kramers-Kronig transformation from the reflectivity is illustrated. The phonon parameters were realized by connecting the conductivity to the total of Lorentz oscillator model which defined the response of bulk $BiMnO_3$ to electromagnetic waves. The ferromagnetic transition was not associated with any structural variations of the sample as could be supported by the perfect fitting of 25 oscillators at 10, 100, and 150 K. Because of line broadening which occurred at 300 K, some modes were going to be superimposed, therefore 21 oscillators were utilized. In order to verify the centro-symmetric structure of $BiMnO_3$ Raman spectroscopy of 3 micro-crystals was carried out and the outcomes were all the same. This was done because modes which are infrared active in systems with center of symmetry or centro-symmetric structure are not Raman active. Taking into consideration that diffraction data phase transformation under 300 K are not included, therefore the experiment was

carried out at room temperature. Only sixteen lines of the anticipated 30 were noted as illustrated in the Raman spectrum in Figure 5. Three of the 30 lines at approximately 400 cm^{-1}, were imperfectly resolved.

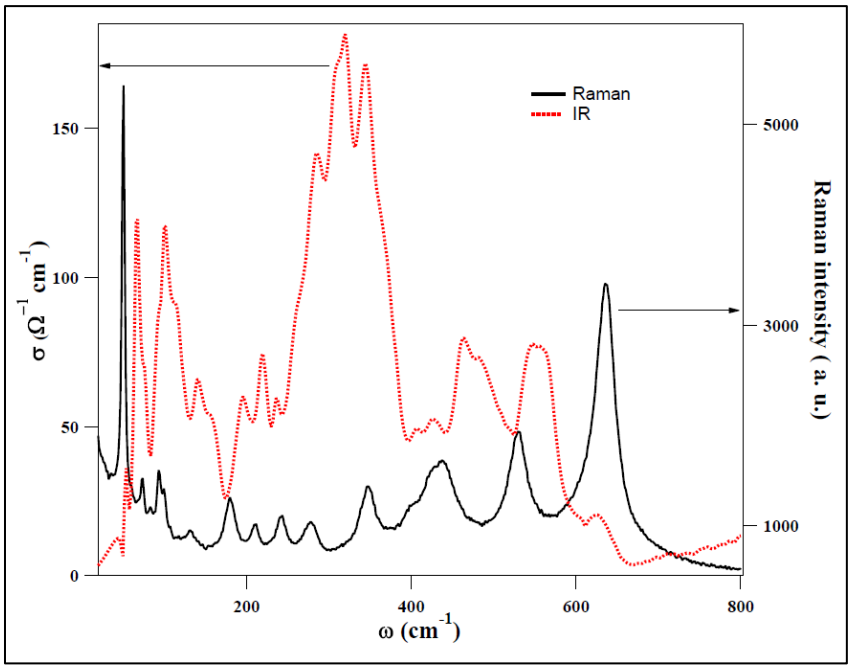

Figure 5: Raman spectrum of multiferroic simple perovskite $BiMnO_3$ (Mohamed, et al. 2016).

1.3.2 Controlling the electric polarization in multiferroic $BiMnO_3$ using magnetic-field

(Hill. 2001) attributed the electric polarization being a result of the stabilization of a distorted simple perovskite structure by Bi 6s electrons. A contradiction however arose in which experimental and direct computation from physical quantities yielded values indicating that $BiMnO_3$ has a C2/c structure. This space group does not allow ferroelectricity in $BiMnO_3$. In (Pchelkina. 2008) the researcher presented the idea that $BiMnO_3$ ferroelectric properties were a result of improper polarization then in (Z. V. Pchelkina. 2010) theoretically showed that the electric polarization in $BiMnO_3$ is of a non-distorted crystal cell and was linked to unseen antiferromagnetism. The problem was tackled by constructing a Hubbard model which comprised of 40 Wanner functions for the 4 Mn 3d bands in each unit cell as shown in the equation below.

$$\hat{\mathcal{H}} = \sum_{ij}\sum_{\alpha\beta} t_{ij}^{\alpha\beta}\,\hat{c}_{i\alpha}^{\dagger}\hat{c}_{j\beta} + \frac{1}{2}\sum_{i}\sum_{\alpha\beta\gamma\delta} U_{\alpha\beta\gamma\delta}\hat{c}_{i\alpha}^{\dagger}\hat{c}_{i\gamma}\hat{c}_{i\beta}\hat{c}_{i\delta} \ldots\ldots\ldots\ldots\ldots\ldots \quad \text{Equation 1}$$

These functions encompassed three t_{2g} and two e_g orbitals, for every individual spin octahedral splitting and for all various four Mn location. $U_{\alpha\beta\gamma\delta}$ represents the coulomb screening interactions and was obtained by merging mathematically limited Density Functional Theory with Random Phase Approximation. The screening effect of the electrons on the Fermi level by 3d electrons on the oxygen which has an effect of reducing the effective Coulomb repulsion U was included in the RPA. The overall model was then solved by Hartree-Fock method.

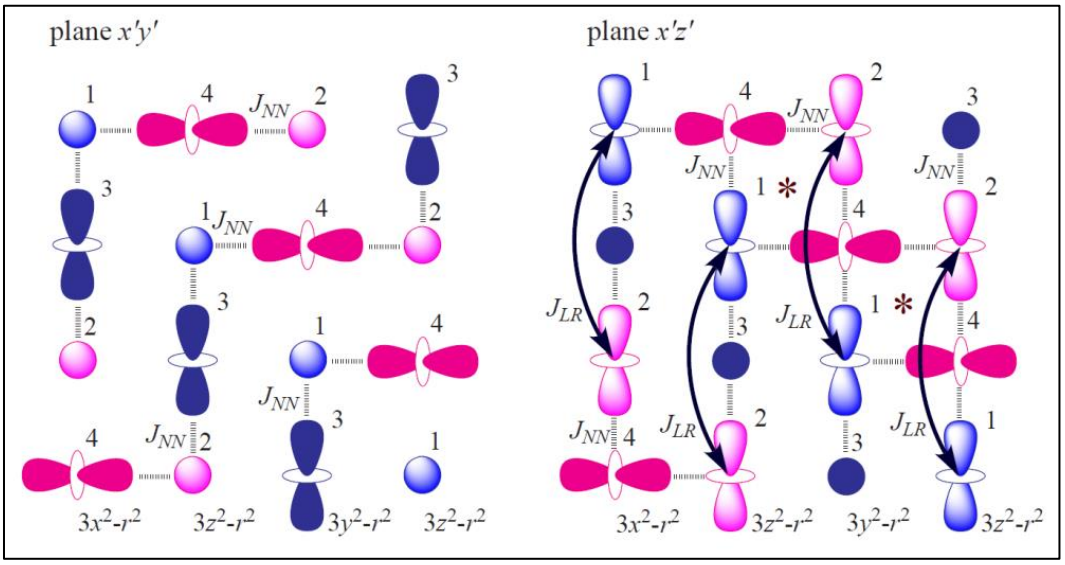

Figure 6: Short range and long range interactions at 4 Bi sites in $BiMnO_3$ orbital ordering. (Z. V. Pchelkina. 2010)

1.3.2.1 Breaking of inversion symmetry in $BiMnO_3$ and associated magnetic properties

The researchers proposed that lattice distortion takes precedence to the atomic orbital arrangement shown in Figure 6. The orbital orientation however presets the electronic interactions that occur in such a system. The architecture itself assumes monoclinic ($C2/c$) or orthorhombic (P_{nma}) which are associated with the normal nearest-neighbor interactions. The presents of longer-range (LR) interactions designated by arrows in Figure 6, via the manganese atoms between on the distant atoms was not overruled in this orbital orientation. The researchers proposed the existence of these long range interactions basing on that the coulomb site repulsion U is inappreciable and will therefore materialize as a higher value in the expansion of $\frac{1}{U}$ coupling the distant sites between the Mn locations. These long range interactions were viewed as being similar in mechanism to superexchange with the character of oxygen being replaced by empty d_{z^2} and $d_{x^2-y^2}$ orbitals of the central manganese locations.

The interatomic bonds of nearest-neighbor and longer-range (LR) interactions were computed by mathematically relating the sum of Hartree Fock energies to the Heisenberg model. The nearest-neighbor values were approximately 5 and 6 meV, while the longer-range value was roughly 3 meV. Between site 4 and 4 and site 1 and 2 they were limited interactions of about 1 meV which spanned over the inversion center. All these interactions were believed to completely characterize magnetic ordering in $BiMnO_3$ at lowest energy state. For an inversion symmetry to be possible, the researcher assumed that they is no spin orbit coupling which then lead to an antiferromagnetic ordering permanence. The AFM architecture tends to extinguish the inversion center represented by arista marks. The destruction of the inversion symmetry results in electric polarization.

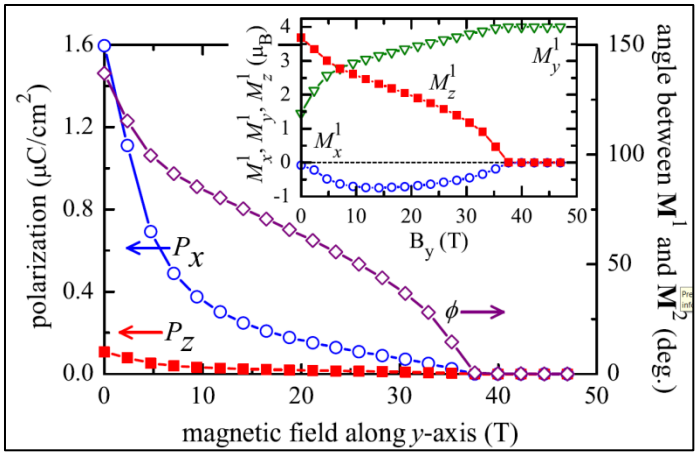

Figure 7: Relationship between magnetic field and polarization (Z. V. Pchelkina. 2010).

Spin orientations at the four manganese locations permit symmetrical operations in which the polarization would orient in the zx plane. A computation of the separate electric polarizations P of the degenerate orbitals t2g and eg-band by (Pchelkina. 2008), yielded $P_x^{t2g} = -0.8\ \mu C cm^{-2}$ and $P_z^{t2g} = -0.3\ \mu C cm^{-2}$. This was interpreted as being an opposite polarity of the t_{2g} when compared to $e_g$band.

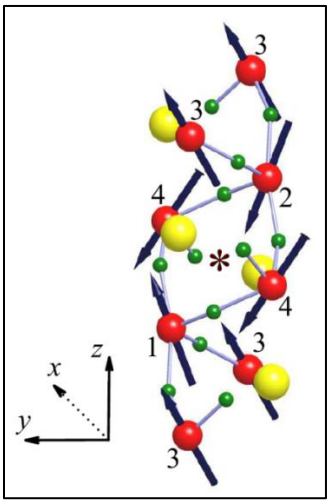

Figure 8; Representatation of magnetic ordering and crystal fragment of the least energy state as calculated by Hartree Fock (Z. V. Pchelkina. 2010).

Spin orbit coupling causes spins to move out of a collinear spin of the AFM state to a ferromagnetic configuration which has the consequence of diminished electric polarization magnitude. As indicated in lowest energy diagram according to Hartree Fock computation in Figure 8, spin magnetic moments at location one and two of the Mn atom have an angle of 137^0. The polarization is corresponding weakened to 0.1 μCcm^{-2} in the z direction and 1.6 μCcm^{-2} in the x direction. By administering a magnetic field in the y axis, it will saturate the ferromagnetism and regulate the effect. Considering that the total magnitude of the local magnetic moment is more or less maintained constant, a reduction of the antiferromagnetic components in both the x and y axis is counteracted by elevation of the FM component in the y-axis direction. This corresponding reduces the ferroelectric polarization.

The ferromagnetic magnetic moment conditions at location 1 and 2 of the manganese sites are therefore fortified by an adequately huge magnetic field of approximately 35 Tesla which in turn reinstitutes the centred space group, C2/c symmetry (Solovyev, Pchelkina and Pisma 2009). There is a relationship between the angle between M_y^1 and $M_z^1$and the electric polarization. The magnitude of polarization totally diminishes when the spins M_y^1 and M_z^1 are parallel and the decrease is more steeper as compared to the decrease of cant angle with magnetic field in the x axis as shown in Figure 7. This steeper decrease is shown by P_x and P_z which fall by more than half in approximately 5 Tesla magnetic field which is about Ø = 100°. It was also observed that P_z was also significantly small as compared to P_x. In this work separation of intrinsic and extrinsic polarization property of the sample still required to be carried out by experimentation.

1.3.3 Multiple magnetic transitions detected in multiferroic $BiMnO_3$ depending on temperature

For a comprehensive understanding of $BiMnO_3$, DC magnetization, AC susceptibility and magnetic hysteresis were the three characteristics investigated in $BiMnO_3$ by (Chou, et al. 2009). By decreasing the temperature of the $BiMnO_3$ sample from 300 K to 0 K in a magnetic field of 50 Oe or 3978.87 amperes/meter the DC magnetization of the sample was determined in a superconducting quantum interference apparatus magnetometer. The measurements were carried

out at three different pressures of 8.7, 9.4 and 11.9 $kbar$. As shown in Figure 9, pressure and temperature affect the DC magnetization of $BiMnO_3$ with the largest magnetization however appearing at ambient pressure and 0 K.

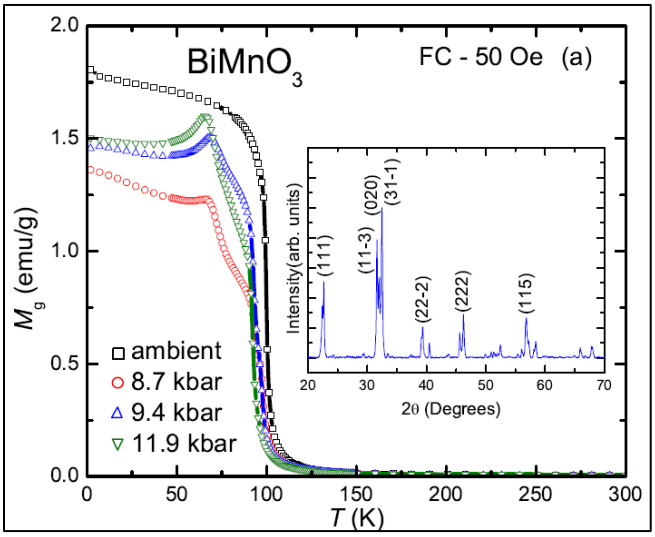

Figure 9: Mg(T) plots with contrasting pressure in fifty Oe. Insert shows the normalized powder diffraction pattern between 20 to 70 (Chou, et al. 2009).

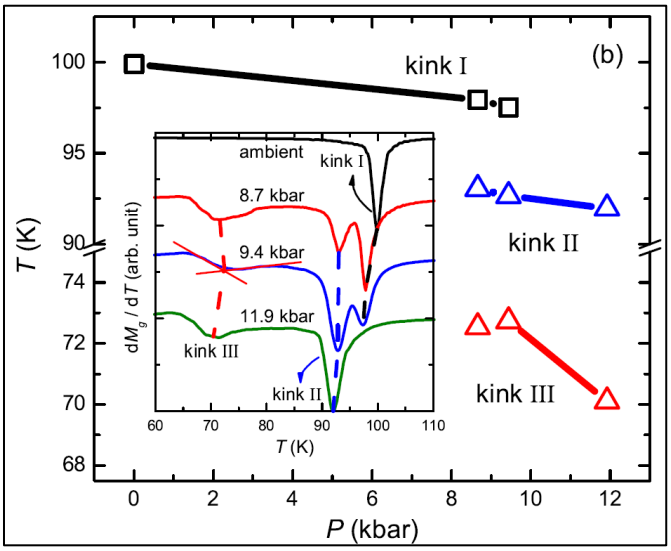

Figure 10: Temperature relationship of kink points, obtained using the sub-picture of (b) illustrating the dM/dT graph at contrasting kbar (Chou, et al. 2009).

1.3.3.1 Relationship between magnetization and pressure at 50 Oe of multiferroic $BiMnO_3$

(Chou, et al. 2009) determined the derivative of the DC magnetization curves in Figure 9 and the resultant is shown in the insert in Figure 10. The derivative was then plotted against the temperature for all the curves at various pressures of ambient, 8.7 $kbar$, 9.4 $kbar$ and 11.9 $kbar$. The minima of all the curves were seen to correspond at a more or less within the same temperature range. These minima were joined together to give three distinct kinks which were characteristic to particular magnetic ordering in the $BiMnO_3$ sample. Kink 1 was however composed of the first three lower pressures ambient, 8.7, and 9.4 $kbar$. At the extreme pressure of 11.9 $kbar$ kink 1 fails to exist. Kink 2 and 3 do not exist at ambient pressure but however manifest at the other higher pressures. A negative slope displayed by kink 1 as the pressure is increased was seen to disappear at 11.9 $kbar$. The graph can be interpreted as follows, increasing pressure on the $BiMnO_3$ sample decreased its temperature this is accompanied by a ferromagnetic transition. The research noted and concluded that a stable magnetic phase was represented by kink 2 and kink 3 as these appear at the same pressure of 8.7 $kbar$ and 9.4 kbar and were farther noted until 11.9 $kbar$. It was observed that kink 1 and kink 2 were characterized by steeper increase in the DC magnetization as compared to kink 3. This was explained in terms of establishment of a ferromagnetic state while decline in the DC magnetization was interpreted as the establishment of an antiferromagnetic state.

1.3.3.2 $BiMnO_3$ properties of the EMU magnetization and magnetic hysteresis loop as a function of various temperatures at pressures, 9.4 and 11.9 $kbar$.

A complete comprehension of the phases appearing at different pressures the researchers farther studied the hysteresis loop and DC magnetization curves at ambient and two last extreme pressures. The data obtained was plotted in the diagrams shown below.

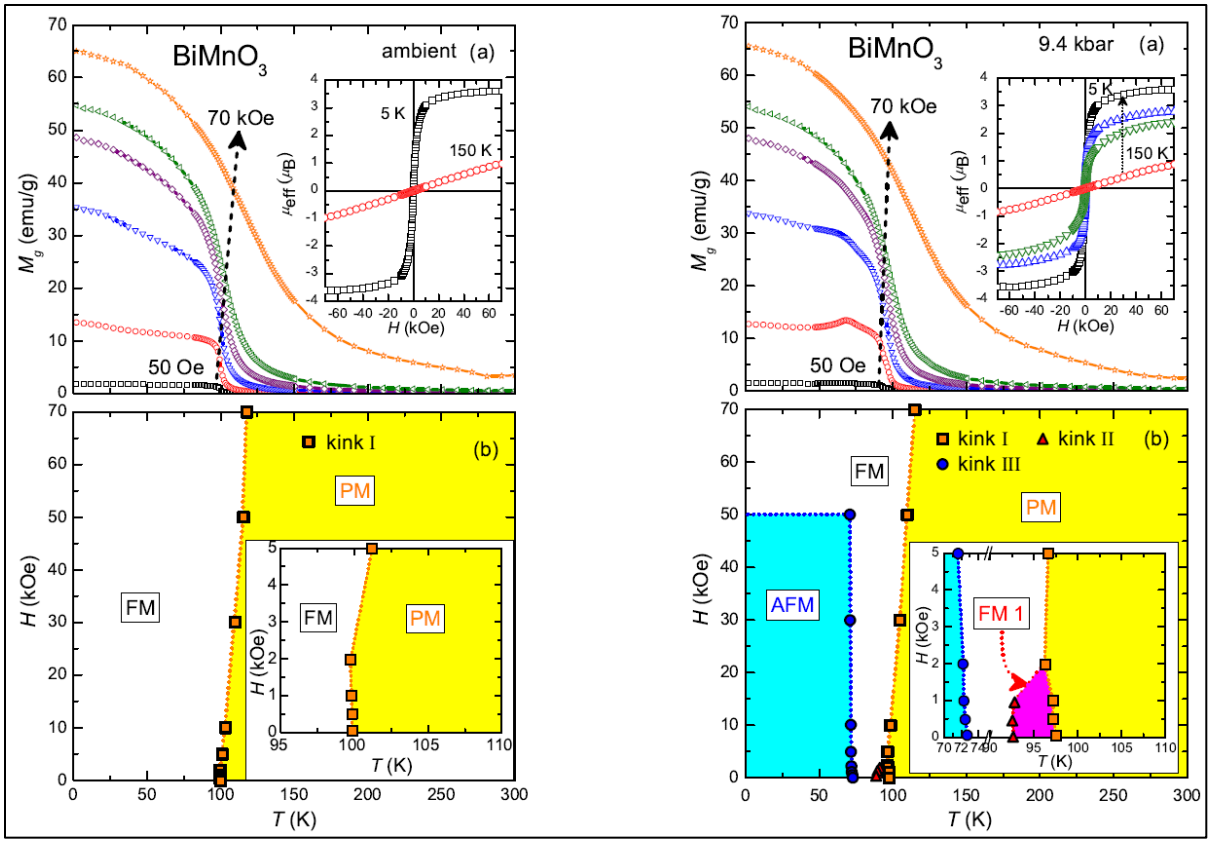

Figure 11: (Top diagrams (a)) DC magnetization vs temperature at ambient and 9.4 kbar pressure. (Bottom diagrams (b)) Magnetic phase transitions with temperature variations (Chou, et al. 2009).

For DC magnetization at ambient and 9.4 $kbar$ was observed to increase with an in the applied magnetic field. This was clearly interpreted as an amplification of the direction in which the electron spins to the applied H. This observation was in harmony with a modified simplified Heisenberg mathematical model of ferromagnetism, Ising model according to (Hassink 2004). The Ising model will allow phase transitions occurring in magnetic ordered systems to be described with less trouble. The hysteresis loop at 5 K temperature rapidly saturated at approximately 10 kOe with a minute loop. This was interpreted in terms of soft ferromagnetism while a paramagnetic behavior was noted at 150 K. The straight line which does not saturate in the hysteresis plot proved the paramagnetic behavior at elevated temperatures of 100 K or more. An interesting behavior is noted when the magnetic force is applied under the influence of an ambient pressure of 9.4 $kbar$. As shown by the DC magnetization curve and phase temperature diagrams on the extreme right in Figure 11, two more magnetic ordering antiferromagnetic and

ferromagnetic phases are generated when an external pressure of 9.4 $kbar$ is introduced. A farther increase in the ambient pressure to 11.4 $kbar$ still generates three magnetic orders of which the antiferromagnetic one disappears with a farther increase in the magnetic above 5 kOe. This was defined by kink 3.

1.3.3.3 Relationship between frequency and AC sensitivity at room kbar and 11.9 kbar for multiferroic $BiMnO_3$

The influence of a sinusoidal varying magnetic field on $BiMnO_3$ at ambient and 11.9 $kbar$ was analyzed. An AC magnetic field of 3.5 Oe and at either 1 Hz, 10 Hz or 100 Hz was applied to the sample firstly at ambient then 11.9 $kbar$. Kink 1 appeared at ambient pressure while kink 2 and 3 where observed at 11.9 $kbar$. These kinks were noted at 90 K for kink 2 and 68 K for kink 3.

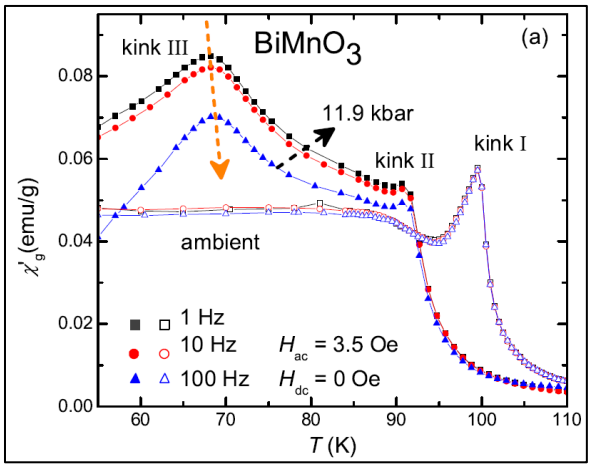

Figure 12: Alternating magnetic field effect on magnetization of $BiMnO_3$ at various temperatures (Chou, et al. 2009).

Evidence of long range ferromagnetic architecture is illustrated in by Figure 12, where a change in number of complete cycles per second of the magnetic field and temperature does not rely on kink 1 at depressed frequencies. However, the relative deviation of kink 3 was noted with a spike in the magnitude of AC magnetization χ_g' per factor of 10 frequency change, was determined to

be 5.88×10^{-3} at 1 and 100 Hz. According to (A. A. Belik and E. Takayama-Muromachi 2008) the magnitude falls within the catergory ($\times 10^{-3}$) for which canonical spin-glass is suited. The spin-glass architecture materialized together with the antiferromagnetic evolution demonstrating an association within them. A brief relaxation time was demonstrated by kink 1 which maintains nearly the same magnitude of intensity. An extensive relaxation time was defined as the reason for the huge intensity variations captured in kink 2 and kink 3. It was suggested that this manifestation could have been a spin canted antiferromagnetic ordering for kink 3 and spin canted ferromagnetic architectures for kink 2. There was a clear variation in the slope at approximately 68 K for kink 3 as shown in Figure 13. It was inevitable that the slope variations were a result of dissimilar magnetic orderings.

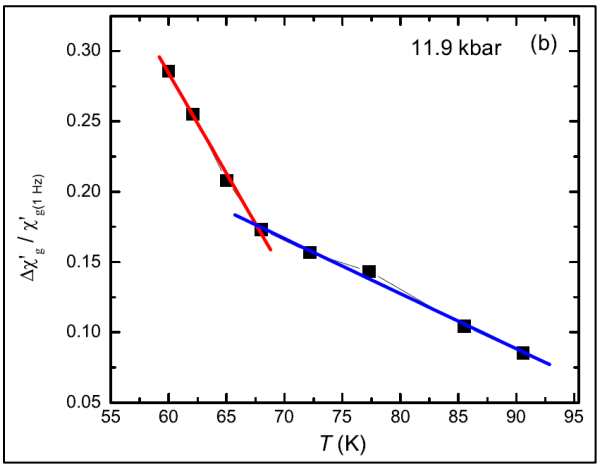

Figure 13: Change in susceptibility over susceptibility against temperature (Chou, et al. 2009).

1.3.3.4 Ferroelectric polarization in multiferroic $BiMnO_3$ at room temperature

Using a frequency of 1000 Hz the electric polarization hysteresis loop of $BiMnO_3$ determined using TF analyzer 2000 ferroelectric tester and the corresponding plot is shown in Figure 14 below.

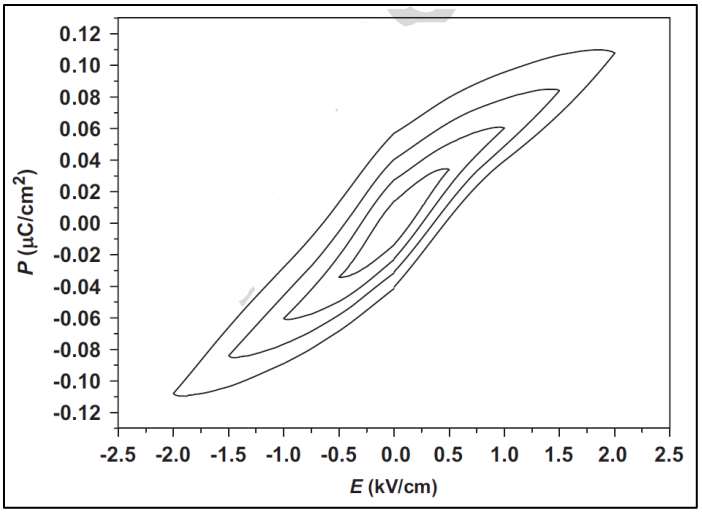

Figure 14: Electric polarization hysteresis in $BiMnO_3$ (Chi, et al. 2007)

At a coercive field E_c of 0.5 kV/cm the researchers measured a spontaneous polarization of 0.11 $\mu C/cm^2$ and a remnant polarization of P_r of 0.06 $\mu C/cm^2$. As compared to data published by (Santosa, et al. 2002) these values where notably lower.

1.3.3.5 Magnetization of multiferroic $BiMnO_3$ as function of temperature

The magnetic hysteresis values were determined utilizing MagLab System and the accompanying plot is illustrated in Figure 15. The magnetization values were measure under field cooled conditions at a magnetic field of 0.1 T. Strikingly sudden elevation of magnetization at a field less than 0.3 T signified an under laying ferromagnetic property of $BiMnO_3$. Saturated magnetic moment and its refined value were approximately equal to each other 3.14 μB and 3.2 μB respectively. The later value was determined by neutron powder diffraction. However both figures were significantly minute in comparison to 4 μB the totally aligned state of high spin $3d^4$ manganese (III). The researchers attributed the low magnetic moment to spin canting caused by lone electrons of the $6s^2$ orbital of the bismuth (III) cation prompting a decrease of the spin magnetic moment being added to the total magnetic moment.

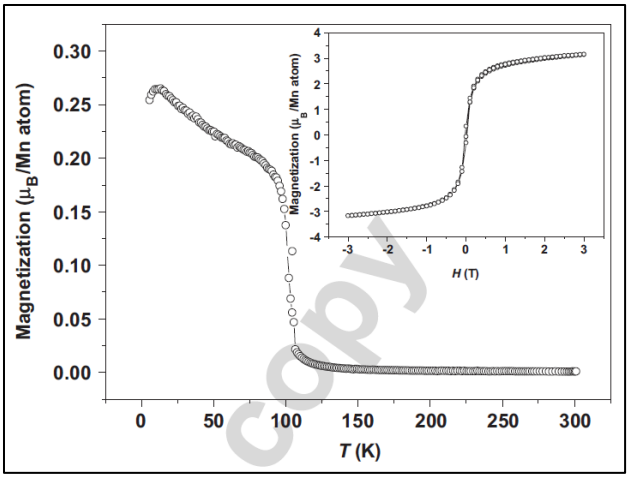

Figure 15: Magnetic hysteresis plot for $BiMnO_3$ (Chi, et al. 2007).

The spin magnetic moments that remained aligned after removal of an external magnetic field remanence magnetization M_r was determined to be 0.34 μB/Mn while the resistance of ferromagnetic $BiMnO_3$ to become demagnetized, coercive field was 0.02 T. In correlation to $BiFeO_3$ and $BiCrO_3$ systems, the remnant magnetization values M_r of $BiMnO_3$ were significantly higher. This was determined to be as a result of the antiferromagnetic nature of the $BiFeO_3$ and $BiCrO_3$ systems compared to the ferromagnetic ordering in $BiMnO_3$. $BiFeO_3$ has a remnant magnetization values M_r of 0.05 μB/Fe and that of $BiCrO_3$ is 0.05 μB/Cr.

An understanding of the source of magnetoelectric properties in $BiMnO_3$ was approached by realizing its crystal structure. By utilizing electron diffraction where minute sample quantity is required and neutron powder diffraction where conventionally larger amounts of sample are required, $BiMnO_3$ was resolved to be in the monoclinic crystal system (C2). The image is shown in Figure 16 and designated by the region I. (Atou, et al. 1999) and (Montanari, et al. 2005) put forward that $BiMnO_3$ irrespective of the preparation conditions will exist in many forms at room temperature. They attributed this characteristic to being an intrinsic behavior which resulted from being quenched from elevated temperatures and pressure.

1.3.3.6 High resolution electron microscope of multiferroic $BiMnO_3$

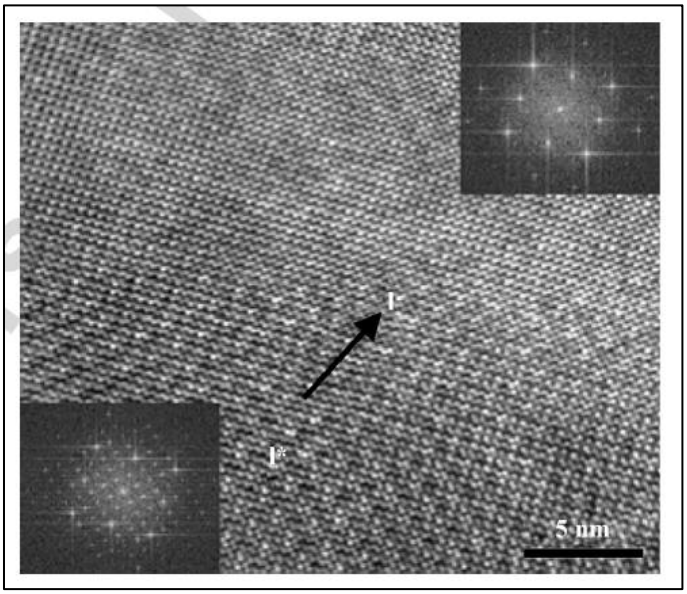

Figure 16: High resolution electron microscope of BiMnO3 (Chi, et al. 2007).

From the HREM being supported secondly with electron diffraction performed on specifically chosen individual grains of $BiMnO_3$, the transition into a clear cut periodic region was not uniform. The well-defined region was developed from a prolonged irradiation to electron beam and was an indication of a metastable crystal $BiMnO_3$ which when heated reconstruct into more ideal or large crystals. The encroachment direction was in the direction of the arrow from I* to I.

1.3.4 Deformations in $BiMnO_3$ crystal architecture along with Jahn-Teller disfiguring

1.3.4.1 Crystal system format along with Jahn-Teller disfiguring in $BiMnO_3$

It was found that $BiMnO_3$ has a heavily distorted perovskite architecture and excluding the elevated temperature values of the Mn-O bonds, the proportionality of most lengthy ones, their magnitudes were much larger as compared to those in $LaMnO_3$ a similar perovskite (B.A.A. Elemans 1971). To comprehend this particular solid state system the gradient of the electron

density or LSDA was employed together with an augmented GGA, (GGA + U) where a localization correction was applied to consider the on-site interaction. The two approaches where then optimized. Coulomb repulsion were taken to be 2, 4 and 8 eV. However regardless of the technique used in optimization, A and D non-centrosymmetric atomic arrangement consistently merged to the indistinguishable inversion center symmetry corrected architecture. The corrected structure was identical to a high temperature monoclinic structure. Low temperature monoclinic also reduced to the same optimized structure after relaxation. Jahn-Teller distortions were observed to decline as a result of structural optimization (D. W. Solovyev 2010).

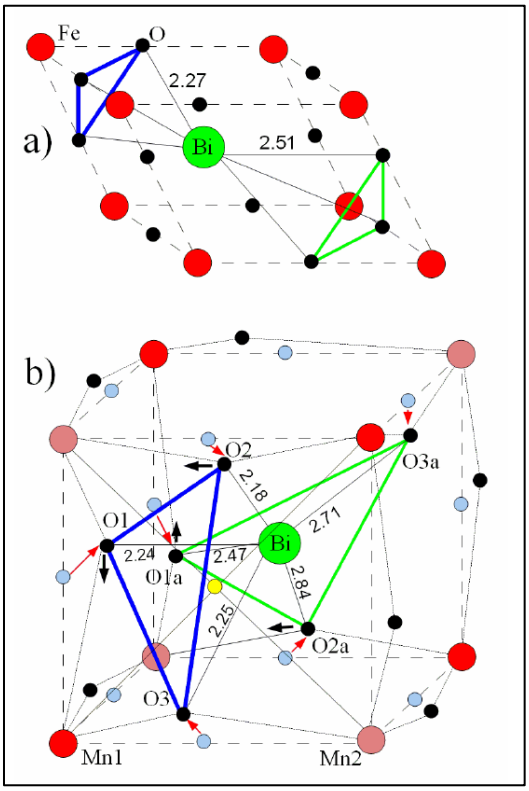

Figure 17: A representation of the ideal and real position of oxygen atoms in $BiMnO_3$ and $BiFeO_3$ at low and high temperatures.

(Kanamori 1960) states the Jahn-Teller distortions are result of electron-lattice interactions and are included in the GGA. The value of U, on-site Coulomb revulsion have an influence of widening the energy gap, thereby maintaining an appropriate value which in turn governs the chemical bonding within the system. This is to say the electronic structure computations must

save the characteristics of an insulating material so as to appropriately depict the impact of Jahn-Teller effect. Genuine metallic system can therefore not substitute highly insulating systems in generalized gradient approximation. This is taken from a stand where the nature of double exchange and superexchange in metallic systems can neither be utilized as a reference point to model magnetic ordering in insulators (Terakura 1999).

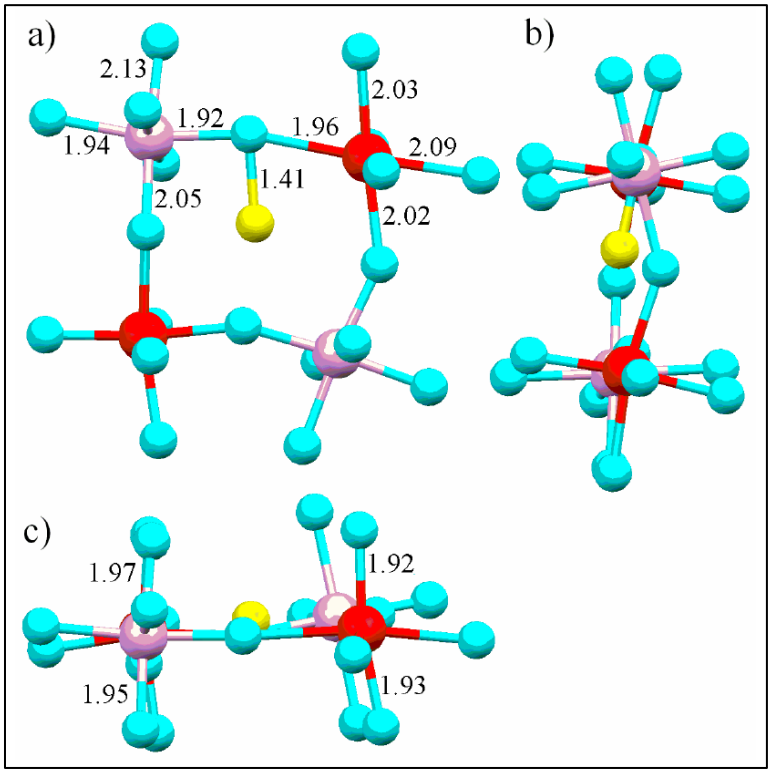

Figure 18: Three dimensional view from (c) top (b) side and (a) front of the $BiMnO_3$ molecule with the yellow atom representing interstitial oxygen.

From their computations susceptibility of MnO_6 octahedra distortion to interdependency consequence and the magnitude of the Coulomb repulsion U in the GGA + U technique was unquestionable. Generalized gradient approximation as a result of surge of 4 small Manganese-Oxygen bond lengths along with reduction of two stretched ones, practical Jahn-Teller distortions are undervalued. The best (despite the fact that not great) concurrence with practical obtained information was acquired at $U = 2\ eV$. This figure was determined corresponding to the miniaturized energy Hubbard representation, which had been formulated from manganese 3d-

bands using first-principles electronic architecture computations (Pchelkina 2009). The combining or interfusion of oxygen 2p orbitals and 3d orbitals of manganites contribute to the shielding of 3d-states positioned closer to the Fermi level. Shielding in this manner is remarkably powerful and considerably decreases the Coulomb interaction U practical value for most transition-metal oxides in the small energy region (V. I. Solovyev 2008). When 4 and 8 eV U values were used the Jahn-Teller distortions were decreased due to an upsurge of the 4 short Mn-O bond distance and the MnO_6 octahedra is also enlarged. It was by all accounts sensible in light of the fact that enormous U diminishes the $3d$-$2p$ hybridization and in this way diminishes the bonding effects. It is believed that the structural differences in $BiMnO_3$, $LaMnO_3$ and $BiFeO_3$ are a result of Jahn-Teller distortion competitions around the manganese cation location and the local off-centrosymmetric alterations encompassing bismuth cation neighborhood.

1.3.4.2 Defects in $BiMnO_3$

It was suggested that defects are the origins of energy unstable structures in $BiMnO_3$ as observed from experimentation data (Solovyev. 2010). To verify the like hood of this proposition the enthalpy of formations of $LaMnO_3$, $BiFeO_3$, and $BiMnO_3$ were computed. The initial parameters used for optimization were from the low temperature BiMnO3. Cation and anionic voids and also oxygen occupying holes between the larger metal cations were taken into account as the defects in the samples. Secondly they considered the tetrahedral void equivalent to 3c location in a cubic crystal, to be filled with an impurity atom. The enthalpy of formation of $BiMnO_3$ was found to be relatively lesser as to that of $LaMnO_3$ and $BiFeO_3$. This observation was true as according to (Belik, Kolodiazhnyi and K. Kosudac 2009). An understanding of how oxygen saturated crystal structure of $BiMnO_3$ affected result was carried out by using three crystal structures of $BiMnO_3$, low temperature, A and D with cell structure of twenty, forty and eighty atoms were determined their enthalpy of formation and fully optimized. The initially used crystal structures had much greater Jahn-Teller distortion than usual conditions. The first observation made was an increase of the oxygen impurity in all the systems considered did not transform the system into a metallic conductor but persisted as an insulator. This was contrary to the large

scale understanding that the $BiMnO_3$ insulator becomes a metal and electrons from the manganese $3d$ band are received by interstitial oxygen.

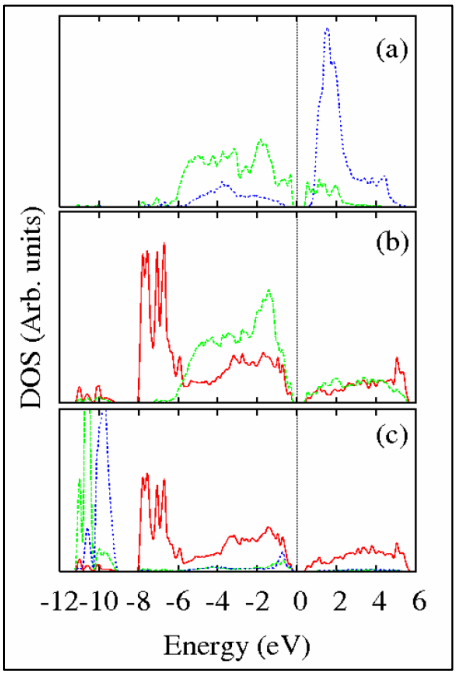

Figure 19: Density of state of $BiMnO_3$ with interstitial oxygen.

It is believed that impurity oxygen shared a pair of electrons with an oxygen atom in the $BiMnO_3$ atomic structural arrangement. The length of the O_i-O2 bond formed is much greater than the one of an oxygen molecule. However it is much smaller as than the oxygen-oxygen bonding in MnO_6 octahedron along with the separation of interstitial oxygen and adjacent O^{2-} locations. The density of states in Figure 19 confirms the formation of a O_i-O2 bond as there is a disturbance of the DOS of the oxygen atom. There is also a decrease of the state of the $6s$ orbital of the Bi^{3+} cation situated close the interstitial oxygen atom by 1 eV. The insulating characteristics of the oxygen interstitial $BiMnO_3$ can be justified by the O_2^{-2} dimer which leads to a Fermi level located in the middle of bond weakening orbitals of the π_g- and σ_u- symmetry, which are situated in the used and vacant energy level, correspondingly (D. W. Solovyev 2010). How huge Jahan-Teller distortions observed in some research activities is sustained by oxygen defects was better understood by tracking the sum of the systems energy in relation to the low temperature structure and the optimized $BiMnO_3$, then put these together as a function of the distance

between the O2 atom and Mn1 cation. It is this bond length which was utterly changed by optimization. In process of O2-Oi bond formation the O2 atom move nearer to cation Mn1. This formation is associated with a considerably huge energy uptake as compared to the oxygen shifts in pure $BiMnO_3$. Jahan-Teller distortions that surround Mn cations locations are partly reinstated by this mechanism. The restoration is seen as two bonds that have an increased length and 4 that have a much shorter length of the Mn-O bond. Despite this the Mn2 surrounding is unalike to that of Mn1 but is also characterized with substantial distortions giving raise to farther contrasting Mn-O bond lengths. The M2 surrounding consists of three long and three short Mn-O bonds (Figure 18).

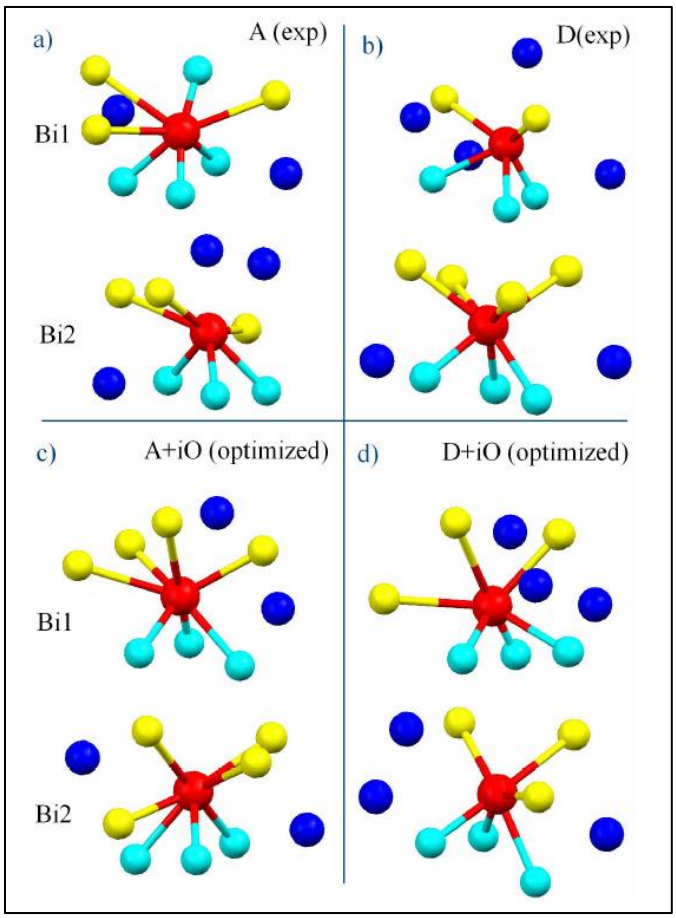

Figure 20: Two experiments to A (exp) and D (exp) to illustrate the variations in the oxygen around the Bi atom in $BiMnO_3$.

The long and shortness of the bonds is in reference to $2\dot{A}$ the normal bond length. The interstitial oxygen could not be located anywhere else in the crystal as this resulted in energy instabilities with enthalpies that were more than 50% larger than the nominal value. Unlike the oxygen pair bond formed with the interstitial oxygen around the Mn1 site this property was absent around the M2 site and farthermore the system was metallic around that site which impedes Jahan-Teller distortions.

Thirdly by considering a number of practically determined magnetic orderings (Solovyev. 2010) proposed that oxygen defects have a stabilizing effect in some of the simple perovskite structures. This was explained using optimized data of a variety of pure crystal structures of $BiMnO_3$ and that with structural defects of interstitial oxygen. The defects were set to be of different concentrations. For the situation with oxygen defects the final optimized structure varied in relation to the starting conditions, while in pure crystal the final optimized structure was the same regardless of the starting conditions. Defects occur at confined places in a crystal and therefore disturb a localized area. Basing on this oxygen defect formation energies were observed to diminish as the defection concentration were reduced in the low temperature and A structures. For the D structure at both high and low defect concentrations formation enthalpies were negative.

This was an indication of an intolerant characteristic to oxygen defects. This characteristic was explained in relation to the surroundings of the Bi^{3+} cation as illustrated in Figure 20. The structures A and D have contrasting oxygen coordination of the Bi^{3+} cation and the unit cell of the D structure is much bigger which permit atomic relaxation. This is also observed in the interstitial oxygen defect D optimized structure. It is these characteristics that are thought to cause instability the oxygen defect abundant D structure.

1.4 Single phase simple perovskite multiferroics $BiFeO_3$ characteristics

1.4.1 Contour restrained polar peak zones in self-constructed BFO miniature-area

It has been found that nano-particles in $BiFeO_3$ self-assembly into a well-arranged architecture from the individual components, due to specific, local interactions among the particles or components < https://www.nature.com/subjects/self-assembly> [Accessed on October 19, 2019]. As of late, self-assembled bismuth ferrite miniature-area of dimensions 200 nm × 200 nm were magnificently synthesized on a inorganic lanthanum aluminate platform by pulsed laser deposition. Captivating practical characteristics of charged domain walls (CDW) and center-type structural domains were realized in BFO nano-islands. (Ma, et al. 2018). A methodical study of numerous nano-island structure of various height revealed that the layout of the domains is related to the lateral magnitude of the nano-island. This is illustrated by Figure 21 below (Maa, et al. 2019).

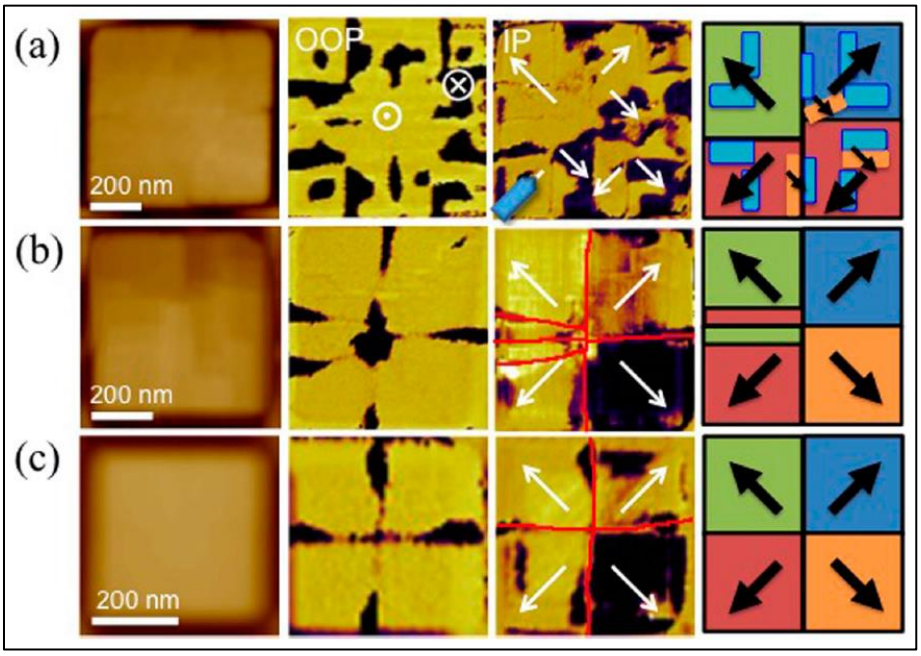

Figure 21: Outward appearance, Out of plan illustration, In Plan phase picture, and graphics of in plan zones of $BiFeO_3$ miniature-area (a) 750 nm ×750 nm, (b) 600 nm × 600 nm and (c) 400 nm ×400 nm (Maa, et al. 2019).

A multi-region structure was observed on the 750 nm miniature-area, and the pair of in-phase (IP) and out-of-phase (OOP) pictures exist as partitioned numerous components thereby decreasing the field which leads to depolarization (Catalan, Seidel and R. Ramesh 2012). They was a general decrease in the multi-domain structure as the Nano island was reduced from 750 nm to 400 nm. For the 400nm Nano island the region is reduced to a four region arrangement with cross-formed fourfold vertex. This was ascribed to reinforcement of depolarization field and the deterioration of substrate interaction effects (Ma, et al. 2018). An observation of the similarities in the 600 nm and 400 nm island indicated that there was 1 more domain wall formed in the 600 nm domain structure than in the 400 nm. This lead to the assumption that only at a particular size of island a 4 domain structure that has fourfold vertex will form. In order to comprehend the impact of island size, they took the quadrant space arrangement that had a four zone boundary peak as the initial state arrangement. Development of an extra area divider over a specific basic size would cause a discontinuity in the fourfold quadrant structure due to the decreased in stress (Catalan, Seidel and R. Ramesh 2012). Critical size of the island was determined by equating the elastic energy in one 4 domain structure to the energy required to form another domain wall as given in the equation below.

$$E_{elastic} = \frac{1}{2} G(s)^2 \frac{W^2 d}{4} \ldots\ldots\ldots\ldots\ldots\ldots\ldots\ldots \quad \text{Equation 2}$$

G refers to the uniform volume deformation and s is the flexibility stress (Catalan, Seidel and R. Ramesh 2012).

$$E_{wall} = \sigma \frac{1}{2} Wd \ldots\ldots\ldots\ldots\ldots\ldots\ldots\ldots\ldots \quad \text{Equation 3}$$

σ the energy per area in creating the new boundary, and Wd will be, domain of the formed zone boundary (Catalan, Seidel and R. Ramesh 2012). By equating the elastic energy and extra domain wall, the critical size at which 4 vertex domain structure forms was determined as

$$E_{elastic} = E_{wall}$$

$$E_{wall} = 4\frac{\sigma}{G(s)^2} \ldots\ldots\ldots\ldots\ldots\ldots\ldots\ldots\ldots\ldots \quad \text{Equation 4}$$

$BiFeO_3$ has σ = 0.44 J/m^2 (Lubk. and S. Gemming. 2009) and a modulus shear G = 30 GPa (Shang, et al. 2009). Inserting figures into Equation 4, yields the critical size was found to be around 590 nm which is correspondingly equal to practical results obtained from experiments.

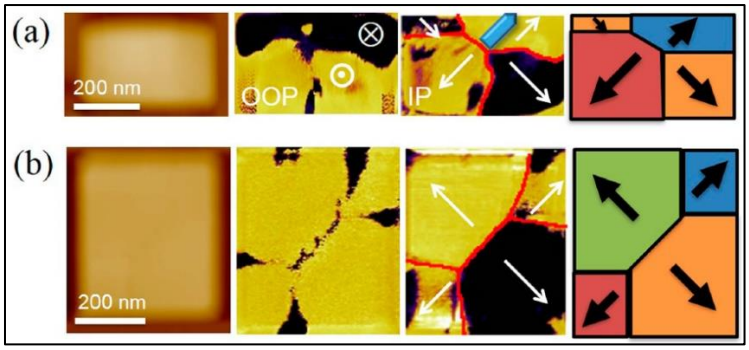

Figure 22: Domain configurations (a) 200 nm × 400 nm, (b) 400 nm ×500 nm. Red contours represent the zone boundaries (Maa, et al. 2019).

Varying the layout of the nano island to a rectangle from square resulted in the fourfold domain configuration being divided into half as a means of reducing the sum energy. A close observation of the almost square-molded 400 nm × 500 nm island Figure 22(b), indicates that a fourfold vertex does not form for non-square islands. A threefold as compared to a fourfold vertex results in even the almost square 400 nm × 500 nm island due to severe interruption of the vertices. A farther increase in the aspect ratio resulted in complicated domain walls being generated.

Notwithstanding the size impact over, pattern of the nano-island rectangular, square etc., additionally change the domain structure. As observed from Figure 22 two asymmetric domain walls were observed on the 200 nm × 400 nm nano island. Stability of the vertex domain configurations nano-islands was investigated using an electric field of ±4 V applied below the Lanthanum strontium manganite electrode. Practical result obtained were the same as those with

the two hundred nm equal sided miniaturized area in which the quadruple peak quaddomains maintain their structure despite a variation in the voltage applied to the electrode. The quadruple peak zones in the equal sided structured miniaturized area were able to be alterably transferred within mid-point merging and midpoint detaching four zones, there are structurally stable (Ma, et al. 2018).

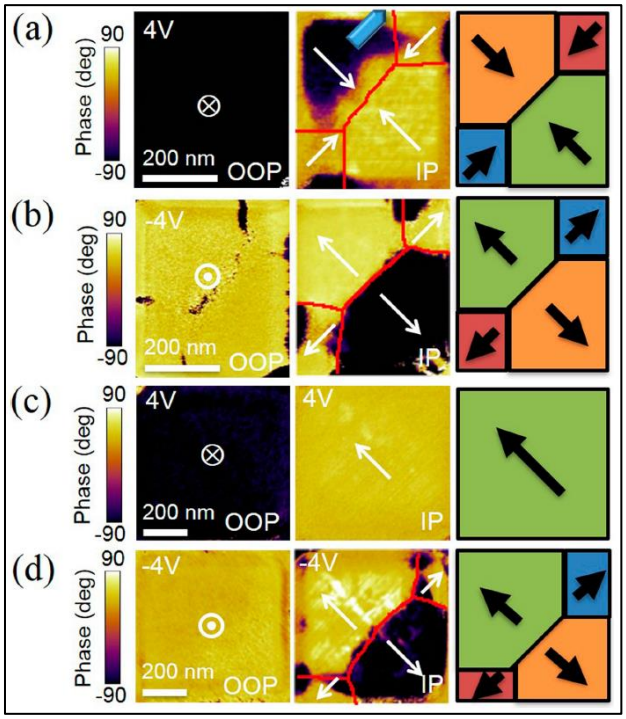

Figure 23: Zone interchanging in $BiFeO_3$ miniaturized area of height (first and second image row) 0.4 x10^3 nm × 0.5 x 10^3 nm, and (third and fourth image row) 0.7 x 10^3 nm × 0.7 x 10^3 nm, accordingly (Maa, et al. 2019).

Thus to the fourfold vertex, it very well may be discovered that the space construction that has two sets of triplicate bases Figure 23(a, b) is likewise very steady in response to a +/-4 V electric field. Application of a +4 V voltage completely transformed the underlying multi-domain structure of 700 nm × 700 nm island. A mono-domain state was justified by out of plan along with in plan polarization which together pointed in a single bearing. When the voltage of ±4 V was applied more than once on the miniaturized area, the space architecture transforms correspondingly, showing an unsteady space architecture under the influence of an electric field.

1.4.2 Multiferroic $BiFeO_3$ nanostructures photo-catalyst characteristics in the degradation of different textile dyes

(C. Ponraja 2017) compared the photocatalysis properties of $BiFeO_3$ to photosensitive semiconductors and concluded that they had an edge due to an adjustable band gap during design phase. From the groups of perovskites utilized in photocatalysts tantalates, titanates and ferrites, $BiFeO_3$ is predominantly superb as it manifests of a number of ferroic properties at approximately 20 to 22°C temperature, giving it an ability to competently isolate charge carriers and the separation of the conduction and valence electrons is in the human eye perceivable wavelengths of the EM spectrum. It is also greatly chemically stable.

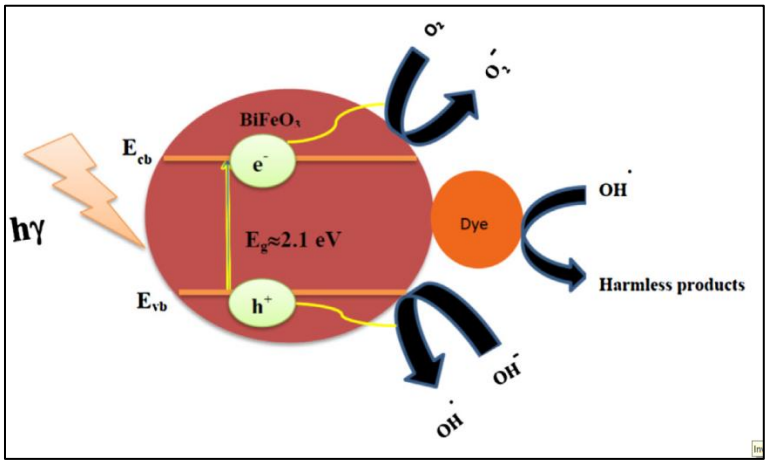

Figure 24: Application of single perovskite BiFeO3 as photocatalyst. (C. Ponraja 2017)

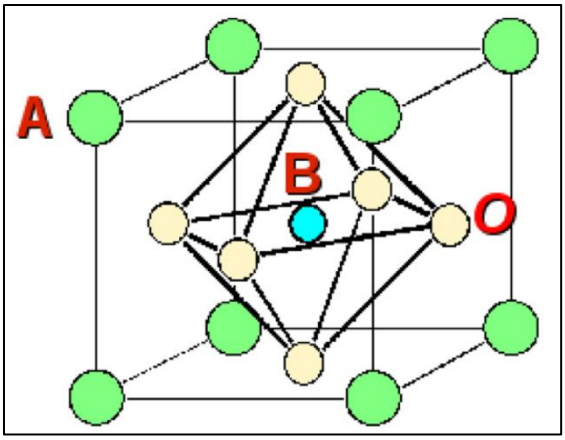

Figure 25: Crystal structure of multiferroic $BiFeO_3$ (C. Ponraja 2017).

1.4.2.1 Using multiferroic $BiFeO_3$ nanoparticles as a catalyst on various textiles dyes.

The catalytic activities of $BiFeO_3$ where found to be highly influenced by a greater surface area and size of the particles. Considering that acceleration of a photoreaction exists as a surface related occurrence, points that have reduced magnitude along with greater surface exhibit an enhanced photo-catalytic action as compared to their bulk equivalent. On the other hand, it was noted that the degree of acidity of the solvent considerably determines bleaching effect of the dye by BFO minute particles. Zeta potential estimations determined that the degree of acidity at which $BiFeO_3$ has no net electrical charge was approximately 2, implying that at reduced pH values a route for more prominent adsorption of the colored dye compound on to the outside of the $BiFeO_3$ as the quantity of co-particles encompassing the BFO nanoparticles are less (Hengky 2012).

1.4.2.2 Multiferroic $BiFeO_3$ heteostructure composites as a catalyst

Heterostructures formed by combining selected materials $BiFeO_3/TiO_2$ displayed enhanced capability in dye degeneration as compared to single perovskite nanoparticles of $BiFeO_3$. A core-shell constructed from single multiferroic perovskite $BiFeO_3$ and TiO_2 was used for photocatalyst experimentation. These two substances have different valence conduction edge

potentials and excitation of electron causes it to be infused into the low edge potential of the two materials, TiO_2. This results in the formation of Ti (III) electron center whilst, quasiparticles concentrate within bands closest to the Fermi level or outer most electron orbital of BFO configure as a hole center.

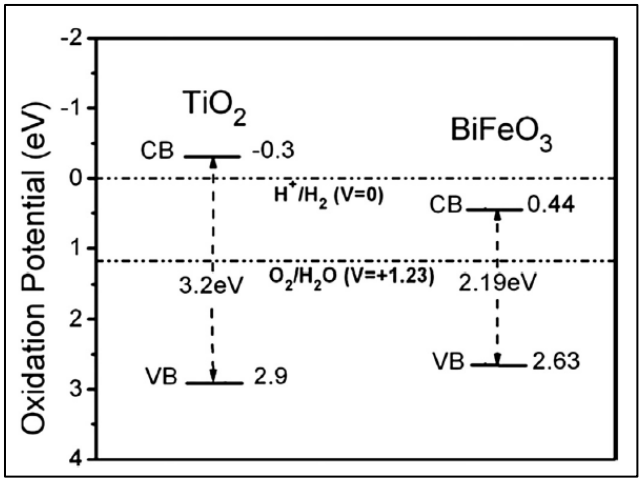

Figure 26: E_c and E_v values for $BiFeO_3$ and titanium dioxide. (C. Ponraja 2017)

Along these lines the falling of negatively charged subatomic particles out of the outer unfilled band into the inner filled energy space, are diminished by expanding the existence duration associated with charge carriers, and accomplishing an upgraded boundary layer, hole-electron movement to the adsorbed organic particle and breaking them down. The titanium oxide molecule is characterized as being dipolar field, this assists with the drifting of charge carriers to the surface. It is through such perovskite heterostructure that hydrogen has been produced by breaking down at a rate of about 0.8 $\mu mol/h$. The single perovskite $BiFeO_3$ as a standalone has a marginally greater conduction band (CB) edge position compared to Standard Hydrogen Electrode (SHE), there can not break down water to release hydrogen (C. Ponraja 2017).

1.4.2.3 Effect of Co doping on $BiFeO_3$ nanoparticle catalytic effect.

In comparison to perovskite undoped $BiFeO_3$ nanoparticles, the Co doped ones displayed an enhanced reduction of the activation energy required to degradation the dyes (F. Niu 2015). This was ascribed to the proficient charge partitioning caused by new energy band of the perovskite heterostructure. The huge work function associated with platinum results in it having a diminished Fermi energy level and when interfaced with a semiconductor such as perovskite $BiFeO_3$ yields a schottky barrier which competently eases the segregation of charges. The barrier is formed between an n type semiconductor $BiFeO_3$ and metal of platinum opens a means to escalate its ability to absorb light energy leading it to a higher energy level. The work function of the metal can be interpreted as being, the mandatory joules to shift the negatron off a solid plane to a vacuum directly after the surface, while the electron affinity is variation in energy when an uncharged particle gains an electron and is represented by the discrepancy of the least conduction band energy and vacuum energy. Electron flow in an interfaced semiconductor and metal depends on stability and usually metals have a reduced Fermi energy than the semiconductor, the direction then is from semiconductor to metal and therefore results in the development of a potential barrier. Discharge of electrons is sustained until the semiconductor fermi energy equalizes with that of the metal. Therefore discharge of electrons sustains resulting in constant fermi energy magnitudes in both the perovskite semiconductor $BiFeO_3$ and metal Pt.

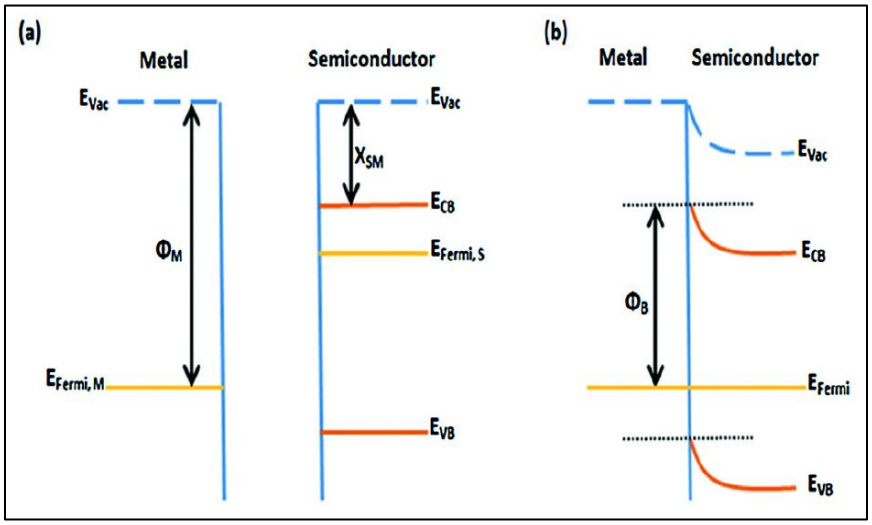

Figure 27: Metal Semiconductor Schottky barrier .

For electrons to flow to the metal (platinum), they have to do work against the potential barrier which results in a reduction of electrons at the semiconductor junction meaning that negatrons out of the platinum collect at the semiconductor boundary while an electron deficient zone is created beneath the semiconductor interface so as to balance the electrical charges. The band as a result is transformed into a conduction band with a Schottky barrier is well represented by Equation 5.

$$\Phi_B = \Phi_M - X_{SM} \ldots\ldots\ldots\ldots\ldots\ldots\ldots\ldots\ldots\ldots \quad \text{Equation 5}$$

It is based on this notation of stability that an electron catch is created where the negatron fails to discharge hindwards into the semiconductor as the conductor platinum simulates a negatron trap to the light produced negatron. What the barrier effectively does is to lengthen the duration of the electron for the photoreaction to occur by inhibiting fission of holes and electrons. In this manner the photocatalytic of Pt/$BiFeO_3$ heterostructure characteristics are intensified.

1.4.3 Electron Spin interference prompted Anormal Polarizations along with Unrealized Magnetization in BFO

$BiFeO_3$ is at present the sole multiferroic material to array twain ferroelectric and ferromagnetism at room temperature. This property of more than one ferroic property at room temperature is of paramount importance as it is fundamental to possibility of new generation of sensors such as radio antennas and data storage devices with better performance as compared to traditional devices. Multiferroic properties at elevated or temperatures below 0 °C is of importance in aviation industries for devices operating at high temperatures such as 40 000 feet were temperatures of approximately -56 °C and space industry where materials are often subjected to high temperatures due to conversion of kinetic energy to heat energy.

A pair of different electron spin interferance prompted anormal polarizations in the $BiFeO_3$ *R3c* where identified and the magnitude of these where determined by a combination of practical experimentation and density function theory *ab initio*. One of the improper polarizations was established to be a result of Lifshitz gradient coupling and the other from magnetostrictive exchange coupling. The property of magnetostriction is observed when the dimensions or measurements of a material will be altered by reason of domination of a change in the magnetic field and will occur at conditions lower than the Curie point. If the curie temperature of the material is at a lower heat condition than the ambient, then it has insignificant practical application. An explanation to this variation in the dimensions by either elongation or shrinking of the material is that the magnetic clusters in the $BiFeO_3$ stabilize themselves by orienting with the externally applied magnetic field. (Sajjia. and M. Hasanuzzaman. 2015).

The phenomena of magnetostriction scarcely is applicable at conditions where the Curie point lies low than the ambient, even though it happen when the temperature is further down as compared with the curie point.

1.4.3.1 Anormal Polarization along with Invariant resulting from Reverse Dzyloshinskii-Moriya Interaction

The property of an incommensurate spin cycloid that has a periodicity of $620\dot{A}$ in $BiFeO_3$ is believed to be linked to with an improper polarization which is a result of reverse Dzyloshinskii-Moriya coupling. The proper polarization of $BiFeO_3$ is however believed to be in the $[001]_h$ direction of a hexagonal close packed cell or $[001]_c$ direction of the cubic cell. The magnitude of the induced polarization due to reverse Dzyloshinskii-Moriya coupling was computed by Equation 6. The researchers evaluated polarization from different sites i and j because there is a variation in the magnetization product from site to site as a result of the annular spin that has transmission vector Q. It was however shown the polarization does not depend on location. It was found to depend on four factors which are the spin canting angle φ, Dzyloshinskii-Moriya coupling coefficient d_{DM}, magnitude of spin density wave $\Delta\varphi$. The resulting polarization in the

$BiFeO_3$ under the influence of the spin canted magnetization in the neighboring sublattices was found to be uniformly distributed as illustrated in Figure 28.

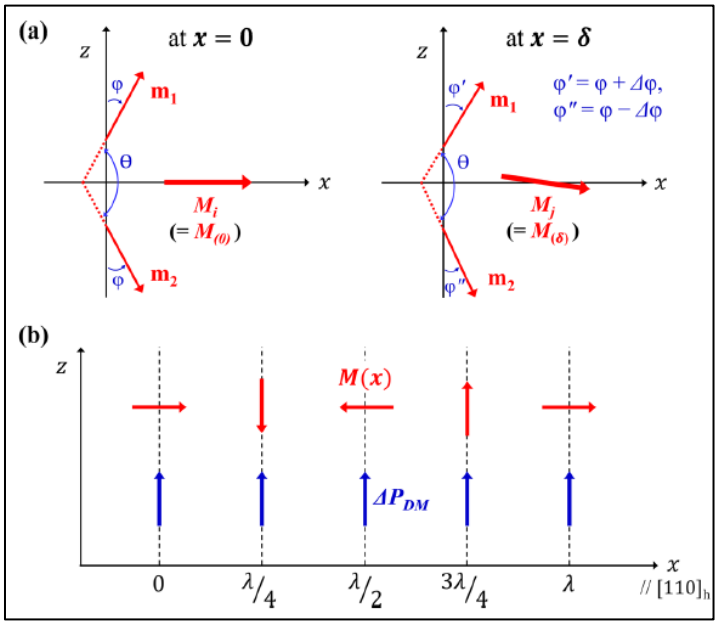

Figure 28: Polarization and spin cant magnetization in the $BiFeO_3$ sublattices (Jang and H. Han 2018).

The diagram illustrates the variation of resultant magnetism from a reference point x = 0 and at a distance δ from the reference point. It can be well noted that the net magnetism changes orientation with distance from the reference point.

$$\Delta P_{DM} = d_{DM}\widehat{e_{ij}} \times \left(M_i \times M_j\right) \ldots\ldots\ldots\ldots\ldots\ldots\ldots\ldots \quad \text{Equation 6}$$

As shown in Figure 29 the resultant proper polarization of $BiFeO_3$ is represented by P_{eq} in the $[001]_h$ direction of a hexagonal close packed cell. It is important to note the architecture of $BiFeO_3$ is such that it is a Bi^{3+} cubic cell inside a hexagonal close packed Fe^{3+} cell as illustrated in Figure 29. Therefore the resultant proper polarization can be referenced to the hexagonal close packed cell or close packed cubic axis.

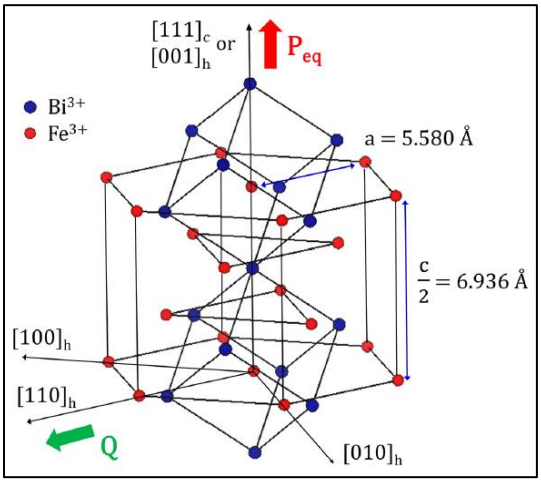

Figure 29: A segment unit-cell sextuple geometry atomic arrangement of BFO that has $R3c$ screw, translation and rotation uniformity (Jang and H. Han 2018).

$$L = |m_1 - m_2| \ldots\ldots\ldots\ldots\ldots\ldots\ldots\ldots\ldots\ldots \quad \text{Equation 7}$$

The possible excitations can be a spin wave in which the motion of the magnetic spins is not coherent and for a situation where the excitation is fixed in space and time resulting in a Neel vector.

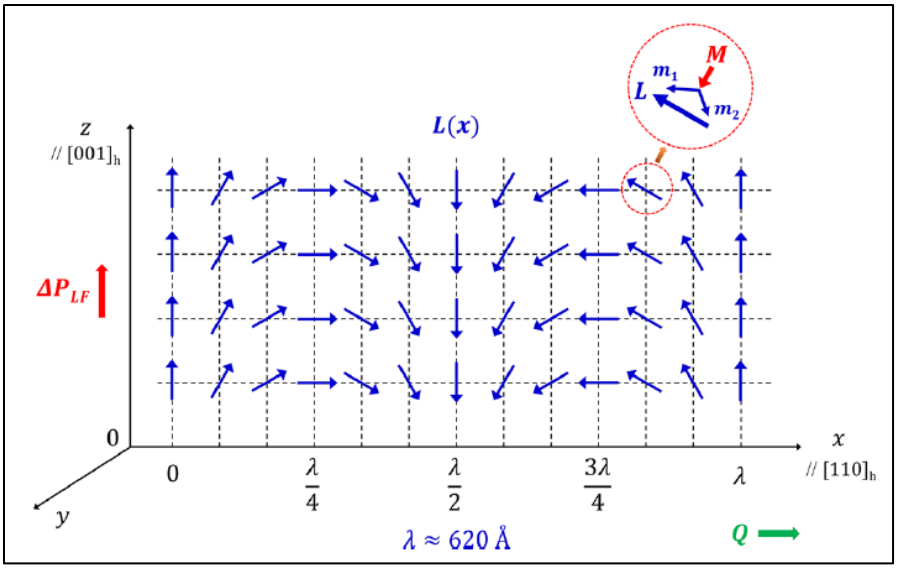

Figure 30: The representation of a 2D antiferromagnetic Neel vector that causes a continuously changing spin density wave with a displacement vector $\boldsymbol{Q}$ towards direction $[110]_h$ (Jang and H. Han 2018).

1.4.3.2 Landau-Lifshitz-Ginzburg Thermodynamic Potential.

(Jang and H. Han 2018) analyzed the free-energy density of $BiFeO_3$ naturally electric substructure using the LGG hypothesis by virtue of a paraelectric prototypic cell having cubic Pm3m screw, translation and rotation uniformity which they expanded. The free energy density on this basis had three coefficients, which where the dielectric stiffness χ_p and two higher order stiffness coefficients ξ' and ξ''. However by farther substitution into Equation 8 they expressed the thermodynamic potential of one $BiFeO_3$ cubic cell in terms of the sum of proper and improper polarization P and L the staggered magnetization in each sublattice. This was achieved by considering the orbicular inflexion of electron gyration moments and Gibbs function density of a spontaneously electric smaller entity, the thermodynamic potential of the single crystalline $BiFeO_3$. P is the ferroelectric polarization in the direction $[001]_h$ of the hexagonal cell in Figure 29. The parameters P and L were independent of each other. L was defined by the modulus of the difference between canted magnetization vectors in the different adjacent lattice systems.

$$\Delta f(P) = f_0 + \frac{1}{2}\chi_p P^2 + \xi'_P P^4 + \xi'''_P (P_x^2 P_y^2 + P_y^2 P_z^2 + P_z^2 P_x^2) \ldots\ldots \quad \text{Equation 8}$$

The antiferromagnetic neel vector and net magnetization are related according to the Equation 9.

$$M^2 - L^2 = \left|m_i \times m_j\right| \ldots\ldots\ldots\ldots\ldots\ldots\ldots\ldots\ldots\ldots \quad \text{Equation 9}$$

Electric polarization in materials can either be of the form proper or improper ferroelectricity depending on what is causing the electric polarization. A dimensional disturbance to an electrically charged lattice results in proper ferroelectric system. While in improper ferroelectrics, symmetry breaking occurs to a nonpolar system as a result of magnetic ordering or architecture dimensional variation. This type of polarization introduces particular characteristics of paramount importance as compared to proper ferroelectrics. This is because in improper

ferroelectrics the mechanism resulting in polarization does not require a vacant d orbital on the B cation as in proper polarization. This permits the concurrent existence of magnetic ordering and electric polarization without a rivalry for partially filled d orbitals for magnetism and completely filled d orbitals for electric polarization.

1.4.4 Spin excitations in multiferroic $BiFeO_3$ generated by hydrostatic pressure

(J. Buhot. 2015) investigated and reported the magnetic disturbances caused by variation in pressure from 0 GPa to 12 GPa in $BiFeO_3$ using theoretical methods, calculations and Raman scattering experiments. It was noted that the structure and magnetic orientation of the material transforms simultaneous indicating a relationship between magnetic phase and structure of the material.

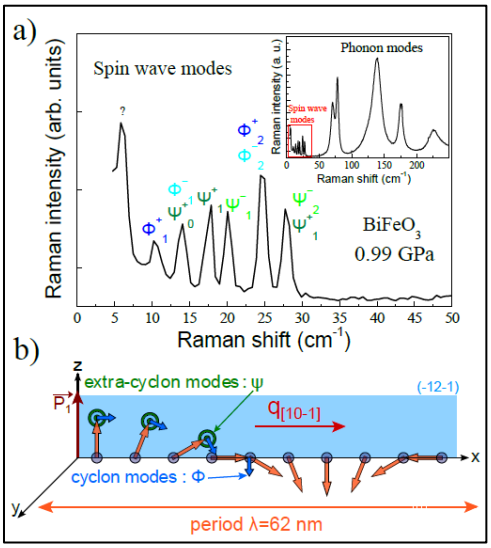

Figure 31: (a) Raman spectrum for the spin wave energized states. (b) Magnetic incommensurate cycloid in $BiFeO_3$ (J. Buhot. 2015).

Propagating interference in the magnetic material is shown and represented by $\Psi^{+/-}$ and $\Phi^{+/-}$ (spin wave mode) in the main diagram while the total excitation at low pressure of the system in a periodic manner is shown in Figure 31 insert. The lattice was taken to have particles that are moving or vibrating out of phase in response to the external disturbance. This is termed optical

phonons contrary to acoustic phonons. The mode and frequency of the phonons was chosen in agreement with (C. Beekman 2012). An existence of cycloidal spin excitation in $BiFeO_3$ was confirmed with the array of slim peaks. The line width of these peaks were approximately 1 cm^{-1} (Cazayous. 2008). The propagating disturbances in BFO were resolved into there respective components cyclon and extra-cyclon modes represented by Φ_n and Ψ_n with the first not being classified under any of the two as it could be due to minute frail magnetization architectures in the $BiFeO_3$ or due to $\Phi^{-/+}$ (Wang and Weerasinghe 2010). The ground breaking investigation of detecting an unfamiliar phonon modes lower than 100, assisted in determination of structural transformation principally those that occurred between O_2 and O_3 phases as shown in figure below.

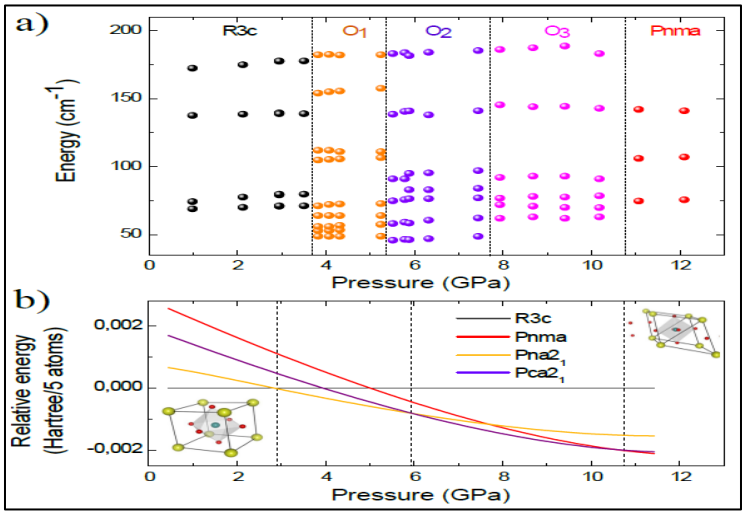

Figure 32: (a) The surfacing of new energies as structure of the sample varies with pressure. (b) The relationship between the pressure acting on the structure and sum of self-contained joules and multiple of the space occupied and pressure (J. Buhot. 2015).

(Cazayous. 2008) detected and reported four crystal structural transformations that happened at pressures 1.595×10^6, 1.124×10^6, 7.977×10^5 and 5.076×10^5 Pa. The initial crystal structure at ambient pressure was rhombohedral (R3c) which then transformed to an orthorhombic construction as represented in O_1, O_3, and O_2. The final crystal structure was an orthorhombic (P_{nma}) space group. This characterization was consistent with other experimentation carried out using X-ray and high energy Raman scattering.

In order to verify the accuracy of the crystal structure of BFO under pressure a Hamiltonian that can be applied in confined space to characterize the eigenvalue spectrum of the entire state was used. This is a means of simplifying the computations (Rahmedov, Wang and Iniguez 2012). The transitions between O_1, O_2 and O_3 were associated with P_{na21} and P_{ca21} layout which have energies of the same magnitude as $R3c$ and P_{nma} structure and sophisticated oxygen octahedral inclinations and are related to nanoscale twined phases as according to (Prosandeev, et al. 2013). The low energies in range 7 cm^{-1} to 45 cm^{-1} and their relationship to the externally applied pressure are presented in Figure 33.

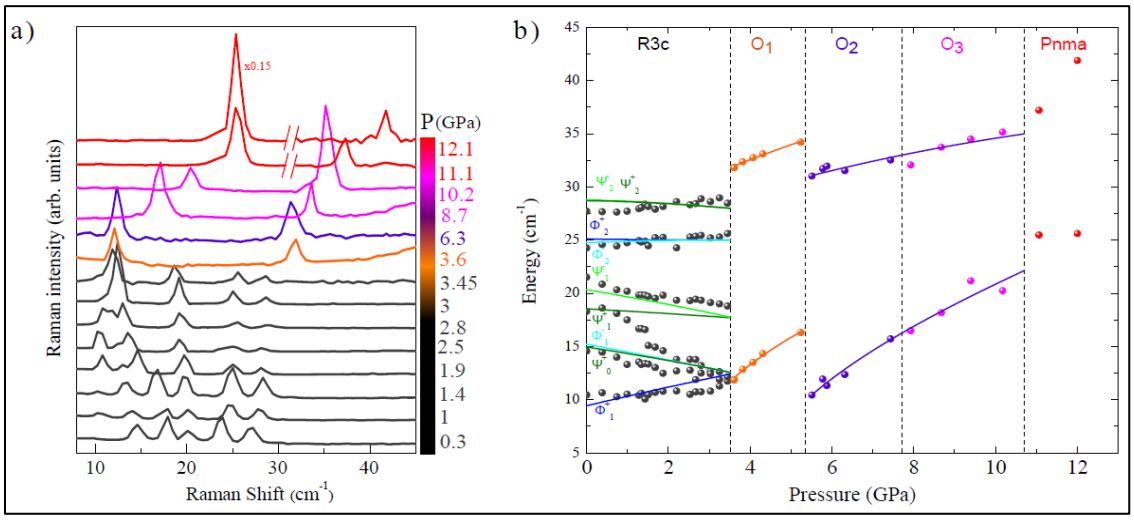

Figure 33: (a) Magnetic excitations as a function of pressure at energy 7cm^{-1} to 45 cm^{-1}. (b) Relationship between propagating disturbances in BFO and applied pressure (J. Buhot. 2015).

For pressures approximately 3.5 GPa part of the spin excitations disappear as new ones appear. However the minimum energy of the first three spin excitations all combine at 12 cm^{-1}, while the width of them all remains unchanged, excitations remain constant despite any changes in the applied pressure. Two spin excitations were realized when the applied pressure exceeded 3.5 GPa which confirmed that the initial spin cycloid had faded on crystal structure transformation. BFO double spin excitation initiating at 11 cm^{-1} and 32 cm^{-1} between O_1 and O_2 was interpreted as the existence of two sub-lattice AFM states. A disruption in spin excitation occurred at 5.6 GPa but the next occurring structure having even higher energies of 30 cm^{-1} and 9 cm^{-1} as the externally applied pressure on BFO was elevated. To explain this observed

phenomena a slightly changed model for the interaction of the ferroelectric and magnetic field in BFO was introduced as shown below (Rahmedov, Wang and Iniguez 2012) and (R. de Sousa 2013).

$$\mathcal{H} = \frac{1}{2}\sum_{\iota\delta}\{JS_\iota \times JS_{\iota+\delta} + [C(u_\iota \times \delta) + D(\omega_\iota + \omega_{(\iota+\delta)})].S_\iota \times S_\iota \times S_{\iota+\delta}\} - K\sum_{\iota}(u_\iota.S_\iota)^2 \ldots \quad \text{Eqn. 10}$$

1.4.5 Slimness reliant atomic arrangement along with magnetic characteristics of $BiFeO_3$ films produced via M.O.D. procedure

(Fengzhen H. 2010) by metal organic decomposition technique prepared BFO films ranging from 35 mm to 300 mm. As a means of taking care of the potential loss of bismuth during the process, they added a surplus of 5 mol % $Bi(NO_3)_3 5H_2O$. For a duration of 30 minutes in an inert environment of nitrogen gas, the solvent was subjected to a temperature of 550 °C thereby forming into a crystal. The corresponding x-ray diffraction pattern accomplished using a x-ray microdiffraction of energy 8.04 keV from a Cu $K\alpha$ radiation is shown in Figure 34 below.

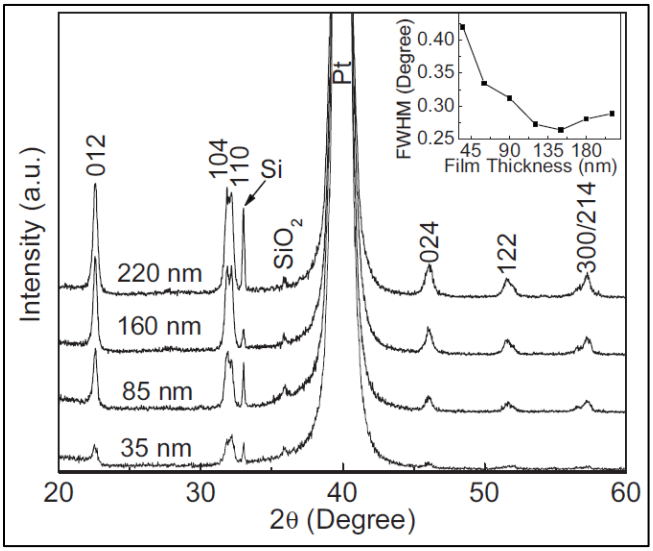

Figure 34: X-ray diffraction patterns of 35 nm, 85 nm, 160 nm and 220 nm BFO film thickness (Fengzhen H. 2010)**.**

From the XRD pattern, all the studied slim layers were composed of a number of minute grains without any contaminants. There was a general reduction in the FWHM due to the growth of film size from 35 nm to 160 nm as is shown in the insert.

1.4.5.1 Surface Morphology in BFO Thin Films.

The corresponding surface morphology was carried out using a Scanning Probe Microscope is shown in Figure 35. The images on the right side of (a) and (b) illustrate the crystal orientation and size when affected by an electric field. There was a considerable escalation of nominal particle size to a maximum of 130 nm from 75 nm due to the variation of the film size to 52 nm from 120 nm. However the variation in the magnitude of the grain when the film thickness was increased beyond 120 nm was a minor variation. Evidence for ferroelectric characteristics in these samples was backed by the curve nature of the piezoresponse phase and amplitude as was determined by the Piezoresponse Force Microscopy. Due to the detected increase in the size of the BFO crystals on the substrate, it was assumed that the ferroelectric characteristics were also enhanced (Y. Wang 2008). For the samples with crystals of size 75–130 nm a single-domain characteristic was found to be more feasible.

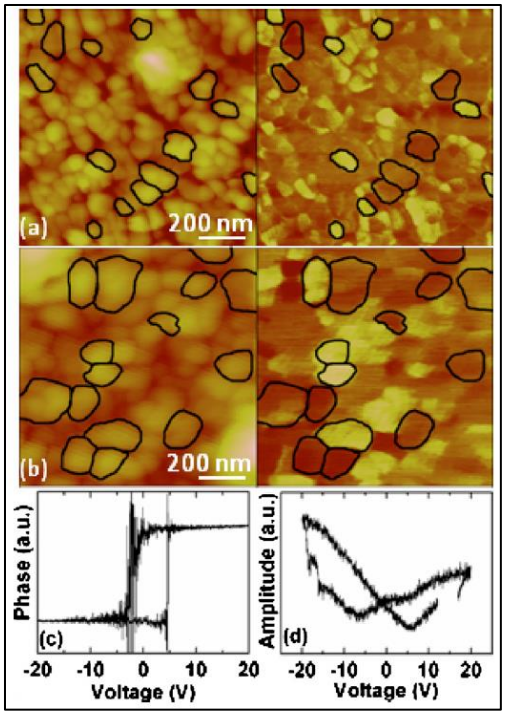

Figure 35: Morphology of (a) 35 nm (b) 160 nm BFO thin films and their respective piezoresonce on the in (c) and (d) (Fengzhen H. 2010).

1.4.5.2 Magnetic characteristics in BFO Thin films

A close observation at the first insert in the figure below will show that the magnetization characteristics of the sample displayed an oscillatory response, with a approximately constant oscillation time of 62 nm. According to the researchers the period was associated with the cycloidal spin architecture of BFO. As a means to comprehend the impact of AFM architecture break in continuity due to the magnitude of magnetization changing crystal particle edges of the BFO rhombohedral ($R3c$), computations performed revealed that magnetic period of spin spiral was 62 nm and the radiation vector was along 101 direction (D. Lebeugle 2008) (C. Ederer and N. A. Spaldin 2005).

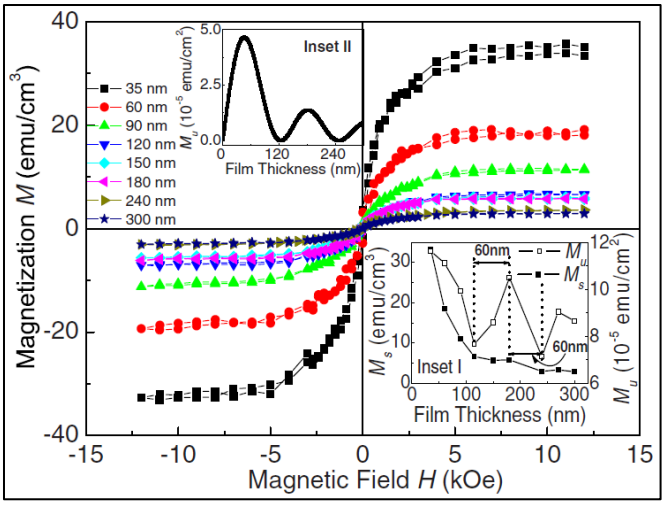

Figure 36: Relationship between magnetic hysteresis loops and film thickness. Inset (1) Relationship between thickness reliant full magnetization *Ms*, together with the atomic magnetic alignment of the elementary region *Mu*. Inside diagram (2) illustrates computed result of thickness-dependent *Mu* (Fengzhen H. 2010).

Mu, the magnetization of unit area was computed by assuming a super crystal structure in which the length of the side was considered as the film thickness.

$$M = NM_O \frac{sin^2(\frac{nqa}{4})}{sin^2(\frac{qa}{4})} \ldots\ldots\ldots\ldots\ldots\ldots\ldots\ldots \quad \text{Equation 11}$$

a represent the separation between two side by side Fe ions. M_O was taken to be 0.11 μ_B/Fe which is the maximum suggested magnetization magnitude of $BiFeO_3$ nanoparticles that are not on substrate. There is substantial evidence from Figure 36 insert II that electromagnetic unit of multiferroic $BiFeO_3$ has an oscillatory behavior as the thickness is increased. The maximum magnetization of $4.3 \times 10^{-5} emucm^{-2}$ was observed at a film thickness of 80 nm while the minimum value was determined to correspond to a film thickness of 180 nm with a value of $1.3 \times 10^{-5} emucm^{-2}$. Despite this value being large enough it still was minute in comparison to other practical values (Eerenstein, et al. 2005). It was suggested that the non-uniformity in the voluminosity of $BiFeO_3$ grains and direction of the grains which was not consistent on the

interface with the substrate resulted in the oscillatory behavior of the magnetization per unit area (Fengzhen H. 2010).

1.5 Single phase double perovskite multiferroic $BiFe_{0.5}Mn_{0.5}O_3$ characteristics

1.5.1 Crystal structural and XRD pattern of $BiFe_{0.5}Mn_{0.5}O_3$

Experimental data from synchrotron powder X-ray diffraction was allocated a space group by referring to single crystal data reported in (Mezzadri, et al. 2016). Of the detected 2644 reflections of bulk BFMO1 the characterization technique used proved to be of high quality as was justified by a R factor of approximately seven percent and weighted profile R-factor = about four percent. Crystal lattice constants obtained after refinement are a = 5.553 Å, b = 11.1755 Å, c = 15.6897 Å and a volume of 973.77 Å. Approximately six percent by weight $(BiO)_2CO_3$ impurity was found in the BFMO1 sample. The impurity was as a result of Bismuth (3+) oxide reacting with CO_2 emitted by heating of the carbon in furnace.

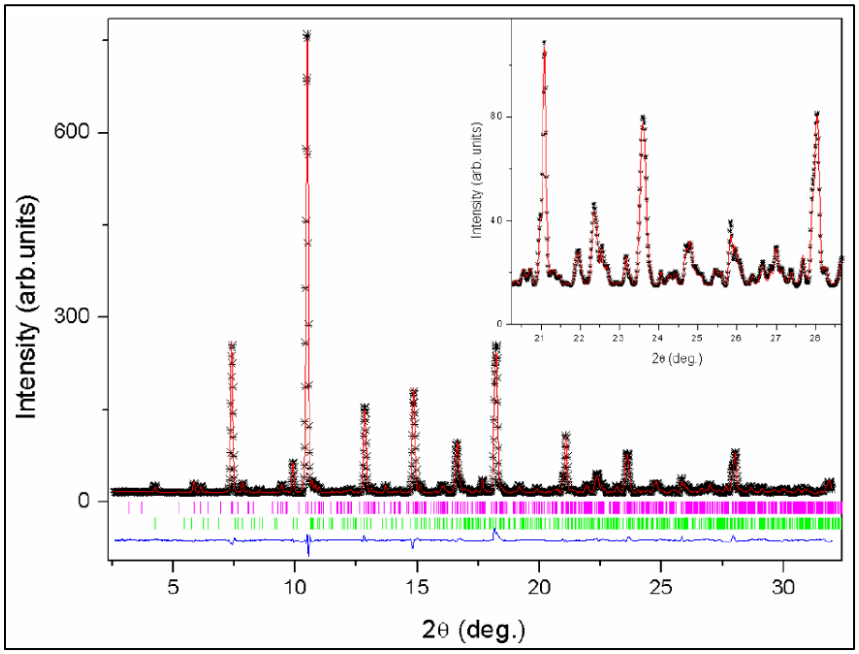

Figure 37: SPXRD of $BiFe_{0.5}Mn_{0.5}O_3$ carried out using λ = 0.50899 Å. The dark line represents observational statistics and the scarlet plot gives the refined data. Variation in computed and experimentation intensity is given in blue plot (Mezzadri, et al. 2016).

How the Fe/Mn cations are numerically ordered throughout the sample at the B location was determined and bond lenghts were found to be 2.02128 Å and 2.02227 Å for Mn-O and Fe-O respectively. From these bond lengths reseachers concluded on the oxidation number of both Fe and Mn cations to be +3. Substantially rotated and inclined transition metal oxide Fe and Mn were noted and were proposed to be sustaining this balanced condition because of relative spatial arrangement of atoms due to Bi^{3+} cation. It was proposed that the Bi cation causes the dispersion of bond to lengths between 1.93120 Å and 2.16592 Å.

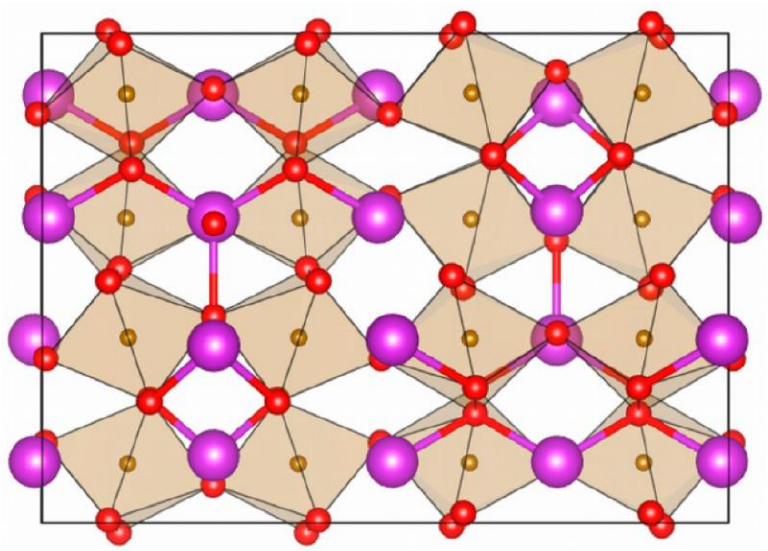

Figure 38: From [100] orientation, BFMO atomic architecture is illustrated with reduced length Bi−O bonds (<2.35 Å) as a means of emphasizing cell bounded dipoles (Mezzadri, et al. 2016).

The lone pair of electrons on the bismuth cation causes it to displace from its polyhedron which has twelve flat faces resulting in a complicated arrangement of dipoles or separation of charges. This effect is thought to be cancelled out by centrosymmetricity of the BFMO1. The resistance per unit length and cross sectional area at 20 V on a logarithmic scale is shown in Figure 39.

1.5.2 Electric transport properties of multiferroic $BiFe_{0.5}Mn_{0.5}O_3$

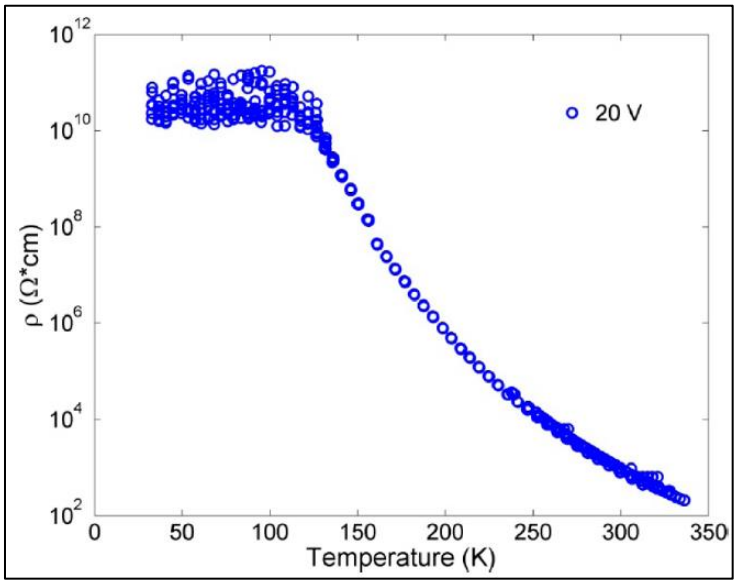

Figure 39: Resistivity as a function of temperature at 20 V of BFMO1 crystal plotted on a logarithmic scale (Mezzadri, et al. 2016).

Saturation from approximately 140 K downwards is shown by the single crystal, while the general decrease of resistivity with temperature rise is typical to semiconductor materials. For the three graphs plotted for bulk $BiFe_{0.5}Mn_{0.5}O_3$ was clearly no relationship between applied voltage and resistivity. However the semiconductor behavior of an increased resistivity with a decrease in temperature was displayed by the bulk system. Due to the agreement of resistive being independent of temperature in both crystal and bulk structures at temperatures below 140 K, researchers concluded that the at that particular temperature of 140 K, there is a genuine transformation of $BiFe_{0.5}Mn_{0.5}O_3$ characteristics.

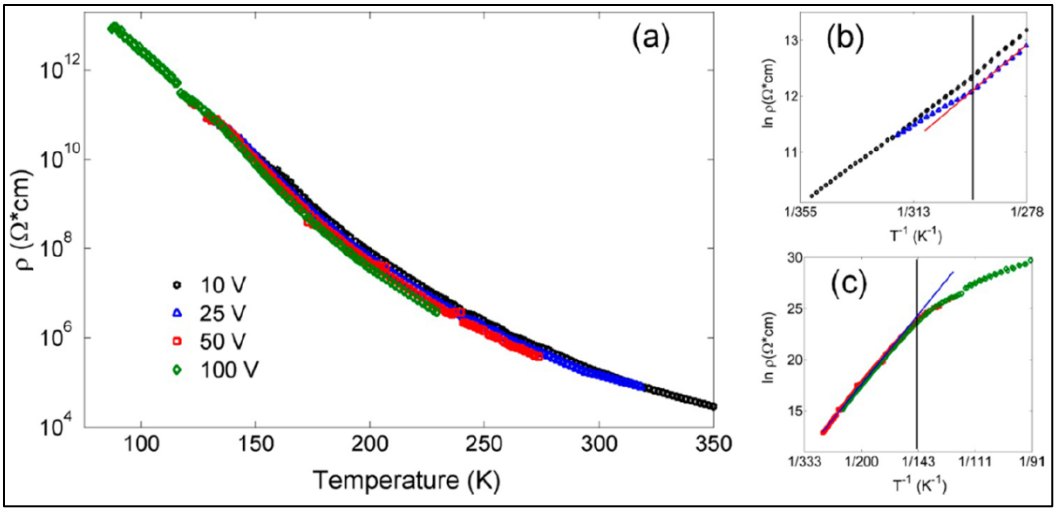

Figure 40: Variation of bulk $BiFe_{0.5}Mn_{0.5}O_3$ electrical resistivity with temperature determined for unique voltages (Mezzadri, et al. 2016).

The accessible information surely proved that farther down than T_p = 140 K the material $BiFe_{0.5}Mn_{0.5}O_3$ is in an uncontaminated state as is shown by the elevated dielectric state, which was described by elevated resistivity value (ρ > 10 Gω·cm). Along these lines, T_p was suggested to be perhaps the cross over temperature from non-conductor to semiconductor. The information were examined by Arrhenius linearization, utilizing the three primary models generally embraced in comparable structures (Zhao, et al. 2015) (Ben Abdelkhalek, et al. 2013) and (Cabassi, et al. 2010). Replicas utilized for data analysis were Holstein polaron model which evolves from exchange of the electron and lattice vibration (Zelevinsky 2016), the thermal activation conduction which formulates how the $BiFe_{0.5}Mn_{0.5}O_3$ sample conduction is related to temperature at high temperatures (Lina, et al. 2013) and Mott's variable range hopping which characterizes carrier transport at low temperature (Lina, et al. 2013) without considering the Coulomb gap. In semiconductors, conduction occurring at elevated temperatures is a result of hopping of electrons from donor energy level to conduction band.

At a temperature of T_N= 288 K which is the same point for the magnetic T_N, an anomaly was detected as can be seen in Figure 40b and exists only at low voltages of 10 V and 25 V. At higher voltages (50 V and 100 V) there is no anomaly. Due to this the electric transport was modeled in two the non-insulating zones where temperature was greater than T_p but smaller than T_N and the

region where the temperature was greater than T_N. When the Mott's variable range hopping model was used to fit the data an excellent convergence was attained of $R^2 = 1$. Systematic deviations were noted when other models were used. For the data observed at temperatures greater than T_N the relationship between resistivy and temperature could not be fitted by the M-VRH model but by a temperature activated kT model.

1.5.3 Dielectric properties of multiferroic $BiFe_{0.5}Mn_{0.5}O_3$.

The experimentally determined dielectric constant for $BiFe_{0.5}Mn_{0.5}O_3$ at various electric field frequencies in relation to temperature is illustrated in Figure 41. $BiFe_{0.5}Mn_{0.5}O_3$ dielectric properties show a robust relationship with temperature. Regardless of the frequency of applied electric field dielectric constant escalate swith an elevation of temperature, commencing from approximately 38 to about 50. The drastic fall in dielectric constant starts at approximately 288 K which corresponds to the temperature T_N, and terminates at 140 K for a 1 MHz and 600 kHz electric field and at 200 K for the 11 kHz and 3 kHz electric field. Below this temperature, the system displays dielectric properties with excellent direct proportional relation between temperature and dielectric constant.

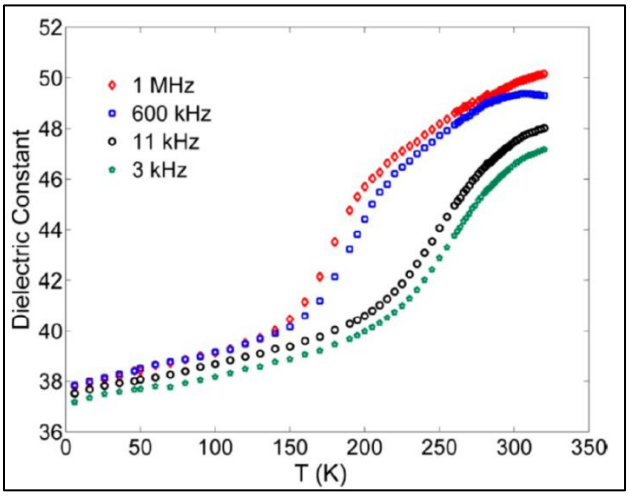

Figure 41: Relative permittivity of BFMO1 for different frequencies in relation to temperature (Mezzadri, et al. 2016).

This is in accordance to the BFMO1 transport properties at temperatures below 140 K, where the values for the dielectric constant reveal an insulating phase forms regardless of the frequency. Farthermore it was observed that BFMO1 deviated from the normal characteristics of dielectrics as it had a dielectric constant that was inversely related to the number of complete cycles per second of the acting electric field. This characteristic was explained to be a result of a delocalized electron in the entire temperature scale under consideration. This means that for an elevated field frequency the electron becomes more confined in one area thereby allowing more negative particles from which the relative permittivity is established. There is a temperature range for which the long range order magnetic properties are well established and the range of temperature where the electrical permittivity is decrease and stabilized. The temperature range at which these two processes occur overlap each other (Mezzadri, et al. 2016).

1.5.4 Pyroelectric and Ferroelectric Characterization of multiferroic $BiFe_{0.5}Mn_{0.5}O_3$.

The relationship between pyrocurrent and temperature of $BiFe_{0.5}Mn_{0.5}O_3$ in the temperature range 5 to 320 K is shown in Figure 42. Initially a polarizing electric field of 1.4 $kVcm^{-1}$ was applied for half an hour at a temperature of 290 K, as the system's temperature was reduced to 5 K. The pyrocurrent relationship with the temperature in the 3 to 320 K range was composed of three distinct zones with current flowing in different directions. At elevated temperatures ($T >$ 288 K) the pyrocurrent signal is characterized by highly negative current which was due to conductive losses through the sample. This was justified by the activation energy of 360 meV from the Arrhenius plot and besides it was almost equivalent to the bulk and crystal values. It was speculated that the interruption of the signal at 345 K was due to contact effect and had no influence on the magnitude of the activation energy. A plot between 340 and 295 K with practically an equivalent magnitude of activation energy substantiated this speculation. A distinct transport mechanism such as (MVRH) at degrees lesser than T_N was affirmed by the curve gradient which continued to diminish.

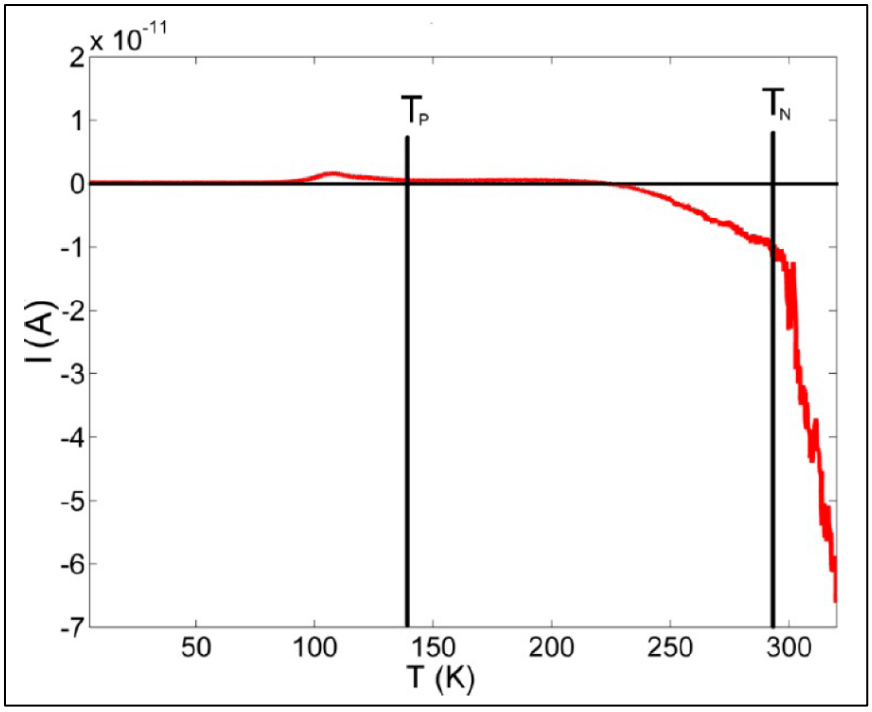

Figure 42: BFMO1 pyrocurrent relationship with temperature (Mezzadri, et al. 2016).

This mechanism is believed to be governed by strengthening of the AFM ordering, which possible cause the electrons to be partially localized at the Mn^{3+} site. The pyrocurrent at decreased temperatures is a result of loss in polarization due to temperature and has a positive magnitude. The antiferroelectric ordering of the bismuth cations which are greatly displaced from their neutral site, giving rise to a local electric moments which are cancelled out by symmetry constraints and is expected with the space group centrosymmetry.

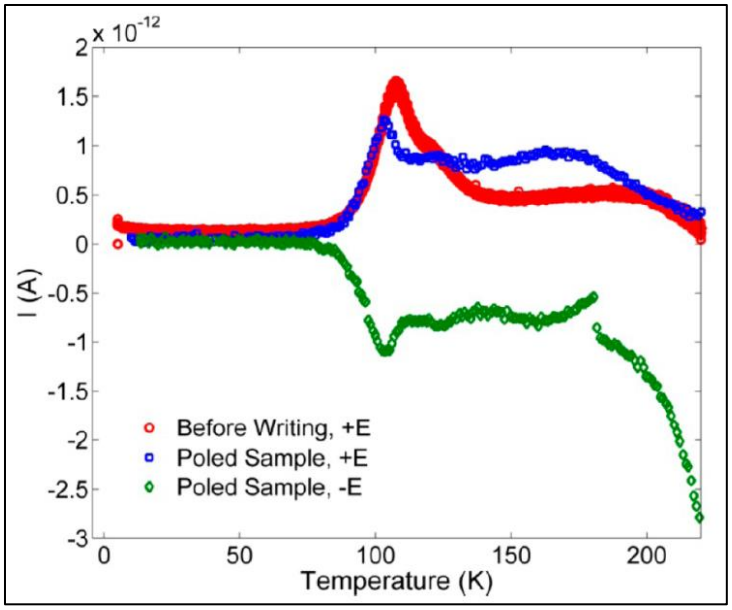

Figure 43: Pyrocurrent responses as temperature is increased following a positive and negative electric field (Mezzadri, et al. 2016).

A direct current electric field of 1.4 $kVcm^{-1}$ on $BiFe_{0.5}Mn_{0.5}O_3$ caused an increase in magnitude of current from 0.4 x $10^{-12}A$ at a temperature of T_N = 140 K up to 1.6 x $10^{-12}A$ at a temperature of 90 K as represented by the red curve. The curve was characterized with two distinct peaks which were of different magnitudes (in amperes). These maxima happened exactly at the temperature at which the BFMO system transforms to the MVRH from the thermal activation conduction. Identical practical determination of pyroelectric on one small crystal is not possible as the current of the bulk $BiFe_{0.5}Mn_{0.5}O_3$ sample was close to minimum value which can be detected by the instrument. So this is to do with limitations of the instrument sensitivity.

The electrical and magnetic hysteresis loop of BFMO1 depending on electric field of a direct current of 5.7 $kVcm^{-1}$ is shown in Figure 44. Dynamic hysteresis measurement was used to determine the magnitude of electric polarity induced in BFMO1. The saturation was determined to be 31 $\mu C/cm^2$ which was remarkably greater than the values in originator compound BFO (Lebeugle, Colson and Forget 2007.) This value was however marginally disturbed by augmentation with leakage current. A reconfigurable property was simultaneously detected which allowed the gained electric polarization to be neutralized with an external electric field of

2.1 kV/cm. This coercive field was ten or hundred times smaller than that in economic value ferroelectrics. As a result they provisional investigated the response of electric polarization to an externally applied electric field at room temperature. However in this system the dielectric characteristic were outweighed by the natural conductive contribution such that the endurance of the induced electric polarization could not be detected at elevated temperatures. At low temperatures the usual electric polarization against external electric filed characteristics of BFMO deviates drastically with a ferroelectric loop which had a center of inversion being detected. A farther analysis into this electric property revealed it attains a fairly high electrical polarization dependent on an elevated electric field. The electric polarization could be reversed from an antiferroelectric to a polar order by an opposite polarity external electric field. At a temperature of 77 K, dynamic hysteresis measurement was utilized to determine the electric properties with electric polarization stress cycles and it was determined to be dielectric and had no hysteresis meaning the ferroelectric loop had been induced.

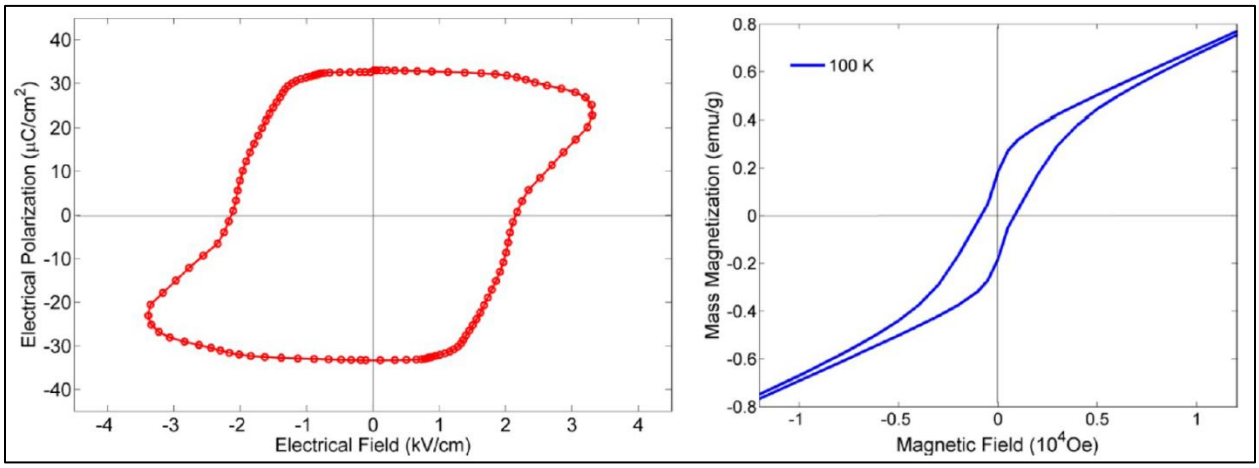

Figure 44: (a) Electric polarization determined by with a ferroelectric tester (b) BFMO1 magnetic loop at hundred kelvin brought about due to a frail ferromagnetism (Mezzadri, et al. 2016).

1.5.5 Reversal of spontaneous magnetization in disordered bulk $BiFe_{0.5}Mn_{0.5}O_3$ and the effect of external magnetic fields.

1.5.5.1 Zero-field intrinsic magnetization

Zero field cooled values affirmed that there was magnetization reversal of room temperature ordered magnetized spin state in $BiFe_{0.5}Mn_{0.5}O_3$ as the ambient temperature was decreased. The room temperature weak FM ordering is attributed to clusters that have been enriched with Fe and the ordering occurs at temperatures above room temperature.

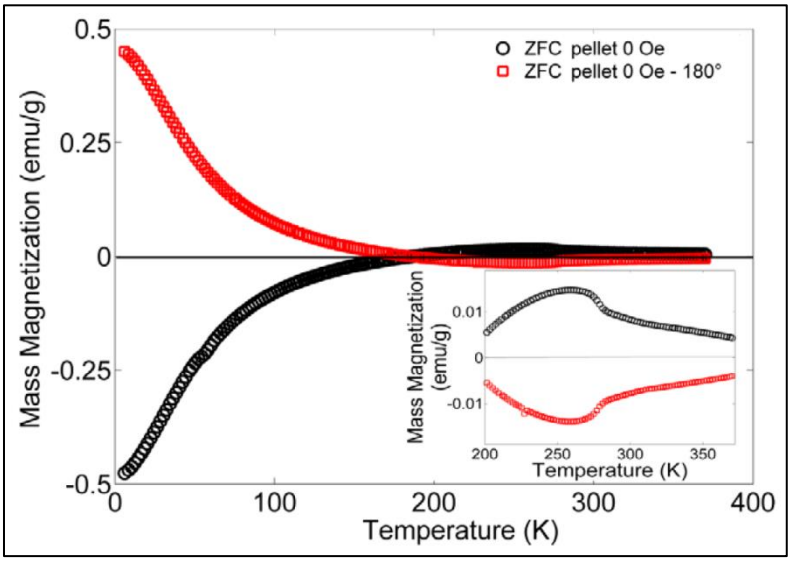

Figure 45: Spontaneous magnetization as the $BiFe_{0.5}Mn_{0.5}O_3$ sample is cooled without an applied external magnetic field (Delmonte, et al. 2015).

As a result a negative magnetization reversal was noted for an initially positive magnetization at room temperature conversely a positive spontaneous room temperature resulted in a negative net magnetization at low temperatures. This is graphically demonstrated in Figure 45. In other words when a negative magnetization reversal is detected in a particular direction rotating the sample by 180° will result in a positive magnetization reversal being determined. Since the process occurs without influence of an external perturbation then this phenomena is considered an

intrinsic property of magnetization reversal of the room temperature spontaneous magnetization and is not influenced by a residual magnetic field.

1.5.5.1.1 The reaction of $BiFe_{0.5}Mn_{0.5}O_3$ to an external magnetic field

The affiliation connecting the magnetization reversal process and magnetic field in $BiFe_{0.5}Mn_{0.5}O_3$ is robust and the magnetic field has a complex nature.

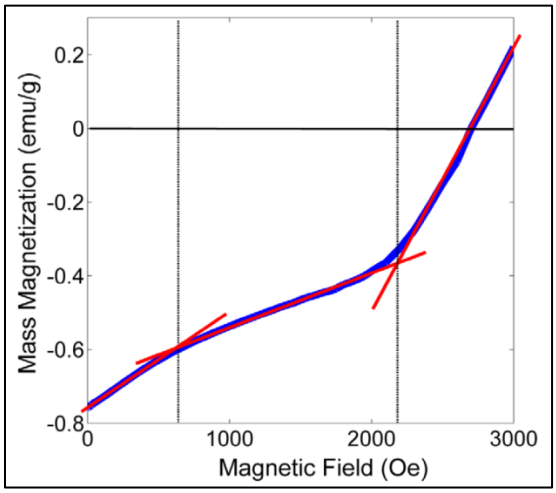

Figure 46: Fixed temperature magnetization determination carried out at 5 K for N-MRV $BiFe_{0.5}Mn_{0.5}O_3$ (Delmonte, et al. 2015).

The mass magnetization of $BiFe_{0.5}Mn_{0.5}O_3$ at 5 K is illustrated in Figure 46. It is at this point that the summations of all magnetic interactions that result in magnetization reversal are totally stabilized. Sharp variations in the gradient of the plot were observed at two points, 650 and 2200 Oe. In farther investigations on the same sample where the temperature of the $BiFe_{0.5}Mn_{0.5}O_3$ system was kept constant while the magnetizing force was varied, these magnetizing forces were reproduced. The resultant magnetization curves of the spontaneous P-MRV sample under the influence of a number of different magnetizing forces as the temperature is decreased is shown in Figure 47a. Figure 47b is an amplification of the field cooled curves in the region from 200 to

350 K. All the curves are characterized by a change in the direction of curvature at a temperature of 288 K which corresponds to the Neel temperature of the BFMO1 sample.

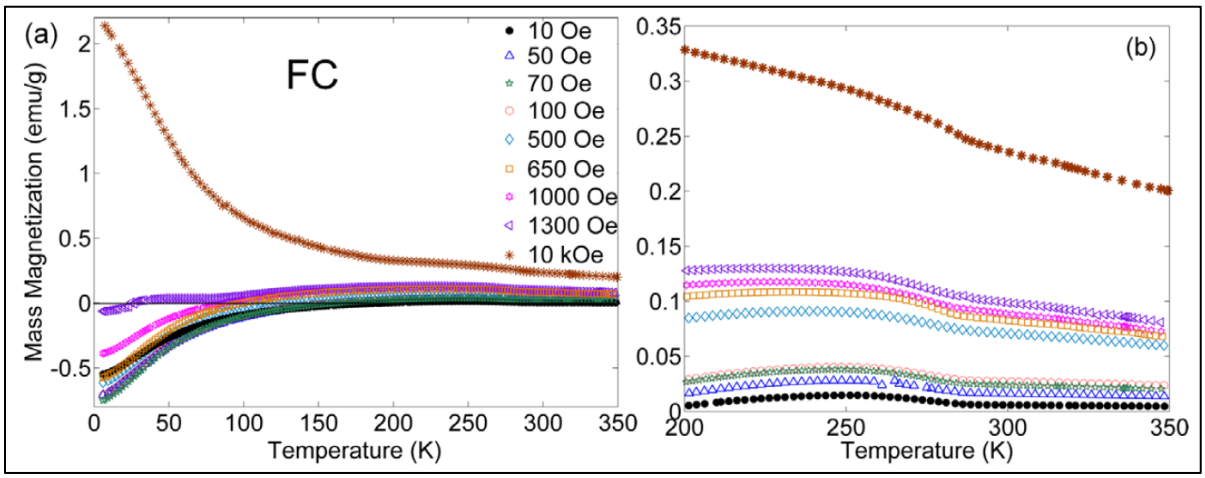

Figure 47: Field cooled magnetization of bulk $BiFe_{0.5}Mn_{0.5}O_3$ (Delmonte, et al. 2015).

For the field cooled plots with a magnetization force between 10 Oe to 1300 Oe a negative magnetization reversal was observed. The negative magnetization reversal is unconstrained by the initial orientation of the sample. However at a highly elevated magnetizing force of 10 kOe the field cooled characteristics of $BiFe_{0.5}Mn_{0.5}O_3$ does not display a negative magnetization reversal. The driving factors for the observed room temperature spontaneous magnetization required a very low magnetization of 10 Oe to reverse the observed RT magnetization. This was interpreted as a low coercivity of $BiFe_{0.5}Mn_{0.5}O_3$ and was consistent with the Mössbauer spectroscopy measurements. From Figure 47b room temperature spontaneous magnetization of $BiFe_{0.5}Mn_{0.5}O_3$ is inevitably positive and will leads to a negative magnetization for a field cooled situation. The severity of the magnetic field also regulates the magnetization reversal characteristics observed in $BiFe_{0.5}Mn_{0.5}O_3$. From a temperature of approximately 70 K down to 5 K there was general increase in the negativity of mass magnetization observed for 10 Oe up to 1000 Oe except for the higher fields of 1300 and 10000 Oe. These variations are accompanied by a decrease in temperature. At magnitudes around 1350 Oe $BiFe_{0.5}Mn_{0.5}O_3$ resists a magnetization reversal from its observed room temperature spontaneous magnetization value.

The magnitude of the H_1 and H_2 are robustly associated with the amount of non-uniformity of the different $BiFe_{0.5}Mn_{0.5}O_3$ samples. The non-uniformity was itself affected by temperature and pressure of the synthesis conditions. Basing on this non-uniformity in the different samples H_1 and H_2 varied from each of the studied samples. The magnitude of H_2 was observed to vary between 1 and 3.5 kOe. However the variation of H_1 was much smaller between 250 and 800 Oe. Despite these differences all the samples portrayed related singular points and similar magnetic behaviors in three similar zones. Any dependable explanation on the magnetic architecture in systems that are similar to $BiFe_{0.5}Mn_{0.5}O_3$ essentially needs magnetic properties in three distinct ranges, H < 650 Oe, 650 < H < 2200 Oe and H > 2200 Oe. An evaluation of magnetic properties in the three separate zones was carried out on a positive magnetization reversal sample of $BiFe_{0.5}Mn_{0.5}O_3$. The measurement of magnetic forces is in a P-MRV introduces a special condition for measurement of magnetic forces and thereby presenting a means of fully comprehending important magnetic features. The sample was not detached from SQuID during measurement of the magnetic field. Between the interval of zero field cooling and field cool the BFMO was heated to 380 K and magnetization confirmed as being negative for the positive spontaneous magnetization reversal and vice versa so as to determine the initial order did not divert.

1.5.5.1.2 H < 650 Oe zone

The property of a positive magnetization reversal and negative magnetic alignment in the zero field cooled field cooled experiments respectively was also detected in the 10 to 100 Oe magnetic field range. The ZFC and FC curves displayed a recognizable minimum and maximum respectively at a temperature of approximately 250 K. The detected minimum and maximum magnetization were contrasting in behavior however occurring under the same conditions. Since at elevated temperatures the applied minute positive magnetic field was abundant to cause reversal of magnetization in $BiFe_{0.5}Mn_{0.5}O_3$ during the heating procedure, then the magnetic property in $BiFe_{0.5}Mn_{0.5}O_3$ was concluded to be fail. This was in contrast to the ZF observations illustrated in Figure 45.

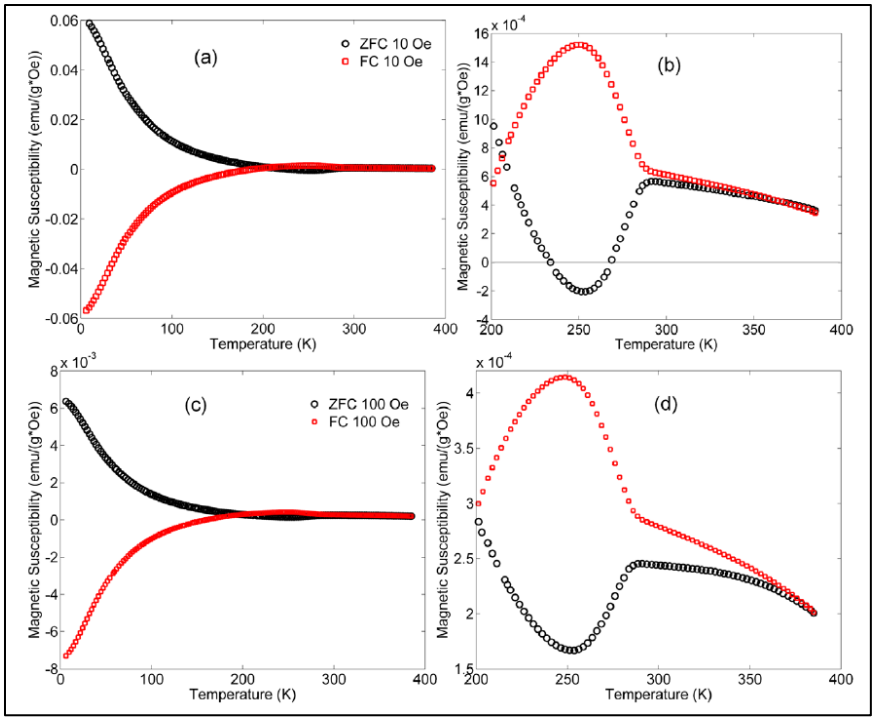

Figure 48: Zero FC together with FC magnetic susceptibility (a) and (c) respectively. (b) and (d) show the magnification of the graphs in the 100 to 400 K range (Delmonte, et al. 2015).

The observation is true since zero field cooled and field cooled graphs had their modulus of susceptibility being the same at suppressed temperatures compared to the compensation temperature. When the measurements at 100 Oe and 10 Oe compared it was observed that magnetic susceptibility readings at 10 Oe had much higher values than those at 100 Oe.

1.5.5.1.3 650 Oe < H < 2200 Oe zone

The previously observed magnetic susceptibility characteristics of BFMO1 were changed entirely by using magnetic fields larger than 650 Oe. This is demonstrated in Figure 49. A negative magnetization reversal was detected even in the zero field cooled sample despite it initially possessing a positive magnetization reversal.

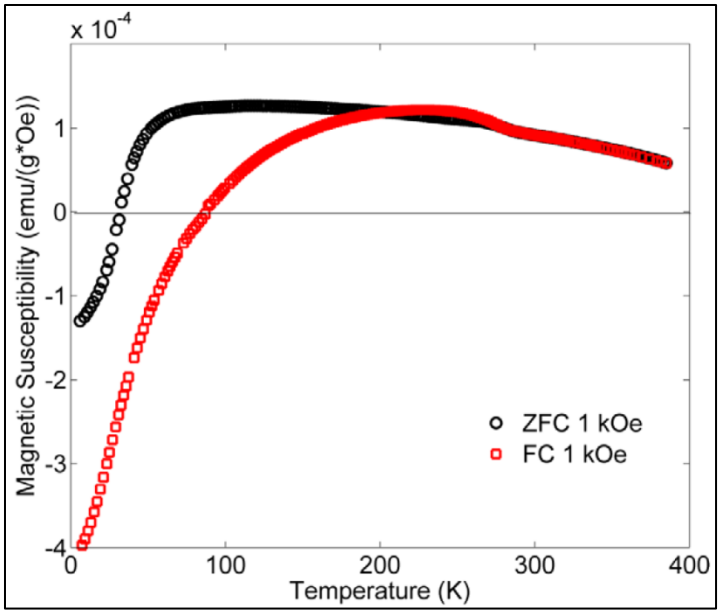

Figure 49: Zero FC along with FC magnetic susceptability at a thousand Oe (Delmonte, et al. 2015).

Since the detected magnetic susceptibility graph did not have a minimum point therefore this was given as the reason why the positive magnetization reversal disappeared under these conditions. It could be stated that using a magnetic field greater than H_1 resulted in the suppression of formation of a minimum in the zero field cooled curve. It was suggested that the BFMO1 system comprised of a pair of unique FM components that contend against each other and hence a moderately small magnetic field will spin the magnetization at 5 K. Thus the superexchange mechanism cannot solely explain the observed magnetization reversal at this temperature. There was similarity in this observation with that of a report by the same researchers (Pernechele, et al. 2013) where soft and hard magnetic characteristics were detected in the magnetization loop at 5 K. The magnetic fields required to completely demagnetize the BFMO 1 sample were approximately equivalent to the H_1 and H_2 values and this was farther validated by Mössbauer spectroscopy. The soft and hard magnetic parts detected were elucidated in connection with a non-uniform scattering of the iron and manganese cations in the BFMO1 sample. This results in some areas in the sample that have a greater concentration of Fe or Mn. Within this magnetic field region of 650 < H < 2200 Oe, the magnetic characteristics of BFMO1 could not be predicted. They were influenced by distribution of Mn and Fe in the different cluters which also relied on the synthesis conditions.

1.5.5.1.4 H > 2200 Oe zone

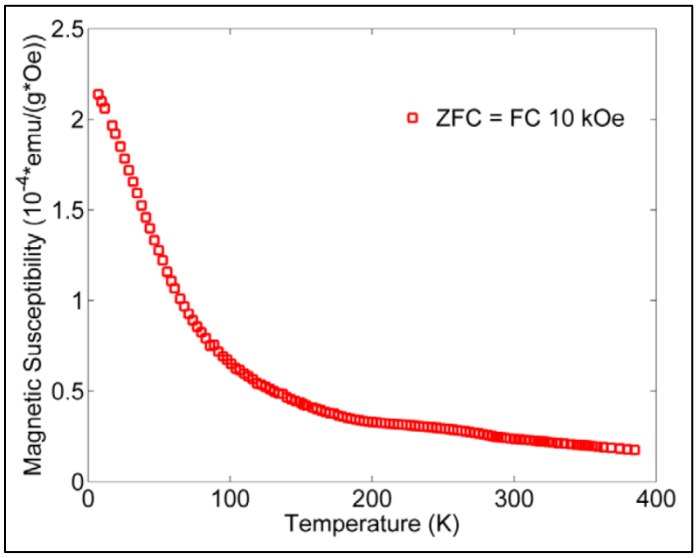

Figure 50: Graph of zero field cooled magnetic susceptibility using an external field of 10000 Oe (Delmonte, et al. 2015).

Using an external magnetic field greater than 650 Oe resulted in a zero field graph shown in Figure 50. The final magnetic susceptibility varies from approximately $0.25 \times 10^{-4}\ emu/(gOe)$ to a maximum of $2.12 \times 10^{-4}\ emu/(gOe)$. The magnetization of BFMO1 does not reverse under the influence of a magnetic force of 10000 Oe as the temperature is decreased from 400 to 5 K, but merely increases in magnitude throughout the experimental temperature range. The applied external field of 10000 Oe totally diminished the source of magnetization reversal. The nature of the graph at temperatures concealed by the Neel temperature was the same as that of a compensated antiferromagnetic system (Benitez, et al. 2011) under elevated magnetic field conditions. This report was consistent with that of (Pernechele, et al. 2013). Two explanations were suggested to be the source of a frail ferromagnetism detected in the BFMO1 system suspected of perovskite B site disordering. Firstly spin canting due interaction of the orbital and spin momentum of the electrons and secondly the non-considered magnetic moments of the Fe and Mn clusters.

1.5.5.2 Mössbauer measurements in BFMO1

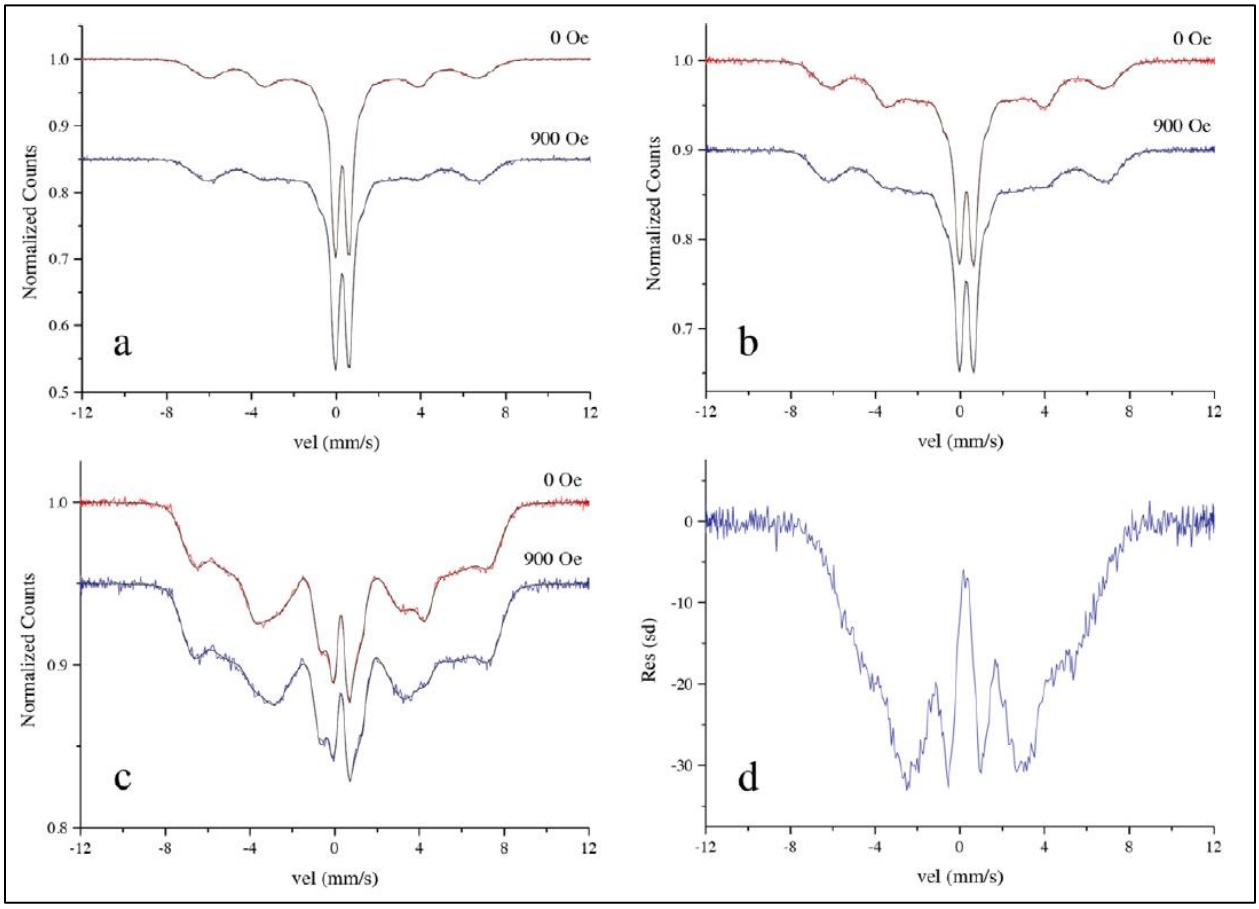

Figure 51: (a, b, c) Mössbauer spectra of BFMO1 at different critical temperatures for the 0 and 900 Oe (d) Residual count with the effect of superparamagnetic property and sub-1 component removed (Delmonte, et al. 2015).

Mössbauer spectra of BFMO1 at different temperatures and magnetic force of 0 and 900 Oe is shown in Figure 51 a, b and c. It was suggested that Fe cation concentrated zones and zones with less Fe concentration (Fe-Mn and Mn-Mn) were the two components make up the spectra the observed spectra. The contribution from the Fe concentrated zones was defined by hyperfine fields the same as those in BFO while those due to low Fe concentration zones were superparamagnetic and consisted of a doublet-like structure with a weak magnetic field aligned part (Pernechele, et al. 2013). The variations of the spectra line shape as the temperature was varied was characterized by a decrease in the superparamagnetic doublet into a superparamagnetic LF part as detected in the spectra where no magnetic field was applied. When

comparing the 0 Oe and 900 Oe spectra, it is evident that the applied magnetic field suppresses absorption of γ-rays at velocities of $(-4, -3)\ mm\ s^{-1}$ and $(3, 4)\ mm\ s^{-1}$ which are the velocities at which the magnetic field has the greatest magnitude. The suppression is less observable at diminished temperature and becomes more pronounced at room temperature. This was elucidated in terms of the robust relationship between the hyperfine inner fields distribution and applied magnetic field. The researchers choose the second interpretation, despite it being contrary to the antiferromagnetic properties of their BFMO1 sample. On condition that the external field interactions are adequately large to break down the anisotropy barrier, absorption would be increased in the mentioned velocity ranges due to initiation of the spin flop mechanism. However if there is supremacy of the anisotropy forces, the line form is not expected to vary considerably (Q. A. Pankhurst 1996). This observed characteristic which appears like a superparamagnetic doublet part that rapidly diminishes was commonly identified with antiferromagnetic nanoparticles that exhibit magnetic anisotropy in one direction (Bodker, et al. 2000). It was suggested that quantum effects influenced this observed characteristic as it lack the aspect of line broadening at average temperatures which are commonly observed in nanoclusters of antiferromagnetic molecules (Cianchi, et al. 2002). The non-consistent distribution of Fe^{3+} and Mn^{3+} within the double perovskite BFMO1 sample was suggested to be the origin of different magnetic islands which in turn act as magnetically and electrically interacting nanoparticle sites in the solid matrix.

The fitting method adapted for the spectra of BFMO1 was similar to the method they had used previously in (Pernechele, et al. 2013). It is for this reason that they preferred to formulate the Mössbauer cross-section σM(E) in terms of seven Voigt sextets using a well establish method as the one used for the distribution of hyperfine field (Rancourt. 1989). The different components that represent the spectra were described by sub-1 to sub-7. The magnetic component of the BFMO1 sample throughout the experimentation temperature range was represented by sub-1. This is the component that defines the spectrum external lines as it is the greatest contributing field. The low energy level superparamagnetic sites that arose from the Fe-Mn lumps were described by four sextets. While sub-6 and sub-7 described the high energy levels that result from clusters that have the same ion clusters. These clusters have are characterized by inner doublet-like architecture. Evidence of good fitting throughout the temperature range was based

on the 0 Oe and 900 Oe spectra which were of high quality. The precision of Mössbauer cross-section was farther also shown by the accuracy of the fits. Figure 51 a to c is an illustration of the spectra for BFMO1 obtained at 300, 285 and 250 K. When the effect of SP doublet component is removed at a temperature of 270 K, Figure 51d is obtained.

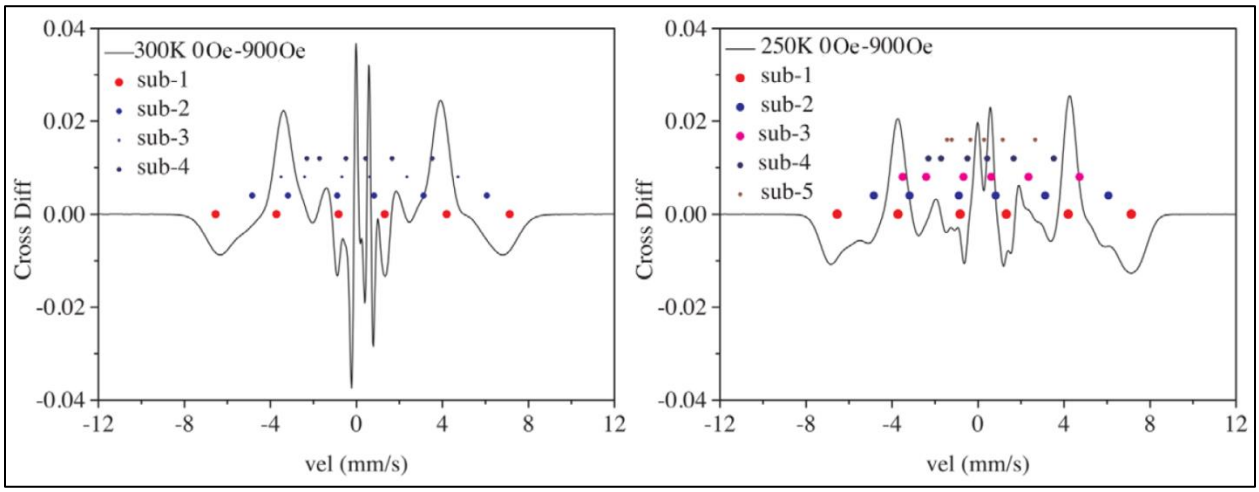

Figure 52: BFMO1 ZF and FC graphs mössbauer coss section at 300 K and 250 K. The contribution of each sub-1 to sub-5 line is shown by the dotted lines (Delmonte, et al. 2015).

Mössbauer cross-section values at a temperature of 300 K and 250 K with a magnetic field of 900 Oe and without a magnetic field is shown in Figure 52 a and b. At both the temperatures the sub-1 which describes the maximum magnetic field defined in the comprehensive temperature boundary of experimentation had the same magnitude and form. Since these features were observed throughout the experimentation temperature range they were taken to be signature of polarization of sub-1 component. The sub-1 is furthermore not sustained magnitude of magnetic field which is the force behind the site which are rich in Fe, which can be attained by not considering the orientations that are not aligned. This leads to the conclusion that the decrease in absorption observed at $[-4, -3]\ mm\ s^{-1}$ and $[3, 4]\ mm\ s^{-1}$was as a result of the maximum field part being polarized. A value of 0.8 was obtained from the intensity of the intermediate and inner absorption lines as a ratio for the 250 K and 300 K spectra. This value was the same as that of the plane of easy magnetic ordering of $BiFeO_3$. This value of the texture parameter could be enhanced by lowering the temperatures below 275 K. It assumed a value of 1.4 when

temperature reached 245 K. These computed magnitude of the sub-1 texture parameters were in accordance with antiferromagnetic interactions of metal cations. This is because sites that are characterized by concentrated antiferromagnetic properties sites have uncompensated moments which manifest either on the surface or within the cluster site due to Mn–Fe substitutions. Influence of the superparamagnetic property on the Mössbauer cross-section resulted in a higher texture parameter of 2. This SP ordering had non-aligned magnetic moments which took the form of magnetic ordering found in powdered compounds which have an axial anisotropy. Such ordering was detected by neutron diffraction and it was anticipated due to magnetic ordering over a long range (Delmonte, et al. 2015). Spin was found to be oriented in the a axis of the unit cell. The electric quadrupolar splitting that arises from exchange between the gradient of the electric field and electric quadrupole moment of the nucleus. This was found to have a value of 0.65 $mm\,s^{-1}$. While the computed angle between quantized electrical field gradient and magnetic hyperfine field was approximately 44.12° a value which had no relationship with the external field throughout the entire experimentation temperatures.

As means of establishing the harmony of observations from the Mössbauer spectroscopy and the information on structuring of the bonded atoms in the BFMO1 grain, the influence of the lattice on the electric field gradient tensor was examined using the a crystallographic axis as the direction of spin alignment. This direction was adopted from the powder neutron-diffraction results. Forty two ions that were positioned in a sphere of diameter 8.85 Å with a magnetic ion as the center were considered during the computation. It had a quadrupolar splitting value 0.45 $mm\,s^{-1}$ with the angle between quantized electrical field gradient and magnetic hyperfine field being 40.11°. Basing on this the easy axis anisotropy determined by Mössbauer spectra was believed to be in accord with the powder neutron diffraction determined atomic moment direction.

The Mössbauer spectra with a magnetic field applied and with an applied magnetic field affirmed that BFMO1 has two parts that have different magnetic characteristics. One of the components contains concentrated Fe and is characterized by soft magnetic properties. Twenty percent of the Fe ions were located at these sites. While the other part which had an axis easy anisotropy was

composed of the remaining eighty percent of the iron. This second component, under constant temperatures it was found to have its high energy state having zero magnetic moment being localized on top of the barrier while the low energy state was localized inside the anisotropy barrier. The transition between the elevated energy state and the minimum energy condition zero magnetic moment, is by second order perturbation, when there are more particles that have energies greater than the barrier force, BFMO1 will display soft magnetic characteristics. This is why hard magnetic characteristics were observed when the temperature was decreased, because the population with high energy had been reduced. This therefore leads to an explanation of the illustration in Figure 46 in which there was superposition of the Fe concentrated and Fe-Mn phase which were the low and high coercivity phase.

1.5.6 Electronic Energies of $BiFe_{(1-x)}Mn_xO_3$ Slim Layers Examined by XAS.

In this research (Abduleziz Ablat. 2012) prepared the sample of $BiFe_{(1-x)}Mn_xO_3$ with compositions in the range $0 \leq x \leq 0.3$ using a Pulsed laser deposition chamber joined to a photoemission spectroscope for the purpose of determining the binding energies in the different systems. By utilizing the solid state reaction method and heating to a temperature of 820°C 20mm thin films of $BiFe_{(1-x)}Mn_xO_3$ were produced from a mixture of manganesse oxide (+3 oxidation state), iron oxide (+3 oxidation state) and Bismuth oxide. All the elements used were 99.99% pure however a minute surplus of bismuth oxide was supplemented for the purposes of taking care of Bismuth losses in the course of sintering. In order to get rid of surface defilement the researchers heated the substrate to 700°C at an O_2 pressure of 0.0056kPa and 550°C temperature. At the same time as the $BiFe_{(1-x)}Mn_xO_3$ was fixed by Pulsed laser deposition at repeated rate of 0.66s, optical energy per unit area was maintained at 2.3 J/cm^{-2}. Subsequently the samples despite composition variations were tempered under duplicate environments of approximately 10^{-8}Pa.

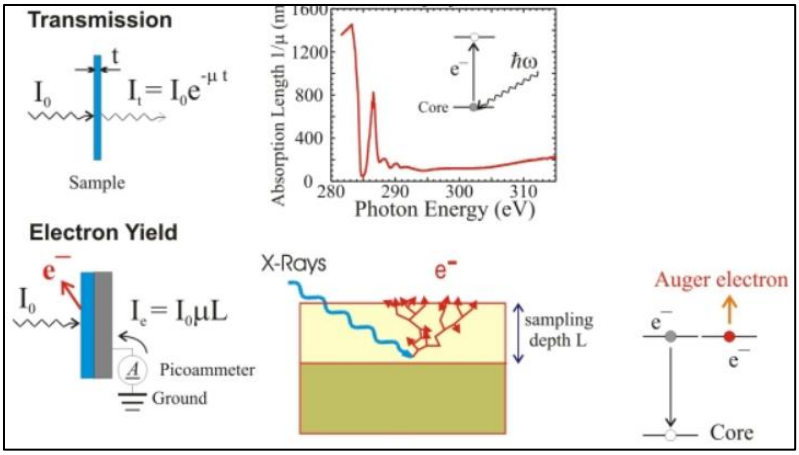

Figure 53: X-Ray Absorbance Spectrum methods. https://www-ssrl.slac.stanford.edu/nexafs.html> [Accessed on: 28 September 2019].

The minimum energy that the spectroscope could resolve was related to the photon energy (Abduleziz Ablat. 2012) and for this instant it was approximately $0.2eV$ to $0.7eV$. From the two available methods of determining electron energies in x-ray absorption spectrum, transmission mode and fluorescence mode the researchers used the later which is normally referred to as total electron yield mode. The transmission method is best suited to thin foils whilst the electron yield method is compatible with regular samples. An illustration of the two techniques is presented in Figure 53. It is of the essence to recognize that the absorbed x-ray energy not straight away determined. The electrons that are generated due to absorption of x-rays are what are determined as a function of the absorbed x-ray energy. Available from: <https://www-ssrl.slac.stanford.edu/nexafs.html> [Accessed on: 28 September 2019].

1.5.6.1 Fe L Edge XAS.

$2p$ orbital high energy EMR assimilation spectra of $BiFe_{(1-x)}Mn_xO_3$ film is illustrated in Figure 54(a). The photon energy of the Fe^{3+} in Fe_2O_3 and Fe^{2+} in FeO is also shown. For the different compositions of the film x = 0, 0.1, 0.2 and 0.3 the photon energy and intensity of the t_{2g} and e_g was observed to change.

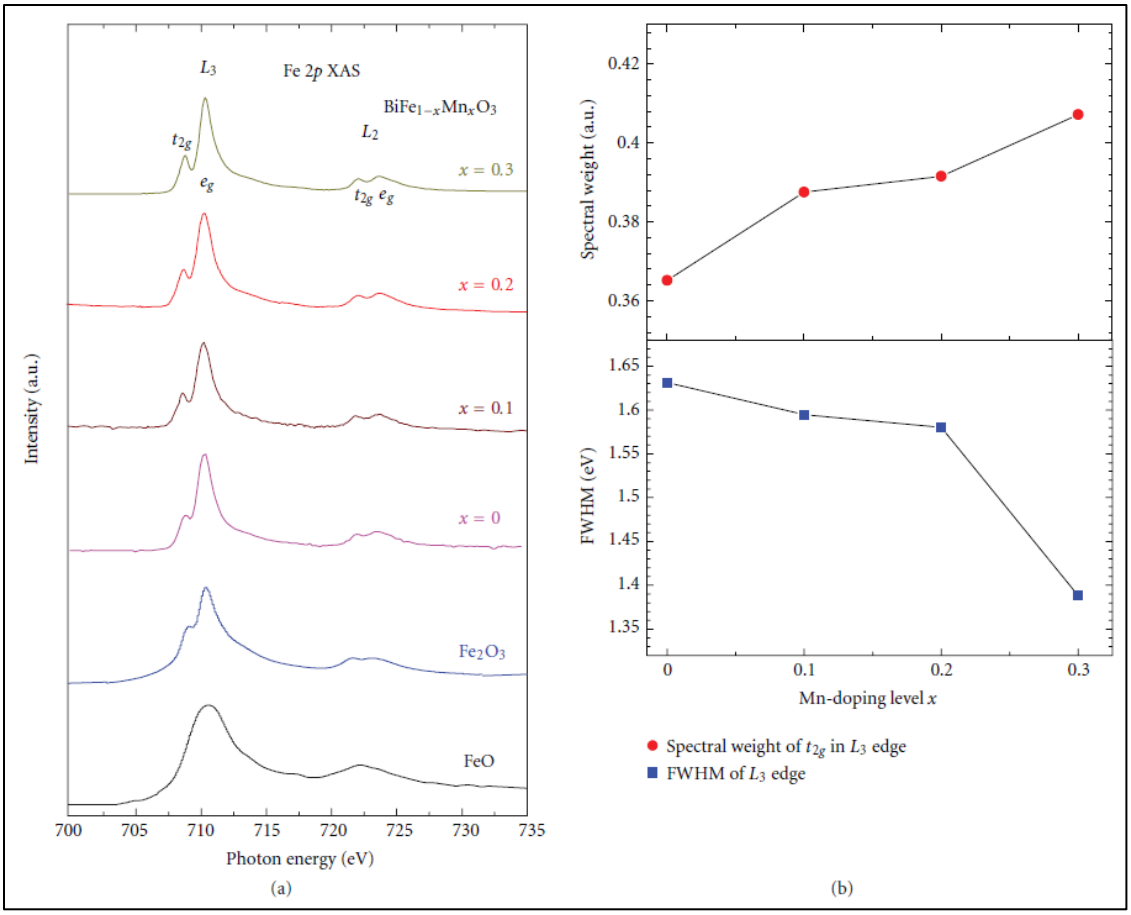

Figure 54: (a) Fe L edge of $BiFe_{(1-x)}Mn_xO_3$ film for $(0 \leq x \leq 3)$ (b) Full width at half maximum of L_3 edge and influence on spectrum of t_{2g} in L_3 edge in relation to x (Abduleziz Ablat. 2012).

From Figure 54 there is evidence that there are $3d$ orbitals which are unfilled in the Fe ion. Orientation of electron spins are generated from splitting of the $3d$ orbitals due to a quantum mechanical effect of interaction of identical particles, which are electrons in this situation. The minority are in the spin down while the majority is located in the spin up. The two spin down and up states are again divided into t_{2g} and e_g attributable to the action of octahedral crystal ligand field. The characteristic X-ray absorption peak of the iron $2p$ orbitals was characterized by a L_3 lower energy shoulder which represented unfilled t_{2g} spin down state. The higher energy shoulder characterized unfilled spin up e_g state. L_2 edge also divided into down spin t_{2g} and e_g. For all the samples the energy difference between the spin down t_{2g} and e_g of this octahedral complex was found to be approximately 1.6 eV. As a result, as in $LaFeO_3$ electrons occupy each of the 3d orbitals before pairing thereby remain in high spin configuration $t_{2g}^3\ e_g^3$. From the form

of X ray absorption spectra of Fe $2p$ the valence state indicates a similarity of the doped compound with the Fe_2O_3 system. However it is distinct from the spectra of FeO compound. It could be deduced from this that the Fe ion in the $BiFe_{(1-x)}Mn_xO_3$ film has a +3 oxidation state and this was similar to a report by (Anjum, et al. 2011). The X-ray absorption peak widths and peak intensities variations are an indication of alteration in the electron density of state due to changes in level of Mn doping. The distribution of the electronic density of state between oxygen 2p orbitals and iron 3d orbitals changes with levels of Mn doping. There was a clear cut difference between the Fe L_3 edge that had been computed by addition of t_{2g} spin down and e_g spin down states and that obtained from the formulae $I_{t_{2g}}$ /($I_{t_{2g}}$ + I_{e_g}).

This is illustrated in Figure 54(b). Increasing the doping level from x = 0 to x = 0.3 increased the t_{2g} spin down intensity from 0.364 to 0.408. However the L_3 edge decreased with an increase in Mn doping level from 1.63 eV to 1.41 eV. In order to comprehend the source of these discrepancies the researchers first considered the oxidation state of $BiFeO_3$ which was not doped. Since these changes were brought about by increasing the level of Mn doping in the $BiFe_{(1-x)}Mn_xO_3$ system, then the hybridization between the O $2p$ and Fe $3d$ was influenced by these changes. Due to the hybridization of the $3d$ orbital in Fe and $2p$ orbital in oxygen the Fe is believed to have different states of $3d_5$ and $3d_6L$. The strong hybridization of Fe $3d$ orbitals with the O $2p$ orbitals results in the generation of ligand holes (Chen, et al. 2012). These ligand holes influence the electronic dynamics of the $BiFe_{(1-x)}Mn_xO_3$ film.

The relocation of charges originating out of the O 2p energy level to the iron 3d orbitals results in the Fe $3d_6L$ state. It is on this basis that the down spin state of the t_{2g} was observed with an upsurge in the level of Mn doping because the quantity of Fe $3d_5$ had increased. A reduction in the peak width was elucidated hinging on the similarity in the modification of the intensity due to decrease in the hybridization strength. Since the energy chasm difference between valence energy to the conduction band of oxygen $2p$ takes the magnitude approximately $6eV$ (R. L. Kurtz 1983), the mixture of Fe $3d_5$ and $3d_6L$ will tend to have a higher amount of Fe $3d_6L$ when there is a more substantial hybridizing action in the $BiFeO_3$ system resulting in decreased

intensity and an increased peak width due to delocalization. Simultaneously, the impact of decreased hybridization brought about by the Mn doping results in a surge of the iron $3d_5$ quantity within a mixed iron $3d_5$ + iron $3d_6L$ states.

1.5.6.2 Oxygen K Edge X-ray Absorption Spectroscopy.

High energy EMR assimilation spectra peaks of oxygen are illustrated in Figure 55 and highlighted as a, b, and c. Intensity variations of the corresponding peaks and FWHM of duplicate crest a is illustrated in Figure 55 . The L edge peak generated by the transition of bound electrons to unfilled orbitals maximizes from approximately 0.10 to 0.21 as the manganese concentration is increased from 0 to 0.3. However the Full Width at Half Maximum starts at an initial value of 1.95 eV and reduces 1.25 eV.

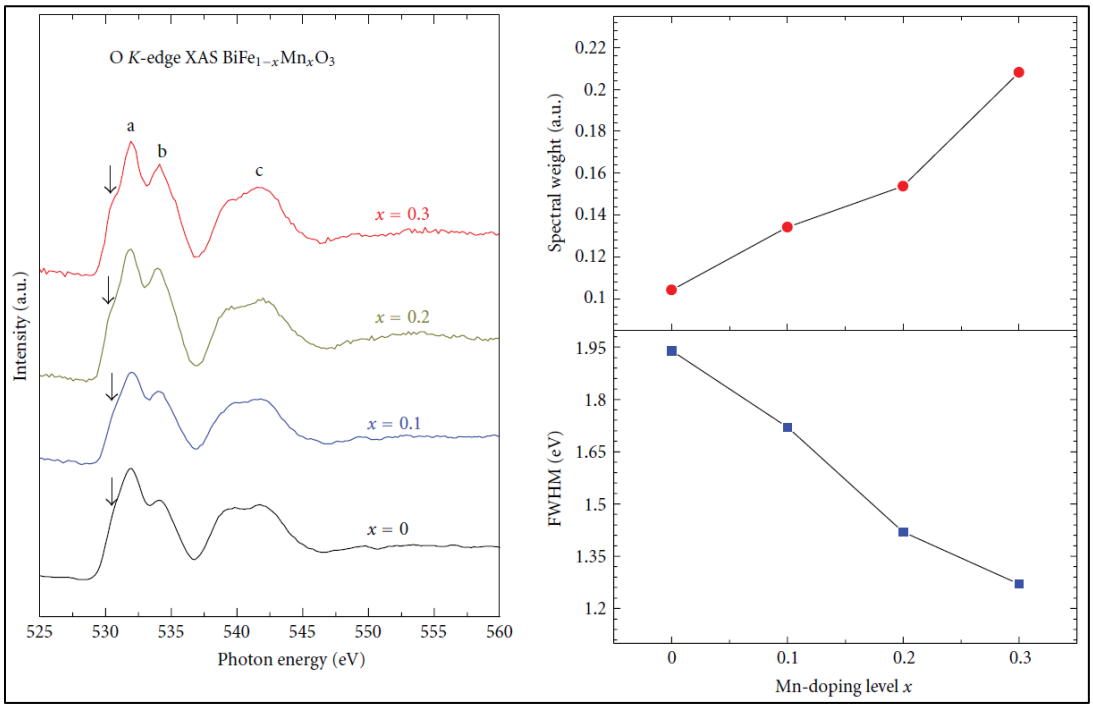

Figure 55: K shell electron X-ray absorption spectroscopy of $BiFe_{(1-x)}Mn_xO_3$ slim sections with a doping of 0 up to 0.3 impurity quantities (Abduleziz Ablat. 2012).

Full comprehensive data about how oxygen 2p orbitals merge with transition metal X $3d^n$ + X $3d^{(n+1)}$ orbitals was obtained from the x-ray absorbance spectroscopy. X $3d^n$ + X $3d^{(n+1)}$ serve as [Fe $3d^5$ + Fe $3d^6\underline{L}$] oxidation state hybridized with [Mn $3d^4$ + Mn $3d^5\underline{L}$]. From the figure the four components Extend x-ray absorption, near edge XR absorption spectral line subdividing, pre-edge and XR absorption near edge structure of the XR absorption spectrum can be easily identified. Extend x-ray absorption was observed at values above $547.5eV$ while near edge XR absorption spectral line subdividing occurred from $542.5eV$ to $547.5eV$ while the pre-edge was noted at values below $528eV$. X-ray absorption near edge structure occurred at energy values above $528eV$ up to $537eV$. The merging of orbitals causes interactions between X $3d$ and oxygen $2p$ orbitals as a result of the the hole state L of the oxygen $2p$ orbital. The quantity of energy states available for portion of X 3dn+1L in X 3dn + X 3dn+1L mixed condition is clear shown in the spectrum.

1.5.6.3 Magnetic Properties of different compositions of multiferroic $BiFe_{(1-x)}Mn_xO_3$

Figure 56 illustrates the magnetic hysteresis loop of $BiFe_{(1-x)}Mn_xO_3$ at x = 0, 0.1, 0.2 and 0.3 doping level for black, red, green and blue plots correspondingly.

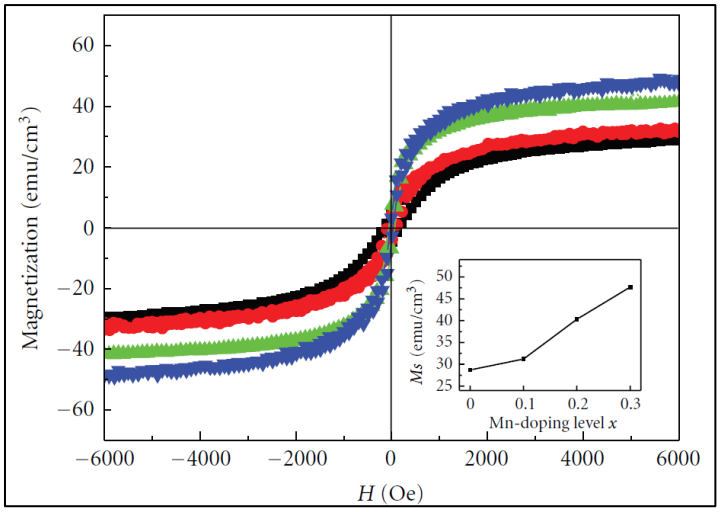

Figure 56: Magnetic hysteresis of $BiFe_{(1-x)}Mn_xO_3$ determined at room temperature (Abduleziz Ablat. 2012).

There was a general increase in the saturation magnetization as the doping level increased and this was rational with the literature by (Gu, et al. 2011) and (Azuma, et al. 2007). The greatest increase was noted between 0.1 and 0.2 doping level. Conversely an escalation of the manganese concentration minimizes the coercive field of the sample. From the magnetic hysteresis loop (Abduleziz Ablat. 2012) concluded that $BiFe_{(1-x)}Mn_xO_3$ exhibits a ferromagnetic behavior when the concentration of manganese is increased from 0 to 0.3. The weak magnetic properties detected at 0% concentration of Mn in $BiFeO_3$ was attributed to canted spins that result from distorted rhombohedral double perovskite architecture. The loop area of the $BiFeO_3$ is very narrow and saturating at $28.7 emu/cm^3$ (Ramesh and J. Wang 2003) and this value was nearly equivalent to that reported by (Huang and X. M. Lu 2010). The 0.1, 0.2 and 0.3 Mn doped $BiFeO_3$ saturated at 31.2, 40.3, and 47.7 $7\, emu/cm^3$ respectively. As compared to bulk $BiFe_{(1-x)}Mn_xO_3$ values determined by (Xu and S. Q. Zhou 2011), the films deposited by pulsed laser deposition had a much higher saturation magnetic moment. An explanation to the elevation of the macroscopic magnetization as the doping level of manganese increase was related to be associated with either two processes.

The first was that film $BiFe_{(1-x)}Mn_xO_3$ transforms in its crystal structure or secondly it contains an unspecified composition of Fe^{2+}/Fe^{3+} (K. Takahashi 2006.). However the X ray photoelectron spectroscopy results confirmed that the incorporation of only Fe^{3+} was in the inevitable. Secondly the X-ray diffraction pattern did not reveal structural mutation from rhombohedra to quadrangular as the impurity level of manganese was varied. Therefore basing on these two factors enhanced magnetization was not a result of structural variation or the differing electron configuration of Fe^{2+} and Fe^{3+}. According to (Huang and X. M. Lu 2010) and (Rana and K. Takahashi 2007) it is not caused by shear arising from non-uniform film thickness. The conditions for the growth of the film were monitor under strict and identical conditions therefore the films were exactly the same in dimensions. The magnification of saturation magnetism in film $BiFe_{(1-x)}Mn_xO_3$ was explained in terms of a change in the hybridization interactions leading to a variation in number of charge carriers states (electrons) per volume at a particular energy between Fe-O and Mn-O combination (Abduleziz Ablat. 2012).

1.6 Single phase double perovskite multiferroic Bi_2FeMnO_6 characteristics

1.6.1 Switching of magnetization direction in Bi_2FeMnO_6 induced by Dzyaloshinskii–Moriya interactions.

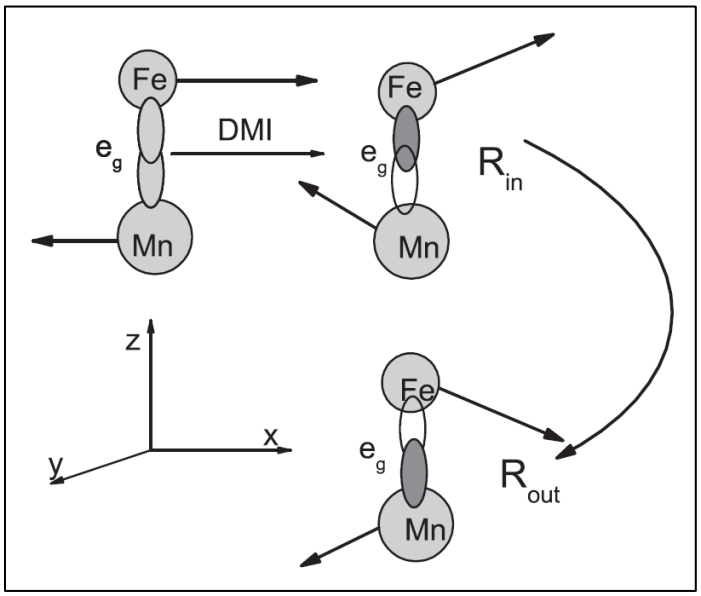

Figure 57: Swiveling of magnetization and Dyzaloshinskii–Moriya interference between the close located iron and manganese ions in BFMO2 (Feng 2012).

A pair of partial waves with a cut-off radii of 1.1, 2.3, 2.3 and 2.5 atomic units for oxygen, iron, manganese and bismuth respectively was utilized for each l quantum number. All computation were based upon a 6x6x6 k point grid sampled by Monkhorst–Pack technique. The electronic characteristics and resultant magnetization for each unit cell were computed in context of the LSDA + U formulation and to account for the intense repulsions due to d localized sites a Hubbard term was included (Anisimov and J. Zaane 1991). For both Fe and Mn d orbitals, the values for the subtraction of the Hubbard parameter and exchange coupling $(U - J)$ and the effective Hubbard parameter were kept in the range 0 and 5 eV. While the difference of the Hubbard parameter and the exchange interaction was assigned a value of zero, the exchange interaction was assigned values of 0, 0.5, 0.8, and 1 eV. Exchange interaction value J was however kept constant at 1 eV while the effective Hubbard parameter was varied. In order to formulate the G-type antiferromagnetic order with an AFM orientation in the x axis, spin orbit

interactions were taken into consideration in the ab initio computations. Computations were done using LSDA to DFT using ABINIT software. Electron and ion interactions were modeled by projector augmented wave method using identical cutoff energies of 500 eV. The oxidation state considered for bismuth were $5d$, $6p$ and $6s$ electrons, for manganese and iron it was $4s$, $4p$, and $3d$ and O2s and $2p$ electrons for oxygen. The strain which results in a phase transition into a stable state (AFD distortion) was represented by a revolving vector which characterized the direction in which the eight faced oxygen polyhedron rotated. The straying away of rotational vectors which represent the revolving away from each other of oxygen octahedral was presented as R_{out} and R_{in}. The twist angle was 10° in the coordinate system. The superexchange interactions which describe the magnetic interaction via a nonmagnetic anion were represented by J while the electrostatic interactions where represented by U. These two figures of U and J were used in the local spin density approximation + Hubbard parameter.

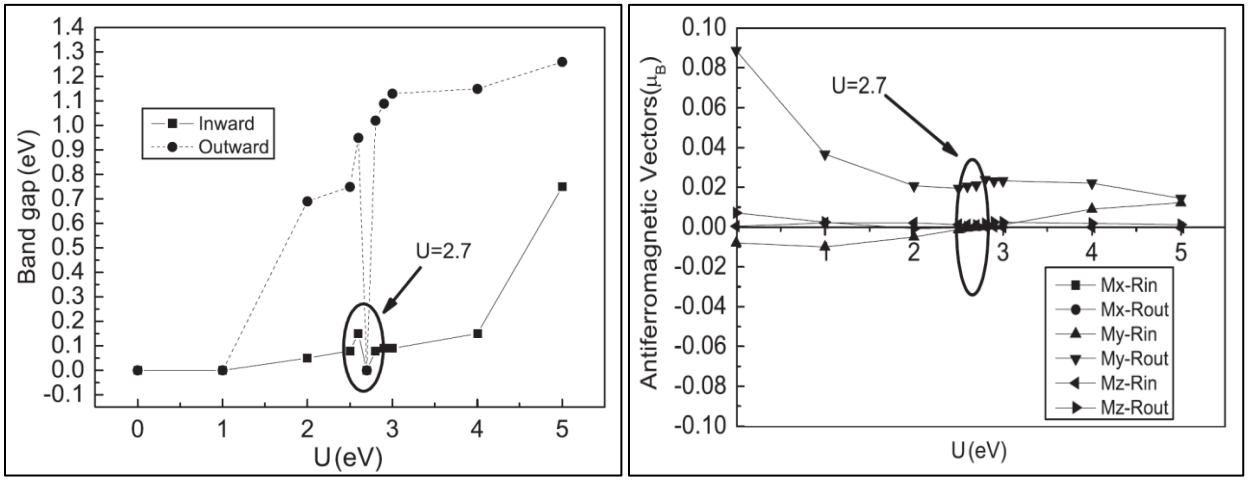

Figure 58: (a) Relationship between band gap and Hubbard parameter, U. (b) Dependence of antiferromagnetic vectors on the quantity U (Feng 2012).

The different values of magnetization per unit cell in the x, y and z direction obtain when the superexchange interactions and Hubbard parameters were varied for an inward and outward rotating vector are published in (Feng 2012). For the purposes of understanding the relationship between parameters under study, superexchange magnitude was varied while the effective Hubbard parameter was kept constant (U-J) at 0 eV. It was noted that the observed that there is no relationship between the superexchange interactions and resultant magnetization for a

constant effective Hubbard parameter, U'. Each Fe cation is encompassed by six other Fe ions with opposite magnetic moment (G-type AFM) and is given an initial orientation in the x direction. The ferromagnetic ordering oriented in the x direction is a result of Fe and Mn interactions. However the interaction of neighboring moments is influenced by Dzyaloshinskii–Moriya interaction and will produce a resultant magnetic moment in the y axis instead of the x axis. For effective Hubbard parameters below 2.7 eV, a 180° orientation change of the rotational vector causes exactly the same effect on the resultant magnetic moment. This revealed a connection between the magnetic ordering and antiferroic distortion and that Dzyaloshinskii–Moriya interactions are influencing the two under these conditions.

However when the U became greater than 2.7 eV the connection between magnetic ordering and AFD is hindered. Under this condition, the DMI were no longer in action. When the effective Hubbard parameter is equivalent to 2.7 eV the magnetic moment component M_y (μ_B) in the y direction becomes 0. It could therefore be deduced that the threshold for eliminating DMI is 2.7 eV and under this condition there are no antisymmetric magnetic moments from Mn and Fe interactions. In $BiFeO_3$ this value for suppressing DMI is much higher. It occurs when the effective Hubbard parameter is approaching 2.9 eV (Feng. 2010). The difference of the two values signifies that the Fe – Fe antisymmetric interactions in $BiFeO_3$ are more robust than Fe–Mn antisymmetric interactions in Bi_2FeMnO_6. The weaker Fe-Mn antisymmetric interactions are derived from $\frac{5}{2}s$ - $\frac{4}{2}s$ while the Fe-Fe antisymmetric interactions are derived from $\frac{5}{2}s$ - $\frac{5}{2}s$. It is proposed that the spiral spin structure is disrupted by varying spin moments and weaker Dzyaloshinskii–Moriya interactions in Bi_2FeMnO_6 compared to $BiFeO_3$. Enhancing of system magnetization reversal and overall magnetization properties in this Bi_2FeMnO_6 is feasible. Resultant antiferromagnetic vectors in Bi_2FeMnO_6 linked to magnetization inversion is shown in Figure 58b. The antiferromagnetic inward and outward rotating vector R_{in} and R_{out} are composed of three components in the x, y, and z direction. From Figure 58b as the effective Hubbard parameter is approaching the critical value 2.7 eV an anomaly can be observed. At 2.7 eV effective Hubbard parameter the DMI disappears. A sign that DMI interactions continue to operate even below the critical values is that magnetization is reversed for all effective Hubbard parameter is below the critical value. The effective Hubbard parameter is conversely correlated

to the Dzyaloshinskii–Moriya interactions. Inversion of magnetic moment is not realized in the z direction because diversion of the original magnetic moment off the x direction solely happens in the xoy plane. The effective Hubbard parameter is below 2.7 eV and that's the region in which the DMI operates. Therefore the magnetization component M_y (μ_B) is revrsed in anticlockwise and clockwise rotation. When the effective Hubbard parameter becomes greater than 2.7 eV, the magnetization component in the y direction will be in the corresponding orientation as the effective Hubbard parameter, which is exclusively steered by the contrasting atomic architecture for CW and CCW swiveling. The connection that exists between Coulomb local exchange and Dzyaloshinskii–Moriya interactions is given by Equation 93.

$$H_{BiFeMnO} = -2 \sum_{Fei,Mnj} J_{Fei,Mnj} S_{Fei}\ S_{Mnj} + \sum_{Fei\ Mnj} D_{Fei,Mnj} S_{Fei}\, S_{Mnj} \ldots\ldots \quad \text{Equation 12}$$

Symmetric superexchange is represented by the first term, while antisymmetric Dzyaloshinskii–Moriya interactions are represented by the last term. On condition that the inversion symmetry of cations is broken in Bi_2FeMnO_6 then DMI will be present. $D_{Fei,Mnj}$ depends on the rotational vector R and antiferrodistortive displacement. D can be computed from the function in Eqn. 13. From this equation it is evident that there is no relationship between symmetric superexchange parameter and it is conversely connected to the local Coulomb exchange.

$$D^2_{Fe,Mn} = \frac{4i}{U}\left[b_{nn'}(Fe-Mn)C_{n'n}(Mn-Fe) - C_{nn'}(Fe-Mn)b_{n'n}(Mn-Fe)\right] \qquad \text{Eqn. 13}$$

From the band gap computation the new Bi_2FeMnO_6 system has exceptional insulating characteristics therefore should be able to invert its ferroelectric state. Assigning a proper value for the effective Hubbard parameter will widen the band gap. In BFO the band gap has been found to be 4.3 eV (Neaton, et al. 2005). By using an effective Hubbard parameter of 5.0 eV for iron and manganese cations in the Bi_2FeMnO_6 system the total density of states was investigated

so as to elevate the band gap by increasing effective Hubbard parameters. The band gap for the rotation vectors R_{out} and R_{in} is illustrated in Figure 58a. Both for the inward and outward rotation vectors become linear as the magnitude of effective Hubbard parameter becomes larger. However the band gap ceases to exist at approximately 2.7 eV with a band gap value of 0.0 eV. For both the inward and outward rotational vector graphs the exists an anomaly on approaching U'= 2.7 eV.

Experimental data tallies with the graphs plotted from theoretical computations in which anomalies are predicted Figure 58b. An extinction of the DMI at a computed effective Hubbard parameter is revealed by the anomalies due to electrons hopping past the Fermi energy. The band gap attained by an outward rotation vector is smaller as compared to the one attained by inward rotation vector. It is suggested this is because of different ligand field located in the Bi_2FeMnO_6 structure. The total density of state with an effective Hubbard parameter of 5.0 eV (Figure 59) and this can be compared with the total density of state without including on-site Coulomb interaction. When the effective Hubbard parameter becomes equal to 5 eV, the finite density of state which is close to the energy level at 0 K, is distanced, thereby assembling into band gap. An outward rotation vector results in a 1.26 eV while an inward rotation vector yields a 0.75 eV. This is evidence of semiconducting characteristics in the 2 antiferrodistortive states. However the expected inverting of the ferroelectric property of the 2 inverted antiferrodistortive states is not obtained due to that if effective Hubbard parameter is not included in the computations then Bi_2FeMnO_6 is metallic. This is evidence that in perovskite metal oxides, on-site Coulomb interactions are required for the expansion of the band gap.

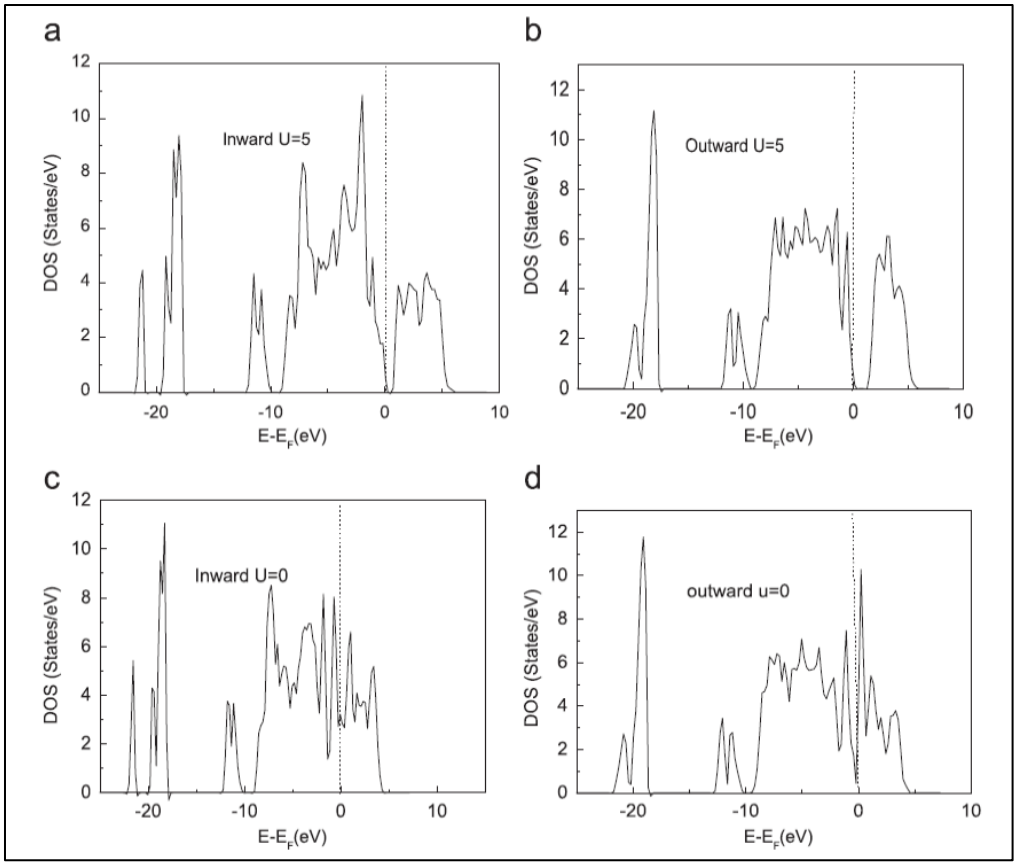

Figure 59: Optical D.O.S. of Fe and Mn for Rin and Rout with U = 2.6 eV and without applying U (Feng 2012).

A complete understanding on how DMI influence local Fe and Mn cations was illustrated by determining the value for the orbital resolved density of states. It was found to be 2.6 eV, a figure which was below the below the critical value for so as to rule out antisymmetric DMI. From Figure 61, the orbital density of state of Fe and Mn when the oxygen octahedral rotational vectors are diverting from each are represented by R_{out} other and when they are rotating towards each other they will be signified by R_{in}. From Figure 61 it is clearly visible that numerous two Fe and Mn e_g orbitals having similar symmetry and equal level of energy in the fermi level. The charge electrons in the Fe-3d and Mn-3d hybridization each other with the interactions being perceived by the e_g- e_g orbitals. This leads to the ideal that antisymmetric DMI acting on Fe and Mn cations are significantly influenced by e_g - e_g antiferromagnetic interaction. Even though $dx^2 - y^2$and $dz^2 - r^2$ make up the e_g orbital, the band between the valence and conduction band (Fermi level) is associated mainly with $dz^2 - r^2$ orbital. It is with

this $dz^2 - r^2$ energy level that finite orbital density of state is determined. It was therefore proposed that there is obstruction of e_g- e_g antiferromagnetic ordering by Fe and Mn cations bordering $dz^2 - r^2$ orbital. By applying the rotation vector with a deviating condition and 5 eV of U, (Feng 2012) determined the orbital density of state of iron and manganese (Figure 60) and used to explain the effect of e_g- e_g states interaction in this system. The unexpected occurred under these conditions with the e_g state of outward rotating Mn being forced out of the Fermi energy band. There is restriction of hybridization of degenerate e_g- e_g of the local Fe and Mn and is observed as a diminished Dzyaloshinskii–Moriya interaction. This is an indicator to that direction of magnetization can be inverted significantly by e_g- e_g state interaction. The variations that occur to the charge between the iron and manganese cation is depicted in Figure 57 and this brings about a inverting of magnetization.

The breaking of the inversion symmetry of cations permits Dzyaloshinskii–Moriya interaction in Bi_2FeMnO_6 to allow electrons to jump between degenerate e_g- e_g orbitals (Feng 2012). As the oxygen octahedra gyrates, the electrons jumping from one orbital to the other couple with this gyration giving rise to a resultant magnetization. The rotating vector polarizes the charge in neighboring e_g- e_g orbitals. The rotational vector's direction is varying therefore the way the charge is spread in nearest e_g- e_g orbital is inversely polarized. If there were no Dzyaloshinskii–Moriya interaction between neighboring magnetic ions the charge would be spread evenly, the homogenous state is however converted to a polarized distribution due to disruption by these interactions. It is therefore proposed on these conditions that the invisible DMI occur in this way in perovskite multiferroics. Antiferromagnetic interaction in the e_g- e_g are more robust than the Antiferromagnetic interactions of the $t_{2g} - t_{2g}$made up ofdxy, dxz and dzy justifying that e_g- $e_g$interactions strongly participate in antisymmetric Dzyaloshinskii–Moriya interaction.

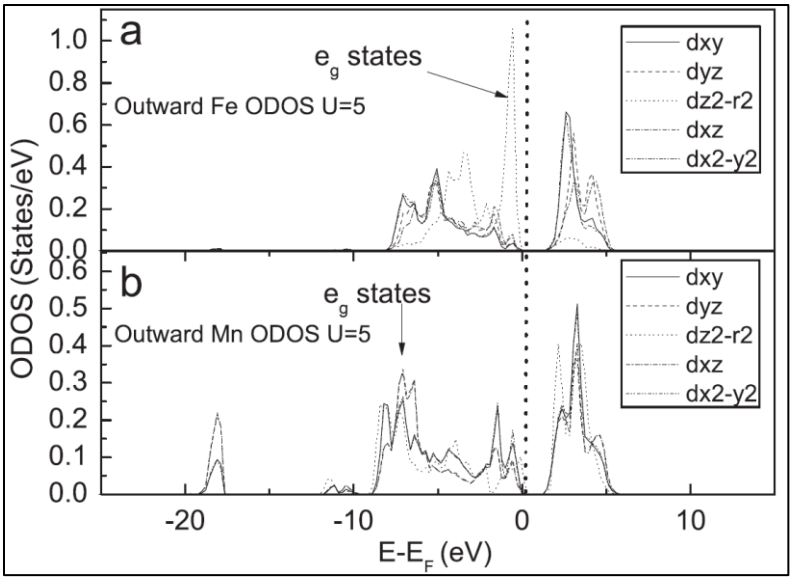

Figure 60: Optical density of states of iron and manganese for R_{out} (Feng 2012).

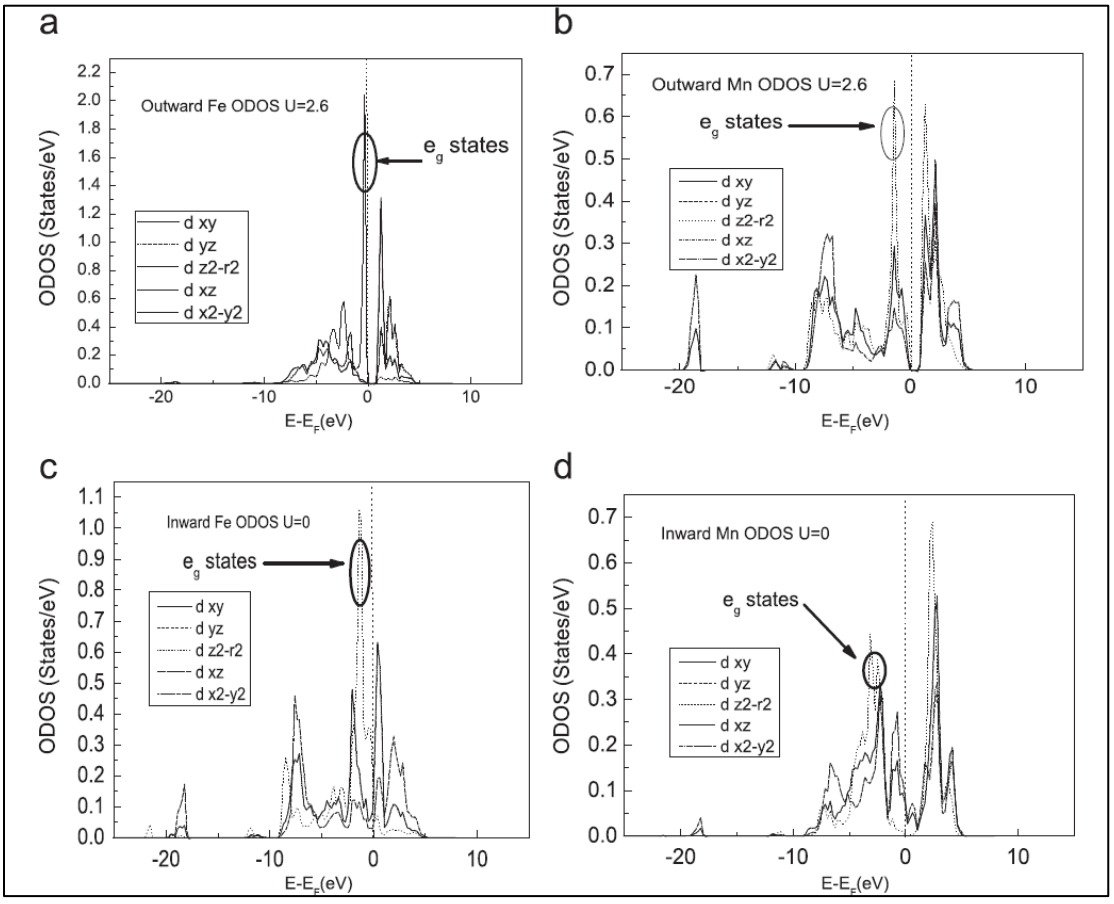

Figure 61: Optical D.O.S of Fe and Mn for R_{in} together with R_{out} with a Hubbard parameter = 2.6 eV and U being 0 eV (Feng 2012).

1.6.2 Electric polarization along with leakage current characteristics of BFMO2/$SrTiO_3$ dual layered slim film by CSD

1.6.2.1 X-ray diffraction pattern and surface morphology.

According to the first principle computations carried out by (Shen, et al. 2014) Bi_2FeMnO_6 absorbs energy for bond formation. It was on this condition of a positive enthalpy that was considered to be metastable. The nature of metastability leads to Bi_2FeMnO_6 crystallizing with atoms arranged differently depending on the methods used for deposition onto thin films (Du, et al. 2010). The initial method involved strontium titanate crystal substrate insulator and chemical solution deposition (overarching). No diffraction peaks for the strontium titanate were detected in the $LaNiO_3$ buffered silicon substrate. As a result a hexagonal perovskite structure with a phase symmetry P63cm three dimension space orientation was concluded basing on six peaks detected in the x-ray diffraction pattern of Bi_2FeMnO_6/ strontium titanate two layered thin films. The chosen direction of expansion of the Bi_2FeMnO_6/ strontium titanate on the $LaNiO_3$ was confirmed by the higher intensity of the ratio $\frac{[I(00l)]}{[I(hkl)]}$ with maximum being (004). Hexagonal perovskite architecture has also been reported in $ErMnO_3$ prepared by the ability of reactants to dissolve in hot water under pressure and powder crystals of $TmMnO_3$ (Zhu, et al. 2010) and also $BiFe_{0.5}Mn_{0.5}O_3$ films (Prokhorov 2012). The high spatial resolution of Bi_2FeMnO_6/ strontium titanate shows a close knit structure which lacks empty spaces or cracks. The degree of fineness of the spaced micro-irregularities was determined to be approximately 14.5 nm with granular swellings of 280 nm.

1.6.2.2 Electric hysteresis of Bi_2FeMnO_6/ strontium titanate capacitor.

At room temperature an electric hysteresis loop with a saturation value of approximately 3 $\mu C/cm^2$ was obtained. The electric polarizing field was 330 $kVcm^{-1}$. This observation justified the presence of ferroelectric property in Bi_2FeMnO_6.

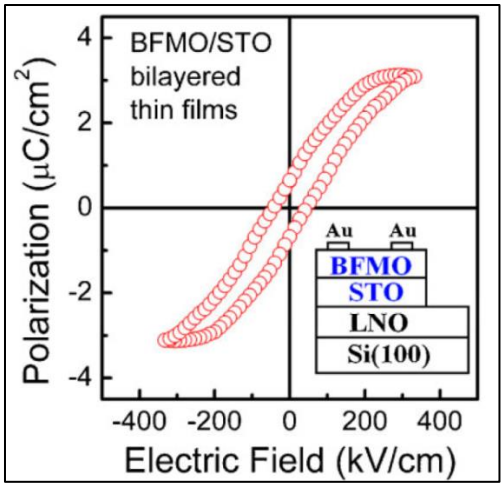

Figure 62: P–E hysteresis loop of Bi_2FeMnO_6 / strontium titanate sample thin-film (Shen, et al. 2014).

The insert (Figure 62) shows the architecture of the constructed capacitor. The electric polarization that remained after removal of the electric field was 0.6 $\mu C/cm^2$. A coercive electric field which total removed the electric polarization of Bi_2FeMnO_6/STO capacitor was 80 $kV\,cm^{-1}$.

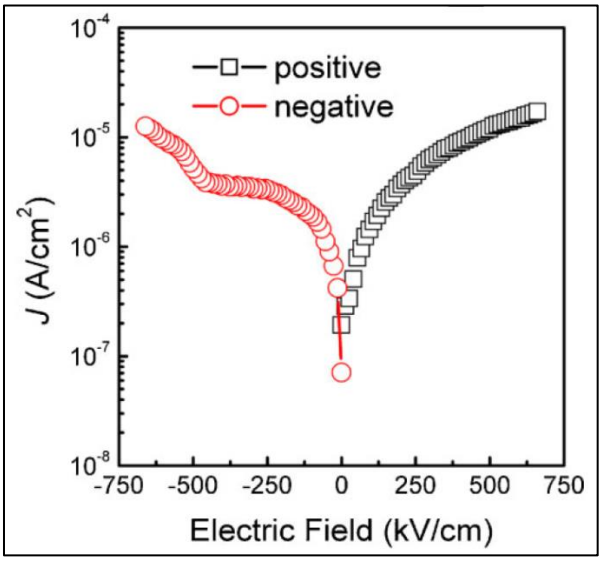

Figure 63: J–E curves with positive and negative voltage (Shen, et al. 2014).

For insulating materials no current should flow when a voltage is applied. This current is referred to as leakage amperage/cm^2 and is reliant on the area of the insulating material. The leakage current at room temperature in relation to the applied voltage is illustrated in Figure 63. A positive bias was when the $LaNiO_3$ electrode was applied a positive potential while the negative bias was defined as a negative potential difference at the gold electrode. A maximum of 10^{-5} A/cm^{-2} leakage current was observed while the minimum value was approximately 7.07 x 10^{-7} A/cm^{-2}. The suggested reason for a diminished leakage current at zero electric field was there was manganese replaced iron in the crystal structure thereby eliminating the valence oscillation due to Fe^{2+} and Fe^{3+}. Such fluctuations have been documented in the basic perovskite $BiFeO_3$ doped with Mn (Kawaea, et al. 2009). Secondly the insulating property of strontium titanate was suggested to lower the leakage current at close to zero electric field. It was also noted that the leakage current density in the negative and positive range as a function of the applied potential difference was not uniform. This was due to the variation of the work function and energy when an electron is transfered to the particular electrode of either gold or $LaNiO_3$. The other suggested reason was the resistivity contrast of Bi_2FeMnO_6/STO thickness. Lastly close to the film/electrode various defects such as oxygen voids result in non-uniform internal fields (J. Wei 2011).

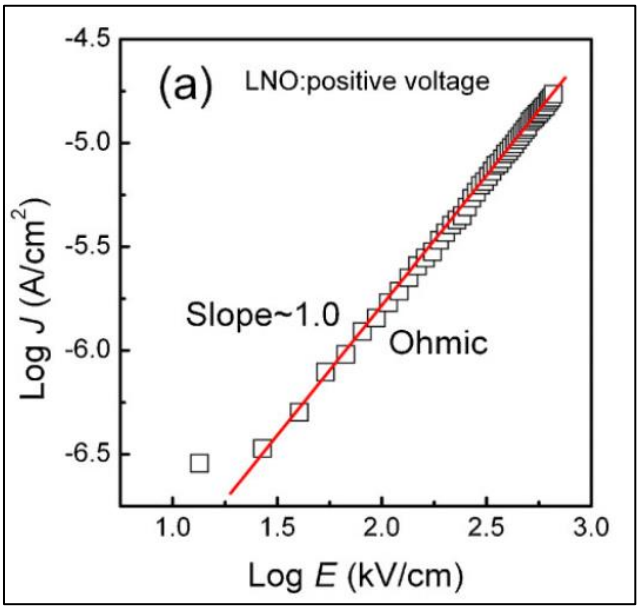

Figure 64: Plot of log_{10} (J) against log_{10} (Electric field) under the effect of positive voltage (Shen, et al. 2014).

The constructed perovskite thin film capacitor was studied for leakage conduction characteristics with a positive and negative potential at the $LaNiO_3$ electrode. The results are graphically illustrated in Figure 64 and Figure 65. The line of best fit of computed logarithm to base ten of leakage current density was found to be a straight line throughout the range of electric field used. A gradient of value one confirmed ohmic characteristics in the thin film capacitor as thermally driven by free electrons. The negative bias plot constituted of multiple gradients at 240 and 460 kV/cm. Below 240 kV/cm the thin film capacitor follows Ohms law with a gradient approximately equal to 1. While above 460 kV/cm the gradient exceeds 3, indicating a considerably high number free electrons derived from carrier injection in comparison to those freely thermally stimulated (Figure 65).

The second law fulfilled by this Bi_2FeMnO_6/STO capacitor is the space-charge-limited conduction mechanism as given in Equation 14 (Tang, Wang and Y. W. Zhang 2003).

$$J_{SCLC} = \frac{9c\varepsilon_0 K v^2}{8d^3} \ldots\ldots\ldots\ldots\ldots\ldots\ldots\ldots\ldots\ldots\ldots\ldots \quad \text{Equation 14}$$

c refers to the carrier mobility and d is the thickness sample capacitor. A deviation of the gradient at low electric fields from approximately 1 to 3 at high electric fields signified a transform of the conduction mechanism from that of a pure metal to SCLC.

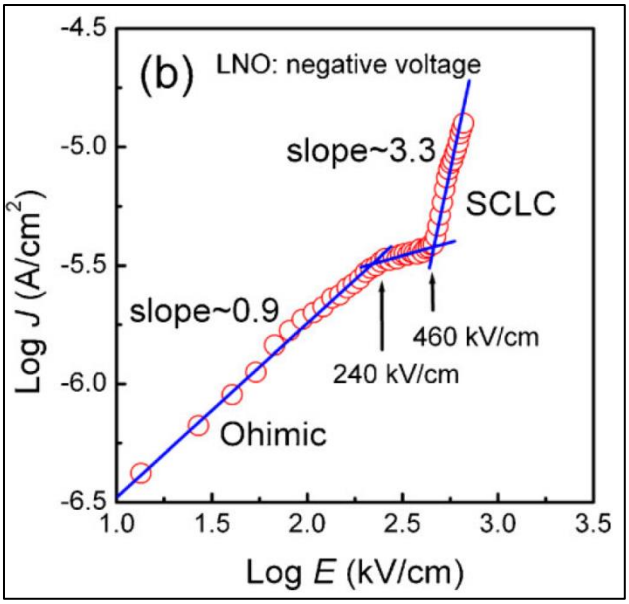

Figure 65: Graph of log_{10} (J) against log_{10} (Electric field) for sample capacitor (Shen, et al. 2014).

1.6.3 A simultaneous condition of frustrated magnetism and spontaneous electric polarization in highly ordered BFMO2 epitaxial thin film.

1.6.3.1 Magnetism characterization and analysis.

At a temperature of 300 K saturation magnetization for Bi_2FeMnO_6 films was determined to be approximately 1.8 emu/cm^3. For each pair of manganese iron this was a magnetic moment of about 0.02 μ_B. Generally there was a dwindle in the saturation magnetization value with an enhancement of the thickness of the BFMO film used as could be noted from the 0.2 μ_B per pair of iron manganese bond at 40 nm thickness. The discrepancy was interpreted in terms epitaxial strain which is more pronounced at decreased thickness of the Bi_2FeMnO_6 film at 40 nm as compared to the 190 nm. Therefore the intrinsic characteristics of Bi_2FeMnO_6 thin film were more defined by the 190 nm film.

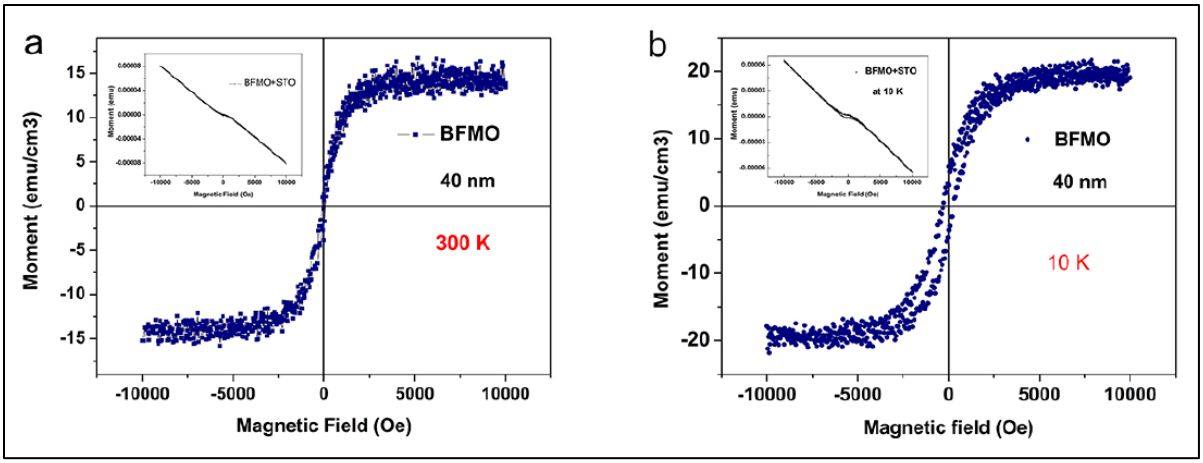

Figure 66: In plane magnetic hysteresis loop of Bi2FeMnO6 at 300 and 10 K (Sun., et al. 2016).

As a result the hysteresis plot at 300 K portrayed a frail magnetism of the BFMO film. Other studies have revealed $BiFeO_3$ to having a small magnetic moment of 0.02 μB/Fe due to a canted antiferomagnetic ordering. This minute value in $BiFeO_3$ when compared to that in Bi_2FeMnO_6 where there is an Fe-Mn in the [111] direction, that in BFMO is significantly higher. XPS has determined the oxidation state of Fe and Mn in Bi_2FeMnO_6 to be +3 for both of them and all having a high spin electron configuration. The high spin in the cations takes the configuration $t_{2g}^3 e_g^2$ for Fe^{3+} and $t_{2g}^3 e_g^1$ for Mn^{3+}) (A. T. L. Bi 2008) (Du, et al. 2010).

By using superconducting quantum interference device (SQUID) (Sun., et al. 2016) experimentally characterized the magnetic response of slim film BFMO with the magnetic field applied collateral to the [100] Strontium titanate ($SrTiO_3$) substrate. More strangely it was noted that the magnetization hysteresis loop at 5 K which is illustrated in Figure 67 had totally unique characteristics to that of Bi_2FeMnO_6 at 300 K. The plot did not come to a point when an elevation in externally applied magnetic field H could not increase the magnetization in thin film Bi_2FeMnO_6 until a magnetization force of 1 T. Within the temperature range 5 K to 300 K, they determined the field-cooled and zero-field-cooled out-of-plane parameters of BFMO film at a magnetic field of 1000 Oe. Figure 68 shows the results.

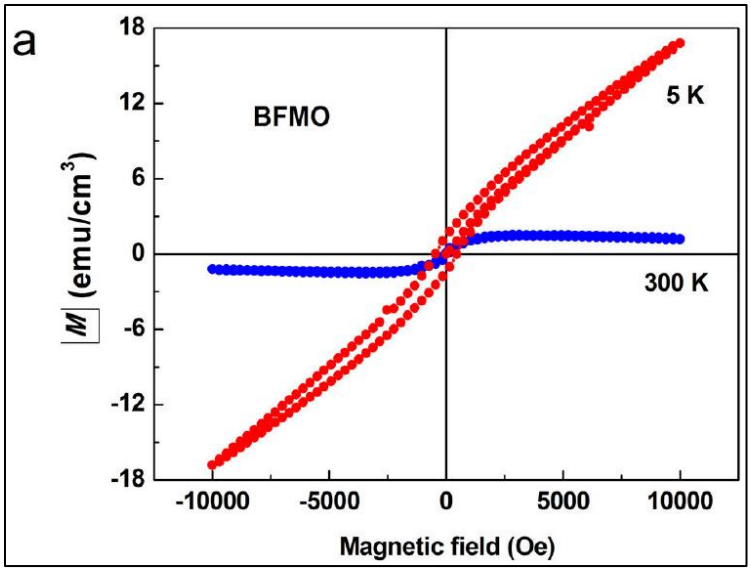

Figure 67: In-plane magnetic hysteresis loop at at 5 K and 300 K (Sun., et al. 2016).

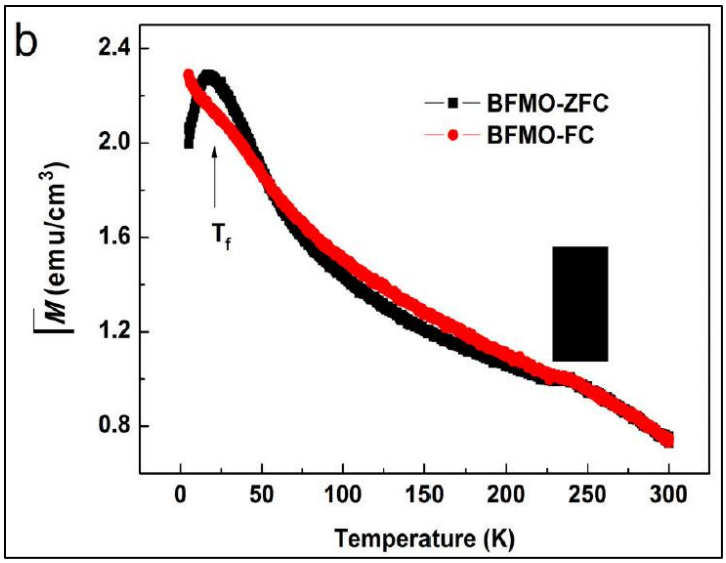

Figure 68: Temperature against magnetization plot of Bi_2FeMnO_6 film (5 K to 300 K) (Sun., et al. 2016).

1.6.3.2 Computer modeling of orbital and magnetic architecture.

According to other references of past studies (A. R. L. Bi 2008) (Du, et al. 2010) (E.M. Choi 2014) Fe^{3+}-Mn^{3+} magnetic ordering was proposed to be antiferromagnetic and on this bases BFMO was expected display significant magnetism without frustration ordering. However, from experimental data, BFMO was found to exhibit properties of a spin frustrated system with negligible or zero resultant magnetic ordering. As a result, there was need to reanalyze the interaction between Fe^{3+} and Mn^{3+} cations.

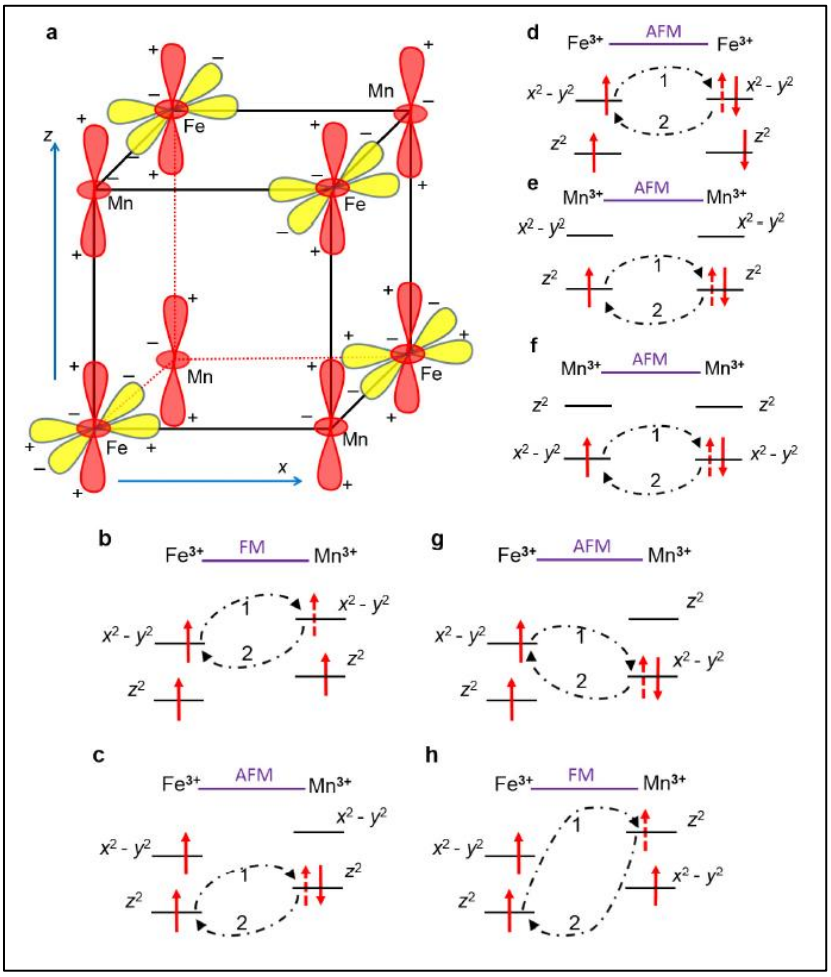

Figure 69: Plot of Fe3+ and Mn3+ orbitals (Sun., et al. 2016).

The e_g octahedral crystal field energy level will result in two different detectable energy states due to effect of an exterior magnetic field. Though this is true for a cubic lattice octahedral crystal system, for this particular situation due to Jahn-Teller ions, e_g orbital splitting is hindered due to decrease of the lattice symmetry dimension to 3.905 $\dot{A}$ and 4.015 $\dot{A}$. As a result of this the e_g orbital of the octahedral crystal system degenerated into $d_{x^2-y^2}$ and d_{z^2} orbitals and this is illustrated in the Figure 69a. For this situation, the in-plane iron (III) and manganese (III) are ferromagnetically coupled as illustrated in Figure 69b and the away-from-plane iron (III) and manganese (III) are antiferromagnetically coupled as shown in Figure 69c. The marginally greatness in size of the c_{pc} lattice constant as compared to a_{pc}, as a result of ferroelectric movement of iron (III) and manganese (III) will result in remarkable influence on the $d_{x^2-y^2}$ and d_{z^2} orbital energy levels. This is graphically shown in Figure 69f g and h where the d_{z^2} and $d_{x^2-y^2}$ energy levels of manganese (III) cations are positioned the opposite way.

This gives raise to antiferromagnetic coupling (Figure 69c) instead of ferromagnetic coupling (Figure 69b), due to a change of the in-plane electron transfer between iron (111) and manganese (111) via a non-magnetic anion and for the out-of-plane superexchange iron (111) and manganese (111) becomes ferromagnetic coupling (Figure 69h) from antiferromagnetic coupling (Figure 69c). Additionally, regardless of magnetic ordering assumed by the Fe^{3+} - Mn^{3+} interactions, due to virtual hopping of electrons in Fe^{3+} - Fe^{3+} and Mn^{3+} - Mn^{3+} exchange support antiferromagnetic ordering due to the availability of partially filled orbitals. This is illustrated in Figure 69d.e. and f. The researchers therefore predicted the existence of a transitional that had a positive ferroelectric shift which had an unquestionably minute exchange interaction of the nearest neighboring Fe^{3+} - Mn^{3+} due to combined modulation of ferroelectric distortion and crystal field. Under such a condition the magnetic ordering is influenced by what prevails in the iron (III) – iron (III) and manganese (III) – manganese (III) next nearest neighboring (NNN) quantum mechanical exchange interactions.

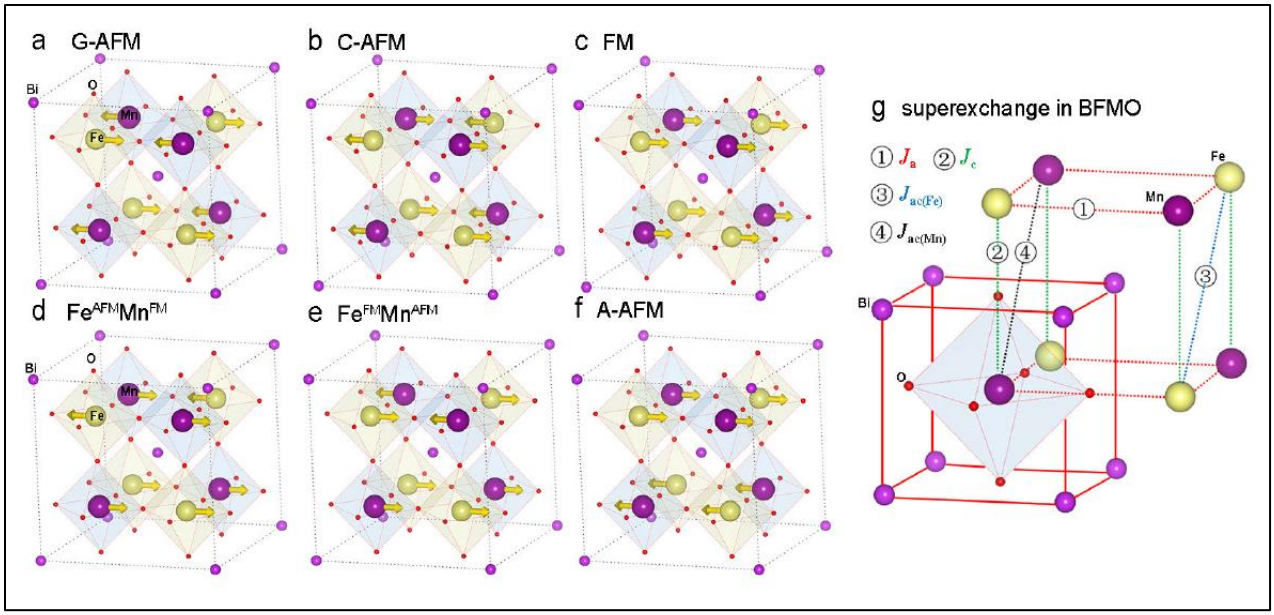

Figure 70: Magnetic structures and superexchange interactions adopted for computations in Bi_2FeMnO_6 (Sun., et al. 2016).

The researchers demonstrated by first principles computation that next nearest neigbhour superexchange in iron (111) – iron (111) and manganese (111) – manganese (111) had a much larger magnitude than the nearest neigbhour superexchange interactions in Fe^{3+} - Mn^{3+}. In order to carry out energy computation six magnetic orderings were used (Figure 70) and the exchange magnitude was characterized using Heisenberg Hamiltonian. Four superexchange parameters were determined, $J_{ac(Fe)}$ (Fe^{3+} - Fe^{3+}), $J_{ac(Mn)}$, J_a between the bismuth ions and J_c between bismuth and iron cations. The value for antiferromagnetic order, $J_{ac(Fe)}$ was 10.50 meV and $J_{ac(Mn)}$ an antiferromagnetic order was 4.02 meV. The values for antiferromagnetic J_c was 1.18 meV while J_a was ferromagnetic and -2.38 meV. Since the superexchange interaction J_a and J_c were 4.4 times and 8.89 times smaller than the antiferromagnetic $J_{ac(Fe)}$, it was proposed that a spin frustration results due to the substantial longe range antiferromagnetic ordering. As a result a glassy ordering was noted experimentally.

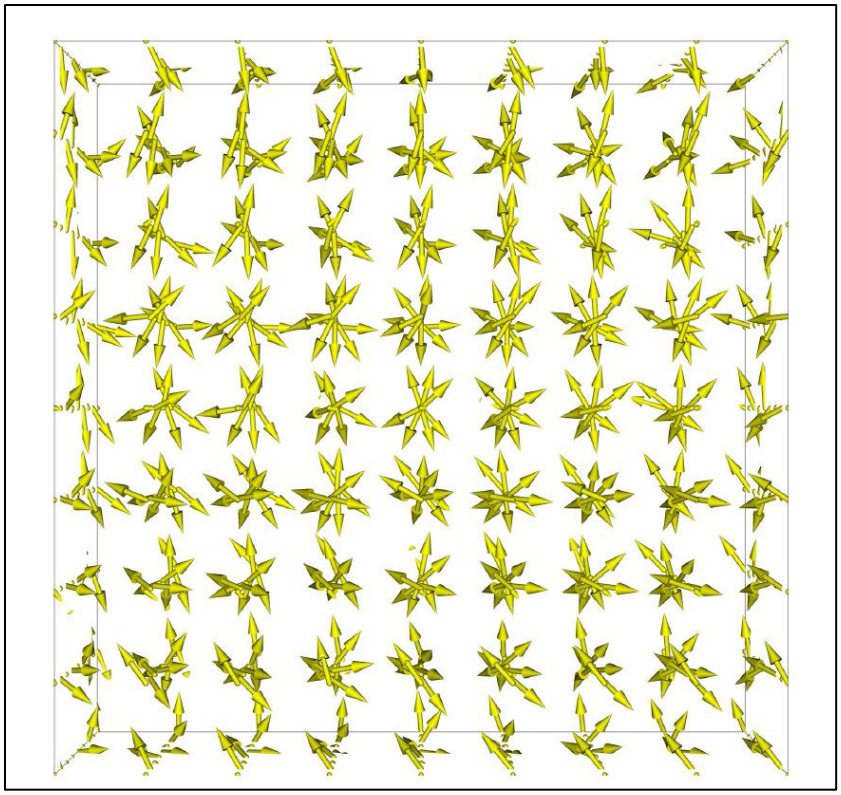

Figure 71: Monte Carlo simulation of superexchange parameters of Bi_2FeMnO_6 (Sun., et al. 2016).

The stochastic system of magnetic states at reduced temperatures was then computed from first principles using parameters obtained from superexchange interactions. A three dimensional pattern of the magnetic orientation obtained from the simulation is shown in Figure 71. The diagram indeed illustrates the ground state magnetism has magnetic moments or electron spins are interacting by virtue of competing exchange interactions and therefore no ordered state can concurrently gratify the complete nearest-neighbor interactions. The resultant magnetism is minute due to the irregularly oriented spins weakening each other. It was noted that perturbations or cause of disturbance such as applied magnetic field to the system caused serve changes in the magnetic architecture. The hypothetical outcome concurred well with their practical measurements.

1.6.3.3 Ferroelectricity characterization and analysis.

To grant an electric field to be tested with ease to Bi_2FeMnO_6 sample and thereby verify the endurance of spontaneous electric polarization at room temperature with a reversed potential, Bi_2FeMnO_6 slim layer on conductive strontium ruthenate perovskite enameled with strontium titanate (001) substrate was utilized. The electric properties of the film were detected applying an electric field and sensing the electric provoked deformation using a Piezoelectric Force Microscopy. Bi_2FeMnO_6 film on SrRuO3/STO and those directed deposited on strontium titanate substrate displayed identical surface architecture as can be seen in Figure 72a.

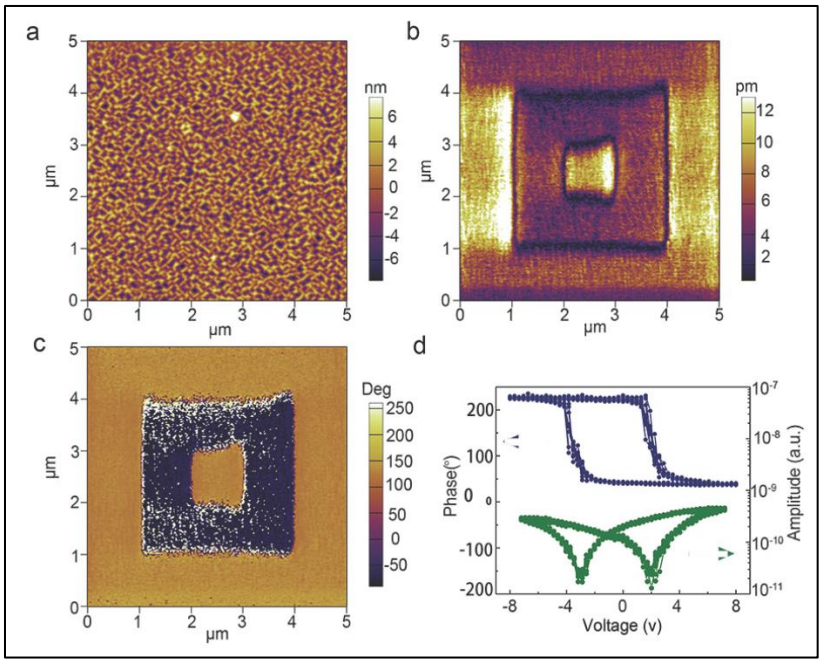

Figure 72: Surface architecture and local ferroelectric switching of BFMO thin film (Sun., et al. 2016).

The size of spontaneous electric polarization and phase on the surface of Bi_2FeMnO_6 film in response to a +/- 9 V switching signal is shown in Figure 72b and c. The existence of a spontaneous electric polarization at room temperature was justified by a clear domain pattern of the Bi_2FeMnO_6 thin film. The yellow and dark line in the phase diagrams in Figure 72b and c, indicate contradicting electric polarization direction which is point down and up respectively.

There was a nearly 180° out of phase electric polarization in the two domains proving a reversed polarization direction. Again the presence of a switchable electric polarization and excellent room temperature ferroelectric property was affirmed by Piezoresponse Force Microscopy as illustrated in Figure 72d. The externally voltage which caused the net polarization of the Bi_2FeMnO_6 ferroelectric film go to zero was approximately -3 V and 2 V and these can be read off as the minimum of the amplitude loop in Figure 72d.

1.6.4 Magnetic properties and specific heat capacity of thin film Bi_2FeMnO_6

(Du, et al. 2010) mixed ammonium hydroxide, bismuth(III) nitrate pentahydrate and ferric nitrate nonahydrate in stoichiometric quantizes in solvent C_3H_8O 2-methoxy ethanol resulting in a deep brown 0.005 molar solution. To produce Bi_2FeMnO_6 thin film, a silicon substrate heat to a temperature of 973 K for a duration of two hours in an electric field of 20 kV subsequently followed by powder sintering at 1173 K for a period of 1 hour. The composition of the synthesized Bi_2FeMnO_6 was accomplished by a combination XRD pattern and refinement computation using data from different crystal structures as reported by other researcher on the same material. Cubic crystal system P_{m3m} which belongs to the 4/m32/m point group and monoclinic crystal system C_2 of the 2 point group are the report structures used for the refinement. From this synthesized Bi_2FeMnO_6 film was found to be a trigonal crystal system of point group 3m, $R3c$. Bi_2FeMnO_6 was found to be stable on condition that it is exposed to other condition other than ambient and was not at its lowest energy state as it had a positive formation enthalpy.

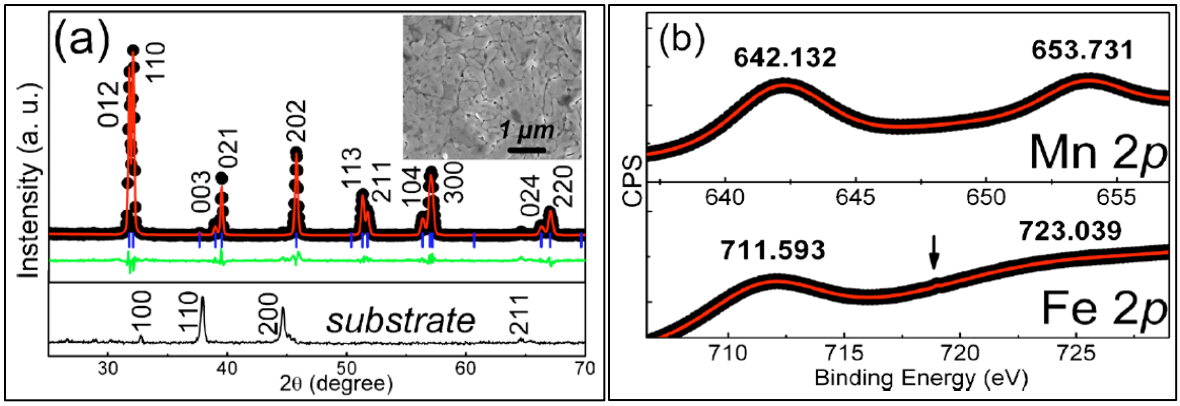

Figure 73: (a) XRD refinement calculation for Bi_2FeMnO_6 films (b) XPS spectra to determine the elemental composition of Bi_2FeMnO_6 film (Du, et al. 2010).

The trigonal crystal system of Bi_2FeMnO_6 was found to be with physical dimensions a=5.2575 Å, b=5.2575 Å, and c =13.072 Å. Polyhedra atomic architecture of MnO_6 and FeO_6 had a stretched appearance oriented in the c axis. Scanning Electron Microscope images (insert in Figure 73) of the Bi_2FeMnO_6 sample displayed many crystallites on a substrate. An x-ray diffraction pattern of the substrate has been included in Figure 73(a). By EDS the proportion of elements Bi, Fe and Mn contained in BFMO2 was found to be 1.97:1:1 respectively. Manganese has been found to have many oxidation states in compounds with out of shape perovskite architecture.

As a result to establish the oxidation states the prepared sample (Du, et al. 2010) carried out X-ray photoelectron spectroscopy and the results are plotted in Figure 73(b). 653.731 eV and 642.132 eV plotted in Figure 73 were associated with $2p1/2$ and $2p3/2$ respectively and are binding energies for the electrons on manganese cation. To be affirmative of the valency of the iron oxide in the sample of their as prepared BFMO2, they used the Fe $2p$ photoelectron amplitudes located at binding energies 723.0389 eV and 711.593 eV which have a relationship with satellite peaks. These they used to find out the chemical states of iron element. The principal peak of $2p3/2$ in Fe was determined to have a difference of 8 eV than the principal peak, therefore leading to a conclusion of +3 oxidation state for Fe. Plots of the relationship between heat in the range 5 to 750 K for thin film BFMO2 and field-cooled together with zero-field-cooled magnetic susceptibility are shown in Figure 74.

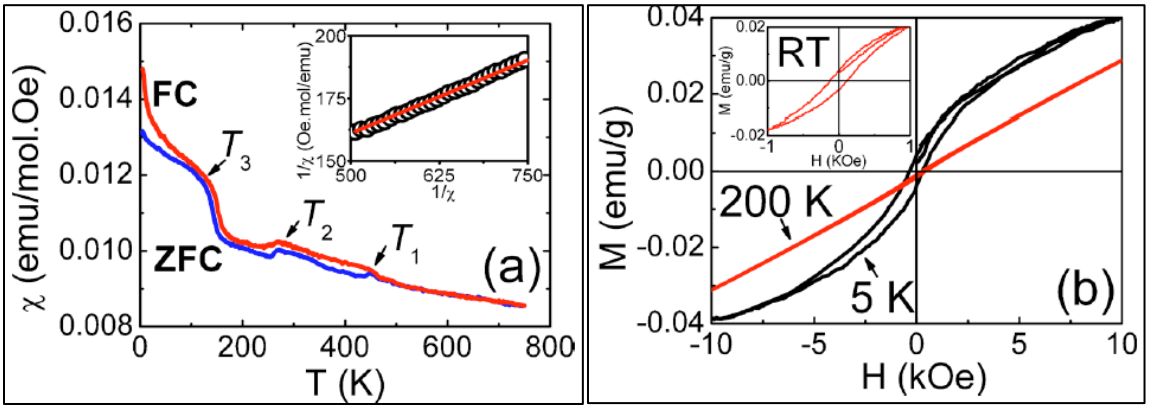

Figure 74: (a) Relationship between temperature and ZFC and FC. (b) Degree of electron spin alignment vs magnetic field at 200 K and 5 K (Du, et al. 2010).

A magnetizing force of H=1000 Oe was used in determining the magnetic susceptibility of thin film BFMO2. Magnetic crests were detected at 166.85 °C, -13.15 °C and -123.15 °C as temperature was decreased from 476.85 °C to -268.15 °C. The magnetic susceptibility (Curie–Weiss fitting) at temperatures from 226.85 °C to 476.85 °C is displayed in the inset of Figure 74(a). (Du, et al. 2010) computed the magnitude of the paramagnetism (effective moment) and found to be 7.5μ_B.

$$\mu_{eff} = \sqrt{n(n+2)} \ldots\ldots\ldots\ldots\ldots\ldots\ldots\ldots\ldots\ldots \quad \text{Equation 15}$$

The magnitude of the paramagnetism (effective moment) was computed and found to be 7.5. This calculation proves the existence of iron (111) and manganese (111) in high spin due to orbital splitting resulting in $t_{g2}^3 e_g^2$ for iron (111) and $t_{g2}^3 e_g^1$ for manganese (111) cations. Evidence of a heavy antiferromagnetic transformation was defined by the substantially elevated Curie–Weiss temperature of 746.85 °C. Whether the transition metal in BFMO2 will be high or low spin state is determined by the comparative energies of the d_{z^2} and $d_{x^2-y^2}$ orbitals in relation to d_{xy}, d_{xz} and d_{yz} orbitals. [1] The relative stabilities of both the Mn^{+3} and Fe^{+3} oxidation states can be varied by ligand binding. The high spin forms are enhanced by type I ligands while type II ligands generally stabilize the low spin state of Fe(111) and Mn(111). Now

to determine whether the elements Mn and Fe are high of low spin, the following formula was used. Based on Goodenough–Kanamori laws for 180° superexchange interation, different cations of Fe (111)–Mn (111) with the two cations having a high spin condition in addition to a partially-populated e_g energy level and the other one unoccupied e_g orbital the electron spin order will undoubtedly end up in antiparallel (Goodenough 1963). The ionic radius of Manganese (111) and iron (111) are almost the same and as a result they have the ability to substitute one another such that the sequential ordering of these two elements is not uniform. Consequently lumps of Fe concentrated and Mn concentrated patterns will form in the BFMO sample. These concentrated regions have an octahedral crystal system and will assume an antiferromagnetic layout by 180° superexchange coupling according to Goodenough–Kanamori coupling laws (W. Tong 2004).

Two magnetic ordering are possible in Mn–O–Mn, the ferromagnetic ordering being facilitated by strong antiferromagnetic coupling between manganese partially filled d_{z^2} and vacant $d_{x^2-y^2}$ throught the O $2p$ orbital. Vacant d_{z^2} to d_{z^2} and $d_{x^2-y^2}$ to $d_{x^2-y^2}$ orbits couple. For the e_g^2e - O - e_g^2 (Fe–O–Fe) coupling a strong antiferromagnetic ordering is favored by due to the preferred movement of charges from one cation of Fe to another Fe cation (A. R. L. Bi 2008). The diagram below shows the shape of the d orbitals in Fe and Mn.

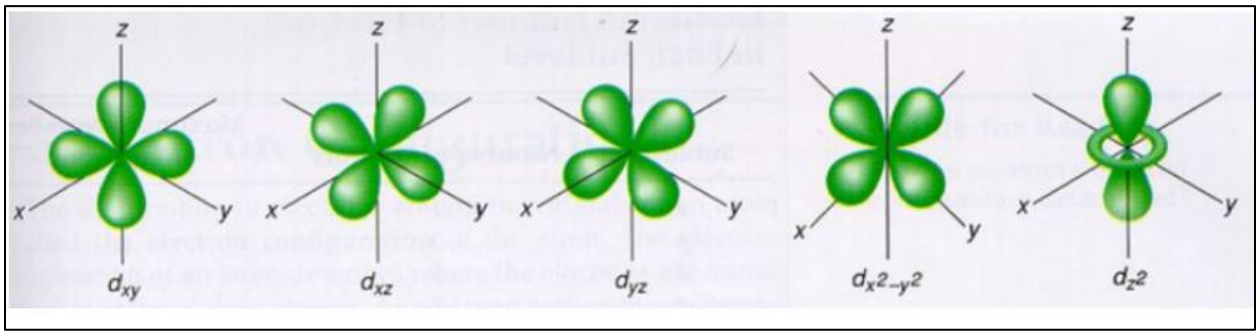

Figure 75: Shape of d orbitals. < https://chem.libretexts.org/Courses/Saint_Mary%27s_College%2C_Notre_Dame%2C_IN/CHEM_342%3A_Bioinorganic_Chemistry/Readings/Metals_in_Biological_Systems_(Saint_Mary%27s_College)/Iron_Storage%3A_Ferritin> [Accessed on: October 7, 2019]

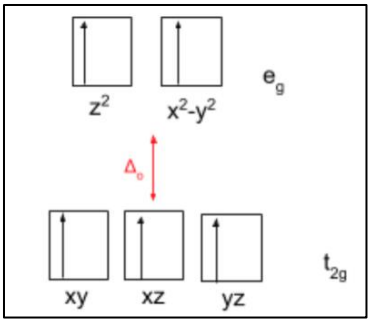

Figure 76: Fe^{3+} high spin electronic configuration. <https://chem.libretexts.org/Courses/Saint_Mary%27s_College%2C_Notre_Dame%2C_IN/CHEM_342%3A_Bioinorganic_Chemistry/Readings/Metals_in_Biological_Systems_(Saint_Mary%27s_College)/Iron_Storage%3A_Ferritin> [Accessed on: October 7, 2019]

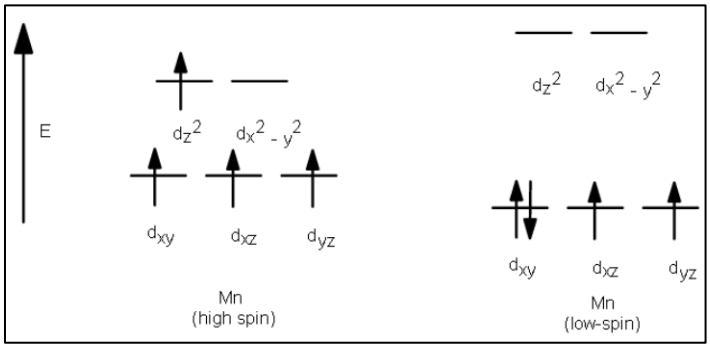

Figure 77: Mn^{3+} high and low spin electron configuration. < https://socratic.org/questions/5666dcbe581e2a2d1d3f1adf> [Accessed on: October 7, 2019].

As shown in Figure 76 and Figure 77 the higher orbital in the Mn–O–Mn has one unpaired electron as compared to Fe-O-Fe which has 2 unpaired electrons. This results in a stronger ordering in Fe-O-Fe than in Mn-O-Mn and a correspondingly higher ordering temperature. In reference to the given explanations the connection between magnetic transformations which occurred at the temperatures 150 K, 260 K and 440 K were linked to iron-oxygen-manganese, manganese-oxygen-manganese and iron-oxygen-iron orbital ordering. In order to ascertain the results they obtained, a graph of magnetization against applied magnetic field was plotted from experimental data at a number of different temperatures. The ability of a BFMO thin film to resist demagnetization was found to be 118 Oe at a temperature of 300 K. The plot obtained had a mixture of ferromagnetic and ferromagnetic ordering. This is illustrated in inset in Figure 74(b). It was interesting to note that BFMO2 thin film retained its hysteresis characteristics at a

temperature of 200 K with a coercive force of 82 Oe but the overall behavior of the material was antiferromagnetic in nature. For data collected at 5 K, the linear behavior was significantly decreased and a more defined hysteresis loop that had a coercive force of approximately 330 Oe was obtained. The predicted value of 4.48 μ_B/ f.u. for magnetic moment was noted to be much less as compared to the theoretical measurement of 9 Bohr magneton per formula unit at a coercive field of 10 kOe. The theoretical value is on condition that the entire Fe^{3+} and Mn^{3+} cations located on the BB′ double perovskite site are arranged ferromagnetically. The origin of magnetic transformation at approximately 150 K was explained in terms of Fe–Mn ferrimagnetic arrangement which was characterized with limited magnetic moment of in BFMO2 at suppressed temperatures.

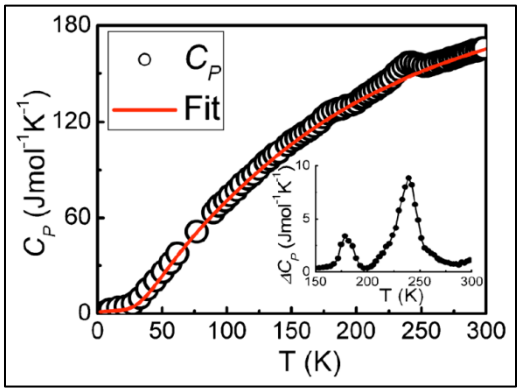

Figure 78: Relationship between heat capacity and temperature in BFMO2 thin film. Influence of temperature on the magnetic heat capacity is given in the enclosed picture (Du, et al. 2010).

$$C_p^{nm} = Nk_B\left\{\frac{9}{1-\eta_D T}\left(\frac{T}{\theta_D}\right)^3\int_0^{\theta_{D/T}}\frac{x^2e^x}{[e^x-1]^2}dx + \sum_{i=1}^{n}\frac{9}{1-\eta_D T}\frac{(\theta_{Ei}/T)^2e^{\theta_{Ei}/T}}{[e^{(\theta_{Ei}/T)}-1]^2}\right\} \quad \text{Equation 16}$$

1.7 Magnetoelectric coupling in single phase multiferroics

The ability to control magnetism by adjusting the electric polarization and vice versa relies on the coupling between the two ferroic properties. The electric polarization between two non collinear magnetic moments that are that located adjacent to each other is given by Equation 17.

$$\vec{P} \propto \vec{e}_{ij} \times \left(\vec{S}_i \times \vec{S}_j\right) \ldots\ldots\ldots\ldots\ldots\ldots\ldots\ldots\ldots\ldots\ldots \quad \text{Equation 17}$$

1.8 Types of composite multiferroics

1.8.1 Composite multiferroics driven by exchange-bias

The quantum mechanical interaction between similar particles, exchange interaction, has been applied to numerous magnetic ordering architectures such as next generation storage devices (Morales, et al. 2015) (Zhang 2016). The structure of such a device comprises of a ferromagnet which is in proximity of ferroelectric/antiferromagnetic thickness. At the point of contact of these two layers, exchange bias occurs as a result of heavy interactions of magnetic field originating from electron spins in ferromagnetic thickness being restrained by the ferromagnet (R. Ramesh 2007). Firstly the polarization of the ferroelectric thickness is altered by the electric force lines then, variations in the antiferromagnetic layer are brought about by the coupling of ferroelectric/antiferromagnetic states.

1.8.2 Composite multiferroics driven by charge

Conversion from one magnetic ordering has a difficulty associated with varying the carrier concentration by exerting of electric force lines in the composite material (Borisov 2011) (Toupet, et al. 2008). A promising strategy for future energy proficient gadgets, is charge concentration per unit volume being changed significantly at the low voltages. A wide range of material characteristics, for example, superconductivity (Nan, et al. 2008), (Nan, et al. 2014) and ferromagnetic metals (Liu, et al. 2013) is feasibly modified by applying an electric field.

1.8.3 Composite multiferroics driven by strain

These are materials in which there is a considerable piezoelectric and magnetic reaction magnitude due to strain. Magnetoelectric coupling is a generated by a force exerted on the material which causes an electric force line to be developed in the magnetic phase in a ferroelectric state. I order to generate a significant magnetoelectric coupling, piezoelectric voltage constant and piezoelectric loss by piezoelectric material then magnetostriction coefficient for magnetostrictive material are the most paramount factors to be taken into consideration. The exerted field is converted to strain resulting in the creation of a polarization in the composites by transformation of the strain. Substantial coefficients of ferroelectric phase for piezoelectric and magnetostriction materials are required for the generation of piezoelectric and magnetostriction results.

1.9 Magnetoelectric coupling coefficent in composite multiferroics

A robust magnetoelectric coupling has been revealed in both fine film and bulk structures of magnetoelectric composite. The applicability of these magnetoelectric coupled composites then depends the type of coupling mechanisms that exists in the composite. Generally two classes which are either converse or direct magnetoelectric coupling exists in these materials. Quick responding sensors and energy trappers take advantage of direct coupled magnetoelectric composites while tunable resonators and band stop filter rely on converse magnetoelectric coupling in which the electric field controls the permeability of the device. In direct coupled magnetoelectric composites, the magnetic field drives the polarization of the gadget.

Interaction of magnetic and electric field	**Means of adjusting ferroic properties**	**Accessories examples**
Direct interaction	Magnetic field adjusts the electric field	Field sensor, Energy harvester
Inverse coupling	Electric field varies the magnetization	Magnetoelectric RAM.
	Electric polarization adjusts permeability	Voltage tunable inductors
	Electric field alters electron spin properties.	Notch frequency filters, Frequency tunable oscillator.

Table 1: Magnetoelectric coupling mechanisms in composite multiferroics and applications.

The phenomenon is numerically characterizes by the magneto-electric interaction multiplicative factor, ß (Fiebig 2005). The magneto-electric interaction multiplicative factor can be electrically instigated to determine the magnitude of adjustment in the magnetic induction (B) of the sample material by use of an electric field (E).

$$ß_{ij}^{E} = \frac{\partial B_i}{\partial E_j} \ldots\ldots\ldots\ldots\ldots\ldots\ldots\ldots\ldots\ldots\ldots\ldots \quad \text{Equation 18}$$

The magnetic and electric interaction multiplier can be described in terms of a magnetically generated variation of the ferroelectric attributes by virtue of administration of a magnetic field. In this situation it will mathematically defined by Equation 19.

$$ß_{ij}^{H} = \frac{\partial P_i}{\partial H_j} \ldots\ldots\ldots\ldots\ldots\ldots\ldots\ldots\ldots\ldots\ldots\ldots\ldots\ldots$$ Equation 19

Since different independent thermodynamic variables can be used to express the interation multiplier, the formulae can also be stated in terms of the magnetization differentiation w.r.t. respect to one variable, the applied electrics field. The actual magnetic field influence on the electric field multiplier is three by three combined magnetic and electric susceptibility matrix, which constitutes of nine components. Even though there are 9 factors in a combined magnetic and electric tensor only one of them in the diagonal or non diagonal is not zero for any particular practical study geometry. Factors that affect which component is non zero are symmetry of the crystal and shape, magnitude and relative position of the sample and administrated magnetic field.

$$ß_{ij} = \begin{pmatrix} ß_{11} & ß_{12} & ß_{13} \\ ß_{21} & ß_{22} & ß_{23} \\ ß_{31} & ß_{32} & ß_{33} \end{pmatrix} \ldots\ldots\ldots\ldots\ldots\ldots\ldots\ldots\ldots\ldots$$ Equation 20

It is according to Maxwell's P.D.E. that the magnetic and electric interaction multiplier due to either magnetic or electric variations are considered equal and any disturbances due to magnetic or electric variations can be determined.

1.10 Applications of composite multiferroics

1.10.1 Multiferroic microwave resonators tuned electrically.

When a FM material is disturbed by a high frequency signal it will undergo ferromagnetic resonance (Kittel 2005). Ferromagnetic harmonic oscillation occurs due to the disturbance of the magnetization vector or the electron spins generates the magnetic vector to relax by the precession of the electron spin to a new equilibrium position. On condition that the precession frequency of electrons in the ferrite material has the same magnitude as that of the incident field then ferromagnetic resonance will occur. Therefore soft opposite to hard ferrite materials are

employed in microwave frequencies where a peak of 70 GHz can be in certain signal processors. A direct current magnetic biasing field is used to mandatory for the functioning of the device and to attain frequency tuning. A number of challenges encompass tuning by means of a magnetic field for example slow operation, considerable level of noise figure, energy inefficient and cannot be reduced in size. Due to a wide range of frequencies in the microwave spectrum radar and communication device have to adapt to shifting from one frequency to the other at the least power possible. The use of multiferroic bi-layer composite instead of ferrite materials introduces the ability to tuning by means of an electric field (Semenov, et al. 2006). Figure 79 shows the diagram of a micro strip-line multiferroic resonator used to practically electric field tune the ferromagnetic resonance of yttrium iron garnet/ $PbZrTiO_3$ multiferroic composite (Y. K. Fetisov 2005). A yttrium iron garnet of length and width $1 \times 2.2\ mm^2$ and thickness 15 μm was used while the $PbZrTiO_3$ was $4 \times 0.5\ mm^2$ in length and 4 μm thick. The micro strip was 50 μm thick and 3 mm long. Ferromagnetic resonance at approximately 5 GHz was detected using input signals with a frequency range from 2 to 10 GHz at a power of 0.1 mW applied on the micro strip and an independent magnetic force line of 1.12 kOe. The linewidth of this FMR was 3.4 MHz as pictorially shown in Figure 80.

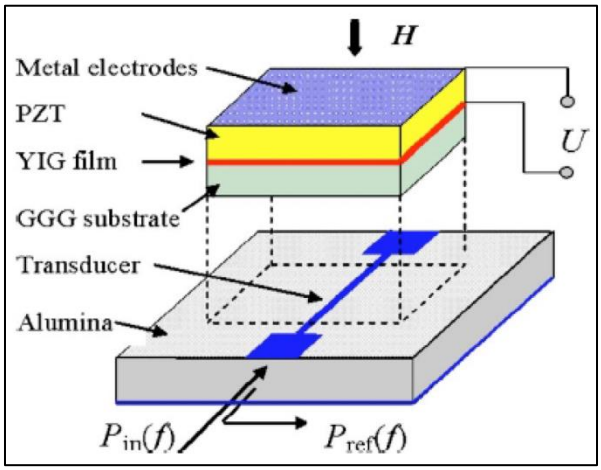

Figure 79: Illustration of μ planer multiferroic resonator (Vopson 2014).

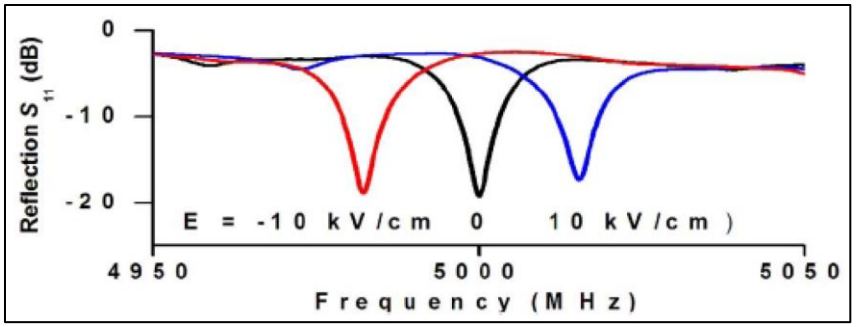

Figure 80: FM resonance absorption peaks of yttrium iron garnet resolved at 1.12 kOe dc magnetic field (Vopson 2014).

1.10.2 Multiferroic microwave phase shifter

These are utilized in high frequency RF oscillators and phased array antenna systems to time delay a signal. The design of phase shifters requires any of these three properties, ferrite, ferroelectric and semiconducting materials. The principle behind ferrite phase shifters is a linear circular twist of EMR by a magnetic field through a Verdet constant. The method is however inefficient as it uses a huge magnetic biasing field (M. M. Vopson 2017). The ferrite type phase shifter can also operate on principle of spreading of a spin wave in the ferrite. This mechanism is preferred as it allows extensive range of frequencies to be utilized as ferrites can be magnetically altered. Frequencies from 1 to 26 GHz can be utilized. Ferrite phase shifters are out classed by ferroelectric phase shifters in terms of a lower power consumption and faster electrical tuning. However at higher frequencies (> 5 GHz) ferroelectric phase shifters are characterized by significantly high losses.

Taking advantages of the different competitive characteristics in ferrite and ferroelectric phase shifters a composite can be formed by combining the 2. The resultant multiferroic composite can function as an adjustable microwave unit at frequencies well above 5 GHz. Such dual units have been designed by (Ustinov, Drozdovskii, et al. 2019) in which a double perovskite $Ba_{0.6}Sr_{0.4}TiO_3$ and yttrium iron garnet ferrite were combined to form a multiferroic composite (Ustinov and G. Srinivasan 2007). The double perovskite was 500 μm thick while the yttrium iron garnet ferrite was 5.7 μm. The upper and bottom electrodes used a 50 nm chromium layer

and 5 μm copper layer respectively. The difference in thickness of the two electrodes was to allow for microwaves to penetrate and get to the ferroelectric Barium strontium titanate layer. Length and width of the multiferroic elements were 5 and 10 mm respectively.

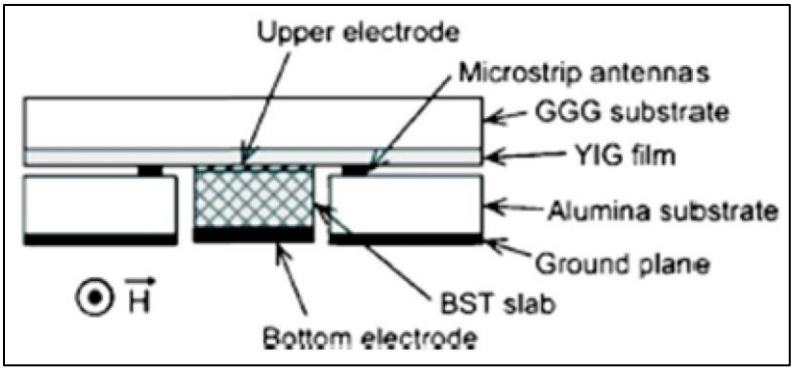

Figure 81: Mixed ferroic properties composite signal shifter (Vopson 2014).

The phase and frequency relationship depending on the potential difference applied to the ferroelectric $Ba_{0.6}Sr_{0.4}TiO_3$ layer through the copper and chromium electrode is illustrated in Figure 82. 0 V, 500 V and 1000 V potential differences with a direct current biasing field of 1413 Oe were used in the experimentation. Employing contrasting magnitudes of direct current magnetic biasing field while maintaining the same electrical fields yielded a tuning performance in the frequency range of 3.5 to 8.0 GHz.

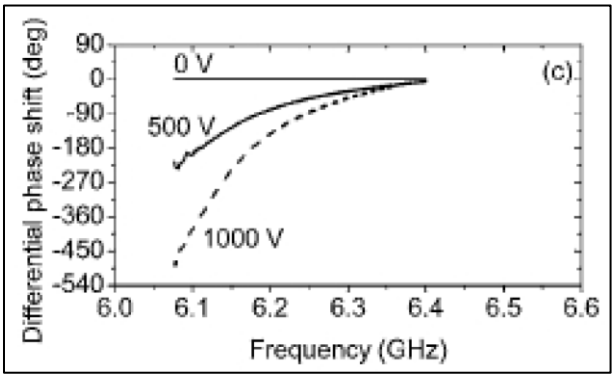

Figure 82: Microwave signal phase tuning in a phase shifter using electrical potential (Vopson 2014).

1.10.3 Multiferroic microwave signal delay line

Usually a delay line is constructed from a thin film of ferrite which is then staked on two micro strips which are microwave transducers. One of the strips is an output transducer and is coupled to the output signal while the other is an input transducer which is coupled to the input signal. High frequency signal processing employs these kind delay lines. The ferrite material in contact with the micro strips acts as a bridge which passes the high frequency electromagnetic input signal to the output. The ferrite bridge propagates the electromagnetic radiation by means of spin waves against the inlet to the output. The spin wave velocity and wavelength is nearly half the magnitude of the electromagnetic radiation input. Basing on this reduction in velocity and wavelength the signal can be delayed by as much as 500 ns using a ferrite that is only a few millimeters long.

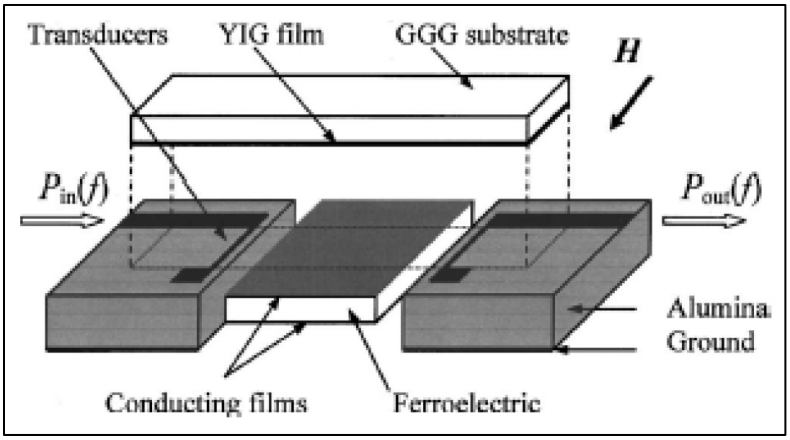

Figure 83: Synthesized combined multiferroic μwave propagation attenuation line (Vopson 2014).

These devices depend on the robust relationship between spin wave velocity and magnetic field bias, permitting a time delay by magnetic field tuning. The disadvantages that surround this method outweigh its successful operation. Firstly these devices cannot be reduced in sized to take the form of solid state chips. Secondly the tuning speed directly depends on the length of the ferrite material and lastly the high power level consumption due to the required biasing magnetic field. In addressing these loop holes Fetisov and Srinivasan constructed the microwave delay

lines that had two thin combined multiferroic instead of the ferrite bridge element (Y. K. Fetisov 2005). Yttrium- Iron-Garnet (YIG) ferrite with a thickness of 4.1 μm and $Pb(Mg,Nb)O_3$-$PbTiO_3$ ferroelectric with a thickness 500 μm were employed in the experimentation. A diagram of the constructed signal delay line is shown in Figure 83. The separation of the input and output transducer was set at 8 mm. The new design enhanced the ability to vary delay duration by applying and electric field to the two layer multiferroic composite. The viability of this mechanism hinges on that the multiferroic element which is a ferroelectric dielectric has its permittivity being related to the electric field.

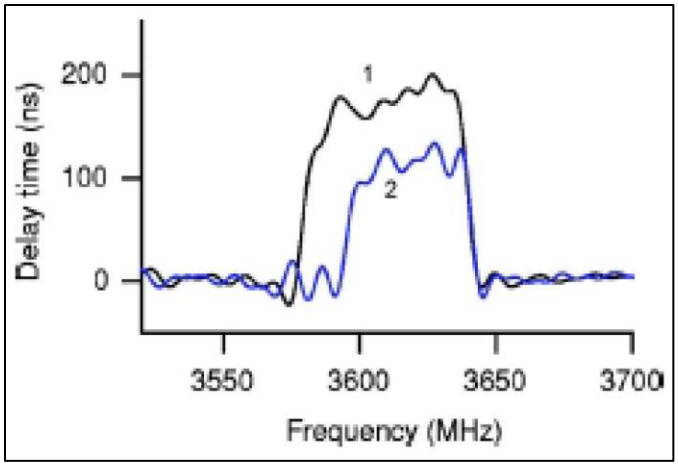

Figure 84: Retardation time as a function of Hertz in $Y_3Fe_2(FeO_4)_3$ and Lead Magnesium Niobate-PT signal delay line (Vopson 2014).

Varying the permittivity using an electric field allows a faster tuning mechanism also saving energy and can farther tolerate device miniaturization. Electric field tuning presented a difference of 10 to 25% in the delay duration as the electric field was varied from 8 kV/cm. This is illustrated in Figure 84.

1.11 Problem statement

To understand the spin properties in multiferroic $BiFe_{1-x}Mn_xO_3$ through electron spin resonance.

1.12 Research aims and objectives

1. Systematic ESR studies of multiferroic $BiFe_{(1-x)}Mn_{(x)}O_3$ system in relation to temperature, down to 4.2 K
2. Correlation of spin properties deduced from ESR with that of peculiar magnetic properties at characteristic temperatures of multiferroic $BiFe_{(1-x)}Mn_{(x)}O_3$.

1.13 Limitations of the study

Temperature measurements are only from 5 K to 300 K.

1.14 Potential research outputs

1. Enhanced knowledge on the spin characteristics of multiferroic double perovskite $BiFe_{(1-x)}Mn_{(x)}O_3$
2. Publications
3. Thesis

Chapter 2

2 Electron spin resonance

2.1 Paramagnetic materials

Magnetism is a result of an electrically charged particle being in motion, therefore in general all matter has certain magnetic characteristics. Electrons due to their inherent characteristics of rotation around the nucleus and axis behave like magnets which line-up along the direction magnetic field. Their magnetic field is along their axis of rotation. Due to the tendency of matter to attain a stable octet by pairing of electrons, this then means few molecules exist as paramagnetic. They are however transition metal ions that have incomplete internal orbitals and radicals that have unpaired outer electron orbitals as a result of dissociation of the chemical bond and therefore are paramagnetic. The main methods used to identify paramagnetic materials are electron paramagnetic resonance and determination of force required to maintain to orientation of these paramagnetic dipoles after a thermal disturbance (Nptel 2012) (Zwiebach 2014) (Kundu 2013).

2.1.1 Paramagnetic susceptibility

If an alternating magnetizing force in Equation 21 is applied to material the magnetism gained by the material is given by Equation 22.

$$H = H(t) + H_{ac}\cos wt \ldots\ldots\ldots\ldots\ldots\ldots\ldots\ldots\ldots\ldots\ldots \quad \text{Equation 21}$$

$$M = M(t) + M_{ac}\cos(wt - \emptyset) \ldots\ldots\ldots\ldots\ldots\ldots\ldots\ldots\ldots \quad \text{Equation 22}$$

When a trigonometry identity for $\cos(wt - \emptyset)$ is introduced the expression is reduced to

$$M = M(t) + M_{ac} \cos wt \cos \emptyset + \sin wt \sin \emptyset \ldots\ldots\ldots\ldots\ldots \quad \text{Equation 23}$$

Architectures which are entirely classical will not exhibit any magnetic moment even in the smallest applied external magnetic field and magnetism will only be observed in those systems that obey quantum mechanics laws <http://web.mit.edu/3.23/www/Lecture14.pdf> [Accessed on 28 December 2019]. Paramagnetic materials are characterized by a resultant magnetic moment due to domains which orient themselves in an identical orientation as the acting exterior magnetic field. By assuming that the resultant magnetic moment is defined by M_o and the externally applied magnetic field to be H_o, then the extent to which a paramagnetic material will be magnetized, paramagnetic susceptibility is computed by the equation below.

$$M_o = \chi_o H_o \ldots\ldots\ldots\ldots\ldots\ldots\ldots\ldots\ldots\ldots\ldots \quad \text{Equation 24}$$

The magnetic susceptibility of such materials is positive and magnetization gained by such a material is conversely complementary to the degree of heat at which the material exists and directly proportional to the magnetizing force. This is expressed in a classical equation give below.

$$M = N\mu L\left(\frac{\mu H}{kT}\right) \ldots\ldots\ldots\ldots\ldots\ldots\ldots\ldots\ldots\ldots\ldots \quad \text{Equation 25}$$

This formulae can be rewritten as Curie Law on condition that $\mu H \ll kT$.

$$\chi = \frac{N\mu^2}{3kT} = \frac{C}{T} \ldots\ldots\ldots\ldots\ldots\ldots\ldots\ldots\ldots\ldots\ldots \quad \text{Equation 26}$$

The quantity of atoms in a given volume of material is represented by N, and μ represents the magnetic moment of each of the atoms. However when migrating to quantum physics the magnetization and resultant angular momentum of a material are interconnected by Equation 27.

$$M = NgJ\beta_J\left(\frac{gJ\beta_J H}{kT}\right) \ldots\ldots\ldots\ldots\ldots\ldots\ldots\ldots\ldots$$ Equation 27

Magnetic dipoles are however restricted from aligning themselves parallel to the applied field due to kinetic energy of the dipoles within the lattice. The relationship between the susceptibility χ_o and temperature of the dipoles is an inverse one meaning at elevated temperature the susceptibility of a material is gradually lower. A significant number of material abide by curies law

2.1.2 Spin and Orbital Moments

The intrinsic and rotational spin sum of Magnetic moment of the nucleus, electron spin magnetic moment and orbital magnetic moments are sources of permanent magnetic moments in different systems. Nuclear magnetic moments magnitudes are three times much smaller than electron spin magnetic moments. The nuclear magnetic moment is given by

$$\mu_N = g_N \frac{e\hbar}{2Mc} \ldots\ldots\ldots\ldots\ldots\ldots\ldots\ldots\ldots\ldots\ldots$$ Equation 28

An electron that is spinning has a magnetic moment μ_S that is given by Equation 29

$$\mu_S = 2\beta S \ldots\ldots\ldots\ldots\ldots\ldots\ldots\ldots\ldots\ldots\ldots\ldots$$ Equation 29

The magnetic moment derived from the electrons orbital angular momentum is given by Equation 30.

$$\mu_S = \beta L \ldots\ldots\ldots\ldots\ldots\ldots\ldots\ldots\ldots\ldots\ldots\ldots$$ Equation 30

β defines the atomic physics constant, Bohr magnetron and is given by the Equation 31.

$$\beta = \frac{e\hbar}{2m} \ldots\ldots\ldots\ldots\ldots\ldots\ldots\ldots\ldots\ldots\ldots \quad \text{Equation 31}$$

$$\mu_S = g\beta S \ldots\ldots\ldots\ldots\ldots\ldots\ldots\ldots\ldots\ldots\ldots\ldots\ldots \quad \text{Equation 32}$$

$$\mu_S = g\beta L \ldots\ldots\ldots\ldots\ldots\ldots\ldots\ldots\ldots\ldots\ldots\ldots\ldots \quad \text{Equation 33}$$

The same equations may be expressed in form of the g factor which takes the numerical value of 2 or 1 in spin and orbital angular momentum respectively as given in Equation 32 and Equation 33. This is because the g factor is an estimate of the proportionality between magnetic moment and the rotational momentum can be expressed mathematically as shown below.

$$\gamma = \frac{Magnetic\ Moment}{Angular\ Momentum} \ldots\ldots\ldots\ldots\ldots\ldots\ldots\ldots\ldots \quad \text{Equation 34}$$

Total or resultant or effective rotational momentum of an electron evolves as a grand total of spin and orbital momentum. When capital letters are used in the equations, it designates a system. While small letters designate a single electron.

$$J = L + S \ldots\ldots\ldots\ldots\ldots\ldots\ldots\ldots\ldots\ldots\ldots\ldots\ldots\ldots \quad \text{Equation 35}$$

J takes the values $|L - S|, |L - S + 1| \ldots\ldots\ldots\ldots |L + S|$. The resultant magnetic moment as a function of Lãnde factor is a product of the the resultant angular momentum, g factor and Bohr magnetron as given below.

$$\mu = g\beta J \ldots\ldots\ldots\ldots\ldots\ldots\ldots\ldots\ldots\ldots\ldots\ldots \quad \text{Equation 36}$$

g or Lãnde factor as a function all three components of angular momentum is given by

$$g = \frac{S(S+1) - L(L+1)}{2J(J+1)} + \frac{3}{2} \ldots\ldots\ldots\ldots\ldots\ldots\ldots \quad \text{Equation 37}$$

Crystalline electric fields in solids interact strongly with the electronic orbital motion resulting in it being decoupled from its spin an effect know as orbital quenching. The extent of quenching determines the value of g, with those systems which are absolutely quenched having a g factor of 2.0037. In a given system with constituents that are highly ordered in microscopic structure such as crystals, g factor has several values that are dependent on the direction within a given crystal lattice. In the situation where g factor is a symmetric tensor, represented as follows.

$$g' = \begin{bmatrix} g'_{x'x'} & g'_{x'y'} & g'_{x'z'} \\ g'_{y'x'} & g'_{y'y'} & g'_{y'z'} \\ g'_{z'x'} & g'_{z'y'} & g'_{z'z'} \end{bmatrix} \ldots\ldots\ldots\ldots\ldots\ldots\ldots\ldots\ldots \quad \text{Equation 38}$$

Most electron spin resonance studies will however only determine the magnitude of g.

2.1.3 Spin Hamiltonian

The various interactions in free radicals and transition metal cations and anions are all summed up in a spin Hamiltonian equation. This spin Hamiltonian is represented by the equation given below.

$$\mathcal{H} = \mathcal{H}_{elect} + \mathcal{H}_{cf} + \mathcal{H}_{LS} + \mathcal{H}_{FF} + \mathcal{H}_{Zee} + \mathcal{H}_{hfs} + \mathcal{H}_{Q} + \mathcal{H}_{N} \ldots\ldots\ldots \quad \text{Equation 39}$$

The electronic energy of the paramagnetic ion in the free state is given by $\mathcal{H}_{elect}$. The interaction of this free ion electronic energy with the electric field of the crystal is $\mathcal{H}_{cf}$. The significance of $\mathcal{H}_{cf}$ is that $\mathcal{H}_{LS}$ is the interaction of gyration and revolving momenta, $\mathcal{H}_{FF}$ is the spin spin interaction, $\mathcal{H}_{Zee}$ is the Zeeman energy, $\mathcal{H}_{hfs}$ Hyperfine structure, $\mathcal{H}_{Q}$ is the Quadrupole energy, $\mathcal{H}_{N}$ is the nuclear spin energy.

2.1.4 Electric Moment

The shape of an electric pole due to electric charge varies from monopoles, dipoles, quadrapoles, octapoles to hexapoles. The potential of these shapes varies inversely with the distance from the electric pole. A charged particle results in an electric potential which can be represented by V_e. For a medium with dielectric constant ϵ, mathematically the expression can be stated as Equation 40.

$$V_e = \frac{e}{4\pi\epsilon r} \ldots\ldots\ldots\ldots\ldots\ldots\ldots\ldots\ldots\ldots\ldots\ldots\ldots \quad \text{Equation 40}$$

The electric field intensity at distance r of this charged particle would be represented by the potential partial derivative corresponding to distance and represented by the equation below.

$$E = \frac{\partial V_e}{\partial r} = \frac{e}{4\pi\epsilon r^2} \ldots\ldots\ldots\ldots\ldots\ldots\ldots\ldots\ldots\ldots\ldots\ldots \quad \text{Equation 41}$$

However a dipole is a result of 2 charges that have a given distance of separation. The potential of such an arrangement is given by the equation below, Equation 42.

$$V_e = \frac{e}{4\pi\epsilon}\left[\frac{1}{r - \frac{1}{2}l\cos\theta} - \frac{1}{r + \frac{1}{2}l\cos\theta}\right]$$

$$= \frac{\mu_e \cos\theta}{4\pi\epsilon r^2} \ldots\ldots\ldots\ldots\ldots\ldots\ldots\ldots\ldots\ldots\ldots\ldots\ldots$$ Equation 42

The electric field intensity of this dipole would take into consideration $r, \theta \; and \; \varphi$ and is a partial derivative with respect to these three terms.

$$E_r = -\frac{\partial V}{\partial r} = \frac{\mu_e \cos\theta}{2\pi\epsilon r^3} \ldots\ldots\ldots\ldots\ldots\ldots\ldots\ldots\ldots\ldots$$ Equation 43

$$E_\theta = -\frac{\partial V}{\partial \theta} = \frac{\mu_e \sin\theta}{4\pi\epsilon r^3} \ldots\ldots\ldots\ldots\ldots\ldots\ldots\ldots\ldots\ldots$$ Equation 44

$$E_\varphi = -\frac{1}{r\sin\theta}\frac{\partial V}{\partial \varphi} = 0 \ldots\ldots\ldots\ldots\ldots\ldots\ldots\ldots\ldots\ldots$$ Equation 45

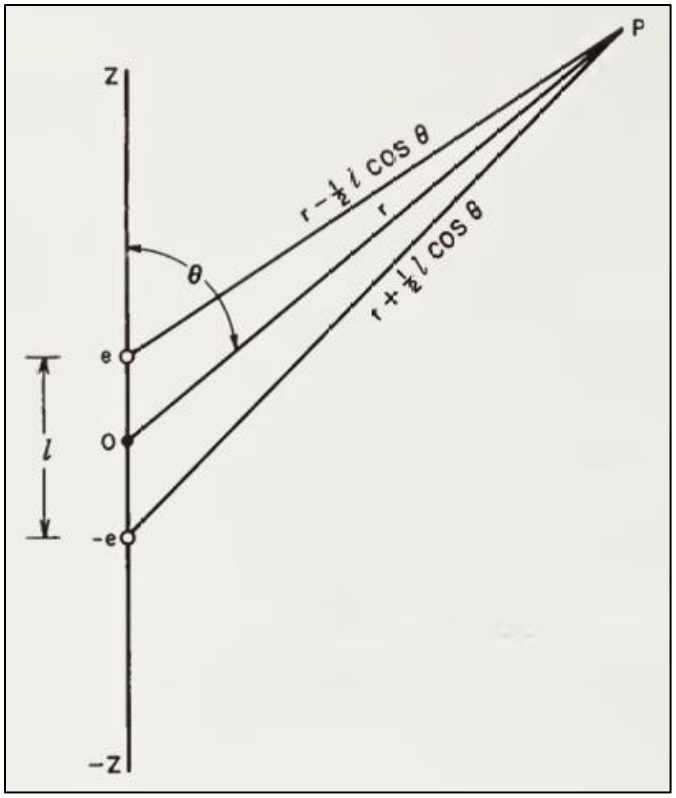

Figure 85: Field due to electric charge at point p as a result of dipole of charge e and e separated by distance l (C. P. Poole 1996).

The potential of a quadrupole can be state as shown in Equation 46. The value of $\frac{\partial^2}{\partial z^2}\left(\frac{1}{r}\right)$ is $-\frac{\cos\theta}{r^2}$.

$$V_{e_z} = \frac{\mu_{e_z}}{8\pi\epsilon}\frac{\partial^2}{\partial z^2}\left(\frac{1}{r}\right) \ldots\ldots\ldots\ldots\ldots\ldots\ldots\ldots\ldots\ldots\ldots \quad \text{Equation 46}$$

2.1.5 Magnetic resonance.

The influence of a constant magnetic field on a paramagnetic sample, is such that the magnetic moments of the particles in the sample will tend to precess around the applied magnetic field (Christman 1988). The precession will occur on non-static magnetic moments as it is a result of the torque that is experienced by the magnetic moment of the electron. We then have two situations the static field can interact with either a static magnetic moment or a varying magnetic moment and precession only occurs when the interaction is with a varying magnetic moment

such as that derived from an electron that is orbiting around the nucleus. For a stationary magnetic moment the torque influences the magnetic dipole moment to orient parallel with the exterior applied magnetic non-varying field <http://hyperphysics.phy-astr.gsu.edu/hbase/magnetic/larmor.html> [Accessed on 20 January 2020].

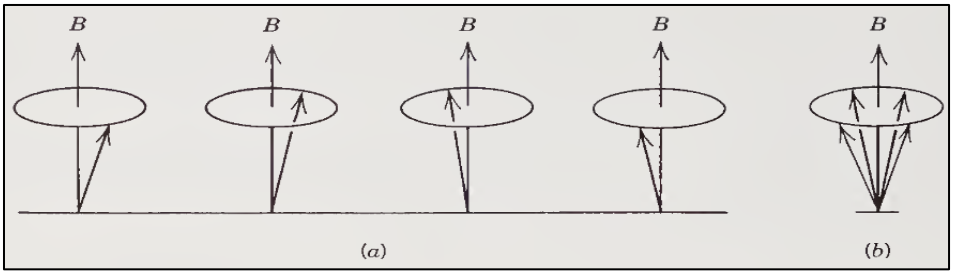

Figure 86: (a) Precession of magnetic atom dipole moments about a static magnetic field. (b) Uniformly distributed magnetic moment on cone surface for atoms with equal magnetic moments towards the z orientation (Christman 1988).

Considering that atoms have different magnetic moments in the z directions the image will have different cones for the different precessions. Practical resonance experiments utilize another magnetic field which is whirling in the orientation of the dipole precession and is in the xy plane. The effect of this second magnetic field is to disturb the dipole distribution. Relaxation and precession occur at the same time with the dipoles precessing around the resultant field while relaxing as indicated in Figure 86 (b). When the introduced rotating field is equal in its frequency to the number of complete oscillations of the precession about the constant magnetic field the system is said to be in resonance.

2.2 Relaxation Times and Magnetization.

According to classical mechanics when relaxation is eliminated then the dipole moment is given by $\frac{d\mu}{dt} = -\gamma\mu \times B$. Here B is the summation of static and rotating magnetic fields and $\gamma = \frac{g\mu_B}{\hbar}$. Magnetization when there is relaxation term is skipped is given by Equation 47.

$$\frac{dM}{dt} = \gamma M \times B \ldots\ldots\ldots\ldots\ldots\ldots\ldots\ldots\ldots\ldots\ldots\ldots\ldots$$ Equation 47

However when the relaxation term is taken into consideration the equation takes the form shown below.

$$\frac{dM}{dt} = \gamma M \times B + (\frac{dM}{dt})_{relaxation} \ldots\ldots\ldots\ldots\ldots\ldots\ldots$$ Equation 48

There are two components of relaxation, one in the z plane and the other in the xy plane and these two are referred to as $\bar{t_1}$ and $\bar{t_2}$ and there are a result of non-identical activities. The diagram below illustrates the axis in which these times are measured.

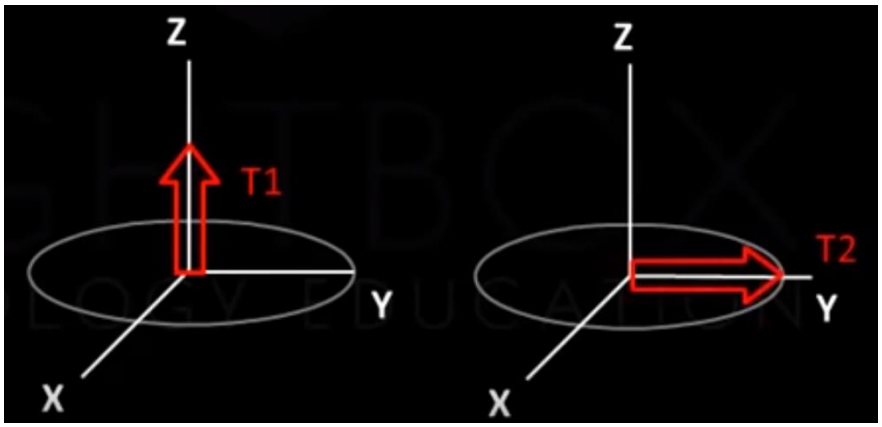

Figure 87: T_1 is determined parallel to applied static field and T_2 is measured transverse or perpendicular to applied static field <https://www.youtube.com/watch?v=Ok9ILIYzmaY> [Accessed on 23 January 2020].

Phonon spin interactions give raise to the z component thereby allowing for transfer of energy from the spin in the form of a phonon (Christman 1988). Spins at limited temperature are believed to be able to attain equilibrium by either emitting or absorbing phonons. The phonons are released or absorbed into the lattice in which the spin exists (Lunghi 2019). The variation in the angle bounded by the dipole moment and the externally applied static magnetic field, z axis, is due to phonon interaction. Magnetization of the x and y components is also believed to vary due to phonon interaction but does not reduce the values to zero. By take the initial values in the

x, y and z of the system at equilibrium to be $(0, 0, M_0)$ but then due to a small change the value changes to $(0, 0, M_z)$. The time taken for the system to return to its equilibrium value M_0 which is the population with higher energy from M_z the population with lower energy is determined by the characteristic relaxation duration and is termed longitudinal relaxation time. Longitudinal relaxation span duration is directly related to spin lattice relaxation and it gives a picture of the release of energy to the surrounding or lattice (Robert and Balaban 2010). The contribution to the rate of change of magnetization due to T_1 is given by Equation 49. The restoration of a stable or equilibrium nuclei position results in a decrease of the nuclear magnetic signal and on this condition perturbations that affect longitudinal relaxation also influence spin-spin relaxation and the spin-spin relaxation is always briefer as compared to spin-lattice relaxation (Moore. 1999).

$$\frac{dM_z}{dt} = \frac{M_o - M_z}{T_1} \ldots\ldots\ldots\ldots\ldots\ldots\ldots\ldots\ldots\ldots\ldots\ldots \quad \text{Equation 49}$$

T_2 represents the decrease in magnetization from values (M_x, M_y, M_z) to an equilibrium value of $(0, 0, M_z)$ and is termed the transverse relaxation time. Under these conditions, the change of magnetization from M_x and M_y to zero over the time in which this change occurs is the contribution to magnetization of these components.

$$\frac{dM_x}{dT_2} = \gamma\left(M_y H_z - M_z H_y\right) - \frac{M_x}{T_2} \ldots\ldots\ldots\ldots\ldots\ldots\ldots\ldots\ldots \quad \text{Equation 50}$$

$$\frac{dM_y}{dT_2} = \gamma(M_z H_x - M_x H_z) - \frac{M_y}{T_2} \ldots\ldots\ldots\ldots\ldots\ldots\ldots\ldots\ldots\ldots \quad \text{Equation 51}$$

$$\frac{dM_z}{dT_1} = \gamma\left(M_x H_y - M_y H_x\right) - \frac{M_o - M_z}{T_1} \ldots\ldots\ldots\ldots\ldots\ldots\ldots\ldots \quad \text{Equation 52}$$

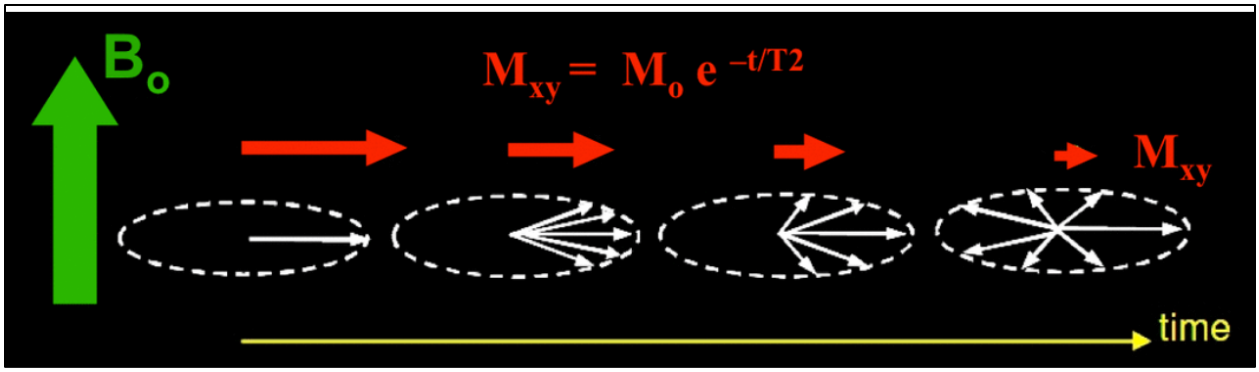

Figure 88: Decay of magnetization in the xy plane with time T2. < http://mriquestions.com/what-is-t2.html> [Accessed on 10 Nov 2019].

A representation of the magnetic fields that are applied during electron spin resonance take the form $(H_1 \cos wt\,, 0, H_z)$. Carefully looking at the components reveals that these are the static and oscillating magnetic fields in the x and z direction respectively. The components of magnetization in the x, y, and z axis can be determined at steady state conditions. Solving these three equations given above gives the real and imaginary components of the susceptibility. These maybe represented mathematically as given below.

$$\chi' = \frac{1}{4}\chi_0\omega_0\left[\frac{2(\omega_0-\omega)T_2'^2}{1+(\omega_0-\omega)T_2'^2+\gamma^2H_1^2T_1T_2'}\right] \ldots\ldots\ldots\ldots\ldots\ldots\ldots\ldots \quad \text{Equation 53}$$

$$\chi'' = \frac{1}{4}\chi_0\omega_0\left[\frac{2T_2'^2}{1+(\omega_0-\omega)T_2'^2+\gamma^2H_1^2T_1T_2'}\right] \ldots\ldots\ldots\ldots\ldots\ldots\ldots\ldots \quad \text{Equation 54}$$

The real component of the susceptibility represents dispersion along with the imaginary part represents absorption of microwave energy. The imaginary part will χ'' will to the following deductions, when $|\omega_0-\omega|$ or $\gamma^2H_1^2T_1T_2'$ are large then χ'' will be minimum for the imaginary part of the susceptibility. The expression therefore predicts that absorption will optimally occur at frequencies that are as close as possible to Larmor frequencies, ω_0. Secondly lengthy spin

lattice relaxation times and immense oscillating magnetic fields drive imaginary susceptibility or quadrature or out-of-phase susceptibility to a minimum which reduces absorption of microwave energy. The reduction in absorbed microwave energy is due to saturation. <http://www.irm.umn.edu/quarterly/irmq13-4.pdf> [Accessed on 02 February 2020]. Thirdly the expression for imaginary magnetic susceptibility Equation 54, when there is no saturation reduces to Equation 55 given below where the normalized Lorentzian function is represented by the expression in the brackets.

$$\chi'' = \frac{1}{4}\chi_0\omega_0\left[\frac{2T_2'^2}{1+(\omega_0-\omega)T_2'^2}\right] \ldots\ldots\ldots\ldots\ldots\ldots\ldots\ldots\ldots \quad \text{Equation 55}$$

2.2.1 Relaxation Mechanisms

It is important to understand relaxation as this is directly linked to the line widths. The major two vital information gained from relaxation are (1) a detailed comprehension of how electron dipole are interacting with other electron dipole and nuclear dipoles in the sample and the magnetic environment in which they are existing. The process of electron spin resonance is highly dependent on the surplus quantity of electrons with the lowest energy for which the spin quantum number is one half ($M_s = -\frac{1}{2}$). However there is a marginal difference of the number of electrons with the lowest energy to compared to those in the upper state ($M_s = \frac{1}{2}$). Administering a magnetic field H_0, to the sample under examination causes splitting of orbitals with electrons in the upper level ($M_s = \frac{1}{2}$) having an energy difference of $g\beta H_0$. The difference in the quantity of electrons in the low energy orbital and those in the upper level is approximated by Boltzmann distribution law. The law can be applied to such a system on condition that it is in thermal equilibrium. Equation 56 gives the proportion of electrons in the $M_s = \frac{1}{2}$ level to those in the ground level.

$$\frac{n_{(+1/2)}}{n_{(-1/2)}} = e^{(-\frac{g\beta H_0}{kT})} \ldots\ldots\ldots\ldots\ldots\ldots\ldots\ldots\ldots\ldots\ldots\ldots \quad \text{Equation 56}$$

T represents the absolute temperate in kelvins, K. For most experimental conditions because $g\beta H_0 \gg kT$ then the exponential term approaches one and therefore the equation can be stated as shown below.

$$\frac{n_{(+1/2)}}{n_{(-1/2)}} = 1 - \frac{g\beta H_0}{kT} \ldots\ldots\ldots\ldots\ldots\ldots\ldots\ldots\ldots\ldots\ldots\ldots \quad \text{Equation 57}$$

Considering the quantity of unpaired electrons per gram to represented by N_0 then the population difference per gram is given by

$$\Delta n_0 = \frac{N_0}{2} . \frac{g\beta H_0}{kT} \ldots\ldots\ldots\ldots\ldots\ldots\ldots\ldots\ldots\ldots\ldots\ldots \quad \text{Equation 58}$$

The sum of the magnetic moment per gram is given by

$$M_0 = \frac{1}{2} g\beta . \frac{N_0}{2} . \frac{g\beta H_0}{kT} \ldots\ldots\ldots\ldots\ldots\ldots\ldots\ldots\ldots\ldots \quad \text{Equation 59}$$

In order to compressively understand the relaxation process three aspects must be taken into consideration how the electronic dipoles in the sample interact with the nuclear dipoles and other electronic dipoles in the sample, the rearrangement of molecular and ionic paramagnetic species which are subjected to the static and oscillating magnetic field ($H_0$and $2H_1 \cos \omega t$) and the result of rotation, translation and vibration of these species. The first effects are termed spin-spin and spin lattice interactions and contain data about how particles are moving in an architecture (Torchia 1969), while the last effect is termed exchange and motion modulation (C. P. Poole 1996).

2.2.1.1 Spin Lattice Relaxation

Is the means by which spin energy is transferred to the lattice and is represented by T_1. It is represented by an exponential decay in the magnetization in an identical orientation as the magnetic field. Spins under the influence of lattice oscillations at frequencies 10^{10} Hz will interchange their spin direction. Since the frequency of precession depends the external magnetic field strength, the Larmor frequency at these conditions corresponds to a magnetic field of 3600 G. this simultaneous flipping of spins provides a mechanism for transfer of energy from the spin to the environment. Two mechanisms to explain T_1, the transfer of energy from spin into the environment are that the electrostatic field having an influence on the motion of the electron about the nucleus. Due to that spin and orbit are connected any variation in the orbital motion is detected by the spin thereby providing a means of by which energy is dissipated to the lattice environment. It is also important to note that T_1 is influenced by the temperature of the environment. In titanium cations it was found to be about 10^{-02} at 300 K and 1 second at 4 K.

2.3 Energy absorption

A paramagnetic sample will magnetize at later as compared to the externally applied magnetizing field. This results in the susceptibility of the sample being out of phase and this being given by the formulae $\chi_0 = \chi' - i\chi''$, where χ' is the real part of the susceptibility and corresponds to the in phase magnetization while χ'' is the imaginary part of the susceptibility and corresponds to the out of phase magnetization. The net magnetization from an applied external magnetic field is therefore

$$M = 2\chi' H_1 \cos \omega t + 2\chi'' H_1 \sin wt \ldots\ldots\ldots\ldots\ldots\ldots \quad \text{Equation 60}$$

The delay in magnetization results in the rate of energy absorption being a product of the rate of change of magnetic moment multiplied by the magnetic field strength. (F.Felix, et al. 2015)

$$P_a = \frac{\omega}{2\pi}\int_0^{\frac{2\pi}{\omega}} H.dM/dt/dt$$

$$-\frac{\omega}{2\pi}H_1^2\int_0^{\frac{2\pi}{\omega}} 4\omega(\sin wt\,.\cos\omega t\,.\chi' + \chi''\cos\omega t\cos\omega t)dt$$

$$2\omega\chi''^{H_1^2} or\ 4\pi\nu\chi''^{H_1^2} \ldots\ldots\ldots\ldots\ldots\ldots\ldots\ldots\ldots \quad \text{Equation 61}$$

Factors that affect the power absorbed in electron spin resonance study are the frequency of the oscillating magnetic field, phantom component of the mass susceptibility and magnitude of the oscillating magnetic field (Isnard. 2019). This is illustrated in Equation 61.

2.4 EPR block diagram and related functional parts

(1) Automatic frequency control. (2) Power supply for gunn diode. (3) Microwave generator (Gunn diode). (4) Unidirectional microwave transmitter. (5) Frequency counter. (6) Microwave power level controller. (7) Dummy load. (8) Oscilloscope. (9) Modulated radio-frequency signal detector. (10) 100 kHz signal level booster. (11) 100 kHz radio frequency signal detector. (12) Computer. (13) Four port waveguide tee. (14) High-frequency resonant cavity system. (15) 100 kHz Magnetic field modulation loops. (16) One hundred kHz energy magnifier. (17) 100 kHz resonantor circuit. (18) Cavity resonator. (19) Electrical energy supply for magnet. (20) A linear magnetic field scan driver with power amplifier.

It is important to note that electron paramagnetic resonance and electron spin resonance are the same phenomena which use the same principles as in nuclear magnetic resonance. Stern-Gerlach research has confirmed intrinsic angular momentum of an electrons and that it is self-sufficient from orbital rotation momentum. <http://230nsc1.phy-astr.gsu.edu/hbase/spin.html#c3> [Access on: 01 November 2019]. By observation from the experiment only two states were found

possible for the angular momentum as was verified by the electrons scattering to the 2 position after interacting with the magnetic field. The quantum number assign to any of the spins was either $\frac{1}{2}$ or $-\frac{1}{2}$. As a result of the intrinsic angular momentum it is can be predicted that a spin magnetic moment the same as an orbiting electron is generate by the electron. Contrary to this the measured value is 2 times the orbital predicted value. < http://230nsc1.phy-astr.gsu.edu/hbase/spin.html#c4> [Access on: 01 November 2019].

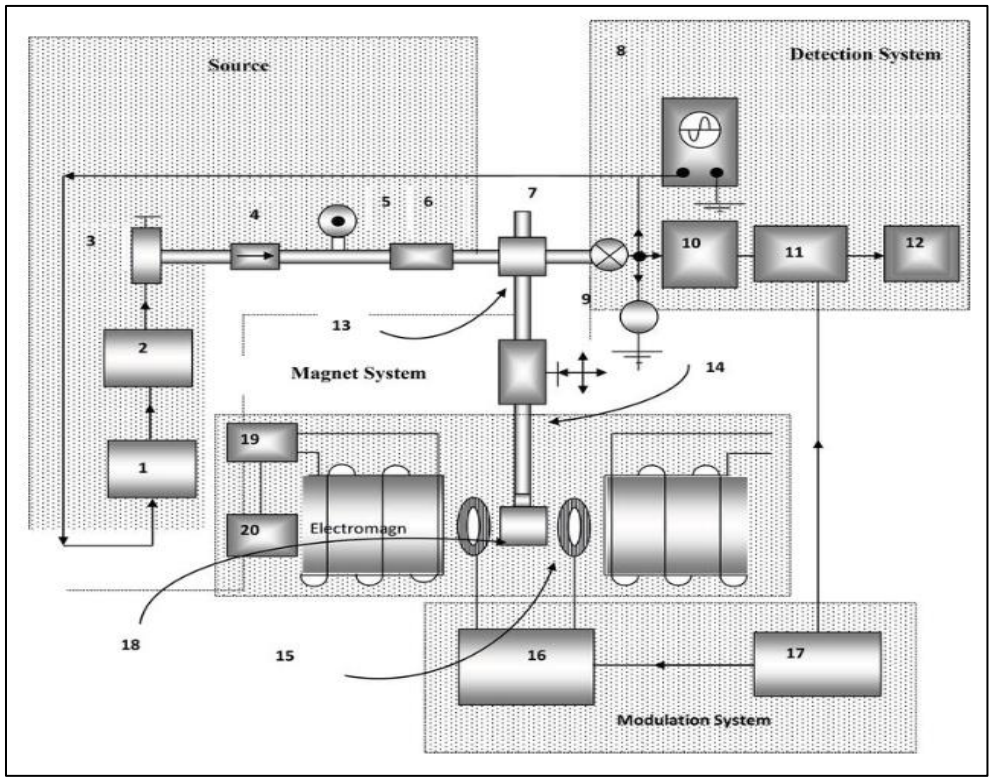

Figure 89: EPR block diagram. < https://www.intechopen.com/books/topics-from-epr-research/introductory-chapter-electron-paramagnetic-resonance> [Accessed on 10 Nov 2019].

$$\mu_Z = \pm\frac{1}{2} g\mu_B \ldots\ldots\ldots\ldots\ldots\ldots\ldots\ldots\ldots\ldots$$ Equation 62

g is known as gyromagnetic ratio and takes the values 2.00232 for spin and 1 for orbital momentum. μ_B is the Bohr magneton. It is simply physical constant defined by B that serves as the magnetic moment which is as result of one of the two, orbital or spin angular momentum.

$$\mu_B = \frac{eh}{4\pi m_e}$$

$$= \frac{eh}{2m_e}$$

$$= 9.2740154 \times 10^{-24} J/T$$

$$= 5.7883826 \times 10^{-5} eV/T$$

Interaction Type	**Name**
Electron Spin/Static Magnetic Field	Electron Zeeman
Nuclear Spin/Static Magnetic Field	Hyperfine
Nuclear Spin/Electric Field Gradient	Nuclear Zeeman
Electron Spin/Nuclear Spin	Nuclear Quadrupole
Electron Spin/Electron Spin (Strong)	Hyperfine
Electron Spin/Electron Spin (Weak)	Zero-Field
Electron Spin/Static Magnetic Field	Exchange
Dipolar Coupling	Dipole-Dipole

Table 2: Type of interactions in resonance studies.

2.5 Origin of the EPR Signal

A negatron is considered as a point mass and a negative charged, and composed of two movements. Spin describes the rotation of the electron about its own axis and orbital motion, which is as a result of spinning about the nucleus. The last mentioned generates orbital magnetic moment while spin results in spin angular moment. Magnetic moment of a system is mainly originates from unpaired electron's spin magnetic moment given by Equation 63.

$$\mu_s = \sqrt{S(S+1)}\,\frac{h}{2\pi} \ldots\ldots\ldots\ldots\ldots\ldots\ldots\ldots\ldots\ldots\ldots\ldots \quad \text{Equation 63}$$

2.6 Substances, which can be investigated by EPR.

The prerequisite for applying electroparamgnetic resonance is presence of unpaired electrons in the material being characterized. Its range of applications is restricted to paramagnetic substances and to substances that can be converted to a paramagnetic form with sufficient stability for a spectrum to be observed.

2.7 Energy Level Structure and the g-factor

In order to be able to distinguish between orbital and angular momenta a scaling factor has to be used. This is because electroparamgnetic resonance will characterize paramagnetic materials in which the spin and angular momenta are coupled. There exists a connection between g factor and quantum number J, which represents the resultant angular momentum. J is given by the equation below.

$$J = L + S \ldots\ldots\ldots\ldots\ldots\ldots\ldots\ldots\ldots\ldots\ldots\ldots\ldots\ldots\ldots\ldots \quad \text{Equation 64}$$

$$g_J = \frac{J(J+1)(g_L + g_S) + (L(L+1) - S(S+1))(g_L - g_S)}{2J(J+1)} \ldots\ldots\ldots \quad \text{Equation 65}$$

g_L and g_S represent the orbital and spin g quantities respectively. The majority of spin systems in which the resultant moment emanates from spin and orbital momentum, spin angular momentum is assigned a value of 2 and is twice large than orbital angular momentum which is assigned a value of 1. As a result the relationship above reduces to Landé formula given in Equation 66 .

$$g_J = \frac{3}{2} - \frac{L(L+1) - S(S+1)}{2J(J+1)} \ldots\ldots\ldots\ldots\ldots\ldots\ldots\ldots\ldots$$ Equation 66

$$\mu_J = g_J \mu_B J \ldots\ldots\ldots\ldots\ldots\ldots\ldots\ldots\ldots\ldots\ldots\ldots$$ Equation 67

Due to that spin and orbit momenta do not couple in all magnetic ordering, therefore the given approximations do not yield expected results when implemented experimentally, mostly in those architecture where the unpaired is exceptionally unbound such as in transition metal cluster. In such structures the electron spin overlaps a number of nuclei. By considering an electron that hos no orbital momenta, in a free environment, the Lãnde factor still has to be revised quantum mechanically to 2.0023193. This is because besides accounting for the total magnetic dipole moment of a paramagnetic species, its value is also affected by the ambient conditions it exists. Electric quadrupoles or a ordering consisting of two dipoles of balanced but reverse directed moment, ligand fields or magnetically order nuclei all lead to a dissimilarity of the sum of magnetic field produced by the electron (Kundu 2013).

$$B_{eff} = B_o + B_{local} \ldots\ldots\ldots\ldots\ldots\ldots\ldots\ldots\ldots\ldots$$ Equation 68

Origins of these confined fields can be from directly applied external field and as a result the aggregate magnetic field is related to gross of externally functional magnetic field and local existing field. Secondly they can be permanent and independent of the externally applied field.

$$B_{eff} = B_o(1 - \sigma) \ldots\ldots\ldots\ldots\ldots\ldots\ldots\ldots\ldots\ldots\ldots$$ Equation 69

σ defines the shielding factor and will lead to an elevation or depression of effective field experienced. According to (Fratter, et al. 2016) and (Matsushima, et al. 2010), so as to realize a domain that has weak magnetic fields at depressed energies a magnetic shield which has elevated

shielding factor is employed. The shielding factor describes the extent of magnetic shielding provided a magnetic shield on application of an alternating current or direct current external field which has a sinusoidal waveform and frequency. As a result a variable g factor has to replace the g factor resulting in the formula below (Ayscough 1967).

$$B_{eff} = B_o * \frac{g}{g_{eff}} \ldots\ldots\ldots\ldots\ldots\ldots\ldots\ldots\ldots\ldots\ldots\ldots \quad \text{Equation 70}$$

In most organic compounds which have unpaired electrons, the angular momenta is negligible, as a result the sum of momentum J is approximately equal to the spin angular momenta S only. In such samples g is near to 2 while in transition metal ions the value is much elevated as L is significant thereby contributing to J. An express for the energy levels that are associated with externally applied magnetic field is therefore stated as in Equation 71.

$$E_{m_s} = m_s g_e \mu_B B_o \ldots\ldots\ldots\ldots\ldots\ldots\ldots\ldots\ldots\ldots\ldots\ldots \quad \text{Equation 71}$$

Changes in energy, correlated to a transition, due to energy difference is therefore given as Equation 72.

$$\Delta E_{m_s} = \Delta m_s g_e \mu_B B \ldots\ldots\ldots\ldots\ldots\ldots\ldots\ldots\ldots\ldots\ldots\ldots \quad \text{Equation 72}$$

The magnetic field of the microwave energy radiating the sample is aligned at 90 degrees to the magnetic field of the magnet in which the sample is situated when in perpendicular mode. Application of the radiating field at 90° allows for the detection of eigenstate transitions in systems where the spin angular momenta takes fractions values, S = $\frac{1}{2}, \frac{3}{2}, \frac{5}{2}$ and so on. So as to permit electroparamagnetic resonance transition, $\Delta ms = \pm 1$ and the transition energy becomes Equation 73 (R. Das 2015).

$$\Delta E_{m_s} = g_e \mu_B B \text{ … … … … … … … … … … … … … ….}$$ Equation 73

Applying the radiation in parallel mode results in a selection rule that takes Δms=±2. For Non-Kramer Systems in which the spin angular momenta assumes integer values, S = 2, detecting the electronic environment will require that the radiating magnetic field be linearly aligned to the cavity magnet magnetic field.

2.8 Sensitivity

Unpaired electrons in a sample will react to an externally applied microwave frequency radiation when the cavity is tuned to $\hbar\omega = g\beta \mathrm{H}_0$. H_0 defines the externally applied microwave radiation magnetic field.

$$\hbar\omega = g\beta \mathrm{H}_0 \text{ … … … … … … … … … . … … … … … …}$$ Equation 74

To determine that a reaction has occurred the either frequency which is a dispersion phenomenon or Q factor which is a absorption of microwave energy will vary. A sample with unpaired electrons will absorb incident microwave radiation of magnetic field H_0 incident on it, on condition that the cavity is at resonant conditions of frequency $\omega_0 = 2\pi \mathrm{v}_0$. $\hbar$ is obtained from dividing 6.62607004 × 10-34 m2 kg / s by 2π. β is equal to 9.274 × 10–24 $\frac{J}{T}$, and is termed Bohr magneton. Lãnde factor is represented by g and is approximately equal to 2 for transition metal complexes and tends to deviate for most organic complexes. The average power absorbed per unit volume is given by Equation 75.

$$P = \frac{1}{2}\omega_0 H_1^2 \chi'' \text{ … … … … … … … … … … … ….}$$ Equation 75

The amplitude of magnetic field of incident microwave energy is defined by H_1. Degree or extent of magnetization of the radio frequency is given by χ'', the susceptibility. A change in quality factor Q, is an indication of power being absorbed from the incident microwave radiation.

$$\frac{1}{Q} = \frac{1}{Q_u} + \frac{1}{Q_\chi} \ldots\ldots\ldots\ldots\ldots\ldots\ldots\ldots\ldots\ldots \quad \text{Equation 76}$$

The unloaded quality factor Q when there is no resonace absorption is represented by Q_u. Q_χ is the proportion of resonant absorption quality factor added to the unloaded quality factor Q. Q is a sum of reductions due to conductivity and dielectric characteristics of the sample together with cavity losses. The variation in Q at resonance is given by

$$\Delta Q = -Q^2 \Delta \frac{1}{Q} = -\frac{Q_u^2}{Q_\chi} \ldots\ldots\ldots\ldots\ldots\ldots\ldots\ldots\ldots\ldots \quad \text{Equation 77}$$

It is assumed that Q_χ » Q_u. Quality factor for an empty cavity is realized by Equation 78.

$$Q_\chi = \frac{\frac{\mu_0}{2}\int_{cavity} H_1^2\, dV}{\frac{\mu_0}{2}\int_{sample} H_1^2 \chi''\, dV} \ldots\ldots\ldots\ldots\ldots\ldots\ldots\ldots\ldots \quad \text{Equation 78}$$

On condition that χ'' is homogenous in the entire sample then Equation 78 becomes Equation 79.

$$Q_\chi = \frac{\frac{\mu_0}{2}\int_{cavity} H_1^2\, dV}{\frac{\mu_0}{2}\int_{sample} H_1^2 \chi''\, dV} = \frac{1}{\chi'' \eta} \ldots\ldots\ldots\ldots\ldots \quad \text{Equation 79}$$

η refers to the filling factor which is the percentage of microwave power that reacts with the unit under test and is related directly to the microwave magnetic field magnitude, $<{H_1}^2{}_S>$ at the volume of the sample. It is that proportion of radiation magnetic field that which possesses an alike orientation as that of the static externally applied magnetic field. For a sample of volume V_S and has a tendency of its magnetization being alter by microwave energy with a factor of χ'', susceptibility, then the power of microwave radiation absorbed is related directly to the product of sample volume V_S, susceptibility χ'' and magnetic field magnitude, H_{1_S} at the sample, $V_S * \chi''$ $*{H_1}^2$. Due to the assimilation of microwave energy from the cavity by the sample quality factor of the resonate cavity decreases. The mathematical expression to represent this decrease in quality factor is realized by adding the inverse of sample loss component as shown below.

$$\frac{1}{Q} = \frac{1}{Q_u} + \frac{1}{Q_\epsilon} + \frac{1}{Q_r} \ldots\ldots\ldots\ldots\ldots\ldots\ldots\ldots\ldots \quad \text{Equation 80}$$

$$\frac{1}{Q} = \frac{1}{Q_u} + \frac{1}{Q_\epsilon} + \frac{1}{Q_r} + \frac{1}{Q_\chi} \ldots\ldots\ldots\ldots\ldots\ldots\ldots\ldots \quad \text{Equation 81}$$

Q_χ is the quotient of power stored in the whole cavity to that which is absorbed by the sample under inverstigation.

$$Q_\chi = \frac{\frac{\mu_0}{2}\int_{cavity} H_1^2\, dV}{\frac{\mu_0}{2}\int_{sample} H_1^2 \chi''\, dV}$$

$$= \frac{V_C<{H_1}^2{}_C>}{\chi'' V_S<{H_1}^2{}_S>} \ldots\ldots\ldots\ldots\ldots\ldots\ldots\ldots\ldots\ldots \quad \text{Equation 82}$$

In terms of filling factor the Equation 82 reduces to

$$Q_\chi = \frac{1}{\chi''\eta} \ldots\ldots\ldots\ldots\ldots\ldots\ldots\ldots\ldots\ldots\ldots \quad \text{Equation 83}$$

2.9 Resonant cavities

Resonant cavities used at microwave frequency cannot take the form of either distributed or lumped resistors, capacitors, inductors and diodes. This is due to skin effect which results in the high frequency alternating current being more concentrated on the surface of the conductor. This results in an escalation of the effective resistance that is offered by the circuit. Therefore the resonate cavities used at microwave frequencies has dimensions that are equal to the wavelength of the microwave signal and is constructed from highly conductive material. At resonance the cavity stores microwave in the form of standing waves which assume different patterns depending on the dimensions and geometry of the cavity. As opposed to a wave guide, in a resonant cavity there is no flow of electromagnetic energy, but only dissipation and storage occurs because the standing electromagnetic radiation patterns are created by transverse magnetic field maximum which will be $\frac{\lambda_0}{4}$ from the electric transverse maximum. The magnetic field loops created in resonant cavities will always encompass electric field lines while the electric fields also encompass magnetic fields by means of closed loops or they will end at the induced surface charges.

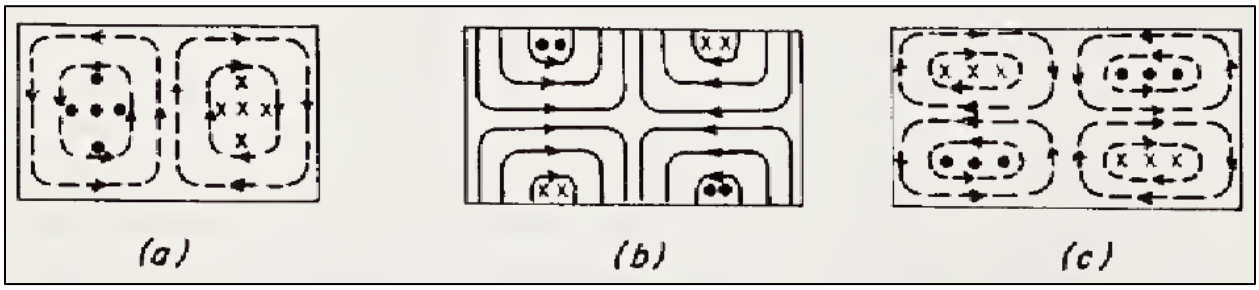

Figure 90: Electromagnetic radiation patterns in cylindrical and rectangular cavities (C. P. Poole 1996).

If the cavity has a high Q factor then the magnetic field and electric field are 90° out of phase such that when one of the fields is a maximum the other is zero. The energy of the electric field and magnetic field under these conditions is given by Equation 84 and Equation 85 respectively.

$$U_E = \frac{\epsilon}{2}\int |E_m|^2 dr \ldots\ldots\ldots\ldots\ldots\ldots\ldots\ldots\ldots\ldots \quad \text{Equation 84}$$

$$U_H = \frac{\mu}{2}\int |H_m|^2 dr \ldots\ldots\ldots\ldots\ldots\ldots\ldots\ldots\ldots\ldots \quad \text{Equation 85}$$

Losses also occur in the resonant cavity and these are a result of skin effect which cause current to distribute itself more on the surface of the conductor. Losses occur in the form of heat energy and these can be represented by the equation given below.

$$P_L = \frac{R_S}{2}\int |H_{tm}|^2 dS \ldots\ldots\ldots\ldots\ldots\ldots\ldots\ldots\ldots\ldots\ldots\ldots \quad \text{Equation 86}$$

The subscript m denotes maximum value of the corresponding field referred to. While tm refers to the peak tangential figure of the field along the surface of the cavity. Losses in the cavity may arise due to lossy dielectrics, which have conduction greater than zero yet they again do not fall in the category of quality standard conductors (Lorence 30th July 2009).

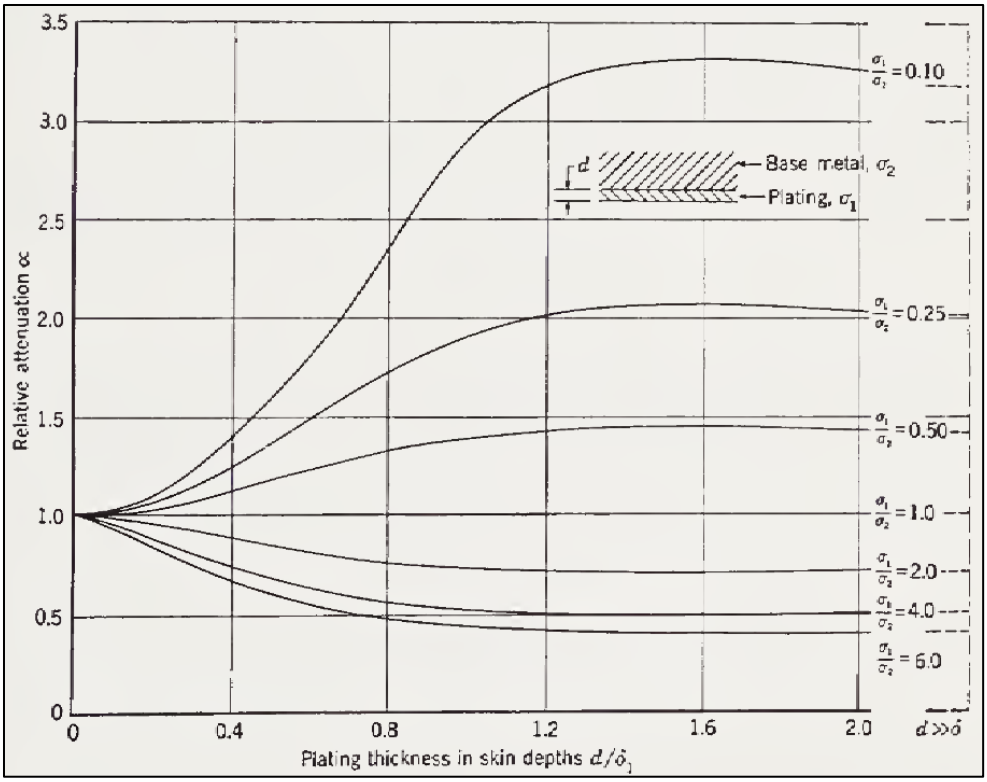

Figure 91: Fading of microwave frequency in a plate conductor (C. P. Poole 1996).

2.9.1 Types of resonant cavities and detectors

2.9.1.1 Direct Current Detection

Paramagnetic spin systems will absorb a fairly low quantity of microwave radiation as compared to ferromagnetic substances. This is to say the detected power changes at the detector due to changes in resonant frequency of the cavity due to absorption of microwave energy by the paramagnetic substance will correspondingly be weak signal which cannot be detected by mill watt meter and bolometer. Any variations in the voltage at the detector during resonance can be detected as power absorption by the sample, there conditions need to be maintained as constant as possible. Taking into account that the operating current of a crystal detect is approximately of the order 10^{-04}A then from Feher's experiment, if the voltage changes due to power stability problems then, the current detected would also vary as is it of a small order. Maintaining the stability of the Klystron power is impractical, therefore the sample has to be strong enough to eliminate sensitivity problem so as to employ direct detection without having modulation distortions.

2.9.1.2 Transmission microwave cavity and a square law sensor.

For a transmission resonator with a square law sensor power input for the load is given by Equation 87 .

$$P_l = \frac{(En_1^2 n_2^2)^2 R_0}{(R_c + R_0 n_1^2 + R_l n_2^2)^2} \ldots\ldots\ldots\ldots\ldots\ldots\ldots\ldots\ldots\ldots \quad \text{Equation 87}$$

During resonance the variation in power to the load as a subject of maximum power $P_W = \frac{1}{4} * \frac{E^2}{R_O}$, available is given by Equation 88.

$$\frac{\Delta P_l}{P_W} = \frac{1}{P_W}\frac{\partial P_l}{\partial R_c}\Delta R_c$$

$$= \frac{8(En_1^2n_2^2)^2 R_0 \Delta R_c}{(R_c + R_0 n_1^2 + R_l n_2^2)^2} \ldots\ldots\ldots\ldots\ldots\ldots\ldots \quad \text{Equation 88}$$

To allow maximum power transfer R_l and R_0 are made equal to each other and when P_l is made as large as possible with reference to $R_0 n_1^2$ and $R_l n_2^2$ then $R_0 n_1^2 = R_l n_2^2 = R_0 n^2 = R_c$. Resultant impedance of the of the cavity input is a total of $R_l n_2^2$ and R_c. Therefore the cavity is over coupled with the voltage standing wave ratio being represented in Equation 89.

$$VSWR = \frac{R_l n_2^2 + R_c}{R_0 n_1^2} \ldots\ldots\ldots\ldots\ldots\ldots\ldots\ldots\ldots \quad \text{Equation 89}$$

By utilizing equal ratio of turns n_1 and n_2 coupling constant, a transmission cavity cannot be under coupled. Therefore equating the ratio of turns n_1 and n_2 yields

$$\frac{\Delta P_l}{P_W} = \frac{1}{P_W}\frac{\partial P_l}{\partial R_c}\Delta R_c = \frac{8}{27}\frac{\Delta R_c}{R_c} = -\frac{8}{27}\frac{\Delta Q}{Q} = -\frac{8}{27}Q_u \chi'' \eta \ldots\ldots\ldots\ldots \quad \text{Equation 90}$$

2.9.1.3 Reflection cavity and square law detector.

Power radiated into the resonant cavity is given by Equation 91.

$$P_C = \frac{\frac{1}{2}(nE)^2 R_c}{(R_c + R_0 n^2)^2}$$

$$= \frac{2P_w(^{R_C}/_{R_O n^2})}{(1 + {}^{R_C}/_{R_O n^2})^2} \ldots\ldots\ldots\ldots\ldots\ldots\ldots\ldots\ldots\ldots\ldots\ldots \quad \text{Equation 91}$$

$$P_W = \frac{1}{4} * \frac{E^2}{R_O} \ldots\ldots\ldots\ldots\ldots\ldots\ldots\ldots\ldots\ldots\ldots\ldots \quad \text{Equation 92}$$

R_C, n and R_O are resistance of the resonant cavity, ratio of turn for an equivalent transformer circuit and resonant cavity resistance respectively. There is a point at which the cavity resistance matches the product of ratio of turns of the supply transform equivalent circuit and microwave generator. This can be expressed mathematically as $R_c = R_0 n$. When resonance conditions are achieved there will be a variation in the reflected power that results from absorption of microwave radiation by the sample. The change in the reflected power is the quantity of microwave power absorbed by the sample as a result of a change in the resistance of the cavity.

$$\frac{\Delta P_C}{P_W} = \frac{1}{P_W}\frac{\partial P_C}{\partial R_c}\Delta R_c$$

$$= \frac{2\Delta R_C}{(R_0 n^2)} \times \frac{(1 - {R_C}/{R_O n^2})}{(1 + {R_C}/{R_O n^2)^3}} \ldots\ldots\ldots\ldots\ldots\ldots\ldots\ldots\ldots\ldots \quad \text{Equation 93}$$

The change in power in the cavity ΔP_C is optimized with respect to the coupling parameter $R_O n^2$ as shown in Equation 94, for a square law detector.

$$\frac{\partial \Delta P_C}{\partial (R_0 n^2)} = \cdots \ldots\ldots\ldots\ldots\ldots\ldots\ldots\ldots\ldots\ldots\ldots\ldots \quad \text{Equation 94}$$

This yield a solution that gives that give an over coupled or under coupled resonate cavity as shown below.

$$\frac{R_0 n^2}{R_C} = 2 \pm 3^{\frac{1}{2}} = \begin{cases} VSWR & R_0 n^2 \geq R_C \\ \dfrac{1}{VSWR} & R_0 n^2 \leq R_C \end{cases} \ldots\ldots\ldots\ldots\ldots\ldots\ldots \quad \text{Equation 95}$$

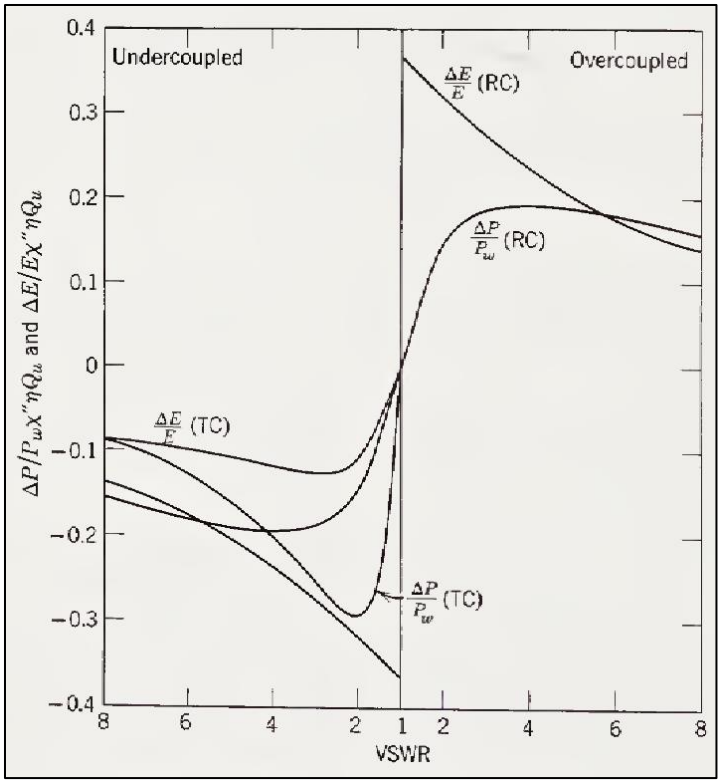

Figure 92: Electron spin resonance signal $(\Delta P_c)/P_w$ and ΔE/E normalized relative to $Q_u\chi''\eta$ as a function of VSWR for square law and linear detectors (C. P. Poole 1996).

2.9.1.4 Reflection cavity and a linear detector

Under this circumstance reflected voltage is sensed and is related to the voltage that hits the surface of the sample as shown in Equation 96.

$$E_r = E\Gamma = -E\left(1 - \frac{2VSWR}{1 + VSWR}\right) \ldots\ldots\ldots\ldots\ldots\ldots\ldots \quad \text{Equation 96}$$

The voltage standing wave ratio of a reflection cavity is defined by

$$VSWR = \frac{R_0 n^2}{R_C} \pm 1 \ldots\ldots\ldots\ldots\ldots\ldots\ldots\ldots\ldots\ldots\ldots \quad \text{Equation 97}$$

For an over coupled condition a positive sign is assumed, while the negative sign corresponds to an under coupled situation. This is variation in reflected voltage at resonance.

2.10 Magnetic Field Scanning and Modulation

The energy gap between the low spin and high spin has to match the energy of incident radiation for transition of electrons from the low spin to high spin (Valenzuela, et al. 2008). This can be represented mathematically by $hv = g\beta H$ the equation given below. To archive this in electroparamagnetic resonance, the field H is kept constant while the frequency v is adjusted. This results in the variation of microwave energy that can be absorbed by the sample in the cavity. Depend on whether the absorption spectrum is Lorentzian or Gaussian the function of absorbed radiation takes the form Equation 99 and Equation 98. Alternative to the frequency the magnetic field is varied, consequently the frequency terms for Equation 98 and Equation 99 are replaced by H and H_0. $v_{1/2}$ and $H_{1/2}$ are the half amplitude full line width in frequency and magnetic field units.

$$Y_v = y_m e^{-0.693\left[\frac{(V-V_0)}{(\frac{1}{2}\Delta V_{\frac{1}{2}})}\right]^2} \quad \ldots\ldots\ldots\ldots\ldots\ldots\ldots\ldots\ldots\ldots\ldots\ldots \quad \text{Equation 98}$$

$$Y_v = \frac{y_m}{\left[1 + (\frac{v - v_0}{1/2\left(\Delta v_{1/2}\right)})\right]} \ldots\ldots\ldots\ldots\ldots\ldots\ldots\ldots \quad \text{Equation 99}$$

2.10.1 Why the magnetic field is scanned instead of the frequency

- There is a direct relationship between the output power of a klystron and frequency of the signal. Varying the magnetic field would therefore require complex power stabilizing circuitry.
- In order to have no reflected microwave energy, impedance of the load and the transmission line are matched. This condition is meet when all values are at the origin of the smith chart. The challenge is there is frequency sensitivity associated with adjusting the frequency of microwave transmission line.
- For klystron microwave generators, there has to be harmony in the mechanical and electronic frequency adjustment so that during scanning the resonant cavity pip is on top of the klystron mode.
- The margin by which klystron microwave generator can be varied is small, approximately 5% to 10% of the center frequency. This implies that if the resonance is broad it will be difficult to scan as a frequency that is a fraction more than the line width is required.

2.10.2 Influence of scanning rate and field range

The size of magnets used in EPR is determined by the magnitude of the scanning range required and this is determined by the nature of sample being analyzed. The uttermost studied sample 3 000 to 3 500 G is required for resonance. A major portion of free radical requires just a couple hundreds of gauss for spectral determination, thereby allowing the employment of a permanent magnet. In the situations where a high magnetic field is require for the EPR spectrum an electromagnetic is utilized as this allows the scanning of the magnetic field at admitted steady rate and simultaneously generating high values of up to 8 000 G in the X band (Ayscough 1967).

2.11 Low and high field microwave absorption characteristics captured by electron spin resonance in other compounds

2.11.1 Doping impact on $Co_xZn_{(1-x)}Fe_2O_4$ E.S.R. spectrum.

(Msomi., et al. 2019) analyzed $Co_xZn_{(1-x)}Fe_2O_4$ nano-sized grains which had been synthesized by disintegration in glycol at elevated temperatures. Experimentation was carried out at approximately $300K$ and a distinct line spectra was obtained which was symbolic of sole phased compounds. Undiluted $CoFe_2O_4$ nano-sized grains where characterized by practically nil magnetic vibration. However accompanying the aluminum and zinc impurity increase, the resonance field was observed to increase to approximately $3000G$. The mutual dipole-dipole synergy in pure $CoFe_2O_4$ was attributed to the boundless electron spin resonance signal for the non-doped compound. A frailer super-exchange was prescribed as being the lead to a compressed absorption signal because the magnetic chromium and iron ions are displaced by aluminum and zinc which are not magnetic.

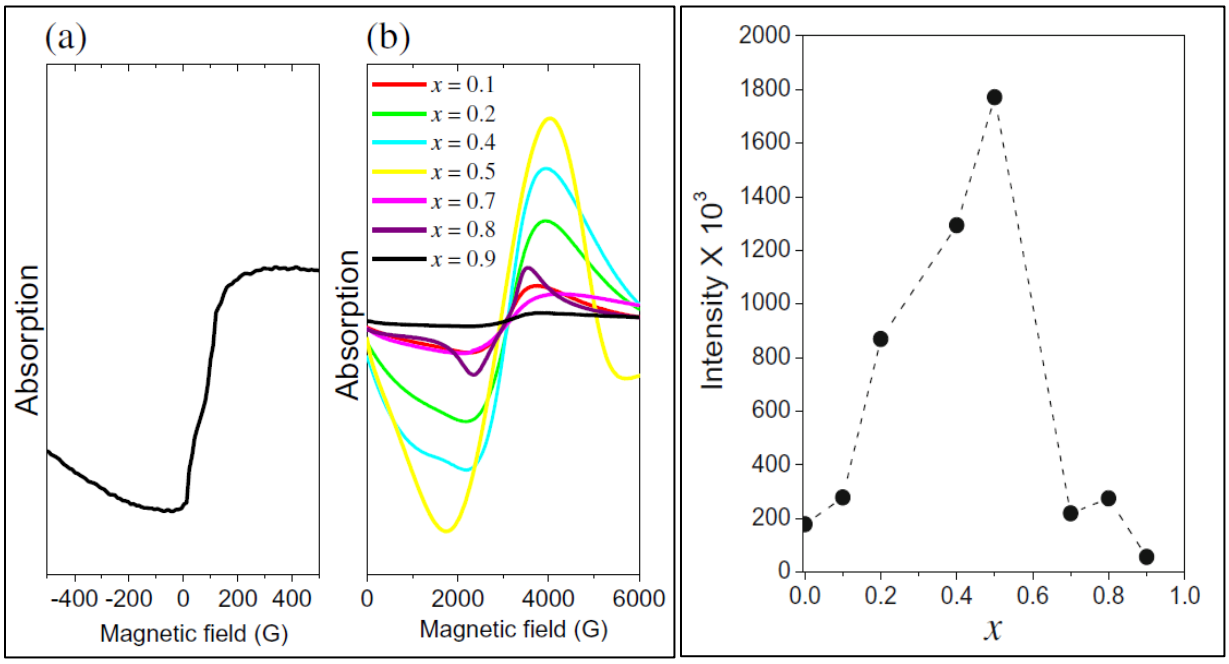

Figure 93: Electron Spin Resonance spectra of (b) Zinc interchanged Co containing Fe (a) pure $CoFe_2O_4$ and signal intensity.

2.11.2 Temperature dependent low field and high field microwave absorption in α-Cr2O3 nanospheres

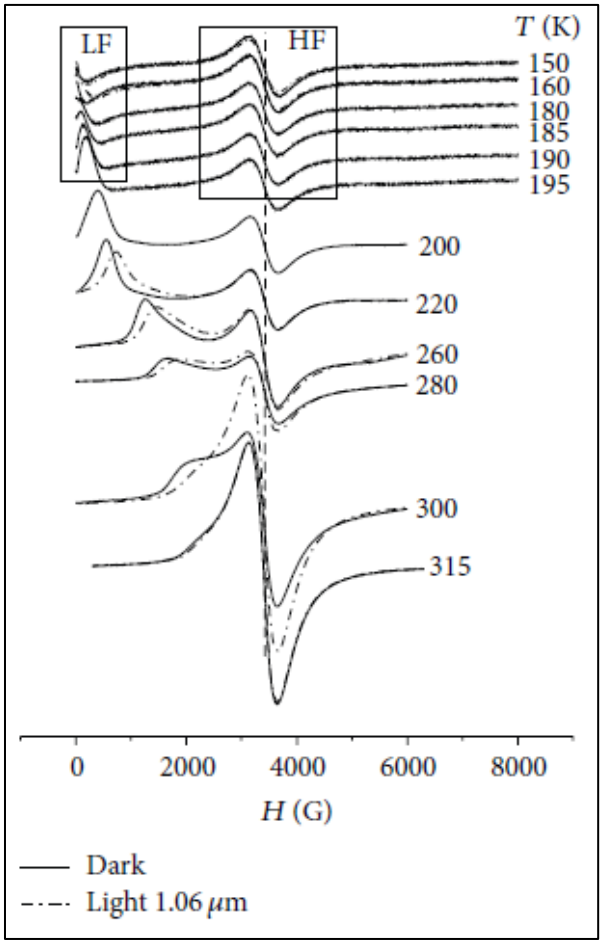

Figure 94: Low field and high field microwave absorption of α-Cr_2O_3 nanospheres

Both high field and low field microwave energy were absorbed from the cavity at temperature between $280\,K$ and $150\,K$. High field microwave absorption was enhanced by elevating temperature of the resonant cavity from $150K$ to $315K$ as can be seen in Figure 94. However the low field component totally vanishes at temperatures beyond $280K$. The sample can therefore be said to migrate from high field microwave absorption to LFMA as temperatures were lowered. It was suggested by (Khamlich., et al. 2014) that the microwave absorption was driven by optical characteristics of the chromium ions $3d^3$ orbitals. These orbital was believed to chasm into different energy levels t_{2g} and e_g that allow for electronic migration from low energy state. The dashed and solid lines signified photo-induced and non-photo stimulated microwave absorption.

2.11.3 Modulating signal variation effects on $Ba_{0.34}K_{0.64}Fe_2As_2$ NRMA.

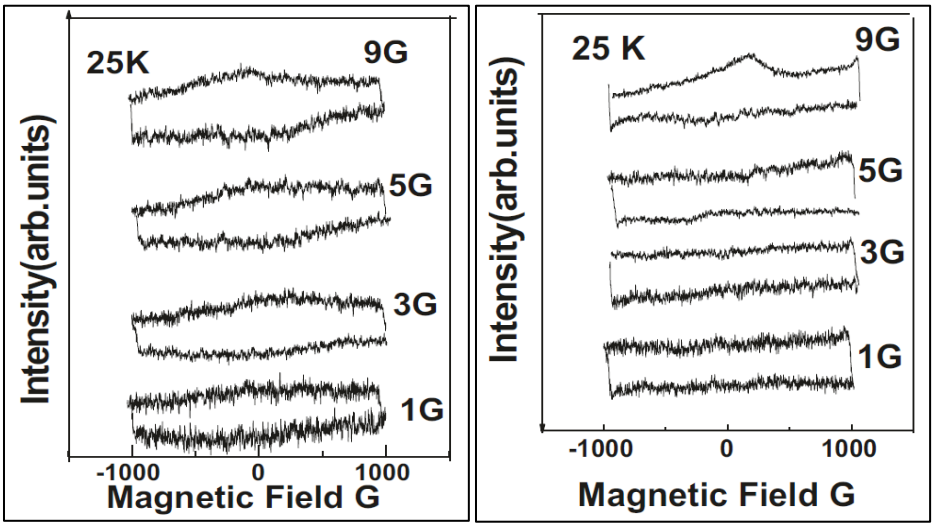

Figure 95: Non-resonant microwave absorption at 25K with a (a) parallel magnetic field (b) perpendicular magnetic field.

By varying the electron spin resonance modulating magnetic field the variation in microwave energy taken up by $Ba_{0.34}K_{0.64}Fe_2As_2$ considerably varied as can be seen in Figure 95. It is also worth noting that in the first image the magnetic field was applied parallel to the sample while in the second one it was perpendicular to it. $Ba_{0.34}K_{0.64}Fe_2As_2$ a superconductor showed without dispute a boundary current hysteresis microwave absorption dependent on the regulating magnetic field magnitude. Frail absorption characteristics which are dependent on orientation of the sample where also observed in $Ba_{0.34}K_{0.64}Fe_2As$.

2.11.4 $SmFeAsO_{0.8}F_{0.2}$ temperature dependent microwave absorption

As indicated in Figure 96 there was a lack of phase change in samarium iron oxyarsenide which affirmed the permanence of exclusively hysteretic Josephson junction at the experimentation microwave power. Its magnitude could be enhanced to until the non-superconducting portions where either nonexistent or in the magnetic nanoscale in the sample. As a result Fraunhofer arrangement of the Josephson junction was not altered by administering a direct current magnetic field, leading to barely any oddity being noted.

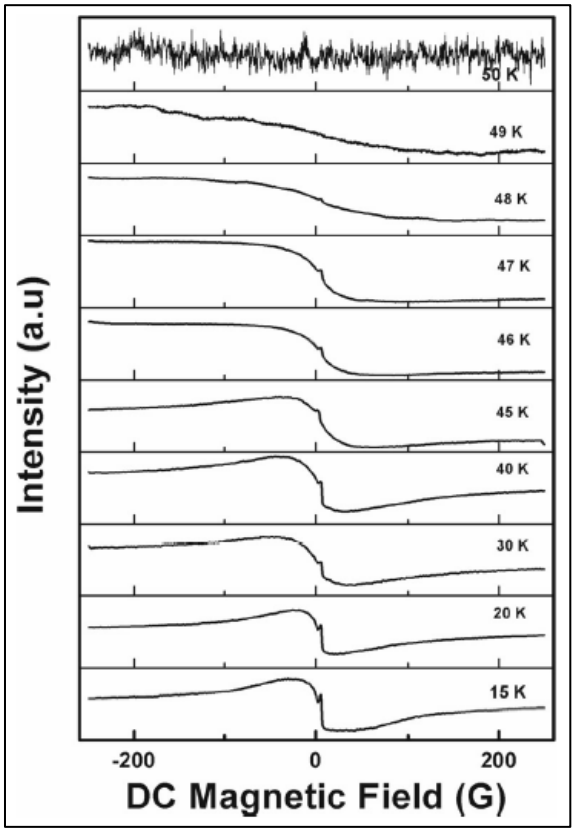

Figure 96: Temperature dependent low field microwave absorption.

Contrast in the absorbed microwave energy at distinct temperatures was detailed by taking into account sticky passage of fluxons as they were pushed by microwave draughts as a consequence of Lorentz force, secondly in fluxing of the magnetic fields in the Josephson junction which resulted in a minimization of vital currents. Administering a magnetic field with a magnitude larger than the diminished JJ fields was suggested to enhance percolation of magnetic flux into the $SmFeAsO_{0.8}F_{0.2}$ allowing it to be restrained or maneuver smoothly amidst the JJs. Energy scattering then results from microwave draughts that would be moving fluxons according to Lorentz force. Elevating the system's thermodynamic energy culminates in a scattering of energy at a rate corresponding to the fluxon quantity but conversely related to coefficient of viscous flow impediment (Onyancha., et al. 2017).

.

2.11.5 Ni–YBCO temperature dependent microwave absorption

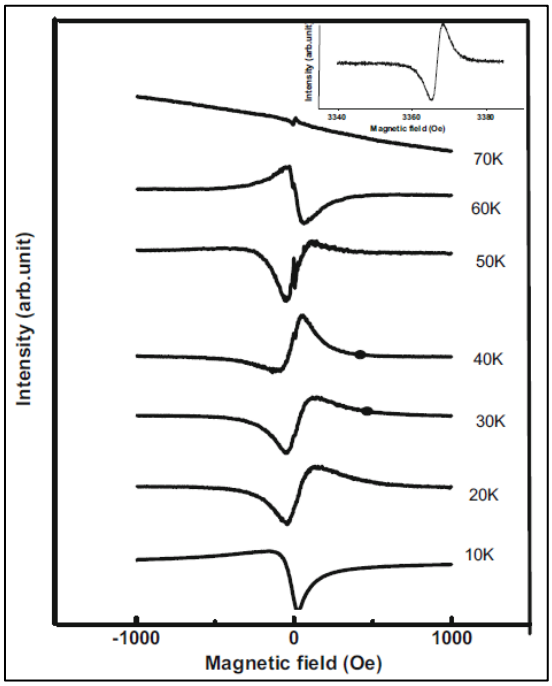

Figure 97: LFMA in yttrium barium copper oxide powder

(Nemangwele., et al. 2017) designedly combined two percent nano Ni patches to Yttrium barium copper oxide powder. This was done as a means of forming zero and Pi Josephson junction that result from the frail coupling between Ni and Yttrium barium copper oxide powder. This arises from the ferromagnetic nature of Ni. Such Josephson junctions are then attributed to numerous phase inversions captured in Figure 97. It is important to note that the numerous phase inversions captured were affected by both temperature and power of the incident microwave energy. The first phase inversion was captured at twenty kelvin, then at sixty kelvin and lastly at seventy kelvin. All these phase inversions occurred at low magnetic fields. When the same experiment was carried out at an elevated microwave power, the fail Josephson junction were thought to disintegrated while the remaining were consolidated. This effect was proposed to cause a vanishing of some of the captured phase inversions at lower microwave power. They also gave an account of how pair breaking effect results in a direct proportional relationship with signal intensity. It was found that when temperatures are approaching the pair breaking effect became more established.

2.11.6 Doping and sintering temperature effects on $Zn_{(1-x)}(Mn, Gd, Ni)_xO$ resonant microwave absorption

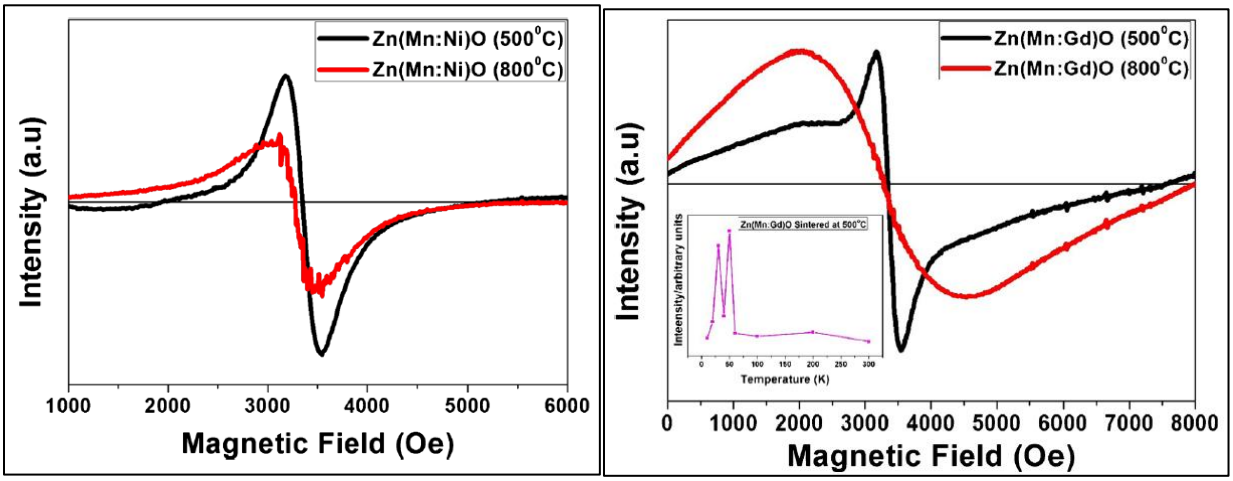

Figure 98: High field microwave absorption.

The was not much of a difference in the line width for the nickel doped same sintered at 500°C and 800°C. However a noticeable difference was in the absorbed signal intensity. A lower sintering temperature resulted in tendency for the sample to absorb more microwave energy from the cavity. This is illustrated in the image the left in Figure 98. Conversely sintering temperature however seemed to play a role in line-width enhancement in the gadolinium doped sample as shown in the figure on the right. A higher sintering temperature was characterized by an enhanced line width (Mahule., Srinivasu and Das. 2017). Dissimilar magnetic states that are linked to the lower level phase were attributed to this rapid line-width variation.

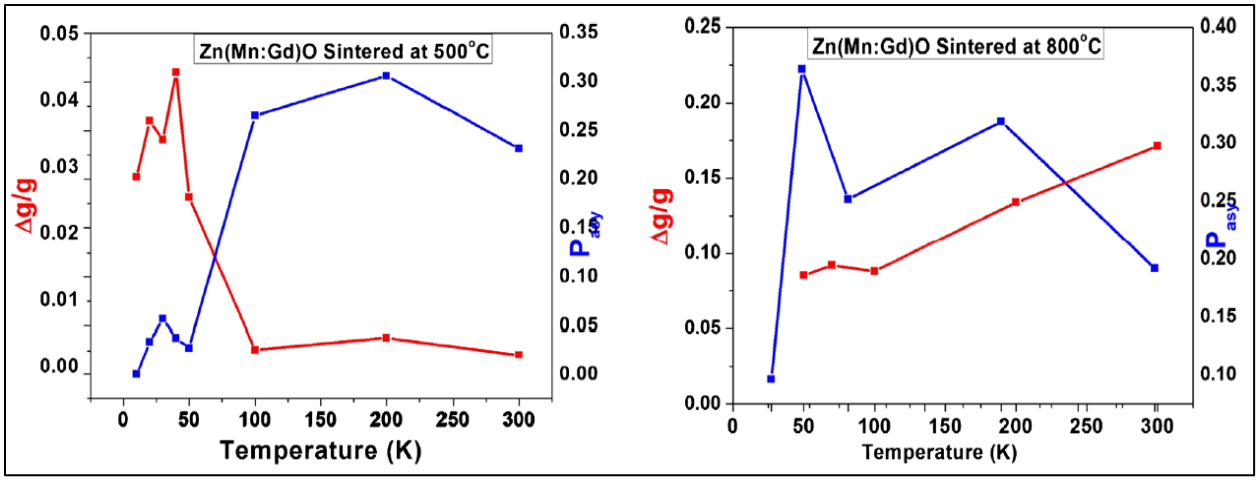

Figure 99: Variation in g

As a means of interpreting the definite source of purported ferromagnetic condition, relationship graphs of Δg/g against temperature were constructed as shown in Figure 99. At temperatures above 100K the value of g remained nearly nominal without any deviation. Then at temperatures slightly below 100K, the value of Δg/g became sensitive to temperature variations, attaining a maximum of approximately 0.045 at about 45K. Inversely in the 800°C sintered sample there was a tendency of Δg/g diminishing as the temperature was lowered below 100 K, its value stabilizing to around 0.08. Such an increase in the Δg/g corresponding causes an escalation in the magnetization of the sample as was observed by . It was therefore proposed that the ferromagnetism that arises in $Zn_{(1-x)}(Mn, Gd, Ni)_xO$ is derived from inclination of electron spins.

2.11.7 Effects of varying attenuation and modulating signal on $Zn_{(1-x)}(Mn:Fe(Ni))_xO$ microwave absorption

(Mahule., Srinivasu and Das. 2019) by E.S.R. studied $Zn_{(1-x)}(Mn:Fe(Ni))_xO$ samples of randomly oriented crystals and powder. They established that microwave absorption is more enhanced in iron and manganese alloyed ZnO in contrast to nickel and manganese doped sample. As can be seen from Figure 100 when the E.S.R. modulating signal amplitude was elevated from 1 G, 3 G, 5 G, 7 G and 9 G, microwave energy absorbed is corresponding surged. (Gavi, et al. 2012) also had similar observations with FeSi deposited on a substrate. This lead to evidence that the

quantity of microwave energy absorbed by the $Zn_{(1-x)}(Mn:Fe(Ni))_xO$ samples can be varied by altering the magnitude of magnetic field. According to the second image in Figure 100 varying the E.S.R. system attention had a significant impact on the absorbed microwave energy. Microwave energy absorbed decreased more at 30 dB compared to at 25 dB and 20 dB subsequently. Such a reduction was credited to resistance waste as a result of microwave currents. In less than 10 dB attenuation change, the microwave electromagnetic energy absorbed was varied significantly.

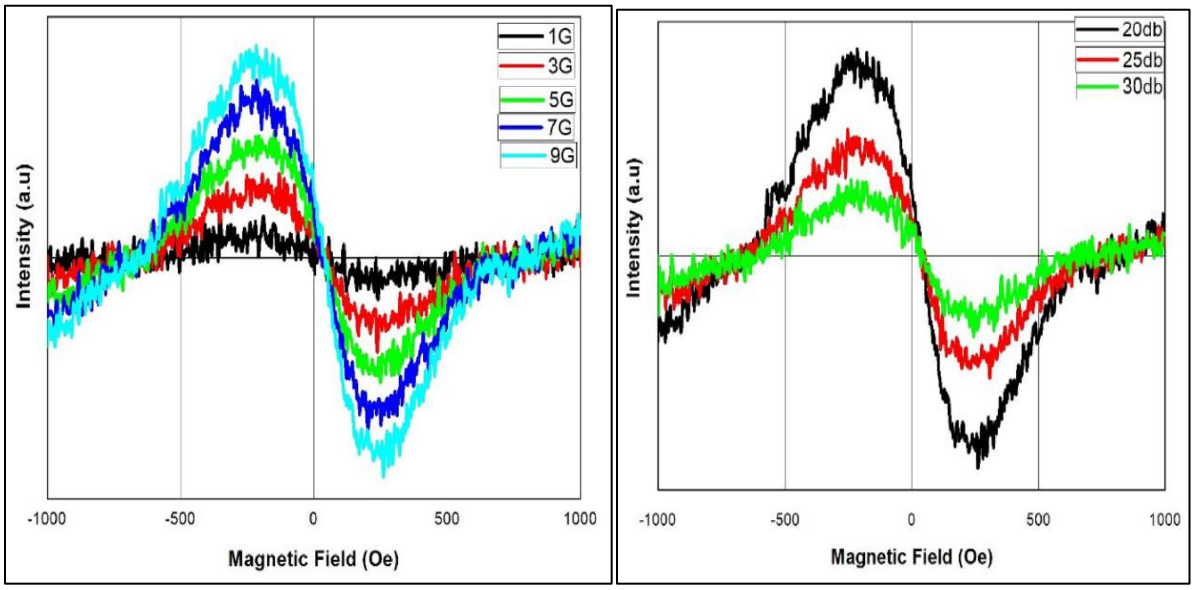

Figure 100: $Zn_{(1-x)}(Mn:Fe(Ni))_xO$ low field microwave absorption.

Chapter 3

3 Material and Methods

3.1 Introduction

Several well-defined steps on operating the electron paramagnetic resonance measurement system for the study of bulk $BiFe_{0.5}Mn_{0.5}O$ so as to obtain an optimum spectrum is well lay out. These include how the ESR measurement system was loaded with the bulk $BiFe_{0.5}Mn_{0.5}O$ sample and tuned so as to match the impedance of the resonance cavity to that of the gunn diode is well laid out. The handling of cryogen dewar has several safety precautions that surround this process. These are well described and explained in this chapter. Secondly, a means of determining electromagnetic moment per gram for the sample is also discussed. The material synthesis process is also given.

3.2 Bulk $BiFe_{0.5}Mn_{0.5}O_3$ synthesis

Multiferroic perovskites occur naturally beneath the earth surface at considerably elevated temperature and inflated pressure regions. Since $BiFe_{0.5}Mn_{0.5}O_3$ is a perovskite, its artificial synthesis in the lab can also be archived by following suite at elevated temperature and pressure as compared to ambient environment conditions in the lab. For this reason a Multi-anvil machine was employed as it can exert pressures of up to two hundred and fifty $kbar$ and thermal conditions of up to 3000°C. Despite its short comings of pressure variations that arise as a result of enlargement and dilation of cell segments as the sample was heated and chilled a well formed granulated bulk $BiFe_{0.5}Mn_{0.5}O_3$ was obtained. A temperature of 1373.15 K was applied at a pressure of 8.7×10^5 Psi to a stoichiometric mixture of bismuth (III) oxide, ferric oxide and manganese (III) oxide placed in the multi-anvil cell. These conditions were maintained for one hour and 30 minutes and then the temperature was reduced to room temperature. Sudden

pressure variations cause a temperature change, therefore thrust on the cell segment was gradually discharged. The stages of sample genesis are in photographs of Figure 101.

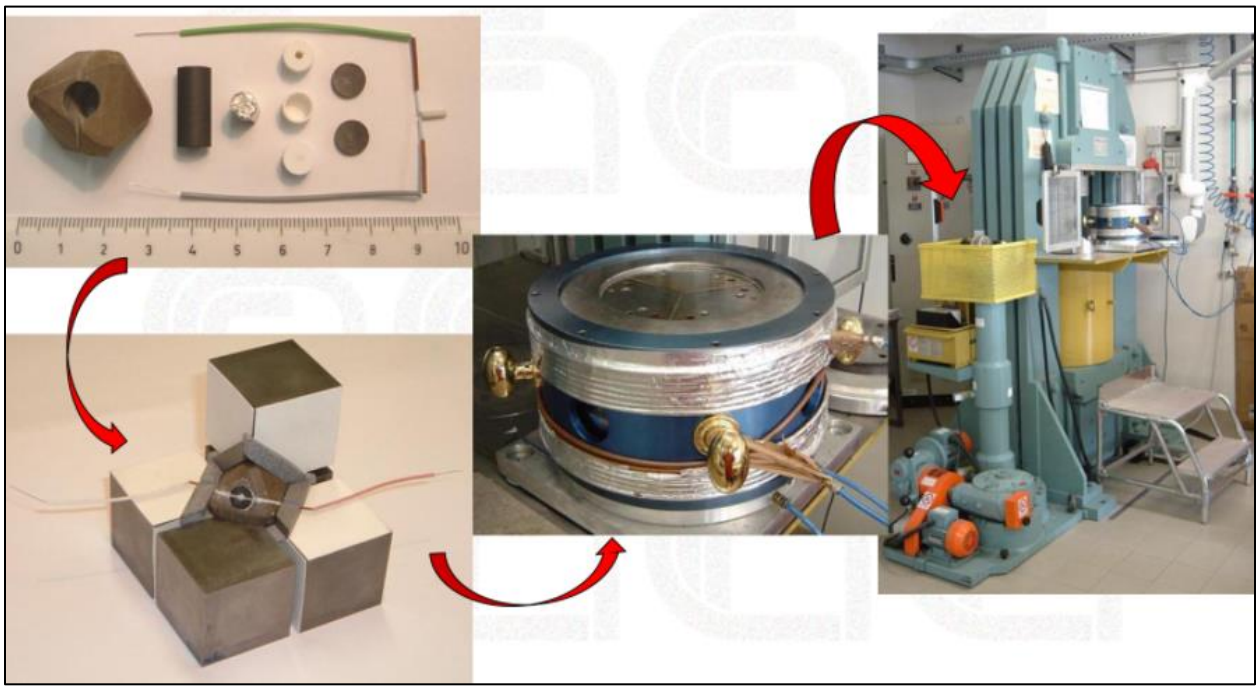

Figure 101: $BiFe_{0.5}Mn_{0.5}O_3$ synthesis equipment courtesy CNR-IMEM Italy.

3.3 E.S.R. and PPMS Cryogenic Studies

The level of the liquid helium in the dewar was first determined by means of a mechanical dip stick. The ESR 900 continuous flow cryostat was connected to the liquid helium dewar by means of a 90° vacuum-jacketed elbow liquid transfer tube. A diagram of the ESR 900 continuous flow cryostat is shown in Figure 108. The distance from the test tube holder to the center of the resonant cavity was determined by means of measurement with a 30 cm rule. This was done so as to accurately position the bulk Bi_2FeMnO_6 sample at the center of the resonant cavity where it will absorb the maximum quantity of magnetic energy generated by the gunn diode. At this location, a minimum quantity of electric field energy is absorbed by the sample. The electric field is marginally absorbed with resonance in the middle of the resonator, but the magnetic field vector of the incident EMR energy drives the EPR transition. The electric field will result in a

non-resonant microwave absorption or a low field microwave absorption due to interaction with the dipole moment of the bulk Bi_2FeMnO_6 sample. We shunned this as it results in a reduction of the Q factor and can culminate in heating of the sample (M. Brustolon 2008). The quantity of the bulk Bi_2FeMnO_6 sample was selected such as not to place a redundant quantity in the cavity which would increase the portion of paramagnetic centers. This has the effect of deteriorating the Q factor thereby negatively affecting the sensitivity.

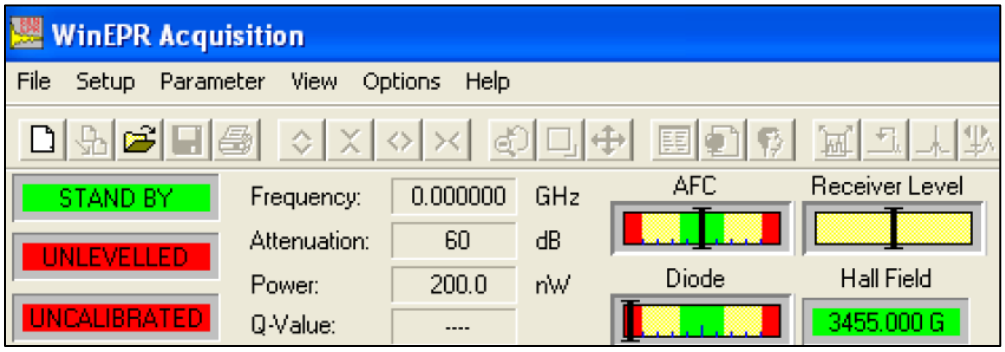

Figure 102: AFC and the Diode window before impedance matching.

The modulating frequency had to be chosen to be smaller than the line width so as to avert to the formation of sideband resonance which locates at distances $\frac{\omega_m}{\gamma}$ from each other. However, the magnitude should not be too small cause a loss of the modulation effect. Generally the modulation frequency was chosen so as to satisfy the Equation 100. Our modulation frequency was therefore set to 100 kHz. The tuned and non-tuned state of the resonance cavity is illustrated in Figure 105 and Figure 102 respectively.

$$\frac{\omega_m}{\gamma} \ll \Delta H \ldots\ldots\ldots\ldots\ldots\ldots\ldots\ldots\ldots\ldots\ldots \quad \text{Equation 100}$$

Properties of the EPR spectrum of bulk Bi_2FeMnO_6 sample which are the line width H_{PP} and the line position entirely relay on the magnetic field measurement and control system for accuracy.

For bulk Bi_2FeMnO_6 cryogenic studies either liquid helium or liquid nitrogen could be employed.

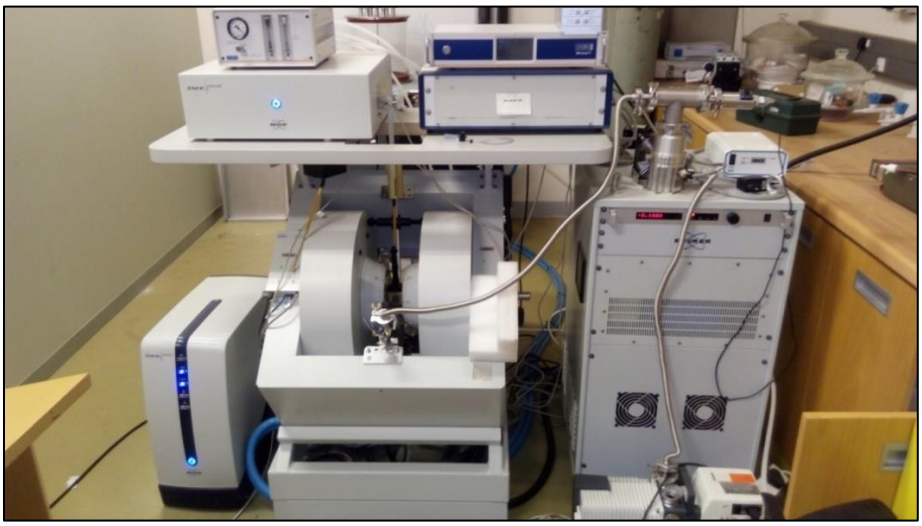

Figure 103: An X-band CW-ESR measurement system located at the University of South Africa.

Notwithstanding due to the dynamics that we want to capture at 5 K, liquid helium was used as liquid nitrogen can only reduce the sample temperature to 77 K. The cryogen was supplied to the sample by means of a pump which forced the liquid helium to flow to a heater where it was heated to the desired temperature according to the temperature selection on the MercuryiTC controller then vapour transferred to the sample.

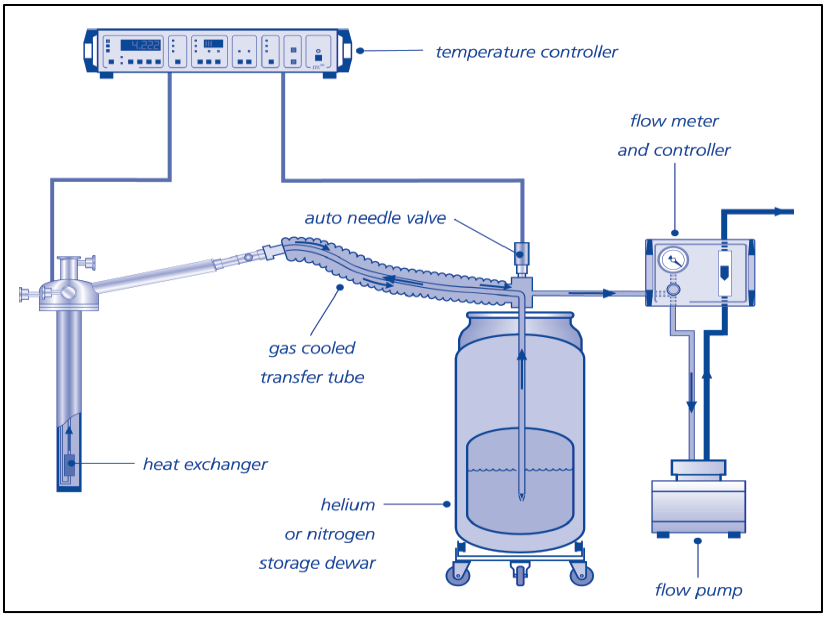

Figure 104: Block diagram to illustrate the setup used for bulk Bi_2FeMnO_6 Cryogenic ESR studies. < https://images.app.goo.gl/6vYftppik5vZUX4N8> [Accessed on 12 Jan 2020]

Temperature affects the overall energy of a system. Therefore before scanning of the bulk Bi_2FeMnO_6 sample the temperature values observed on the MercuryiTC were first waited for to stabilize. This increases the EPR signal amplitude by increasing the magnitude of the signal amplitude temperature dependent Boltzmann factor, $\frac{E}{kT}$ where E is the energy of the BFMO system and T is the temperature of the BFMO sample. It also allows for the slowing down of T_1 and T_2 in order to permit detection of the ESR spectrum. This is applicable in those systems in which the transition metal ions have a rapid relaxation (M. Brustolon 2008).

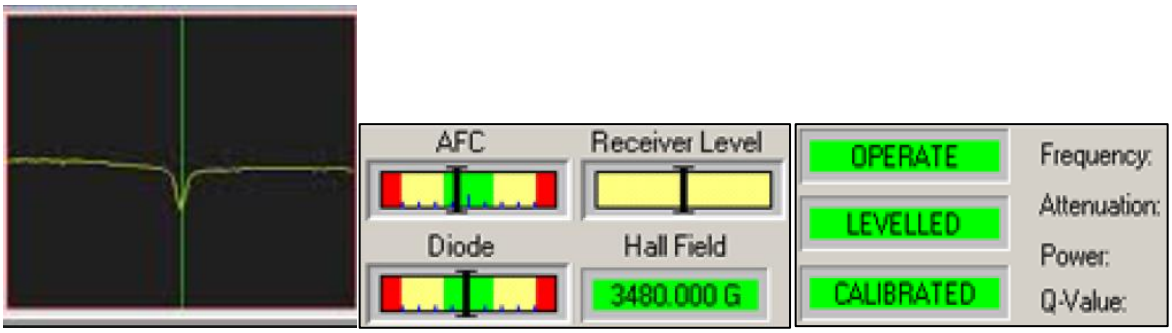

Figure 105: Tunned cavity state as shown by the deep, AFC and Diode which are centered.

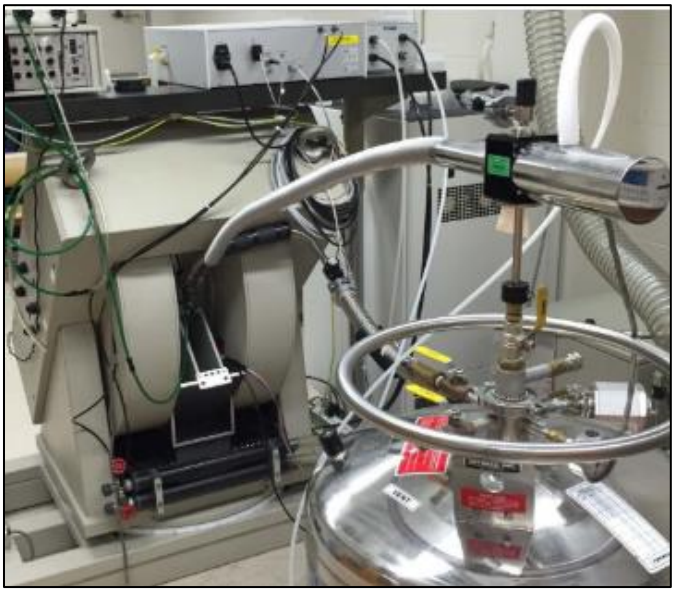

Figure 106: Illustration of liquid helium tank connection to a ESR900 Continuous flow Cryostat. <https://epr.chem.wisc.edu/content/instruments> [Accessed on 12 Jan 2020].

The E.P.R. measurement system was first run with an unloaded cavity. This was to insure there is no contamination within the cavity. An intensity with a peak of 4375 $a.u.$ and a minimum of -3982 $a.u.$ was observed after a scanning from -1000 $Gauss$ to 9000 $Gauss$. A graphical representation of this signal is shown in Figure 107.

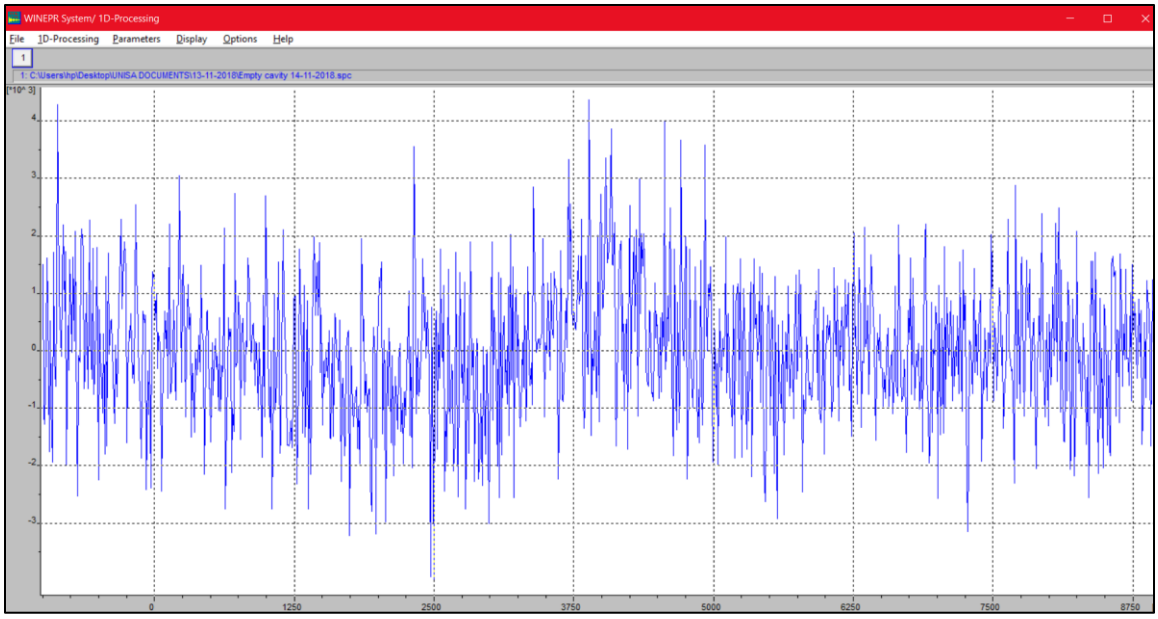

Figure 107: The empty cavity EPR spectrum.

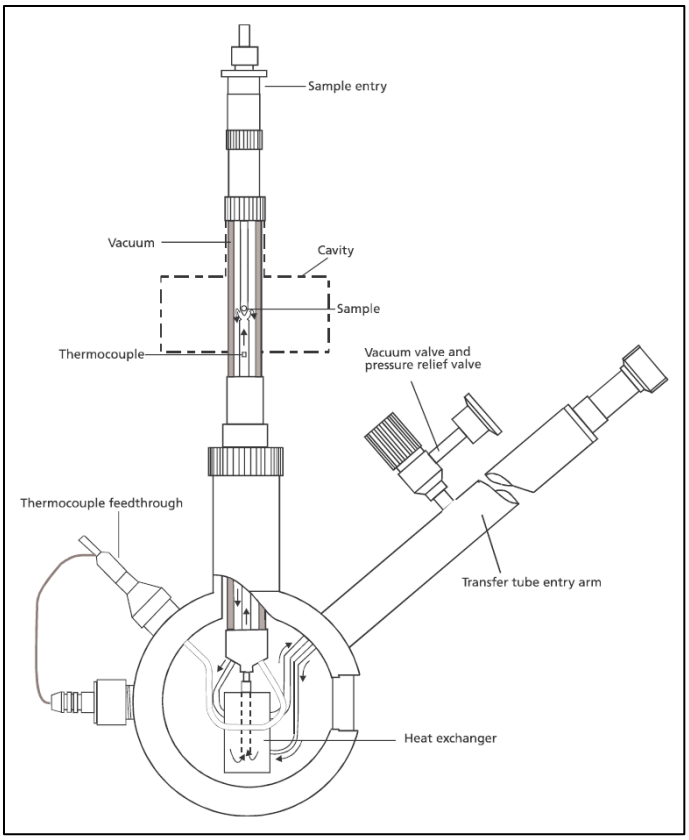

Figure 108: Variable temperature setup to allow sample, thermocouple and heater to be isolated from the environment (Cady 2013).

Figure 109: Ambient temperature controller (MercuryiTC) located at the University of South Africa.

3.3.1 Linewidth computations

The line-width was computed from subtracting crest and trough magnetic field strength value of the electron spin resonance signals detected at different temperatures. This is mathematically expressed as given in Equation 101.

$$H_{PP} = H_1 - H_2 \ldots\ldots\ldots\ldots\ldots\ldots\ldots\ldots\ldots\ldots \quad \text{Equation 101}$$

3.3.2 Safety precautions observed during handling and using of Cryogen.

- It consistently ensured that the position of three valves that were of paramount importance to the safe use of liquid helium were complied with during storage, transfer or shipping of the liquid helium dewar. During storage of the cryogen container the white and yellow handles which correspond to liquid transfer valve and vent valve were placed

in the closed position while the green handle which actuated the isolation valve was placed in the open position. This was done to prevent the formation of hazardous ice plug on the neck of the liquid helium dewars.

- In order to establish a positive flow from the cryogen dewar, the needle of the vacuum-jacketed liquid helium transfer line had to be positioned above the level of liquid helium in the container. Determination of the liquid level was carried out using
- During the handling of the cryogenic liquid personal protective equipment which comprised of, a transparent face screen, protection goggles and hide gauntlets were used.
- Low loss liquid helium transfer lines that had one elbow were used during this experimentation.

The test tubes were handled by means of test tube holder and placed on a test tube rack when not in use. The diagram of both these tools is shown in Figure 110. Cleaning of test tubes before placing in the resonant cavity was done using swabs and isopropyl alcohol. Cleaning of test tubes was done as a means of eliminating contaminates that would give false resonance spectra.

Figure 110: Test tube holder and a test tube rack.

3.3.3 Determination of the magnetization per gram of Bi_2FeMnO_6

A quantum design physical characteristics quantifying system (PPMS) was used to determine the electromagnetic unit per gram for the Bi_2FeMnO_6 bulk sample. This system is illustrated in Figure 111 excluding the cooling mechanism normally located outside the building. During characterization of the emu/g of the sample below room temperature the following safety precautions were observed, the room was well aerated so that as to allow for free circulation of air in case of the spillage or dewar explosion due to expansion or boiling of cryogen. The pressure relief valves and rapture disc on the dewar were ensured to be in the correct position and not obstructed by any obstacle. Metallic objects such as tools and pearls were ensured to be a minimum of 5 m from the dewar due to the intense magnetic fields generated by superconducting magnets.

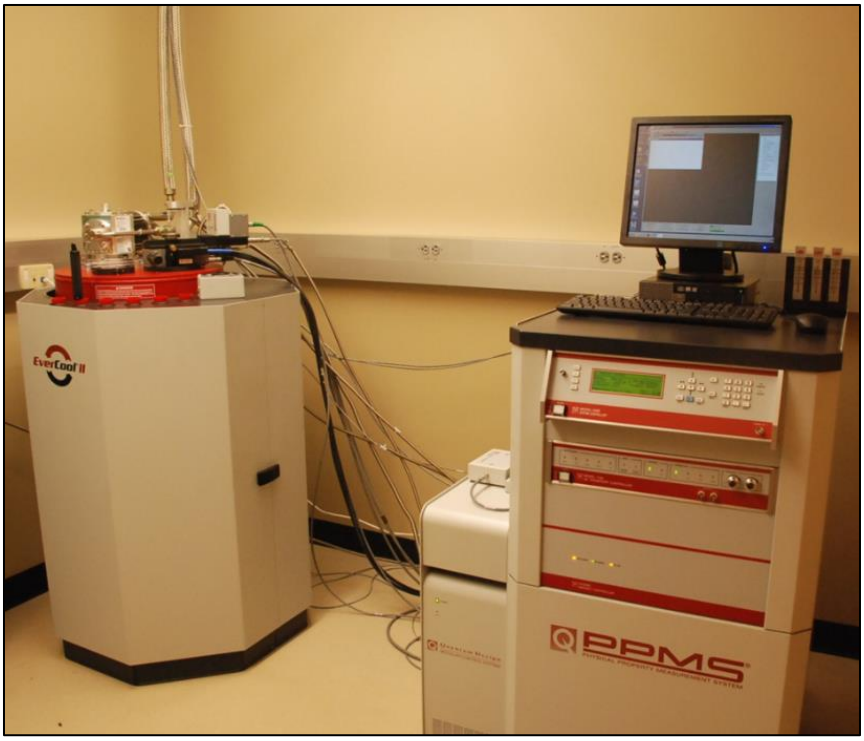

Figure 111: Principal functional parts of the physical property measurement system <https://tulsa.okstate.edu/helmerich/imagingsuite/ppms> [Accessed on 27 Dec 2019].

3.3.4 Geometry and dimensions sample of bulk Bi_2FeMnO_6 sample.

Since the sample vibration amplitude is affected by the shape and magnitude of the sample, these specifications of the Bi_2FeMnO_6 sample had to be limited to allow accurate measurements. Since a bulk sample was being used, An X ACTO Knife was used to precisely cut the bulk sample to smaller size of diameter approximately 3 mm which was less than 6.35 mm which is the limit to allow placing in the sample in the coilset. The resulting minute Bi_2FeMnO_6 sample was handled using forceps as it was moved from point to point for mounting and dismounting purposes. According to (Aris 2009), an increase in the ratio of the length to diameter a given sample causes a decrease in the measured magnetic moment, due to the geometry affecting the oscillation amplitude of the sample. Therefore, cutting of the bulk sample was done in such a manner as to try and make the length and diameter match and also ensure that a cylindrical shape is approximated.

Figure 112: Knife for reducing the size of the bulk sample.

3.3.5 Positioning of the Bi_2FeMnO_6 sample onto the sample holder

In order to maintain the sample as point dipole during characterization the bulk Bi_2FeMnO_6 sample was affixed to the grooved sample holder, ensuring that it is located 35 mm from the

base. This assured that the sample is positioned at the optimum location to the coil-set in such a manner as to exclude the effects of the ends of the sample holder as the sample is vibrated at the center. Affixing of the sample to the quartz paddle sample holder was done by means of kapton tape part number ATK1-050 (Kathleen 2016). The selection of this attachment method was based on the range of temperature over which magnetic measurements were going to be carried out. Alternatively, this could have been carried out using glue or polyethylene terephthalate glycol (PETG). However, kapton tape was determined to be the most appropriate as it had stable characteristics from 5 K to 400 K temperature range. This substantial thermal stability is due the material used for which it is derived kapton polyimide film. The different agents which could be used for attaching the sample are shown in Figure 113.

Figure 113: Different securing agents that can be used in the PPMS (Kathleen 2016).

3.3.6 Regulating temperature of the sample

To vary the heat energy within the sample surroundings in the PPMS probe, the high temperature control mode was used since the temperature was only decreased to 70 K form 300 K using liquid helium as the cryogen. In order to minimize the effects of rapidly varying the temperature of the Bi_2FeMnO_6 if its hysteresis loop is temperature dependent, the set point was reached in the

no overshoot mode, despite the challenge that the steady state temperature takes longer to be achieved (Christina 2009). The level of the cryogen, (helium) was monitored and maintained above 30 percent. This was done so as to prevent contaminants entering the system and blocking the impedance which would create server problems associated with temperature readings (Christina 2009). It is import to note that the obtained magnetic moment can be higher or lower than the actual value depending on the degree of centralization of the sample in the coil-set. Therefore placing of the sample was done in a way that centralizes it to minimize the determined magnetic moment. A PPMS sample insertion tool was used to place a coil-set puck into the sample compartment by attaching it to the mounting ring on the puck. The serial number on the coil-set puck electrical connector was noted and later entered in the program software to provide calibration details were used to configure the detection coils. A typical coil-set puck is illustrated in Figure 114.

Figure 114: Coil-set puck containing a thermometer and detection coils (Aris 2009).

Cleaning of the sample holder was done with reference to the Physical Property Measurement System Hardware Manual Part Number 1070-150. The cleaning solvent used was isopropyl alcohol and a cotton tipper. However, it is important to note that the other cleaning solvent shown in Figure 115 could also be used.

Figure 115: Sample holder cleaning materials and solvents (Kathleen 2016).

Chapter 4

4 First detection of low field microwave absorption in the disordered multiferroic double perovskite $BiFe_{0.5}Mn_{0.5}O_3$

4.1 Introduction

Microwave absorption can be very sensitive to small magnetic fields in magnetic materials. A colossal magnetic field dependence of microwave loss, at very low fields of the order of a few hundred Oe, was firstly reported in the half-metal manganite system by Srinivasu et al. (Srinivasu., et al. 1999), (Vallabhapurapu. and S. E. Lofland 1998). Later on, several groups have observed this low magnetic field dependent microwave absorption in different magnetic systems, such as, Co-based amorphous ribbons (Montanari, et al. 2005), glass-coated magnetic microwires, (Chiriac and C.N. Colesnuic. 2000) (Betancourt, et al. 2005) ferrites, (Montiela, et al. 2004) single and multilayer magnetic films, (Dubowik and F. Stobiecki 2002) (Lee and J. Kim. 2014) iron nano-structures, (F.Felix, et al. 2015) conducting polymers, (Madhumita Bhaumika 2019) iron nanoparticles embedded polyaniline nanofibers, (Bhaumika, Maity and T. S. Mahule 2019) dilute magnetic systems like Co-doped ZnO (Mahule and Vijaya V. Srinivasu 2016) (Srinavasu., Das and D. R. Sahu. 2018) (Onyanchaae, et al. 2020) and in the normal state of $SmFeAsO_{(1-x)}F_x$ ironpnictide superconductors. (Mahule., Srinivasu and Das. 2019)

The low field microwave absorption (LFMA) technique has gained increasing attention, both from the fundamental point of view, as this is a spin contributed phenomenon (the sample is subjected to microwave magnetic field and not the electric field) and for the potential applied physics interest, since the microwave absorption is tunable with very low applied magnetic fields, leading to a field-controlled microwave absorber. However, not all the magnetic systems show the LFMA and the phenomenon itself is not fully understood, yet. It is therefore important to probe LFMA in novel magnetic systems, which can give new insights on this phenomenon.

Besides, while most of the systems studied are magnetically well-ordered systems, the study of a structurally and magnetically disordered or inhomogeneous system with competing spin ordering of more than one spin subsystems is of fundamental interest. This is possibly the case of $BiFe_{0.5}Mn_{0.5}O_3$ (BFMO), (Pernechele, et al. 2013) (Mezzadri, et al. 2016) (Ren 1998) (Belik, Kolodiazhnyi and K. Kosudac 2009) a multiferroic metastable perovskite displaying bulk antiferromagnetism at about room temperature and an externally induced ferroelectric state above liquid nitrogen boiling point. Moreover, BFMO shows the peculiar feature of a spontaneous magnetization reversal (MRV) vs. temperature in the low field regime. This phenomenon was observed also in few other similar perovskites (A. A. Belik and E. Takayama-Muromachi 2008) (Ren 1998) and their origin are still debated. On the basis of the original hypothesis, the phenomenon is ascribed to the competition between Dzyaloshinskii-Moriya (DM) interaction, arising from a canted antiferromagnetic long-range ordering and single ion anisotropy (SIA). A complementary approach describes the MRV in terms of a competition between magnetically independent subsystems (Fe- and Mn- rich regions), whose presence is determined by the intrinsic inhomogeneity and disorder at the B site between the metal cations due to the high-pressure high-temperature (HP/PT) synthesis conditions. These local-order weak competitions and/or eventually frustration occur at low temperature and they are typically very sensitive to an external magnetic field, usually appearing only in the low field regime. Such a property is therefore particularly suitable for the LFMA investigation.

4.2 Results

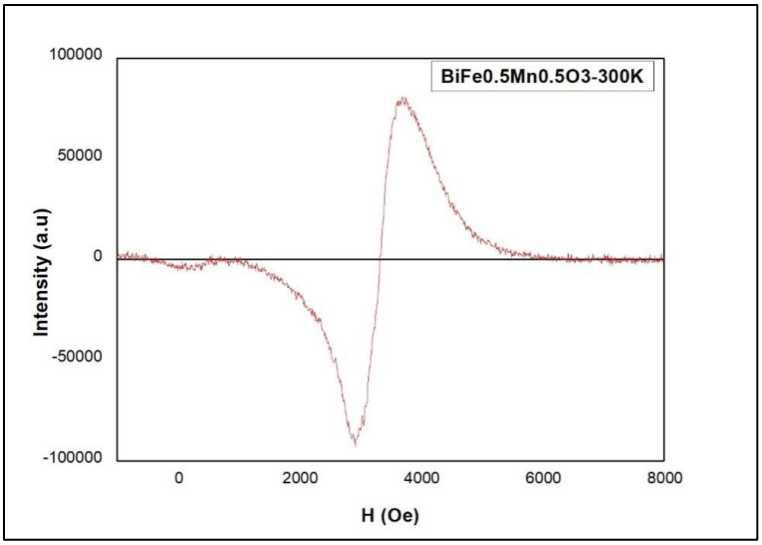

Figure 116: LFMA signal along with the ESR signal for the bulk BFMO sample measured at 300K. Note the phase of LFMA is opposite to that of ESR signal.

In Figure 116 we report the first observation of LFMA signal in a disordered BFMO polycrystalline sample in the very low field regime around 0 Oe. The LFMA phase, opposite to the regular ESR signal (with larger intensity at higher field), shows a minimum near zero. It is important to notice that LFMA usually occurs in small systems like micron, sub-micron powders and nano-scale thin films. For example, LFMA signal, first observed in micron size powders manganites, vanishes in the corresponding bulk form (Srinivasu., et al. 1999), (Vallabhapurapu. and S. E. Lofland 1998). Remarkably, it was possible to observe LFMA directly in the as-grown BFMO bulk pellet. The evolution of LFMA as a function of temperature is shown in Figure 117.

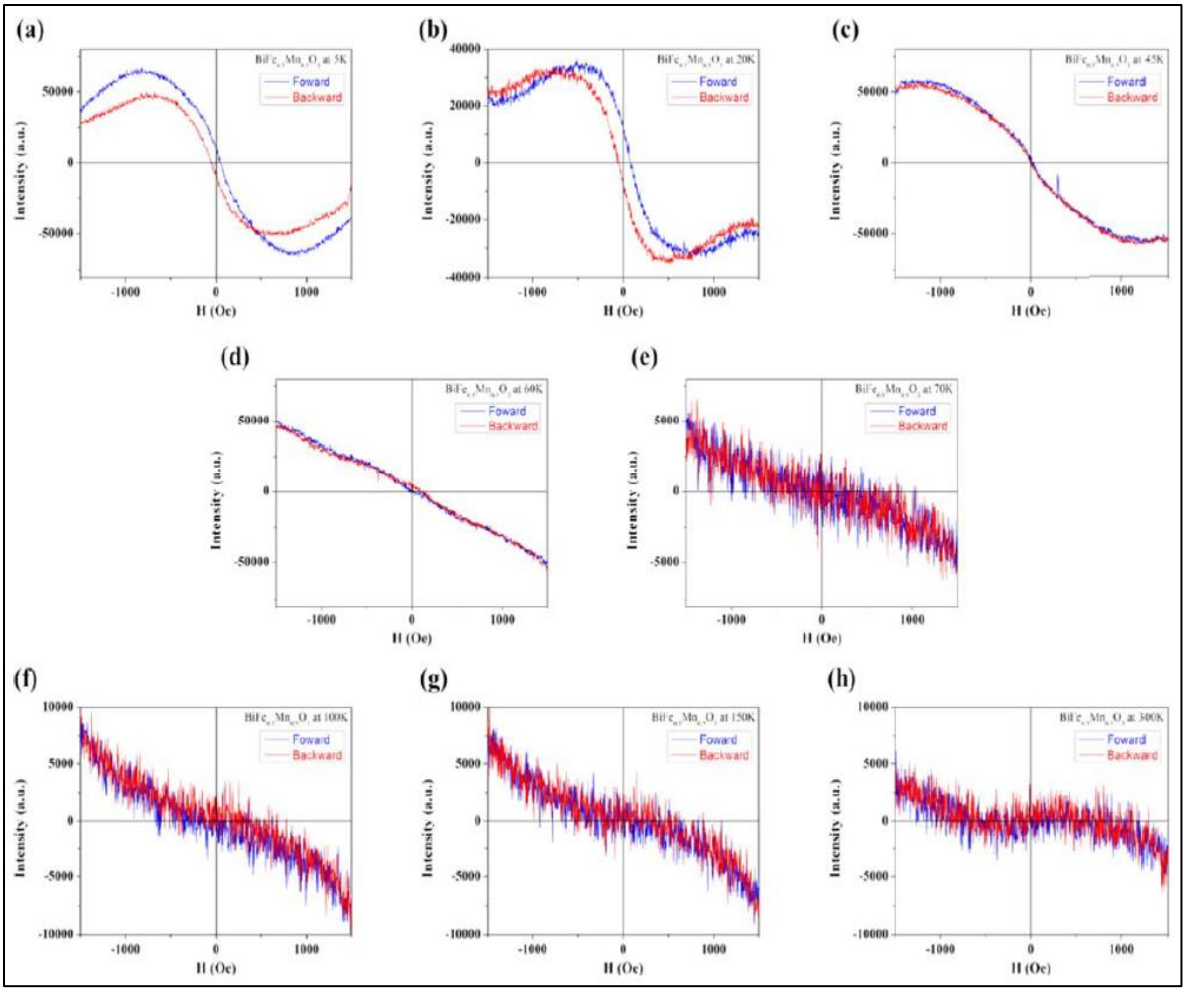

Figure 117: Evolution of LFMA signal with different temperatures from 5K to 300K of BFMO pellet sample. Noteworthy, LFMA hysteresis vanishes at T≥45K.

The most important features are:

i. LFMA highlights hysteresis at 5K and 20K (Figure 117 (a) and (b), respectively). At 45K (See Figure 117 (c)), the hysteresis collapses. From 45K to 300K (See Figure 117 (d) – (h)), LFMA is non-hysteretic: though the magnetization shows a substantial hysteresis as shown in Figure 119. In comparison, a characteristic hysteresis data for LFMA and M-H loop, both collected at 70K are reported, for example, in Figure 120 (a) and (b).

This last observation depicts an intriguing scenario: LFMA hysteresis disappears at lower temperature, while a significant weak ferromagnetic hysteresis is retained in the M-H loop at higher temperatures.

ii. Above 45K, the LFMA shows different line shapes. It is well established that LFMA is observed only when the sample is placed in H_{mw} maximum position in the cavity (Vallabhapurapu. and S. E. Lofland 1998), (Srinivasu., et al. 1999), indicating that LFMA is originated by the spin system of the sample.

It is of fundamental importance to place BFMO sample in the cavity Hmw maximum position to probe the spin system through LFMA. LFMA hysteresis vanishes above 45Kand the line shape is different beyond 45 K, suggesting that LFMA is originated from two different spin subsystems in ranges of 5–45K and 45–300 K, respectively.

4.3 Discussions

Different spin sub-systems working in different ranges of temperature are well established in this BFMO samples (Madhumita Bhaumika 2019) (Bhaumika, Maity and T. S. Mahule 2019). For example, it was shown in Fig. 10a) of (Madhumita Bhaumika 2019), that the $5K$ M-H loop clearly shows symmetric kinks. This was attributed to ‘soft’ and ’hard’ magnetic components. Furthermore, spin canting is expected in this sample. Canted spin systems can be influenced by very low fields (Lin Hao 2018)which can aid the low field tenability or dependence of microwave absorption. However, there can be pinning defects, due to inherent disorder and inhomogeneity present in the sample, which can pin the canted spin domains and hinder their rotation with applied fields, leading to possible hysteresis in LFMA. Otherwise, the same hysteresis can arise from a weak interaction (as for instance a second order competition) acting in locking the canted spin rotation. This is what exactly happens in BFMO when the competition between different clusters (i.e., Fe-rich, and Mn-rich) is settled, precisely in the same thermal region in which the LFMA hysteretic behaviour is detected. This is supported also by linewidth analysis of ESR signal: it increased substantially around 45K as the sample was cooled. Increase in ESR linewidths can be attributed to defects and inhomogeneities.

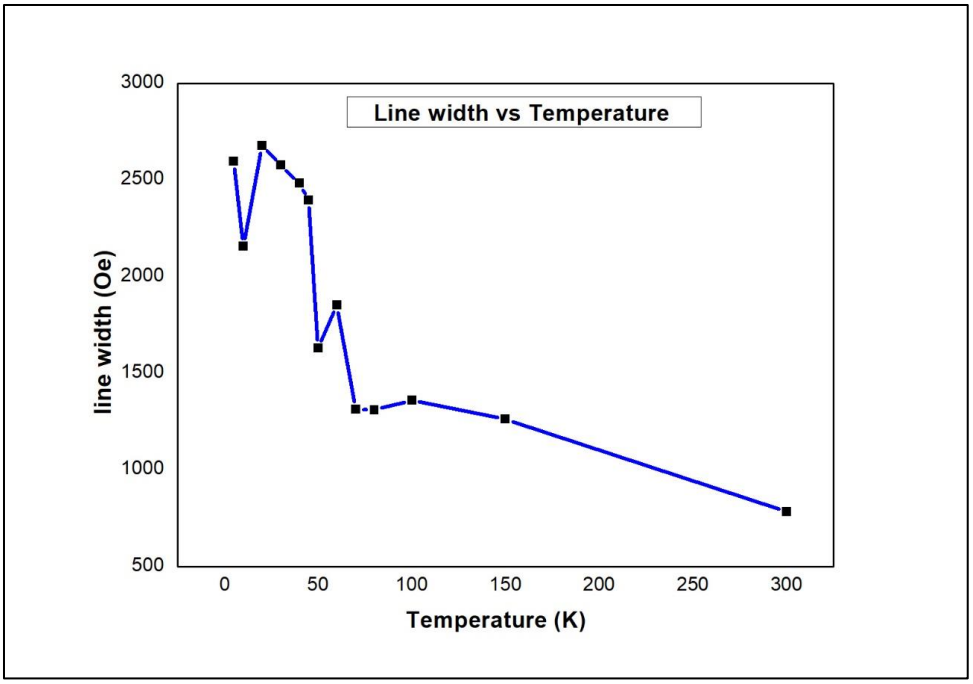

Figure 118: ESR linewidth vs. temperature for BFMO.

Beyond 45 K, the linewidth decreased as shown in Figure 118. Thus, thermal energy overcomes the pinning above 45 K. Both the ESR linewidths fall and the LFMA hysteresis collapse at 45 K. At the same time, the M-H loop hysteresis persists in the range from 5Kto 300 K. Above 45 K, the LFMA hysteresis vanishes and, moreover, the line shape changes completely, indicating that LFMA in the 45 to 300Krange presents different functional forms of dependence to the applied field. These findings confirm a lack of correlation and therefore a possible different origin for the two mentioned hysteretic behaviour. Nevertheless, the correlation can be found by comparing LFMA hysteresis with another phenomenon taking place in BFMO: the spontaneous MRV. It is interesting to notice that the LFMA hysteresis vanishes in the same thermal range in which the second derivative of the ZFC susceptibility reaches the maximum (Figure 121 elaborated from ZFC collected at 100 Oe during the study reported in (Delmonte, et al. 2015) and plotted as inset). This threshold represents the onset of a gradual decay of the ‘second-order’ interaction responsible for the MRV observed in BFMO. LFMA drastically changes both hysteresis and line-shape around the same critical temperature where the second derivative of the ZFC magnetization shows the maximum. Therefore, LFMA seems to be able to probe the incoming interaction between the two independent magnetic subsystems responsible for MRV, thus

sustaining the hypothesis proposed in the previous works (Madhumita Bhaumika 2019) (Bhaumika, Maity and T. S. Mahule 2019) (Pernechele, et al. 2013) (Francesco Mezzadri 2015).

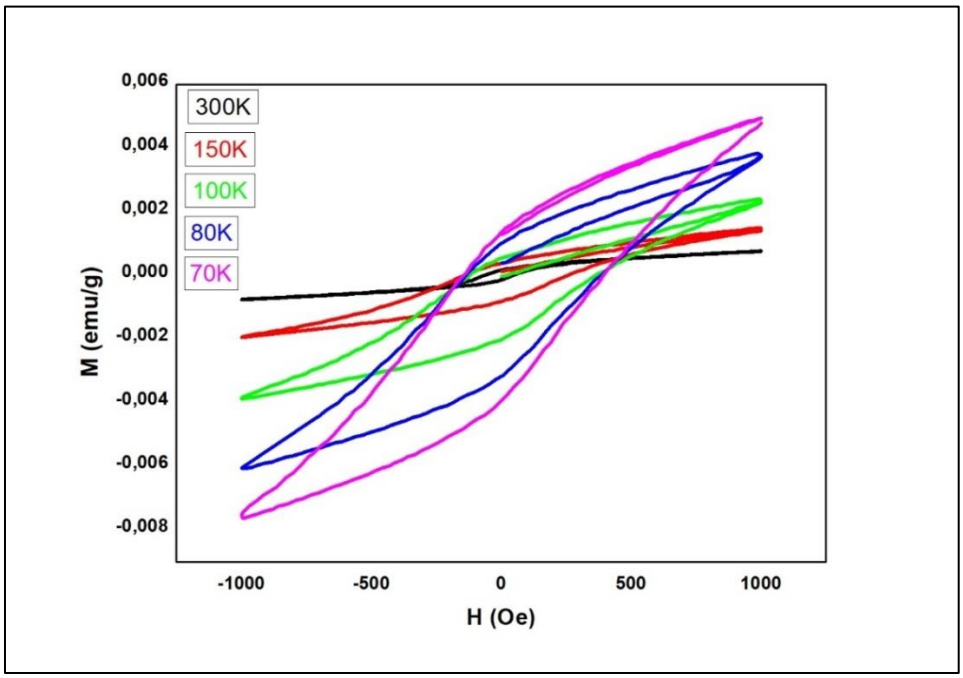

Figure 119: Low field M-H hysteresis data for BFMO pellet.

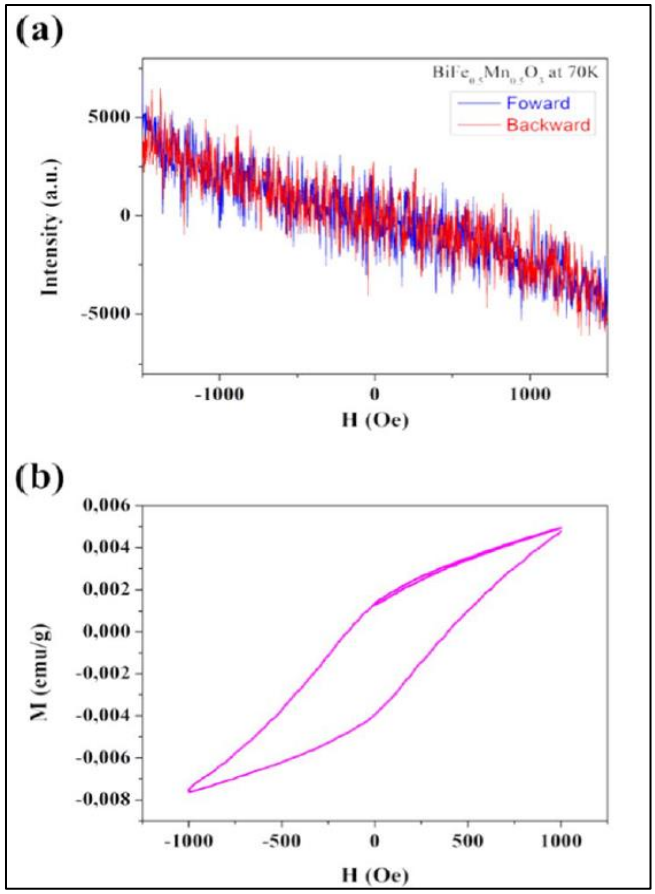

Figure 120: 4 - 70K hysteresis data of LFMA and M-H loops for BFMO.

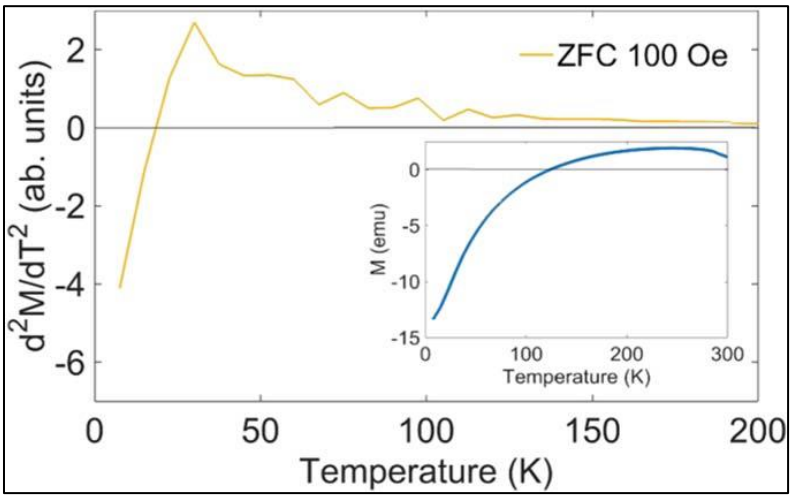

Figure 121: Second Derivative of the ZFC magnetic susceptibility of BFMO collected at 100 Oe.

Chapter 5

5 Conclusion

5.1 Summary

LFMA was reported for the first time in the disordered and magnetically exotic bulk BFMO, obtained by HP/HT synthesis. This is a new functionality of this very exotic and intriguing material. This system is known to be multiferroic at least up to the liquid nitrogen boiling point and to display spontaneous reversal magnetization versus temperature arising from the magnetic a very weak competition between different spin subsystems characterized weak ferromagnetic interactions determined by the canted antiferromagnetic structure. The LFMA hysteresis properties are totally different from that of magnetization hysteresis. LFMA hysteresis evidence two regimes: (i) below $45K$, LFMA has a measurable hysteresis while; (ii) from $45K$, hysteresis collapses and completely vanishes up to $300K$. Moreover, the line shape of LFMA changes completely in these two temperature ranges. This is indicative of two different functional dependence of LFMA from applied low field and the related spin subsystems. The behaviour is proved with an ESR linewidth observation that started a decreasing trend above 45 K.

On the fundamental side, LFMA data clearly establish the existence of two spin subsystems. Hysteresis in the LFMAoverlaps to the magnetic regime of BFMO in which the negative response under positive field (magnetization reversal) is stabilized, thus in the region in which the weak competition of the different subsystems is maximum. However, the magnetization and LFMA data depends on these two competing subsystems differently. The question why LFMA and magnetization responses depend on the two spin subsystems, opens to theoretical debate and to further experimental investigations.

On the applied science aspect, the fact that LFMA occurs in the bulk form of materials, is a new and important feature by itself, as all the previous LFMA studies were reported on ‘small’ systems (e.g. micron size powders, thin films, and nano-systems). Indeed, first observation of

low field tuneable microwave absorption in bulk materials means that it is possible to obtain such a property without going through complex processes usually needed to obtain low dimensional or nanoscaled systems.

5.2 Future Studies

5.2.1 Determination of complex dielectric permittivity and magnetic permeability characteristics of $BiFe_{0.5}Mn_{0.5}O_3$

By the use of electron spin resonance it was possible to establish that $BiFe_{(1-x)}Mn_xO_3$ is a microwave absorber. Absorption under these conditions can be linked to magnetic reordering or electron spin rearrangement. Its applicability within microwave absorber classes can further be comprehended by also probing the microwave signal attenuation to signals of different frequency at varying temperatures. This will be done by analyzing the relative complex dielectric permittivity and complex magnetic permeability and their associated tangents. The real part of these signals will be a pointer as to how excellent $BiFe_{(1-x)}Mn_xO_3$ stores electromagnetic energy while the imaginary part elaborates on its scattering ability (Cui., et al. 2019). It is anticipated that study of the sample over a range of signal frequencies will allow probe into potential use of $BiFe_{(1-x)}Mn_xO_3$ as a wide band microwave absorber. Wide band absorbers allow for absorption of signals of multiple frequencies thereby allowing application in stealth technology and multi-frequency smart sensors.

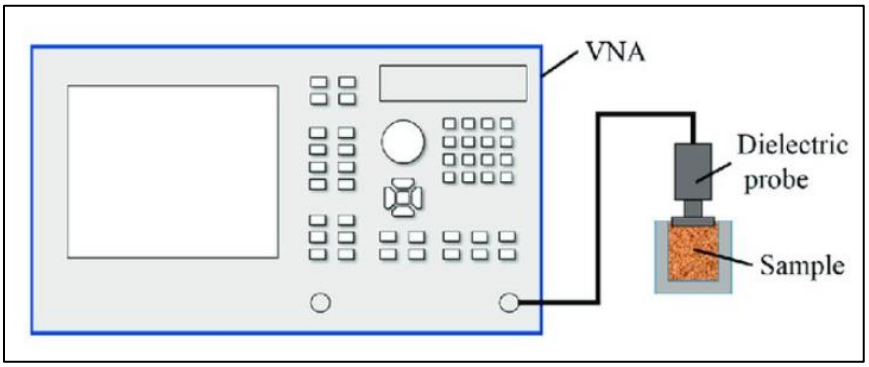

Figure 122: Layout for relative permittivity and permeability (Ellison., et al. 2017).

These characteristics will be capture by employing a vector network analyzer, the layout is shown below (Figure 122). From the computed complex permittivity and permeability the dissipation due to backscattering will be calculated from the input and space sum of capacitive, inductive and resistive impedances.

$$Z_0 = \sqrt{\frac{\mu_0}{\varepsilon_0}} \quad \text{Equation 102}$$

$$Z_{in} = Z_0 \sqrt{\frac{\mu_r}{\varepsilon_r}} \tanh\left(j \frac{2\pi f d}{c} \sqrt{\mu_r \varepsilon_r}\right) \quad \text{Equation 103}$$

$$R_L = 20 \log\left(\frac{Z_{in} - Z_0}{Z_{in} + Z_0}\right) \quad \text{Equation 104}$$

5.2.1.1 Possible application in aerospace industry

The measurement of microwave attenuation depending on the ambient temperature is crucial in the aerospace industry. This is because the flight attitude drastically alters the environment thermodynamic energy in which the airframe is subjected to thereby adjusting the absorption characteristics of $BiFe_{(1-x)}Mn_xO_3$ if it is to be employed as a sensor or absorber. For airframe bodies which are invisible on the air traffic radar, a principle of primary radar, the microwave absorber has to be able to absorb microwave without scattering. Conventionally in secondary radar, transponder interrogator, by means of electronic pulses enable the aircraft ATC transponder to furnish the air traffic control radar with flight level and aircraft identification. The F-22 Raptor and B-2 Bomber are typical stealth jets which are microwave absorbing.

Figure 123: F-22 Raptor is microwave absorbent and thereby reduces its radar cross section considerably (USAAF. 2015).

Figure 124: B-2 Bomber is microwave absorbing and primary radar invisible (Okonkwo and Smith. 2015).

5.2.2 Magnetoimpedence measurements using impedance analyzer

Magnetic sensors are meant to sense a magnetic field. They are generally magnetoresistive however under certain circumstances magnetoimpedance transducers can be employed (Coey

2009). The magnetoimpedance of double perovskite $BiFe_{0.5}Mn_{0.5}O_3$ when determined will aid in distinguishing the ability of this material being used as a magnetic sensor. It is import that analysis of this property be carried out over a wide range of frequency. For this purpose an impedance analyzer (Figure 125) will be used and the layout in use is shown in Figure 126. For the application of $BiFe_{0.5}Mn_{0.5}O_3$ as a magnetic sensor, it has to be a have the applied alternating magnetic field being several times higher as compared the magnetic field that is desired to be determined.

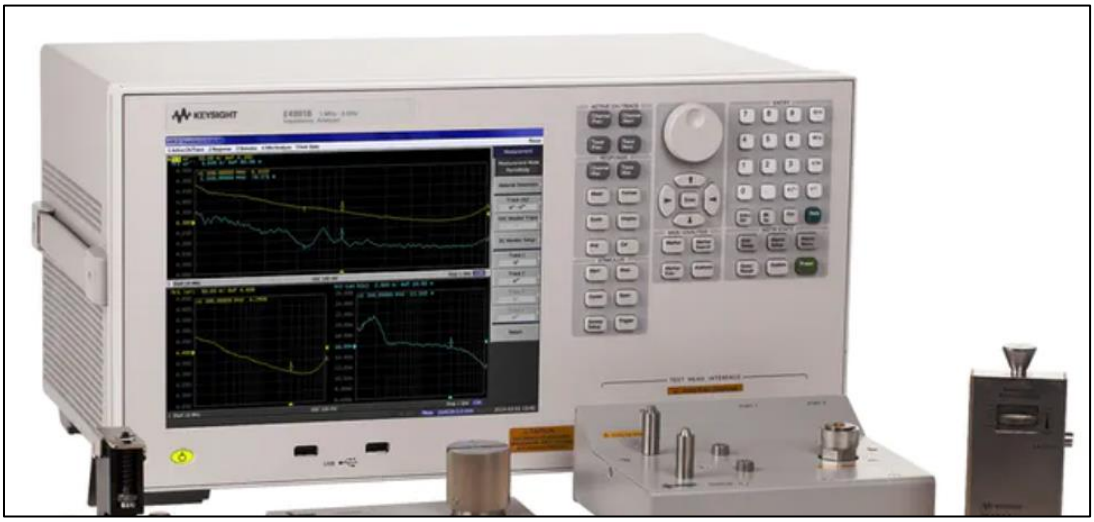

Figure 125: Impedance analyzer by keysight technologies (Technologies 2000).

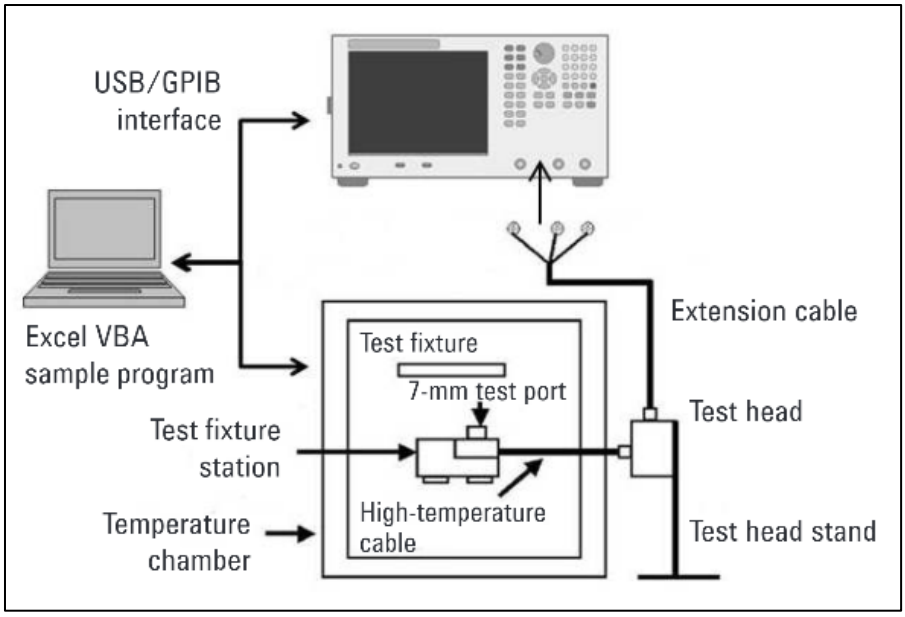

Figure 126: Layout for temperature sensitive measurements (Technologies 2000).

5.2.3 Domain wall analysis of $BiFe_{0.5}Mn_{0.5}O_3$ by scanning electron microscope

The remaining magnetic flux in the $BiFe_{(1-x)}Mn_xO_3$ system when magnetizing force- was removed as detected by PPMS can be further understood by studying its domain wall characteristics. Domain walls are considered as interfacial defects as these introduce magnetic domains of different orientation and points of resistance during magnetization and demagnetization. This is because in the process of magnetizing a material's domain walls are adjusted sometimes to a point of extinction as the administered magnetic field is escalated (Callister and Rethwisch. 2008). Such a hysteresis loop is given in Figure 119.

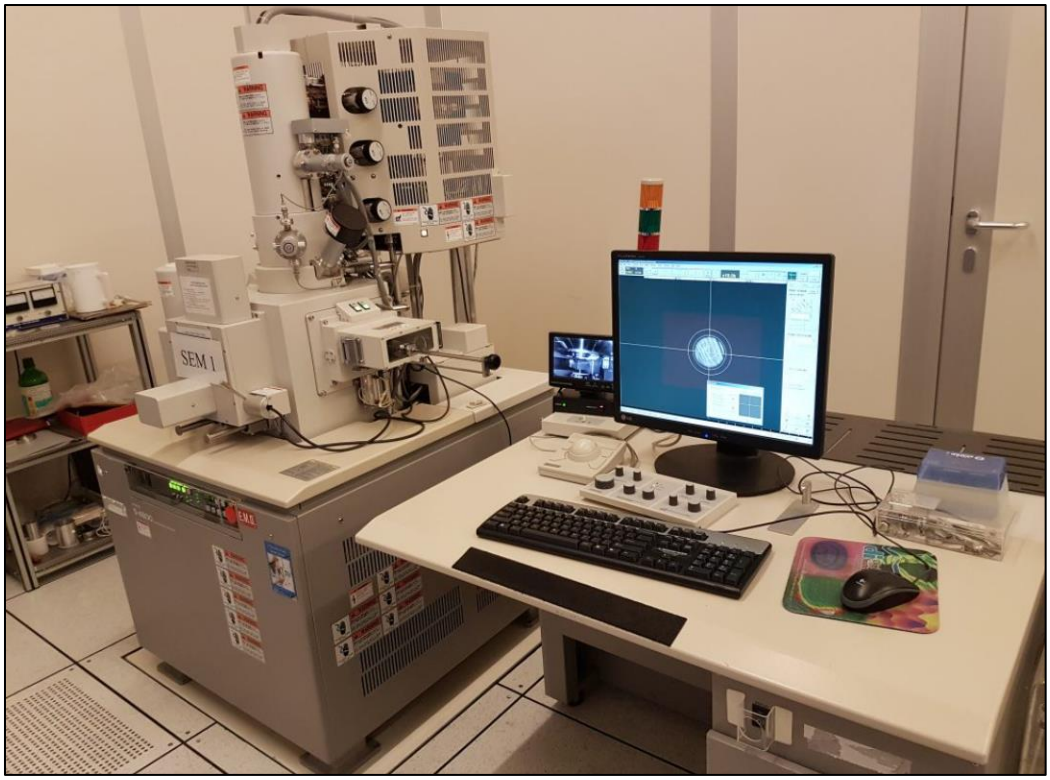

Figure 127: High resolution scanning electron microscope to be used for $BiFe_{0.5}Mn_{0.5}O_3$ domain wall analysis (Sara., Moshe and Wolfson. 2003).

5.2.4 Doping of $BiFe_{0.5}Mn_{0.5}O_3$ with $ZnCr_2O_4$ for magnetic response enhancement

As a means of improving the magnetic field response of $BiFe_{(1-x)}Mn_xO_3$ at ambient room temperature, a chromium spinel ferrite zincochromite, $ZnCr_2O_4$ will be integrated into the $BiFe_{(1-x)}Mn_xO_3$ system to form a nanocomposite of $(BiFe_{(1-x)}Mn_xO_3)$-($ZnCr_2O_4$). Solid-state reaction technique will be used for the synthesis of this system. This will involve crushing bulk $BiFe_{0.5}Mn_{0.5}O_3$ and $ZnCr_2O_4$, then heating to a given temperature to allow the different compounds to inter-diffuse. Despite it being low-cost and utilizing elementary equipment it main challenges will be the variance of particle magnitude and geometry, the deviation of desired chemical composition and failure to yield similar results (Aimar., et al. 2010). In simple perovskite $BiFeO_3$, $CoFe_2O_4$ as the doping agent resulted in a significantly enhanced ferromagnetic and ferroelectric system, $BiFeO_3$- $CoFe_2O_4$ (Dong., et al. 2016). The time solid state reactants are exposed to heating determines the ratio of phase change of the materials as

shown in Figure 128. Therefore the duration of heating will be dependent on the sample phase homogeneity.

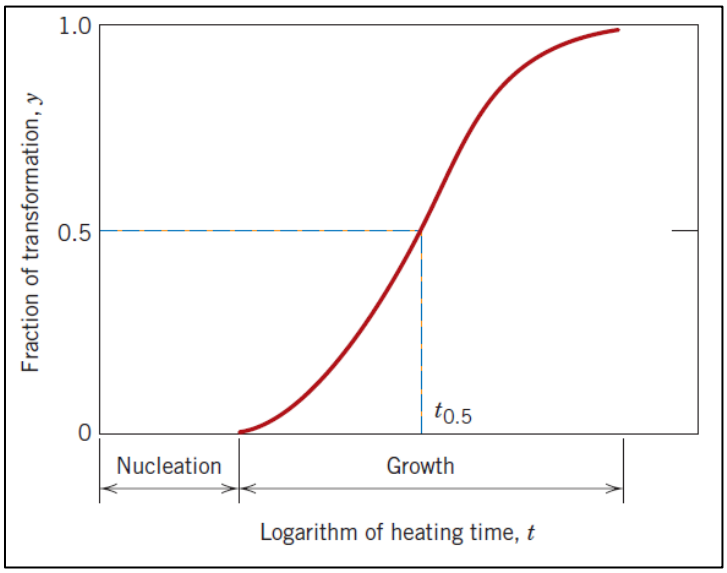

Figure 128: Solid state reaction phase transformation as a function of $\log[t/(s)]$ (Callister and Rethwisch. 2008).

6 Bibliography

1. A. A. Belik and E. Takayama-Muromachi. "Synthesis and properties of oxygen non-stoichiometric BiMnO3." *Journal of Physics: Condensed Matter* 20 (2008): 025211.
2. Abduleziz Ablat., Emin Muhemmed., Cheng Si., Jiaou Wang., Haijie Qian , R. Wu., N. Zhang., R. Wu., and K. Ibrahim. "Electronic Structure of BiFe1−xMnxO3 Thin Films Investigated by X-Ray Absorption Spectroscopy." *Journal of Nanomaterials* (Hindawi Publishing Corporation), 2012: 123438.
3. Aimar., P., P. M. Ajayan., G. Alberti., V. Arcella, and and M. Avataneo. *Basic Aspects of Membrane Science and Engineering.* Amsterdam: Elsevier Science, 2010.
4. Aken, B. B. Van, T. T.M. Palstra, and and N. A. Spaldin. A. Filippetti. "The origin of ferroelectricity in magnetoelectric YMnO3." *Nature Materials.* 3 (2004): 164-170.
5. Anisimov, V. I., and and O. K. Andersen. J. Zaane. "Band theory and Mott insulators: Hubbard U instead of Stoner." *Phys. Rev. B* 44 (1991): 943.
6. Anjum, G., R. Kumar, S. Mollah, P. Thakur, and and K. H. Chae. S. Gautam. "NEXAFS studies of La0.8Bi0.2Fe1−xMnxO3($0.0 \leq x \leq 0.4$) multiferroic system using x-ray absorption spectroscopy." *Journal of Physics D* 44 (2011): 075403.
7. Aris. *New Jersey Institute of Technology.* Febraury 14, 2009. https://web.njit.edu/~tyson/PPMS_Documents/PPMS_Manual/1096-100%20Rev.%20A3%20VSM.pdf (accessed August 14, 2020).
8. Atou, T., H. Chiba, K. Ohoyama, and Y. Yamaguchi and Y. Syono. "Structure Determination of Ferromagnetic Perovskite BiMnO3." *Journal of Solid State Chemistry* 145 (1999): 639-642.
9. Ayscough, Peter. *Electron Spin Resonance In Chemistry.* USA.: Barnes and Noble, 1967.
10. Azuma, M., H. Kanda, A. A. Belik, and Y. Shimakawa and M. Takano. "Magnetic and structural properties of BiFe1−xMnxO3." *Journal of Magnetism and Magnetic Materials.* 310 (2007): 1177–1179.

11. B.A.A. Elemans, B. Van Laar, K.R. Van Der Veen and B.O. Loopstra. "The crystallographic and magnetic structures of La1−xBaxMn1−xMexO3 (Me = Mn or Ti)." *Journal of Solid State Chemistry* 3 (1971): 238-242.

12. Belik, A. A., T. Kolodiazhnyi, and and E. T. Muromachi. K. Kosudac. "Synthesis and properties of oxygen non-stoichiometric BiMnO3." *Jounal of materials chemistry.* 19 (2009): 1593.

13. Belik, A.A. "Magnetic properties of solid solutions between BiCrO3 and BiGaO3 with perovskite structures." *Science and Technology of Advanced Materials*, 2015: 026003.

14. Belik., A. A. "Origin of Magnetization Reversal and Exchange Bias Phenomena in Solid Solutions of BiFeO3–BiMnO3: Intrinsic or Extrinsic?" *Inorganic Chemistry* 52 (2013): 2015-2021.

15. Ben Abdelkhalek, S., N. Kallel, S. Kallel, T. Guizouarn, and O. and Oumezzine, M. J. Penna. "Combined magnetic, electric, ferroelectric and magnetoelectric characterization of novel multiferroic perovskites obtained by high pressure/temperature synthesis." *Journal of Superconductivity and Novel Magnetism* 26 (2013): 3171 − 3180.

16. Benitez, M. J., O. Petracic, H. Tüysüz, and and H. Zabel. F. Schüth. "Fingerprinting the magnetic behavior of antiferromagnetic nanostructures using remanent magnetization curves." *Phys. Rev. B* 83 (2011): 134424.

17. Betancourt, I., R. Zamorano, G. Alvarez, and and R. Valenzuela. H. Montiel. "Correlations between low-field microwave absorption and magnetoimpedance in Co-based amorphous ribbons." *Applied Physics Letters* 86 (2005): 072503.

18. Bhaumika, M., A. Maity, and and V.V. Srinivasua. T. S. Mahule. "Low field microwave absorption in rion nanoparticles embedded polyaniline nanofiber composites." *Synthetic Metals journal*, 2019: 63-69.

19. Bodker, F., M. Hansen, C. B. Koch, and and S. Morup. K. Lefmann. "Magnetic properties of hematite nanoparticles." *Phys. Rev. B* 61 (2000): 6826.

20. Borisov, P., and Kleemann, W. "Exchange bias and ferromagnetic coercivity in heterostructures with antiferromagnetic Cr2O3." *Journal of Applied Physics.* 110 (2011): 3.

21. C. Beekman, A. A. Reijnders, Y. S. Oh, S.W. Cheong, and K. S. Burch. "Raman study of the phonon symmetries in BiFeO 3 single crystals." *Physics revision B* 86 (2012): 020403.

22. C. Ederer and N. A. Spaldin. "Weak ferromagnetism and magnetoelectric coupling in bismuth ferrite." *Physics revision B* 71 (2005): 060401R.

23. C. Ponraja, G. Vinitha and Joseph Daniel. "A review on the visible light active BiFeO3nanostructures as suitablephotocatalyst in the degradation of different textile dyes." *Environmental Nanotechnology, Monitoring & Management* 7 (2017): 110-120.

24. Cabassi, R., F. Bolzoni, E. Gilioli, F. Bissoli, and A., and Gauzzi, A. Prodi. "Jahn-Teller-induced crossover of the paramagnetic response in the singly valent." *Condensed matter physics* 81 (2010): 214412.

25. Cady, Sarah. "Elexys E580 EPR Training Manual." *IOWA State University.* 07 30, 2013. https://www.cif.iastate.edu/nmr/epr (accessed December 29, 2019).

26. Callister, W. D., and and D. G. Rethwisch. *Fundamentals of Materials Science and Engineering.* United States: Wiley, 2008.

27. Catalan, G., J. Seidel, and and J. Scott. R. Ramesh. "Domain wall nanoelectronics." *Reviews of mordern physics.* 84 (2012): 119 - 156.

28. Cazayous., M. "Possible Observation of Cycloidal Electromagnons in BiFeO3." *Physics Revision Letter*, 2008: 037601.

29. Chen, W. T., T. Saito, N. Hayashi, and and Y. Shimakawa. M. Takano. "Ligand-hole localization in oxides with unusual valence Fe." *Scientific Reports* 2 (2012): 449.

30. Chi, Z. H., H. Yang, S. M. Feng, F. Y. Li, and and C. Q. Jin. R. C. Yu. "Room-temperature ferroelectric polarization in multiferroic BiMnO3." *Journal of Magnetism and Magnetic Materials.* 310 (2007): 358–360.

31. Chiriac, H., and and T.A. Ovari. C.N. Colesnuic. "FMR investigation of the nanocrystalline FeCuNbSiB glass-covered wires." *J. Magn. Magn. Mater.* 215216 (2000): 407-409.

32. Chou, C. C., et al. "Multiple magnetic transitions in multiferroic BiMnO3." *Physics Revision B.* 80 (2009): 184426.

33. Christina. "New Jersey Institute of Technology Education." *Physical property measurement system.* Febraury 18, 2009. https://web.njit.edu/~tyson/PPMS_Documents/PPMS_Manual/1070-150%20Rev.%20B5%20PQ%20%20PPMS%20Hardware.pdf (accessed August 15, 2020).

34. Christman, J. R. *Fundamentals of Solid State Physics.* New York: John Wiley and Sons Ltd, 1988.

35. Chu., K. R. *National Tsing Hua University Continuing Education.* December 18, 2019. www.phys.nthu.edu.tw › ~thschang › notes › MWPA6 (accessed December 18, 2019).

36. Cianchi, L., F. Del Giallo, G. Spina, and and A. Caneschi. W. Reiff. "Spin dynamics study of magnetic molecular clusters by means of Mössbauer spectroscopy." *Phys. Rev. B* 65 (2002): 064415.

37. Coey, J. M. D. *Magnetism and magnetic materials.* U.S.A.: Cambridge University Press, 2009.

38. Cui., G., et al. "Excellent Microwave Absorption Properties Derived from the Synthesis of Hollow Fe3o4@Reduced Graphite Oxide (RGO) Nanocomposites." *Nanomaterials.*, 2019: 141.

39. D. Lebeugle, D. Colson, A. Forget, M. Viret, A. M. Bataille, and A. Gukasov. "Electric-Field-Induced Spin Flop in BFO Single Crystals at Room Temperature." *Physics revision letter.* 100 (2008): 227602.

40. Das, Prof. Ranjan. *Mod 01 Lec 24 Spin relaxation and Bloch Equations.* April 16, 2015. (accessed 08 10, 2019).

41. Das, R. *Nptelhrd.* April 16, 2015. https://www.youtube.com/watch?v=K_my_6jR8Ck (accessed Decemeber 2019, 24).

42. Das., R. *Nptelhrd.* January 14, 2019. https://www.youtube.com/watch?v=yUU8Vavsr88 (accessed January 14, 2019).

43. Dasari, N., P. Mandal, and and N. S. Vidhyadhiraja. A. Sundaresan. "Weak ferromagnetism and magnetization reversal in YFe1− xCrxO3." *Europhys. Lett.* 99 (2012): 17008.

44. Delmonte, D., et al. "Field effects on spontaneous magnetization reversal of bulk BiFe0.5Mn0.5O3, an effective strategy for the study of magnetic disordered systems." *J. Phys.: Condens. Matter.* 27 (2015): 286002.

45. Dong., G., G. Tan., Y. Luo., T. Wang., H. Ren, and and A. Xia. "The phase transition and superior multiferroic properties of (Mn, Co) co-doped BiFeO3/CoFe2O4 double-layer films." *Journal of Alloys and Compounds*, 2016: 419-423.

46. Dresselhaus., M. S. *SOLID STATE PHYSICS.* Decemeber 14, 2019. web.mit.edu › www › 6.732-pt3.pdf (accessed Decemeber 14 , 2019).

47. Du, Y., Z. X. Cheng, S. X. Dou, X. L. Wang, and and H. Kimura. H. Y. Zhao. "Magnetic properties of Bi2FeMnO6: A multiferroic material with double-perovskite structure." *Appl. Phys. Letters* 97 (2010): 122502.

48. Dubowik, J., and and I. Gościańska. F. Stobiecki. "Effect of GMR and magnetization reversal on microwave absorption." *Czechoslovak Journal of Physics* 52 (2002): 227.

49. E.M. Choi, T. Fix, A. Kursumovic, C. J. Kinane, D. Arena, S.L. Sahonta, Z. Bi, J. Xiong L. Yan, J. S. Lee, H. Wang, S. Langridge, Y. M. Kim A. Y. Borisevich, I. MacLaren, Q. M. Ramasse, M. G. Blamire, Q. Jia and J. L. MacManus-Driscoll. "oom temperature ferrimagnetism and ferroelectricity in strained, thin films of BiFe0.5Mn0.5O3." *Advanced Functional Materials.* 24 (2014): 7478-7487.

50. Eerenstein, W., F. D. Morrison, J. Dho, M. G. Blamire, and and N. D. Mathur. J. F. Scott. "Comment on "Epitaxial BiFeO3 multiferroic thin film heterostructures"." *American Association for the advancement of science* 307 (2005): 1203.

51. Ellison., C., M. S. McKeown., S. Trabelsi, and and Dorin Boldor. "Dielectric Properties of Biomass/Biochar Mixtures at Microwave Frequencies." *Energies*, 2017: 502.

52. F. Niu, Y. Huang, x. Sun, l. Qin, T. Gao, N. Zhang, Z. Chen and D. Chen. "Synthesis of Pt/BiFeO3 heterostructured photocatalysts forhighly efficient visible-light Photocatalytic performances." *Solar Energy Materials and Solar Cells* 143 (2015): 386–396.

53. F.Felix, J., L. C. Figueiredo, J. B. S. Mendes, and and C. I. L. de.Araujo. P. C. Morais. "Low-field microwave absorption and magnetoresistance in iron nanostructures grown by electrodeposition on n-type lightly doped silicon substrates." *Journal of Magnetism and Magnetic Materials* 395 (2015): 130-133.

54. Feng, Hong-Jian. "The reversal of magnetization driven by the Dzyaloshinskii–Moriya interaction in Bi2FeMnO6." *Journal of Magnetism and Magnetic Materials* 324 (2012): 178–182.

55. Feng., H. J. "Magnetism and electronic properties of BiFeO3 under lower pressure." *Journal of Magnetism and Magnetic Materials.* 322 (2010): 1765.

56. Fengzhen H., Xiaomei L., Weiwei L. Yi K., and Junting Z. "Thickness-dependent structural and magnetic properties of BiFeO3 films prepared by metal organic decomposition method." *Appplied Letter of Physics* 97 (2010): 222901.

57. Fiebig, Manfred. "Revival of the magnetoelectric effect." *Journal of Physics D: Applied Physics* 38 (2005): 8.

58. Francesco Mezzadri, Chiara Pernechele, Edmondo Gilioli, Gianluca Calestani, Riccardo Cabassi, Fulvio Bolzoni, Gabriele Spina, Marco Lantieri, Massimo Solzi, and Davide Delmonte. "Field effects on spontaneous magnetization reversal of bulk BiFe0.5Mn0.5O3, an effective strategy for the study of magnetic disordered systems." *J Phys Condens Matter*, 2015: doi: 10.1088/0953-8984/27/28/286002.

59. Fratter, I., J. M. Léger, F. Bertrand, T. Jager, G. Hulot, and L., and Vigneron, P. Brocco. "Swarm Absolute Scalar Magnetometers first in-orbit results." *Acta Astronaut.* 121 (2016): 76 – 87.

60. Galsin, Joginder Singh. *Solid State Physics an Introduction to Theory.* U.S.A.: Academic Press, 2019.

61. Gavi, H., et al. "Low-field microwave absorption in pulse laser deposited FeSi thin film." *J. Magn. Magn. Mater*, 2012: 1172.

62. Ghosh, D. K. *Nptel.* January 16, 2020. nptel.ac.in › downloads › lectures-doc › Lecture-8 (accessed January 16, 2020).

63. Golrokh., S. *Microscopic modeling of multiferroic bulk systems, thin films and nano structures.* PhD Thesis, Germany: Martin Luther University, 2013.

64. Goodenough, J. B. *Magnetism and the Chemical Bond.* New York: Wiley, 1963.

65. Gruner., M. Dressel and G. *Electrodynamics of Solids.* United Kingdom.: Cambridge Univ. Press., 2002.

66. Gu, J. J., G. L. Zhao, F. W. Cheng, J. R. Han, and and H. Y. Sun. L. H. Liu. "Magnetoelectric properties of Mn-substituted BiFeO3 thin films with a TiO2 barrier." *Physica B.*, 2011: 4400–4403.

67. Gutiérrez, M.P., H. Montiel, G. Alvarez, and and R. Valenzuela. R. Zamorano. "The effect of metal-to-glass ratio on the low-field microwave absorption at 9.4 GHz of glass-coated CoFeBSi microwires." *Institute of Electrical and Electronics Engineers* 42 (2006): 3380-3382.

68. H. A. Farach, and C. P. Poole. *Handbook of electron spin resonance.* New York: Springer, 1999.

69. Hassink, G. J. Master's thesis, Netherlands: University of Twente, 2004.

70. Hengky, Chang, Moya, Xavier, Mathur, Neil D., Dunn, Steve,. "Evidence of highrate visible light photochemical decolourisation of Rhodamine B with BiFeO3 nanoparticles associated with BiFeO3 photocorrosion." *RSC Advances.* 2 (2012): 11843–11849.

71. Hill, N. A. "Why Are There so Few Magnetic Ferroelectrics?" *J. Phys. Chem B*, 2000: 6694-6709.

72. Hill., R. Seshadri and N. A. "Visualizing the Role of Bi 6s “Lone Pairs” in the Off-Center Distortion in Ferromagnetic BiMnO3." *Chemistry of materials.* 13 (2001): 2892-2899.

73. Huang, F. Z., and and W. W. Lin. X. M. Lu. "Thickness-dependent structural and magnetic properties of BiFeO3 films prepared by metal organic decomposition method." *Applied Physics Letters* 97 (2010): 22.

74. I. A. Sergienko, and E. Dagotto. "Role of the Dzyaloshinskii-Moriya interaction in multiferroic perovskites." *Phys. Rev. B* 73 (2006): 094434.

75. I. V. Solovyev, and Z. V. Pchelkina. "Magnetic-field control of the electric polarization in BiMnO3." *Magnetic-field control of the electric polarization in BiMnO3* 82 (2010): 094425.

76. Isnard., O. "Susceptability- Magnetism." *University of Joseph Fourier.* Nov 12, 2019. magnetism.eu/esm/2013/questions/isnard-susceptibility.pdf imaginary magnetic susceptibility (accessed Nov 12, 2019).

77. J. Buhot., C. Toulouse., Y. Gallais., A. Sacuto., R. de Sousa., D. Wang., and L. Bellaiche. "Driving spin excitations by hydrostatic pressure in BiFeO3." *Physical Review Letters* 115 (2015): 267204.

78. J. Wei, and D. Xue. "Effect of non-magnetic doping on leakage and magnetic properties of BiFeO3 thin films." *Applied Surface Science* 258 (2011): 1373-1376.

79. Jang, H. M., and and J. H. Lee. H. Han. "Spin-coupling-induced Improper Polarizations and Latent Magnetization in Multiferroic BiFeO3." *Scintific Reports*, 2018: DOI:10.1038/s41598-017-18636-9.

80. K. Takahashi, and M. Tonouchi. "Influence of Mn doping on ferroelectric-antiferromagnet BiFeO3 thin films grown on (LaAlO3)0.3(Sr2AlTaO6)0.7 substrates." *Japanese Journal of Applied Physics Part 2.* 45 (2006.): 755–757.

81. Kanamori, Junjiro. "Crystal Distortion in Magnetic Compounds." *Journal of Applied Physics* 31 (1960): 10.1063/1.1984590.

82. Kathleen. "Quantum Design." March 16, 2016. https://www.google.com/url?sa=i&url=https%3A%2F%2Fqdusa.com%2FsiteDocs%2FappNotes%2F1096-306.pdf&psig=AOvVaw1GBubIONVulyf8R9d6WNxk&ust=1600442373583000&source=images&cd=vfe&ved=0CAMQjB1qFwoTCJD4js--8OsCFQAAAAAdAAAAABAH (accessed August 09, 2020).

83. Katsura, H., and and A. V. Balatsky. N. Nagaosa. "Spin Current and Magnetoelectric Effect in Noncollinear Magnets." *Physics Revision Letter.* 95 (2005): 057205.

84. Kawaea, T., Y. Terauchi, H. Tsuda, and and A. Morimoto. M. Kumeda. "Improved leakage and ferroelectric properties of Mn and Ti codoped BiFeO3 thin films." *Appl. Phys. Lett.* 94 (2009): 112904.

85. Khamlich., S., et al. "Photoinduced Electron Spin Resonance Phenomenon in α-Cr2O3 Nanospheres.." *Journal of Nanomaterials*, 2014: 8.

86. Khomskii., D. "Classifying multiferroics: Mechanisms and effects." *APS Physics.* 2 (2009.): 20.

87. Kittel, C. *Introduction to solid state physics.* 8. Vols. Rev. 73, 155 (1948). U.S.A.: John Wiley & Sons, Inc, 2005.

88. KOPOT., A. *AK Lectures.* January 12, 2020. https://aklectures.com/lecture/electric-potential-and-voltage-difference/electric-potential-due-to-electric-dipoles (accessed January 12, 2020).

89. Kundu, T. *Nptelhrd.* January 3, 2013. nptel.ac.in › courses › downloads › module2 › lecture20 (accessed Decemeber 22, 2019).

90. L. Bi, A. R. Taussig, H. Kim, L. Wang, G. F. Dionne, D. Bono and K. Persson,. "Structural, magnetic, and optical properties of BiFeO3 and Bi2FeMnO6 epitaxial thin films." *Physics revision B* 78 (2008): 104106.

91. L. Bi, A.R. Taussig, H. Kim, L. Wang, G. F. Dionne, D. Bono, K. Persson, G. Ceder and C. A. Ross. "Structural, Magnetic, and Optical Properties of BiFeO3 and Bi2FeMnO6 Epitaxial Thin Films: An Experimental and First-Principles Study." *Physical review. B* 78 (2008): 104106.

92. Lebeugle, D., D. Colson, and A., and Viret, M. Forget. "Very large spontaneous electric polarization in BiFeO3 single crystals at room temperature and its evolution under cycling fields." *Appl. Phys. Lett.* 91 (2007.): 022907.

93. Lee, J., and and K. H. Kim J. Kim. "Effect of the magnetization process on low-field microwave absorption by FeBN magnetic thin film." *Physica Status Solidi*, 2014: 1900-1902.

94. Lin Hao, D. Meyers, Hidemaro Suwa, Junyi Yang, Clayton Frederick, Tamene R. Dasa, Gilberto Fabbris, Lukas Horak, Dominik Kriegner, Yongseong Choi, Jong-Woo Kim, Daniel Haskel, Philip J. Ryan, Haixuan Xu, Cristian D. Batista, M. P. M. Dean, Jian Liu. "Giant magnetic response of a two-dimensional antiferromagnet." *Nat. Phys.* 14 (2018): 806-810.

95. Lina, T. T., S. L. Youngb, C. Y. Kunga, H. Z. Chenb, M. C. Kaob, and and C. R. Ou M. C. Changa. "Variable Range Hopping and Thermal Activation Conduction of Y-doped ZnO." *IEEE Transactions on Nanotechnology* 13 (2013): 425 - 430.

96. Liu, M., J. Hoffman, J. Wang, Jinxing. Z, and B., and Bhattacharya, A. Cheeseman. "Magnetoelectric coupling effects in multiferroic complex oxide composite structures." *Scientific Reports*, 2013: 1876.

97. Lorence, Peter Pesheck and Matthew. *Development of Packaging and Products for Use in Microwave Ovens.* Elsevier Science, 30th July 2009.

98. Lubk., A., and and Spaldin N. A. S. Gemming. "First-principles study of ferroelectric domain walls inmultiferroic bismuth ferrite." *Physics revision B* 80 (2009): 104110.

99. Lunghi, A., and Sanvito, S. "How do phonons relax molecular spins?" *Science Advances* 5 (2019): 10.1126/sciadv.aax7163.

100. M. Brustolon, and E. Giamello. *Electron Paramagnetic Resonance: A Practitioner's Toolkit.* U.S.A.: John Wiley & Sons, Inc., 2008.

101. M. M. Vopson, Y. K. Fetisov, G. Caruntu and G. Srinivasan. "Measurement Techniques of the Magneto-Electric." *Materials Review* 10 (2017): 963.

102. Ma, J., et al. "Controllable conductive readout in self-assembled, topologically confined ferroelectric domain walls." *Nature Nanotechnology* 13 (2018): 947 – 952.

103. Maa, J., J. Wanga, M. Chena, R. Peng, J. Maa, and and C. Nana. J. Zhangc. "Geometry confined polar vertex domains in self-assembled BiFeO3 nano-islands." *Materials research letters.* 7 (2019): 399–404.

104. Madhumita Bhaumika, , Arjun Maityb,c, , T.S. Mahulea, V.V. Srinivasua,. "Low field microwave absorption in iron nanoparticles embedded polyaniline nanofibers composite." *Synthetic Metals* 249 (2019): 63–68.

105. Mahule, Tebogo S., and and Jayashree Das. Vijaya V. Srinivasu. "Observation of low field microwave absorption in co-doped ZnO system." *Solid State Communications* 243 (2016): 60-64.

106. Mahule., T S, V. V. Srinivasu, and and J. Das. "Electron Spin Resonance Study of Co-doped ZnO System: Spin-Canted Magnetism and Sintering Effects." *J Supercond Nov Magn*, 2017: 1377–1380.

107. Mahule., T., V.V. Srinivasu, and and J. Das. "Low-field microwave absorption in Zn1−x(Mn:Fe(Ni))xO (x = 0.02) system: hysteresis, line shapes and powdering effects." *Applied Physics A*, 2019: 125.

108. Mandal, P., et al. "Temperature-induced magnetization reversal in BiFe0.5Mn0.503 synthesized at high pressure." *Physical review B.* 82 (2010): 100416.

109. Markus, Z. *Electromagnetic Field Theory - A Problem-Solving Approach – Chapter 9: Radiation.* Febrauary 1, 2016. ocw.mit.edu › MITRES_6_002S08_chp09_pset (accessed Decemeber 27, 2019).

110. Matsushima, M., et al. "Magnetic Cleanliness Program Under Control of Electromagnetic Compatibility for the SELENE (Kaguya) Spacecraft." *Space Science Reviews.* 154 (2010): 253–264.

111. Mezzadri, F., D. Delmonte, E. Gilioli, M. Solzi, G. Calestani, and and R. Cabassi. F. Bolzoni. "Poling-Written Ferroelectricity in Bulk Multiferroic Double-Perovskite BiFe0.5Mn0.5O3." *Inorganic Chemistry* 55 (2016): 6308−6314.

112. Mohamed, W. S., et al. "Optical study of the vibrational and dielectric properties of BiMnO3." *Condensed Matter*, 2016: DOI: 10.1103/PhysRevB.92.054306.

113. Montanari, E., L. Righi, G. Calestani, A. Migliori, and E. Gilioli and F. Bolzoni. "Room Temperature Polymorphism in Metastable BiMnO3 Prepared by High-Pressure Synthesis." *Chemistry of Materials*, 2005: 1765-1773.

114. Montiela, H., G. Alvarez, M. P . Gutiérrez, and and R. Valenzuela. R. Zamorano. "Microwave absorption in Ni–Zn ferrites through the Curie transition." *Journal of Alloys and Compounds* 369 (2004): 141-143.

115. Moore., P. B. *Comprehensive Natural Products Chemistry.* Pergamon: Elsevier, 1999, 1999.

116. Morales, R., et al. "Exchange-bias phenomenon: the role of the ferromagnetic spin structure." *Physics Revision Letters.* 114 (2015): 097202.

117. Mostovoy., M. "Ferroelectricity in spiral magnets." *Phys. Rev. Lett.* 96 (2006): 067601.

118. Msomi., J. Z., T. Moyo., S. Mahule, and and V. V. Srinivasu. "Electron Spin Resonance Study of ZnxCo1−x Fe2−x AlxO4 Nanoparticles." *Journal of Superconductivity and Novel Magnetism*, 2019: 1817–1820.

119. N. A. Spaldin, and R. Ramesh. "Multiferroics: progress and prospects in thin films." *Nature Materials* 6 (2007): 21.

120. Nan, C.W., M. Bichurin, D. Shuxiang, and D., and Srinivasan, G. Viehland. "Multiferroic magnetoelectric composites: historical perspective, status, and future directions." *Journal of Applied Physics* 103 (2008): 031101.

121. Nan, T., et al. "Quantification of strain and charge co-mediated magnetoelectric coupling on ultra-thin Permalloy/PMN-PT interface." *Scientific reports*, 2014: 3688.

122. Neaton, J. B., C. Ederer, U. V. Waghmare, and and K. M. Rabe. N. A. Spaldin. "First-principles study of spontaneous polarization in multiferroic BiFeO3." *Physical Review B* 71 (2005): 014113.

123. Nemangwele., F., V. Sankaran., B. K. Roul., J. Das, and and V. V. Srinivasu. "Non-resonant Microwave Absorption in Nano Nickel Added YBCO Powders: Observation of Multiple Phase Reversals." *J Supercond Nov Magn*, 2017: 1353–1357.

124. Nptel. January 01, 2012. nptel.ac.in › storage2 › courses › downloads › lec-14 (accessed Decemeber 23, 2019).

125. Okonkwo, P., and and H. Smith. "Review of evolving trends in blended wing body aircraft design." *Progress in areospace sciences.*, 2015: http://dx.doi.org/10.1016/j.paerosci.2015.12.002.

126. Onyancha., R. B., J. Shimoyama., J. Das., K. Hayashi., H. Ogino, and and V. V. Srinivasu. "Non-Resonant Microwave Absorption in SmFeAsO0.80F0.20: Line Shape and Structure Evolution with Temperature." *J Supercond Nov Magn*, 2017: 2429–2434.

127. Onyanchaae, R. B., J. Shimoyama, Jayashree Das, H. Ogino, and U. O. Aigbea and V. V. Srinivasu. "Novel normal-state low field microwave absorption in SmFeAsO1−xFx iron pnictide superconductors." *Solid State Communications* 307 (2020): 113800.

128. Pchelkina, I. V. Solovyev and Z. V. "Magnetic ground state and multiferroicity in BiMnO3." *Journal of Experimental and Theoretical Physics* 89 (2009): 597–602.

129. Pchelkina., V. I., and Solovyev Z. V. "Orbital ordering and magnetic interactions in BiMnO3." *New Journal of Physics.* 10 (2008): 073021.

130. Pernechele, C., et al. "Thermally activated magnetization reversal in bulk BiFe0.5Mn0.5O3." *Physical Review B* 88 (2013): 014431.

131. Physics, Department of. *University of Liverpool.* December 21, 2019. pcwww.liv.ac.uk › AdvancedElectromagnetism-Part5 (accessed December 21, 2019).

132. Poole, C. P. *Electron Spin Resonance: A Comprehensive Treatise on Experimental Techniques.* U.S.A.: Interscience Publishers, 1967.

133. Poole, Charles P. *Electron Spin Resonance: A Comprehensive Treatise on Experimental Techniques.* U.S.A.: Dover Publications, 1996.

134. Prokhorov, V. G., and Kaminsky, G. G. "Evidence of the Griffiths phase in multiferroic BiMnO3 and BiFe0.5Mn0.5O3 films." *Low Temperature Physics* 38 (2012): 531.

135. Prosandeev, S., D. Wang, W. Ren, and and Bellaiche, L. Iniguez J. "Novel magnetic arrangement and structural phase transition induced by spin-lattice coupling in multiferroics." *Advanced functional matter* 23 (2013): 234.

136. Q. A. Pankhurst, and R. J. Pollard. "Applied field Mössbauer Spectroscopy of magnetic powders." *Mössbauer Spectroscopy Applied to Magnetism and Materials Science*, 1996: 77-113.

137. R. de Sousa, M. Allen and M. Cazayous. "Theory of spin-orbit enhanced electric-field control of magnetism in multiferroic BiFeO3." 110 (2013): 267202.

138. R. L. Kurtz, and V. E. Henrich. "Surface electronic structure and chemisorption on corundum transition-metal oxides: V2O3." *Physical Review B* 28 (1983): 6699–6706.

139. R. Ramesh, and N. A. Spaldin. "Multiferroics: progress and prospects in thin films." 6 (2007): 21.

140. Rahmedov, D., D. Wang, and J., and Bellaiche, L. Iniguez. "Size-dependent bistability in multiferroic nanoparticles." *Physics Revision Letter* 109 (2012): 037207.

141. Ramesh, R., and and J. B. Neaton. J. Wang. "Epitaxial BiFeO3 multiferroic thin film heterostructures." *Science* 299 (2003): 1719–1722.

142. Rana, D. S., and and K. R. Mavani. K. Takahashi. "Thickness dependence of the structure andmagnetization of BiFeO3 thin films on (LaAlO3)0.3 (Sr2AlTaO6)0.7 (001) substrate." *Physical Review B* 75 (2007): 060405.

143. Rancourt., D. G. *Nucl. Instr. Methods Phys. Res.* Sect. B 44. (1989): 199.

144. Ren, Y., Palstra, T. T. M., Khomskii, D. I., Pellegrin, E., Nugroho, A. A., Menovsky, A. A. and Sawatzky, G. A. "Temperature-induced magnetization reversal in a YVO3 single crystal." 396 (1998): 441-444.

145. Robert, S., and D. C., and Peters, R. Balaban. "Basic Principles of Cardiovascular Magnetic Resonance." *Cardiovascular Magnetic Resonance*, 2010: 3-18.

146. Rusakov, D. A., A. M. Abakumov, K. Yamaura, A. A. Belik, and and E. T. Muromachi. G. V. Tendeloo. "Structural Evolution of the BiFeO3−LaFeO3 System." *Chem. Mater.* 2 (2010): 285-292.

147. Sajjia., M., and and G.A. Olabi. M. Hasanuzzaman. "Magnetostrictive Cobalt Ferrite, Nanoparticles Preparation and Magnetic Characterization." *Materials Science and Materials Engineering.*, 2015: 10.1016/B978-0-12-803581-8.03996-5.

148. Santosa, A. Moreira dos, S. Parashar, R.Raju, Y. S. Zhao, and A. K. Cheetham and C. N. R. Rao. "Evidence for the likely occurrence of magnetoferroelectricity in the simple perovskite, BiMnO3." *Solid State Communications* 122 (2002): 49-52.

149. Sara., Moshe, and and Wolfson. *Sara and Moshe Zisapel nanoelectronic center & Wolfson microelectronic center.* Jauary 01, 2003. https://mnfu.technion.ac.il/hr-sem-hitachi-s-4800/ (accessed October 21, 2021).

150. Semenov, A. A., S. F. Karmanenko, V. E. Demidov, B. A. Kalinikos, G. Srinivasan, and and J. V. Mantese. A. N. Slavin. *Appl. Phys. Lett.* 88 (2006): 033503.

151. Shang, L., Y. Sheng, L. Q. Wang, and and Z. Liu. K. Chen. "Elastic properties of cubic and rhombohedral BiFeO3 from first-principles calculations." *Physics reveiw B* 80 (2009): 052102.

152. Shen, L. M., X. G. Tang, Q. X. Liu, Y. P. Jiang, and and W. P. Li. Y. G. Wang. "Room temperature ferroelectric properties and leakage current characterics of Bi2FeMnO6SrTiO3 bilayered thin films by chemical solution deposition." *Physica Status Solidi*, 2014: 10.1002/pssa.201330617.

153. Solovyev, D. W. and Boukhvalov, I. V. "Defects of the crystal structure and Jahn-Teller distortion in BiMnO3." *Physical Review B.* 82 (2010): 245101.

154. Solovyev, I. V. "Combining DFT and many-body methods to understand correlated materials." *Journal of Physics: Condensed Matter* 20 (2008): 293201.

155. Solovyev, I. V., Z. V. Pchelkina, and Z, and Teor, E. Pisma. *JETP Letter.* 89 (2009): 701.

156. Solovyev, V. I. "Combining DFT and many-body methods to understand correlated materials." *Journal of Physics: Condensed Matter* 20 (2008): 293201.

157. Solovyev., D. W. Boukhvalov and I. V. "Defects of the Crystal Structure and Jahn-Teller distortion in BiMnO3." *Physical Review B* 82 (2010): 245101.

158. Srinavasu., V. V., J. Das, and and Mahule, T. D. R. Sahu. "Low Field Microwave Absorption in Mn:Ni Co-Doped ZnO μm Size Powders." *Acta Physica Polonica A* 134 (2018): 326-328.

159. Srinivasu., V. V., et al. "Ferromagnetism at room temperature in La0.8Ca0.2MnO3 thin films." *Applied Physics Letters* 74 (1999): 1886.

160. Sun., Lin, et al. "Coexistence of spin glass and ferroelectricity in highly ordered Bi2FeMnO6 epitaxial thin film." *Condensed matter and material science*, 2016.

161. Tang, X. G., J. Wang, and and H. L. W. Chan. Y. W. Zhang. "Room temperature ferroelectric properties and leakage current characterics of Bi2FeMnO6/SrTiO3 bilayered thin films by chemical solution deposition." *Journal of applied physics.* 94 (2003): 5163.

162. Technologies, Keysight. *Keysight Technologies.* January 01, 2000. https://www.keysight.com/zz/en/product/E4991B/impedance-analyzer-1-mhz-500-mhz-1-ghz-3-ghz.html (accessed October 20, 2021).

163. Terakura, I. V. Solovyev and K. "Zone Boundary Softening of the Spin-Wave Dispersion in Doped Ferromagnetic Manganites." *Physical Review Letters.* 82 (1999): 2959.

164. Torchia, D.A. "Spin-lattice relaxation in solids." *Journal of Magnetic Resonance* 49 (1969): 107 - 121.

165. Toupet, H., V.V. Shvartsman, F. Lemarrec, P. Borisov, and W., and Karkut, M. Kleemann. "Enhanced magnetization in BiFeO3/BaTiO3 multilayers: an interface effect." *Integrated Ferroelectrics* (Taylor and Francis Ltd.) 100 (2008): 165-176.

166. USAAF. *United States Air Force.* September 23, 2015. https://www.af.mil/About-Us/Fact-Sheets/Display/Article/104506/f-22-raptor/ (accessed October 21, 2021).

167. Ustinov, A. B., and and B. A. Kalinikos. G. Srinivasan. *Appl. Phys. Letter.* 90 (2007): 031913.

168. Ustinov, A. B., et al. "Dynamic electromagnonic crystal based on artificial multiferroic heterostructure." *Communications Physics* 2 (2019): 137.

169. Valenzuela, R., et al. "Characterization of magnetic materials by low-field microwave absorption techniques." *Journal of Magnetism and Magnetic Materials* 320 (2008): 1961 - 1965.

170. Vallabhapurapu., V. S., and and S. M. Bhagat. S. E. Lofland. "Room temperature colossal microwave magnetoimpedance in micron-size powders of La0.7Ba0.3MnO3 and La0.7Sr0.3MnO3." *Appl. Phys* 83 (1998): 2866.

171. Vopson, Melvin M. "Fundamentals of Multiferroic Materials and Their Possible Applications." *Researchgate.* April 15, 2014. www.researchgate.net (accessed 10 12, 2019).

172. W. Tong, B. Zhang, S. Tan, and Y. Zhang. "Probability of double exchange between Mn and Fe." *Physics revision B*, 2004: 014422.

173. Wang, D., and J., and Bellaiche, L. Weerasinghe. "Novel magnetic arrangement and structural phase transition induced by spin-lattice coupling in multiferroics." *Physics Revison Letter* 109 (2010): 067203.

174. Xu, Q. Y., and and Z. Wen. S. Q. Zhou. "Magnetic characterization of Bi(Fe1−xMnx)O3." *Physics Letters A* 375 (2011): 1209–1212.

175. Y. K. Fetisov, and G. Srinivasan. "Electrically tunable ferrite-ferroelectric microwave delay lines." *Appl. Phys. Lett.* 85 (2005): 103502.

176. Y. Tokura, and S. Seki. "Multiferroics with Spiral Spin Orders." *Advanced materials.* 22 (2010): 554–1565.

177. Y. Wang, Y. H. Lin, and C. W. Nan. "Multiferroic behavior and impedance spectroscopy of bilayered BiFeO3/CoFe2O4 thin films." *Journal of Applied Physics* 104 (2008): 123912.

178. Z. V. Pchelkina., and I. V. Solovyev. "Magnetic-field control of the electric polarization in BiMnO3." *Magnetic-field control of the electric polarization in BiMnO3* 82 (2010): 094425.

179. Zelevinsky, A. Tayebi and V. "The Holstein polaron problem revisited." *Journal of Physics A* 49 (2016): 10.1088/1751-8113/49/25/255004.

180. Zhang, W., and Krishnan, K. M. "Epitaxial exchange-bias systems: from fundamentals to future spin-orbitronics." *Materials Science and Engineering.* 116 (2016): 1-20.

181. Zhao, H. F., et al. "Structure, magnetic and electrical properties of disordered double perovskite Pb2CrMoO6." *Solid state communications* 204 (2015): 1 - 4.

182. Zhu, L. L., et al. "Hexagonal and orthorhombic perovskite phases of ErMnO3 and TmMnO3 from hydrothermal systems." *Chem. Res. Chin.* 26 (2010): 707.

183. Zwiebach, B. *MIT open courseware.* June 17, 2014. https://ocw.mit.edu/courses/physics/8-05-quantum-physics-ii-fall-2013/video-lectures/lecture-24-addition-of-angular-momentum/ (accessed December 22, 2019).